Radiology for PET/CT Reporting

Cristina Nanni
Stefano Fanti
Lucia Zanoni
Rita Golfieri
Editors

Second Edition

Springer

Radiology for PET/CT Reporting

Cristina Nanni • Stefano Fanti
Lucia Zanoni • Rita Golfieri
Editors

Radiology for PET/CT Reporting

Second Edition

Springer

Editors
Cristina Nanni
Department of Nuclear Medicine
IRCCS Azienda Ospedaliera-Universitaria di Bologna
Bologna, Bologna, Italy

Stefano Fanti
Department of Nuclear Medicine
IRCCS Azienda Ospedaliera-Universitaria di Bologna
Bologna, Bologna, Italy

Lucia Zanoni
Department of Nuclear Medicine
IRCCS Azienda Ospedaliera-Universitaria di Bologna
Bologna, Bologna, Italy

Rita Golfieri
Department of Radiology
IRCCS Azienda Ospedaliera-Universitaria di Bologna
Bologna, Bologna, Italy

ISBN 978-3-030-87640-1 ISBN 978-3-030-87641-8 (eBook)
https://doi.org/10.1007/978-3-030-87641-8

This Springer imprint is published by the registered company Springer Nature Switzerland AG
The registered company address is: Gewerbestrasse 11, 6330 Cham, Switzerland

Preface

PET/CT interpretation may sometimes be challenging. It is common experience to meet abnormal findings on CT images (not necessarily related to the neoplastic disease under evaluation) that are functionally silent and, consequently, unclear for nuclear medicine practitioners. Frequently, these findings are clinically relevant and deserve to be reported, interpreted, and compared to previous scans. This may have an impact on patient management since the highest diagnostic information must be provided by an expensive test such as PET/CT.

Furthermore, there are several highly metabolic benign findings whose correct interpretation depends on the capacity to read all the corresponding CT images.

CT reading can, in few words, contribute to increase PET specificity.

Generally, CT images associated to a PET scan are acquired in a low-dose modality, thick slices, and without intravenous contrast injection. They are, therefore, optimal for PET findings, anatomical localization but suboptimal for CT image interpretation, especially in complicated areas such as the abdomen where diagnostic CT previously acquired may be of great help for PET/CT reading or comparison.

Oncological patients usually need a diagnostic CT evaluation beside PET. In many PET centres, therefore, a contrast-enhanced full-dose CT acquisition is now routinely associated to PET and reported beside.

Whether the PET doctor is reading a PET/low-dose CT comparing it to a previous diagnostic CT or a PET/full-dose contrast-enhanced CT, a common knowledge on CT interpretation is now necessary.

This atlas provides chapters on normal anatomy, including images from both low-dose and contrast-enhanced full-dose CT, identifying the most relevant anatomical structures to easily support the PET/CT reader in accurately describing all FDG-positive findings extension. Other chapters (thorax, abdomen, pelvis, musculoskeletal system) present cases with common and uncommon anatomical abnormalities and pathological findings on both low-dose and full-dose contrast-enhanced CT.

In the end, this atlas is aimed to help nuclear medicine practitioners routinely reading PET/CT scan in easily recognizing and interpreting the most common CT abnormalities.

Bologna, Italy — Cristina Nanni
Bologna, Italy — Stefano Fanti
Bologna, Italy — Lucia Zanoni
Bologna, Italy — Rita Golfieri

Contents

1 Normal Anatomy 1
Cristina Nanni, Stefano Fanti, Lucia Zanoni, Rita Golfieri, Alberta Cappelli, Maria Adriana Cocozza, and Laura Bartalena

2 Head and Neck 79
Cristina Nanni, Stefano Fanti, and Lucia Zanoni

3 Thorax 83
Cristina Nanni, Stefano Fanti, Lucia Zanoni, Rita Golfieri, Stefano Brocchi, Nicolò Brandi, and Anna Parmeggiani

4 Abdomen 153
Cristina Nanni, Stefano Fanti, Lucia Zanoni, Rita Golfieri, Cristina Mosconi, Anna Parmeggiani, and Nicolò Brandi

5 Pelvis 191
Cristina Nanni, Stefano Fanti, Lucia Zanoni, Rita Golfieri, Alberta Cappelli, and Arrigo Cattabriga

6 Musculoskeletal 199
Cristina Nanni, Stefano Fanti, Lucia Zanoni, Rita Golfieri, Cristina Mosconi, and Arrigo Cattabriga

Normal Anatomy

1

Cristina Nanni, Stefano Fanti, Lucia Zanoni, Rita Golfieri, Alberta Cappelli, Maria Adriana Cocozza, and Laura Bartalena

C. Nanni (✉) · S. Fanti · L. Zanoni
Department of Nuclear Medicine, IRCCS Azienda Ospedaliera-Universitaria di Bologna, Bologna, Italy
e-mail: cristina.nanni@aosp.bo.it; stefano.fanti@aosp.bo.it; lucia.zanoni@aosp.bo.it

R. Golfieri
Department of Radiology, IRCCS Azienda Ospedaliera-Universitaria di Bologna, Bologna, Italy
e-mail: rita.golfieri@unibo.it

A. Cappelli
University of Bologna, Bologna, Italy
e-mail: alberta.cappelli@aosp.bo.it

M. A. Cocozza · L. Bartalena
Department of Radiology, IRCCS Azienda Ospedaliera-Universitaria di Bologna, Bologna, Italy
e-mail: mariaadriana.cocozza@studio.unibo.it; laura.bartalena@studio.unibo.it

C. Nanni et al. (eds.), *Radiology for PET/CT Reporting*,
https://doi.org/10.1007/978-3-030-87641-8_1

Normal Anatomy Low Dose Non Contrast Enhanced CT

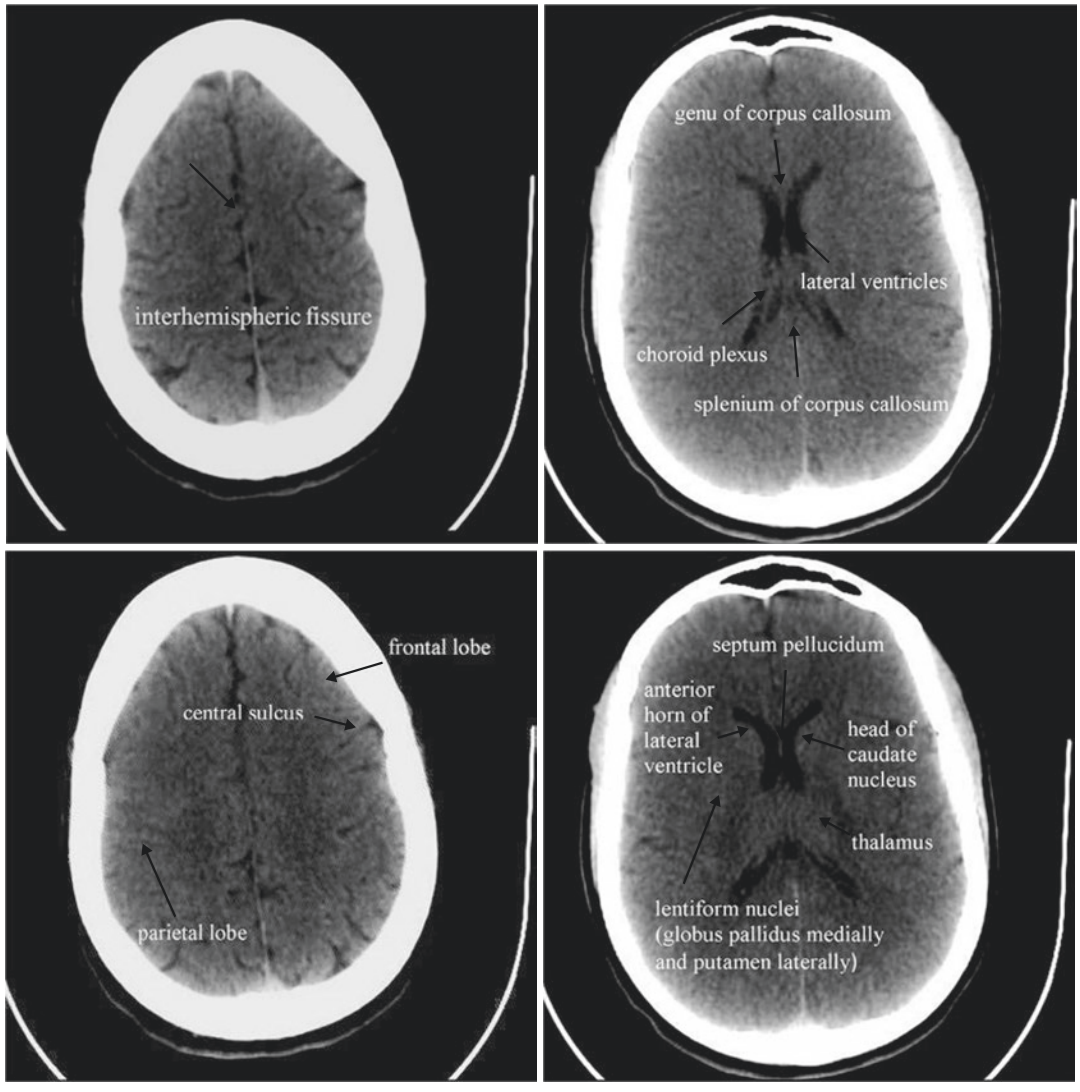

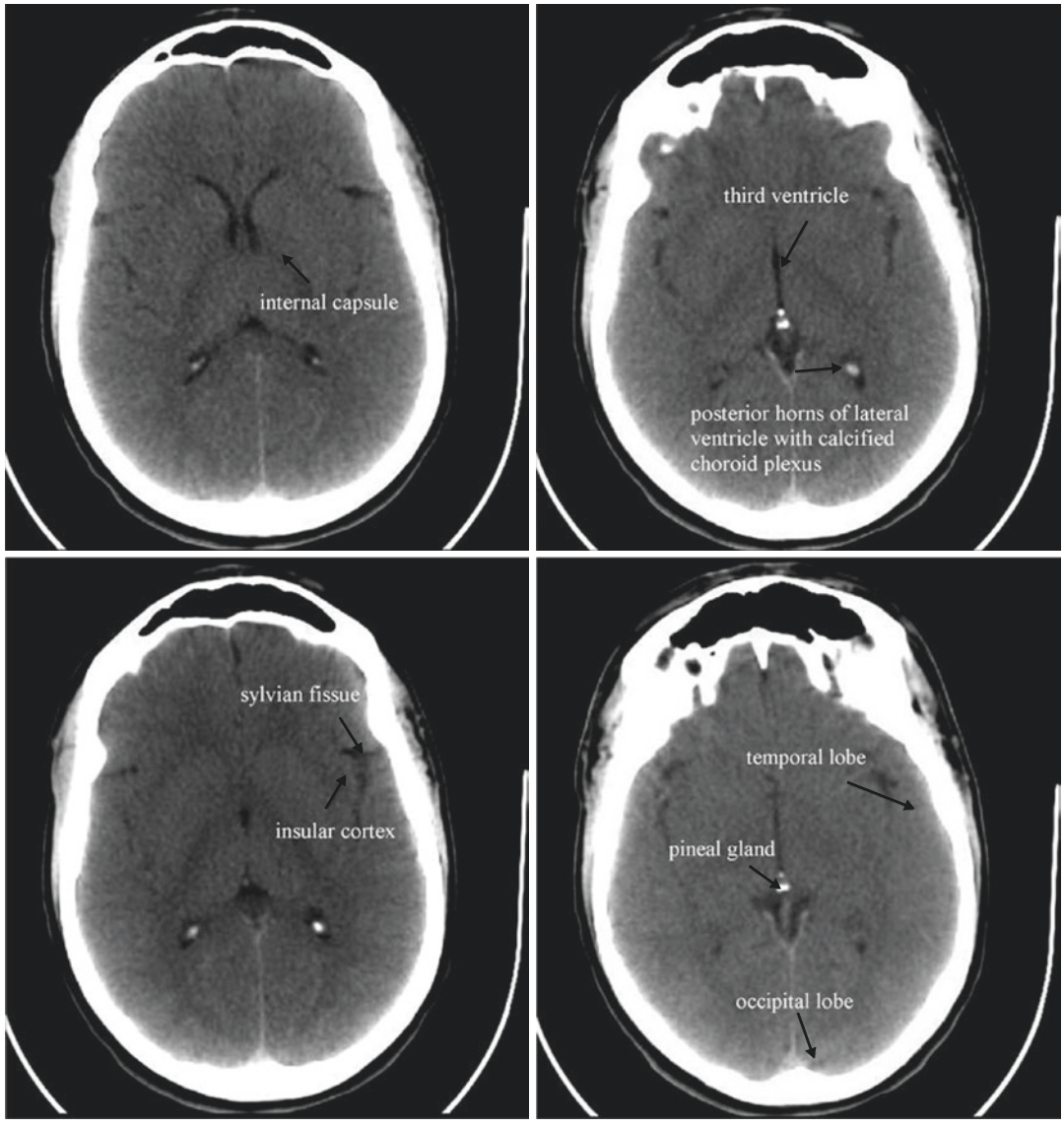
internal capsule
third ventricle
posterior horns of lateral ventricle with calcified choroid plexus
sylvian fissue
insular cortex
temporal lobe
pineal gland
occipital lobe

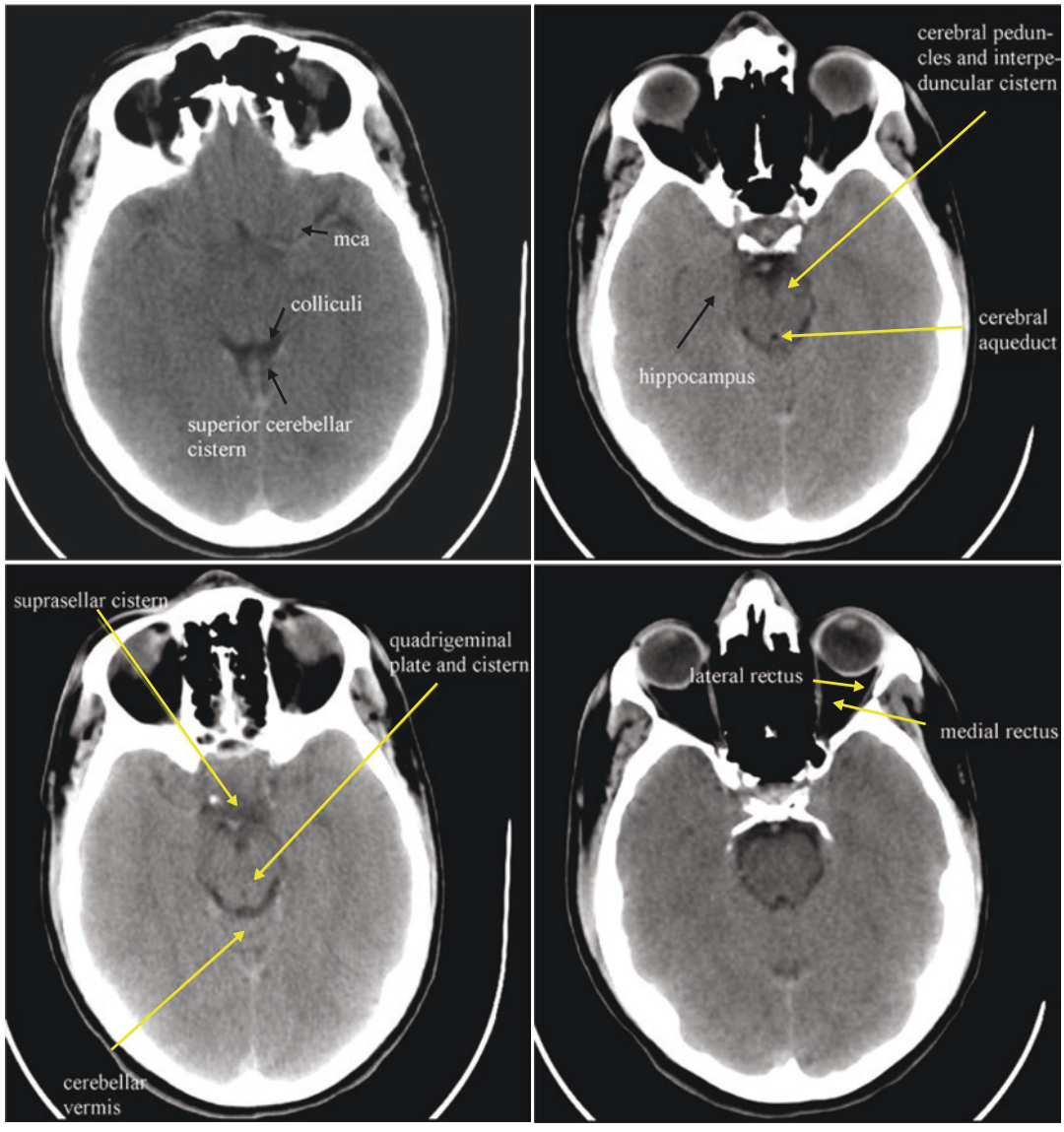
mca
colliculi
superior cerebellar cistern
cerebral peduncles and interpeduncular cistern
cerebral aqueduct
hippocampus
suprasellar cistern
quadrigeminal plate and cistern
cerebellar vermis
lateral rectus
medial rectus

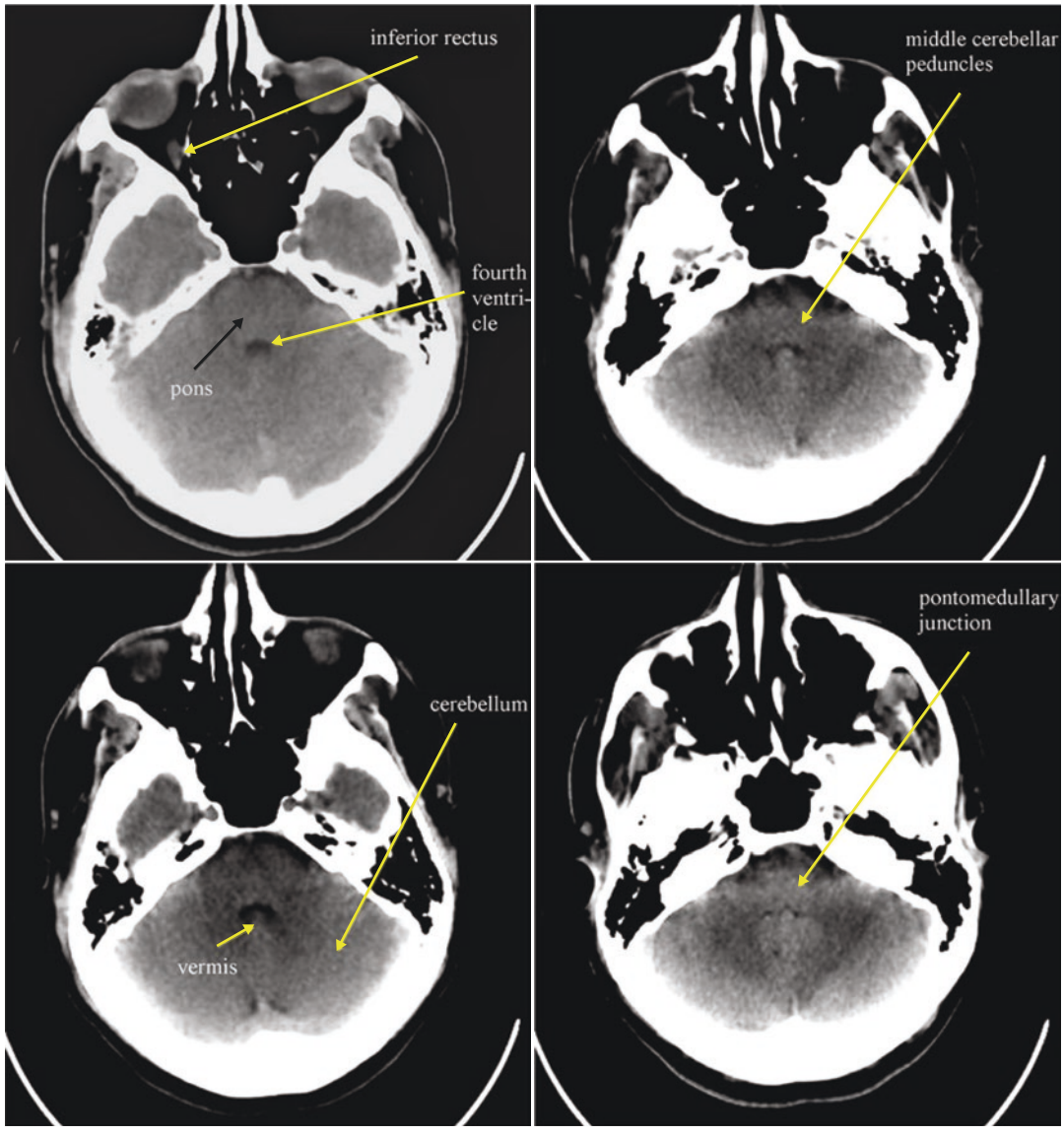
inferior rectus
fourth ventri-cle
pons
middle cerebellar peduncles
cerebellum
vermis
pontomedullary junction

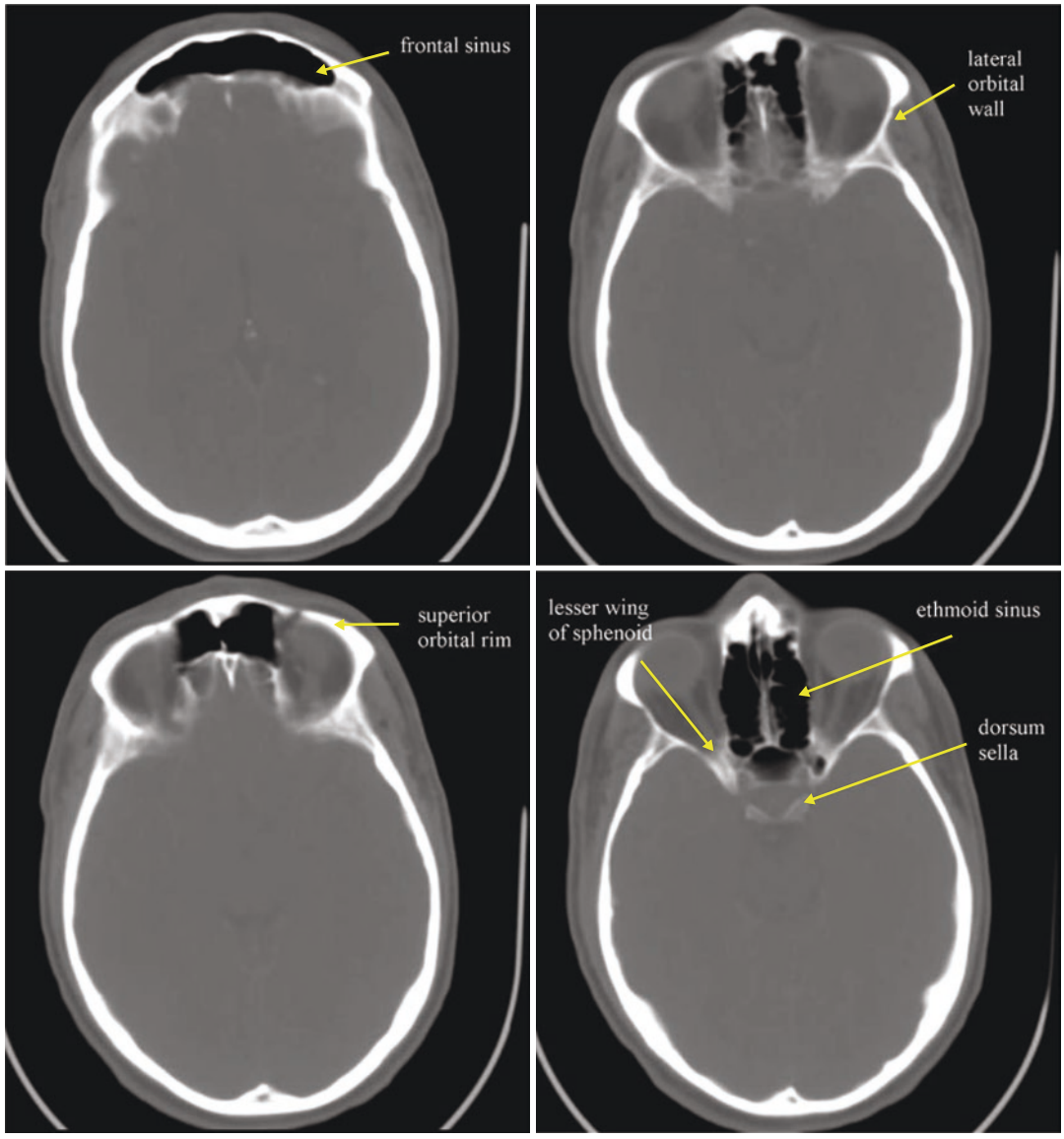
frontal sinus
lateral orbital wall
superior orbital rim
lesser wing of sphenoid
ethmoid sinus
dorsum sella

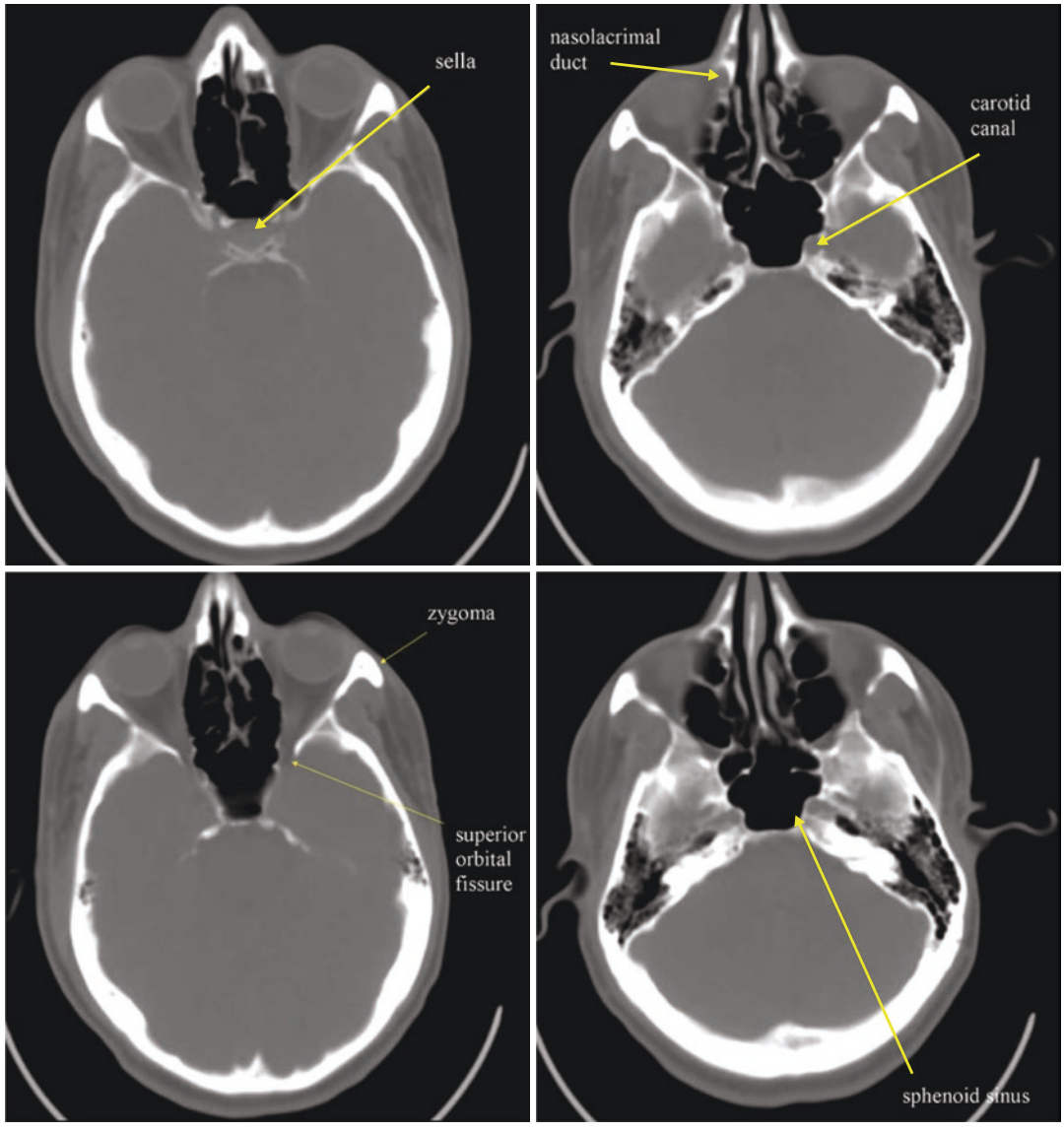
sella
nasolacrimal duct
carotid canal
zygoma
superior orbital fissure
sphenoid sinus

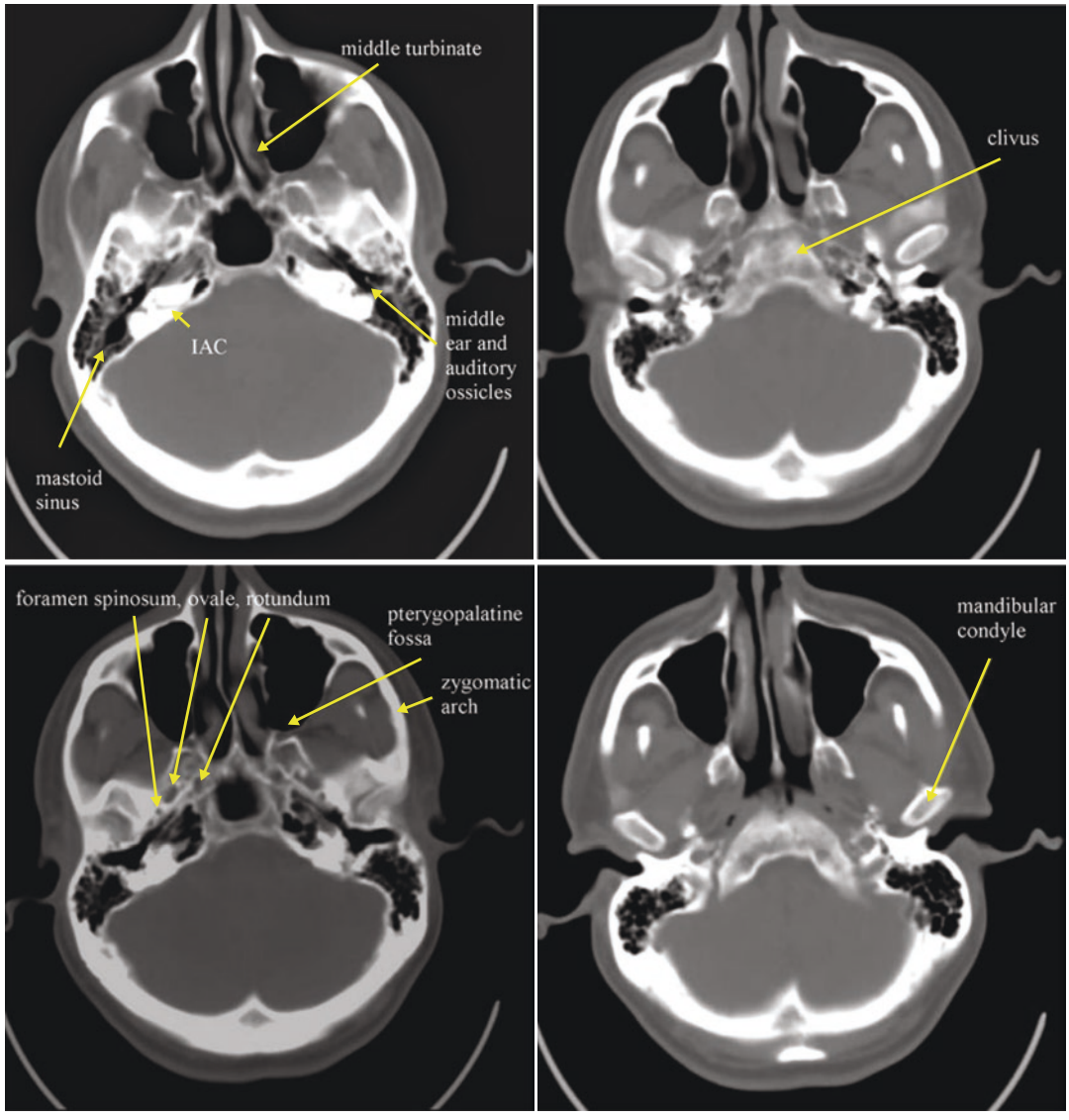
middle turbinate
IAC
middle ear and auditory ossicles
mastoid sinus
clivus
foramen spinosum, ovale, rotundum
pterygopalatine fossa
zygomatic arch
mandibular condyle

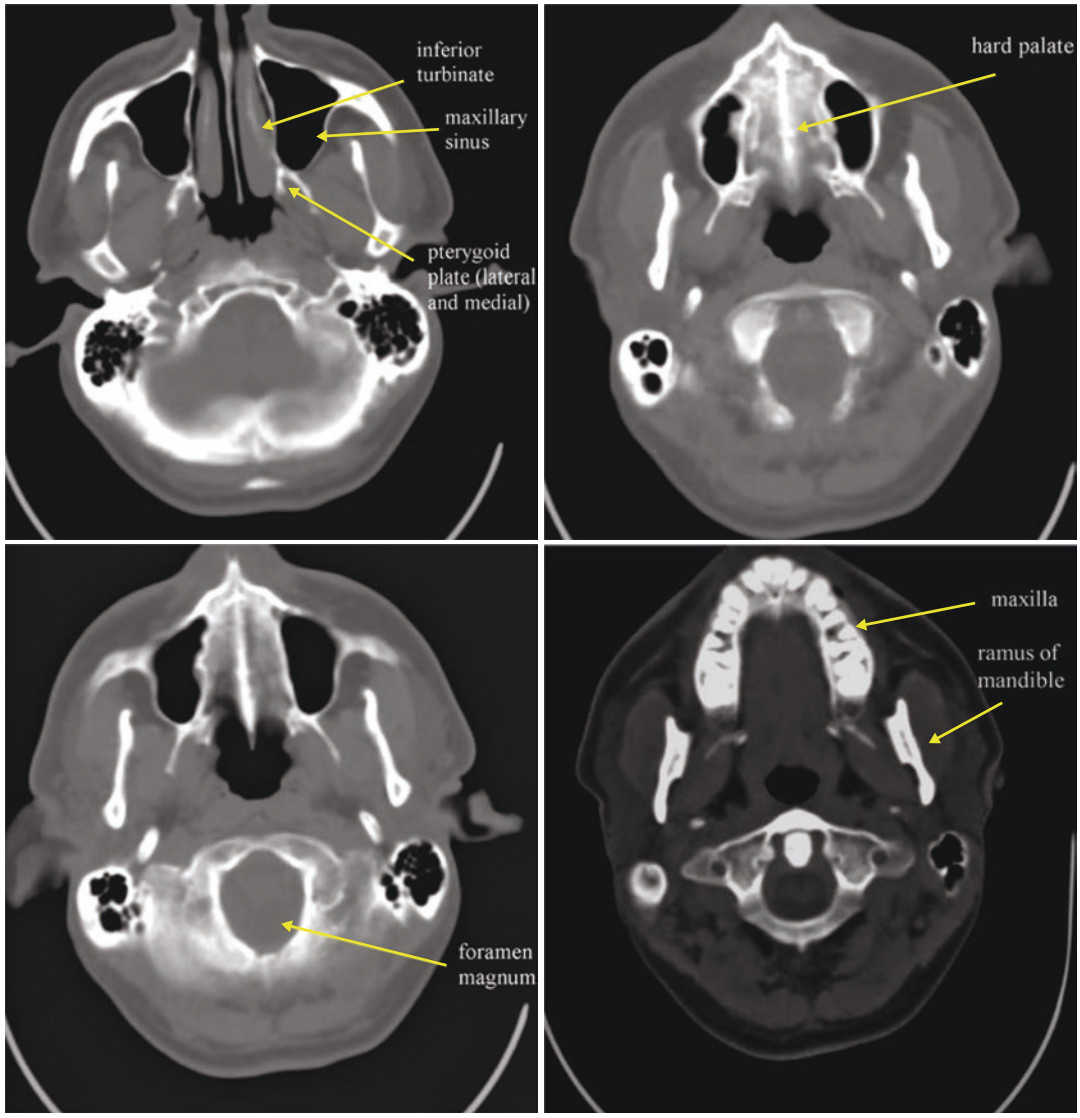
inferior turbinate
maxillary sinus
pterygoid plate (lateral and medial)
hard palate
foramen magnum
maxilla
ramus of mandible

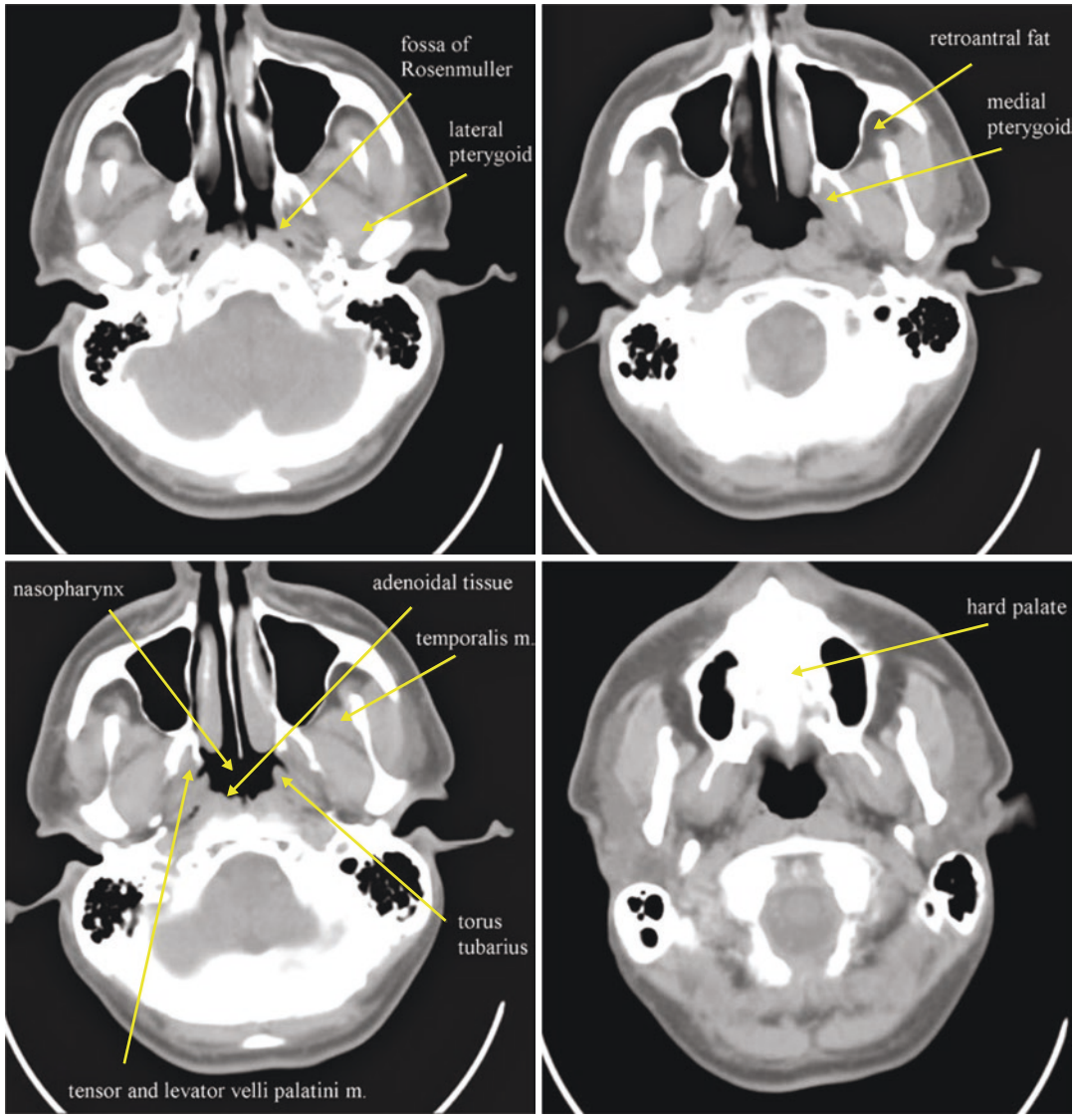
fossa of Rosenmuller
lateral pterygoid
retroantral fat
medial pterygoid
nasopharynx
adenoidal tissue
temporalis m.
torus tubarius
tensor and levator velli palatini m.
hard palate

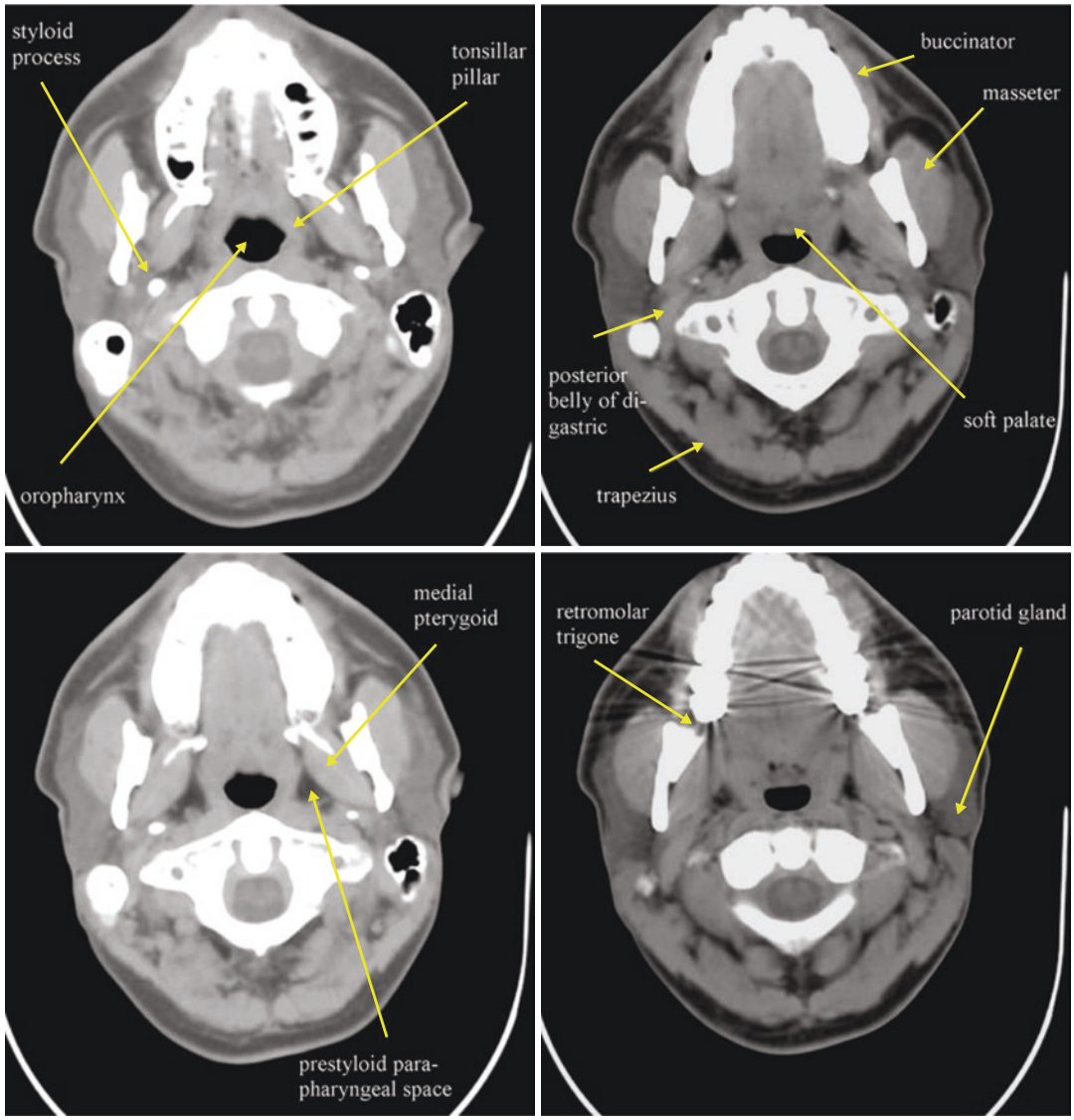
styloid process
tonsillar pillar
oropharynx
buccinator
masseter
posterior belly of digastric
soft palate
trapezius
medial pterygoid
prestyloid parapharyngeal space
retromolar trigone
parotid gland

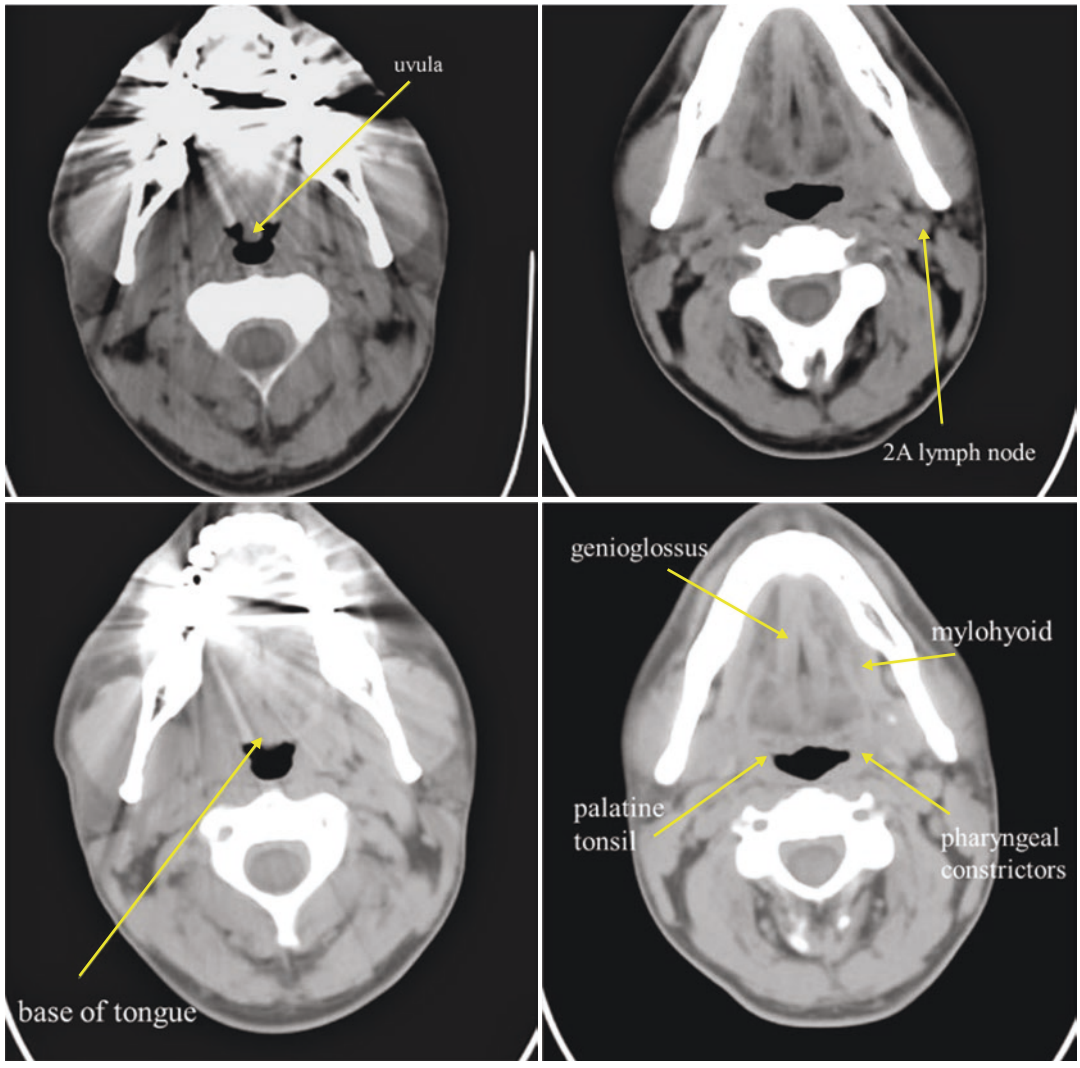
uvula
2A lymph node
base of tongue
genioglossus
mylohyoid
palatine tonsil
pharyngeal constrictors

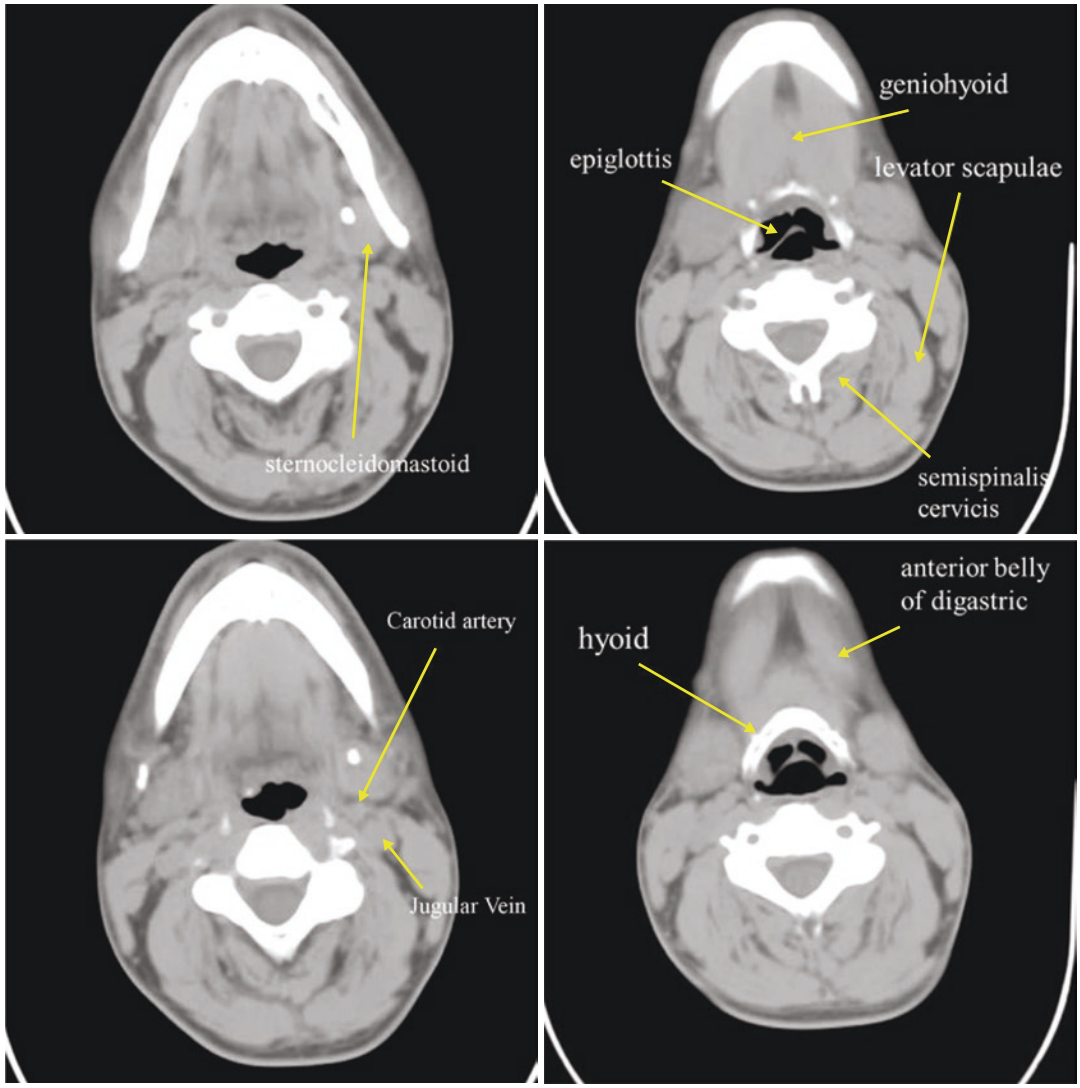
sternocleidomastoid
geniohyoid
epiglottis
levator scapulae
semispinalis cervicis
Carotid artery
Jugular Vein
anterior belly of digastric
hyoid

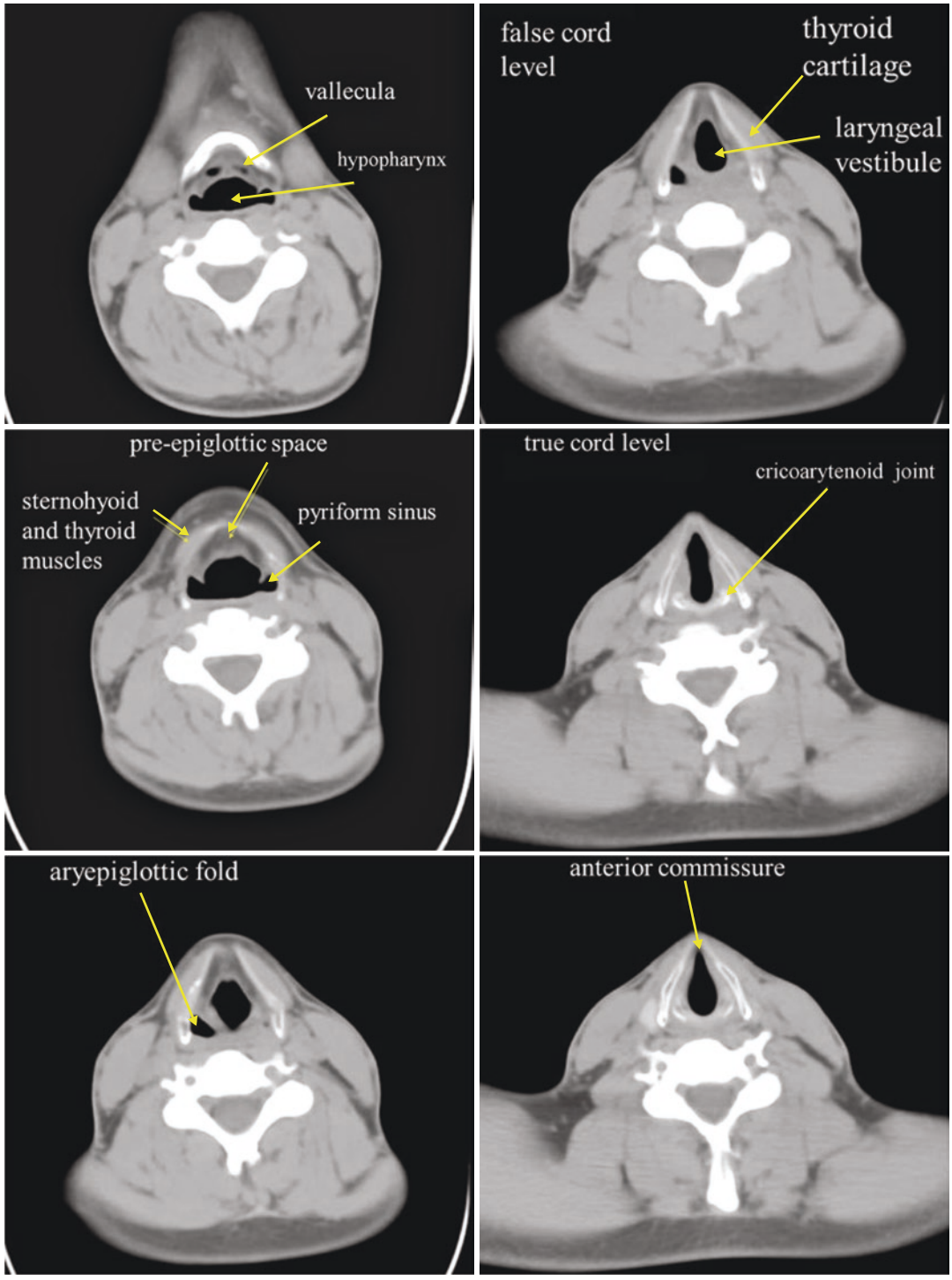
vallecula
hypopharynx
false cord level
thyroid cartilage
laryngeal vestibule
pre-epiglottic space
sternohyoid and thyroid muscles
pyriform sinus
true cord level
cricoarytenoid joint
aryepiglottic fold
anterior commissure

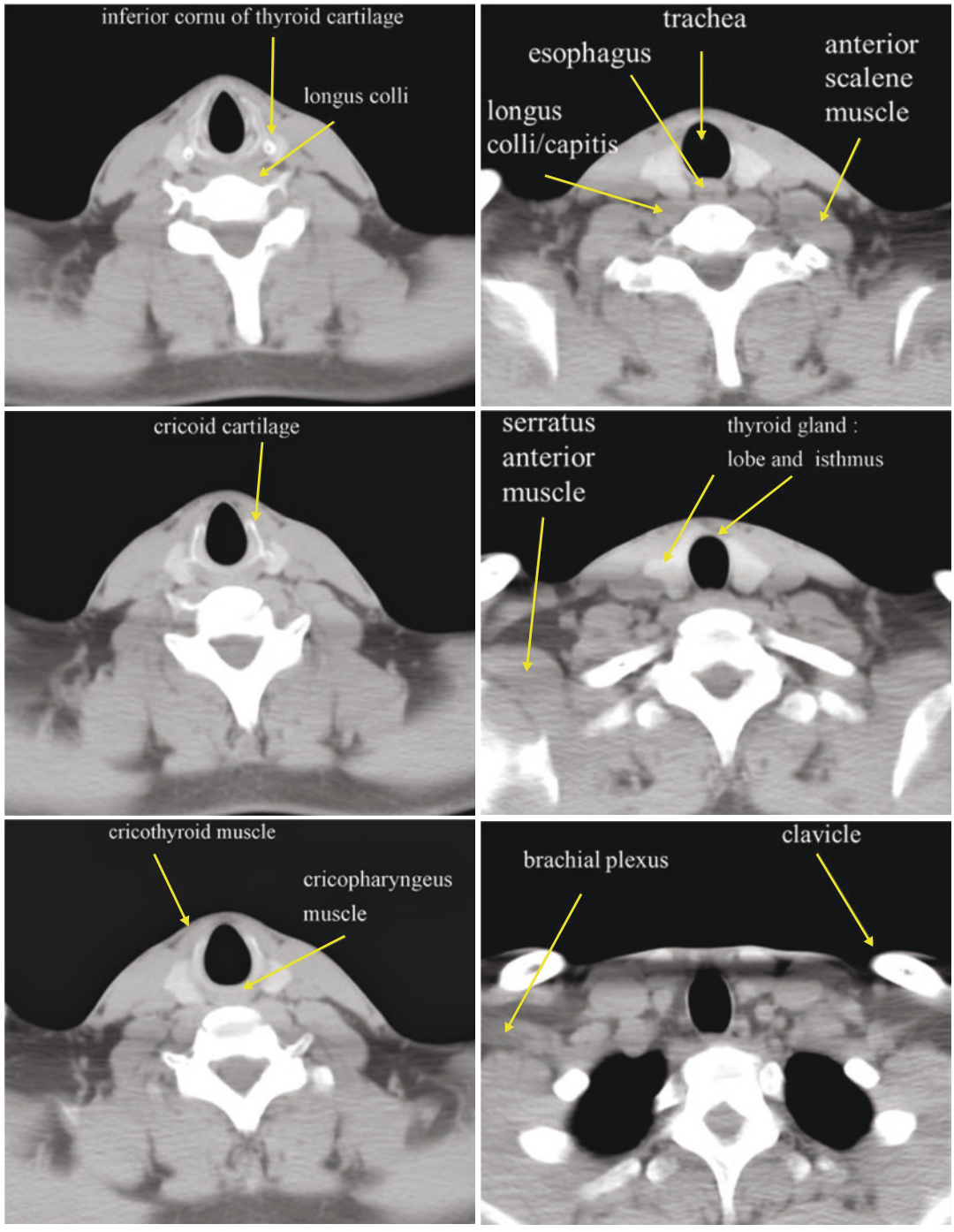
inferior cornu of thyroid cartilage
longus colli
trachea
esophagus
anterior scalene muscle
longus colli/capitis
cricoid cartilage
serratus anterior muscle
thyroid gland : lobe and isthmus
cricothyroid muscle
cricopharyngeus muscle
brachial plexus
clavicle

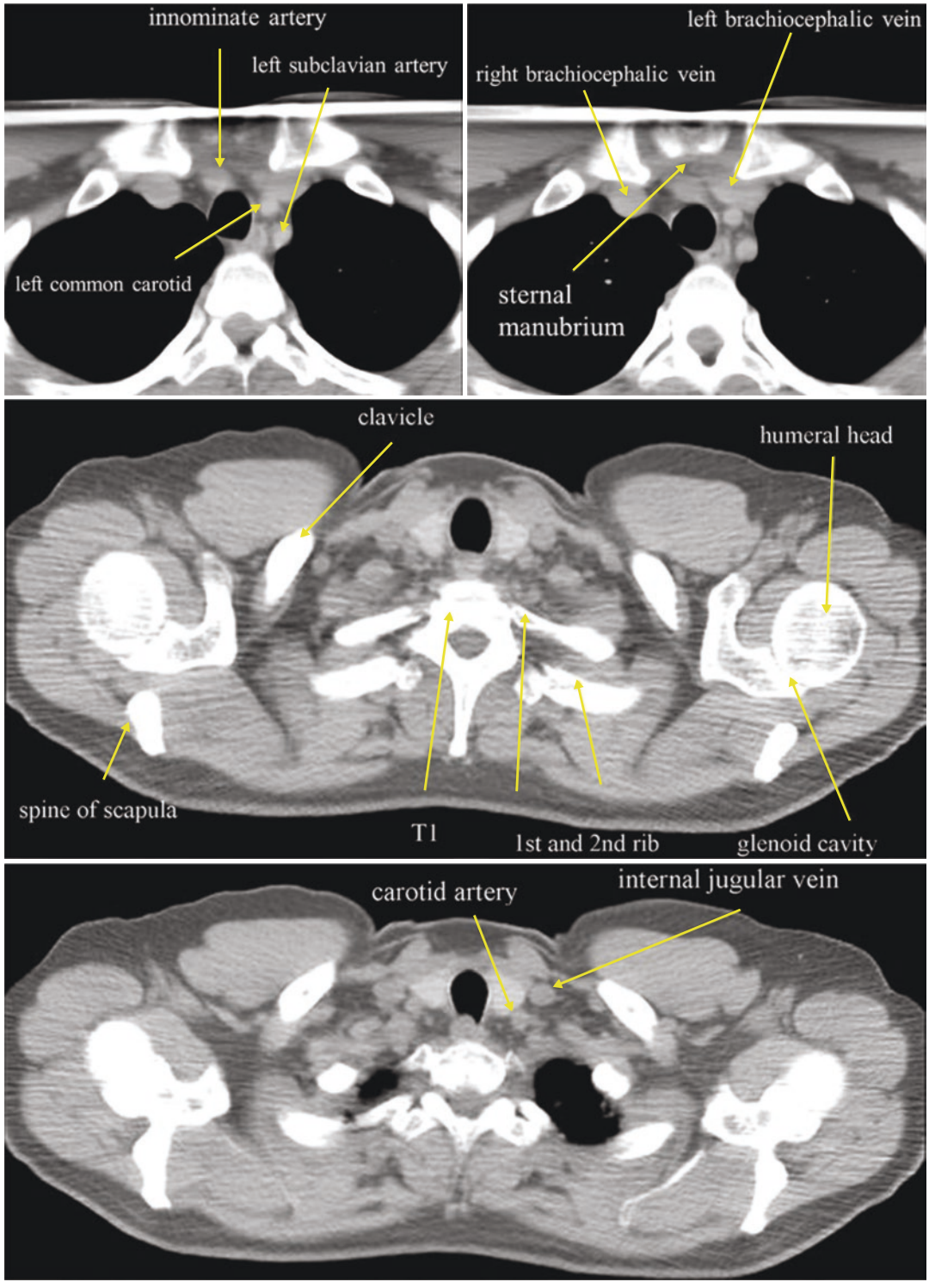
innominate artery
left subclavian artery
left common carotid
left brachiocephalic vein
right brachiocephalic vein
sternal manubrium
clavicle
humeral head
spine of scapula
T1
1st and 2nd rib
glenoid cavity
carotid artery
internal jugular vein

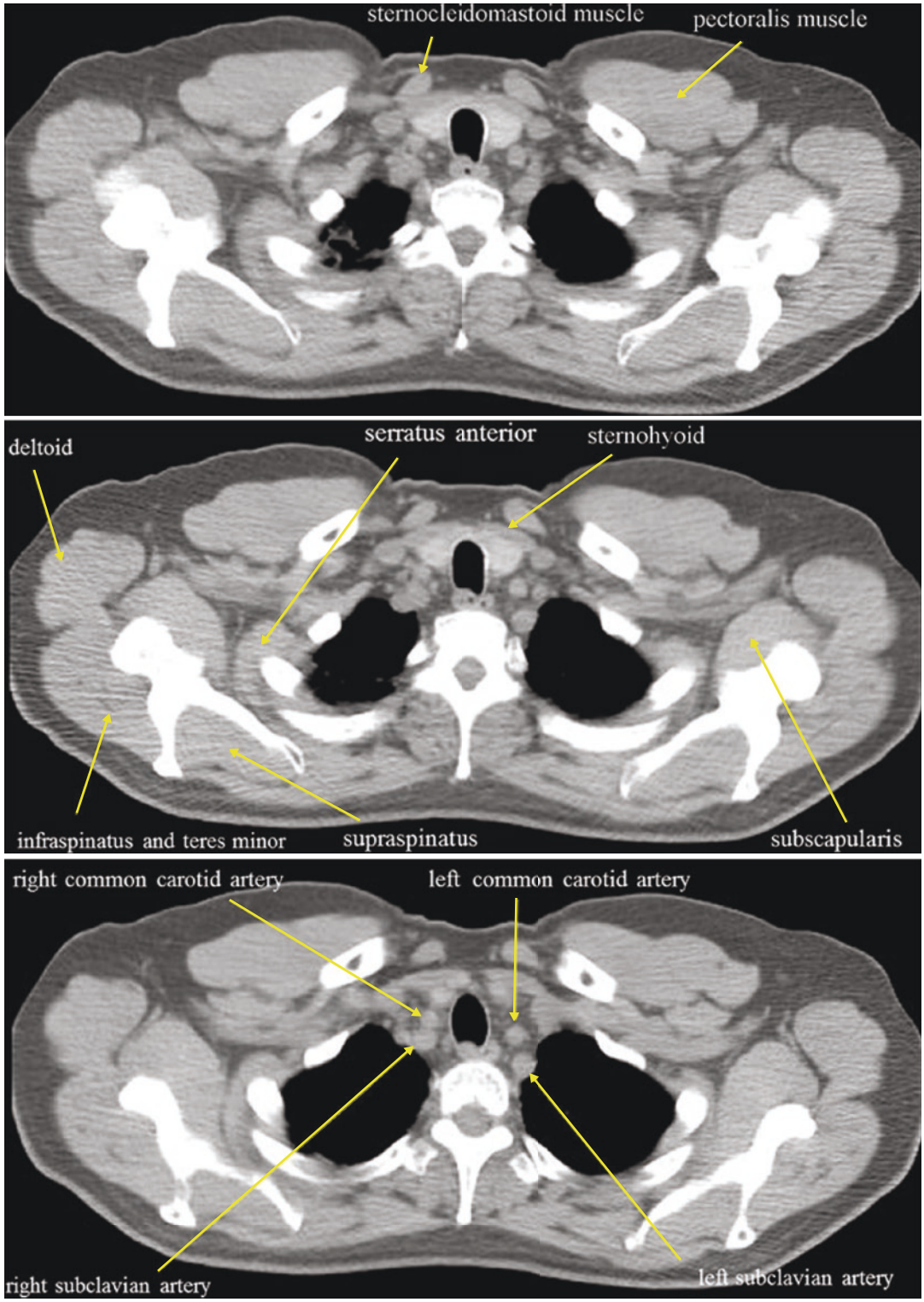
sternocleidomastoid muscle
pectoralis muscle
deltoid
serratus anterior
sternohyoid
infraspinatus and teres minor
supraspinatus
subscapularis
right common carotid artery
left common carotid artery
right subclavian artery
left subclavian artery

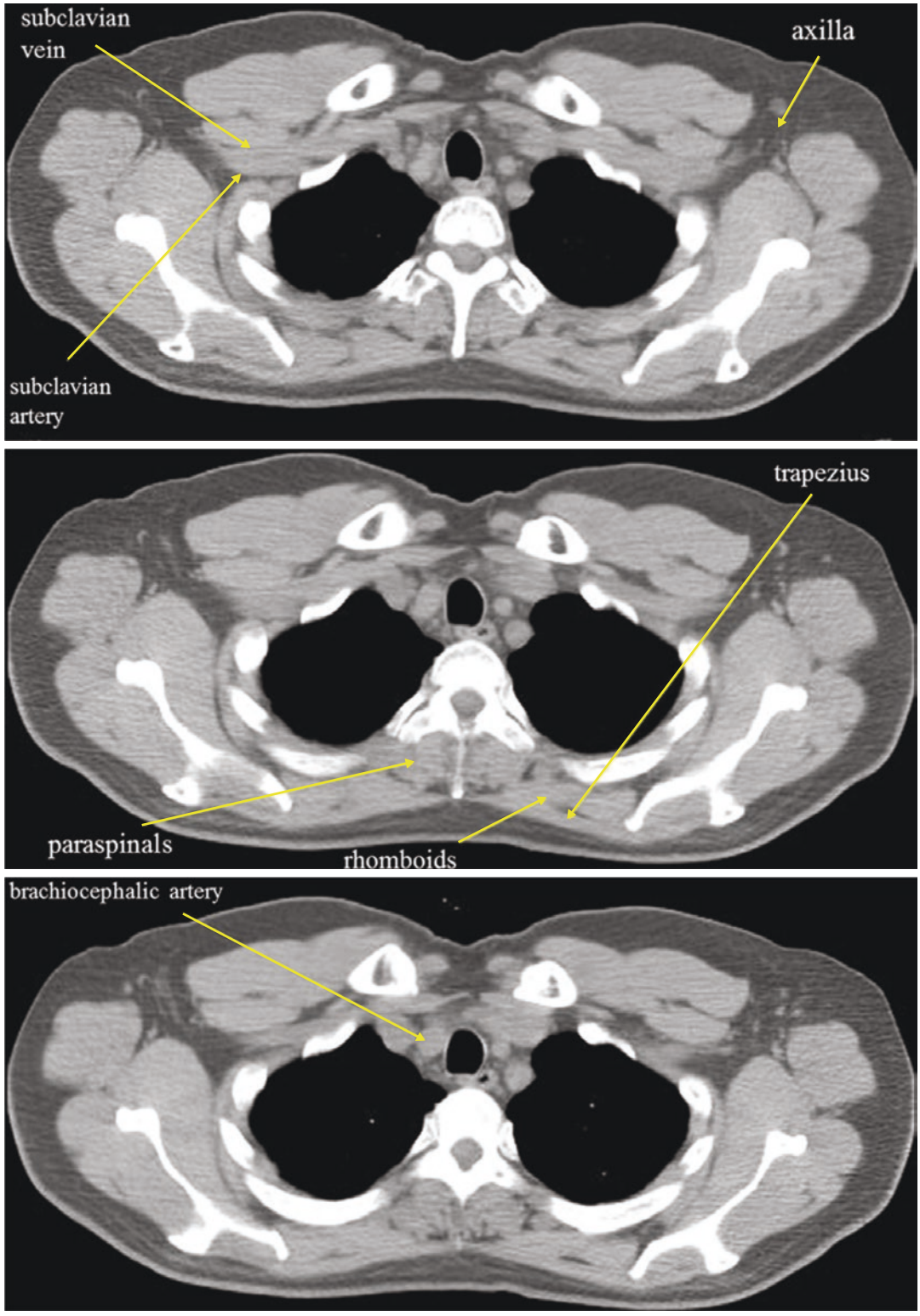
subclavian vein
axilla
subclavian artery
trapezius
paraspinals
rhomboids
brachiocephalic artery

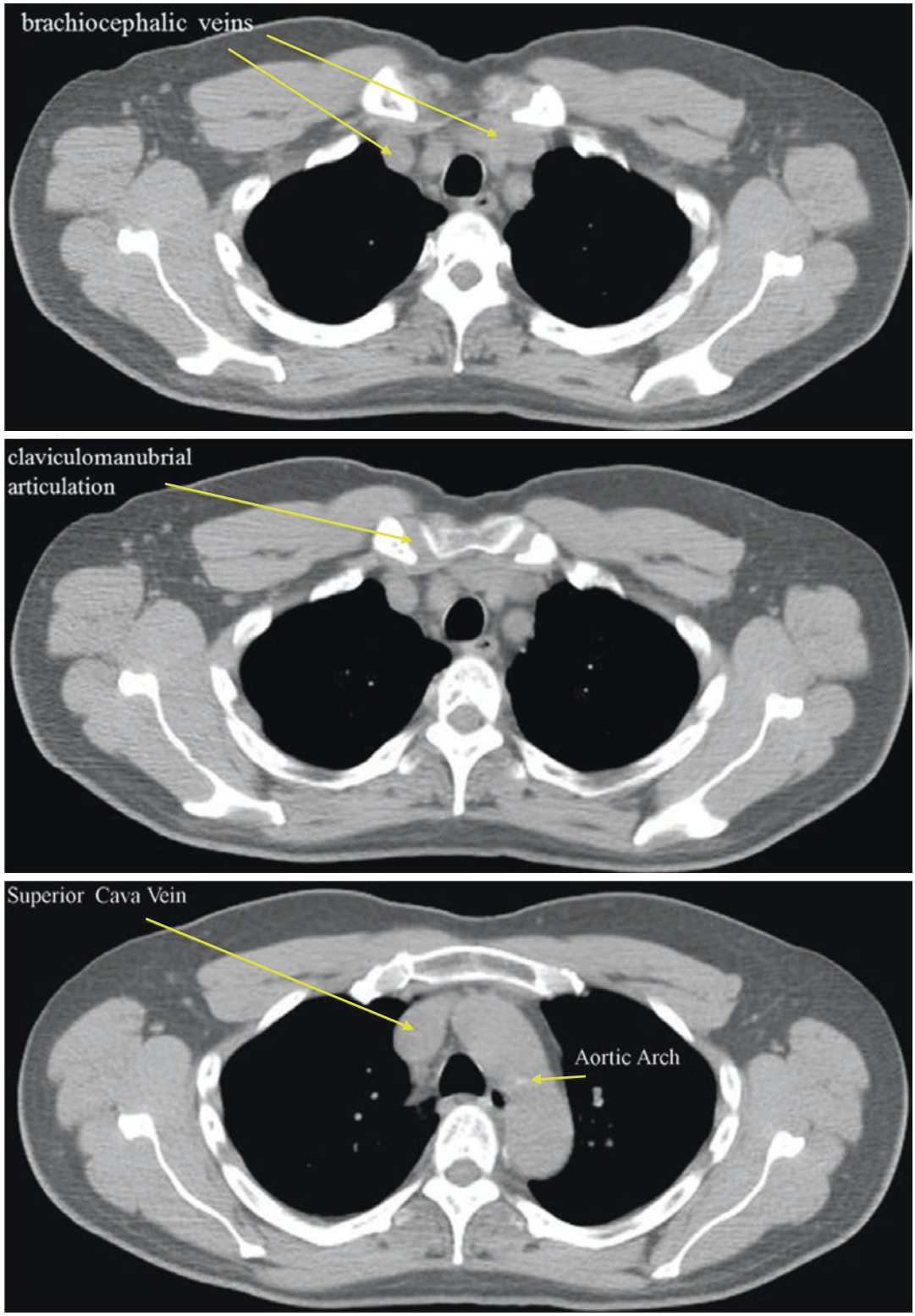
brachiocephalic veins
claviculomanubrial articulation
Superior Cava Vein
Aortic Arch

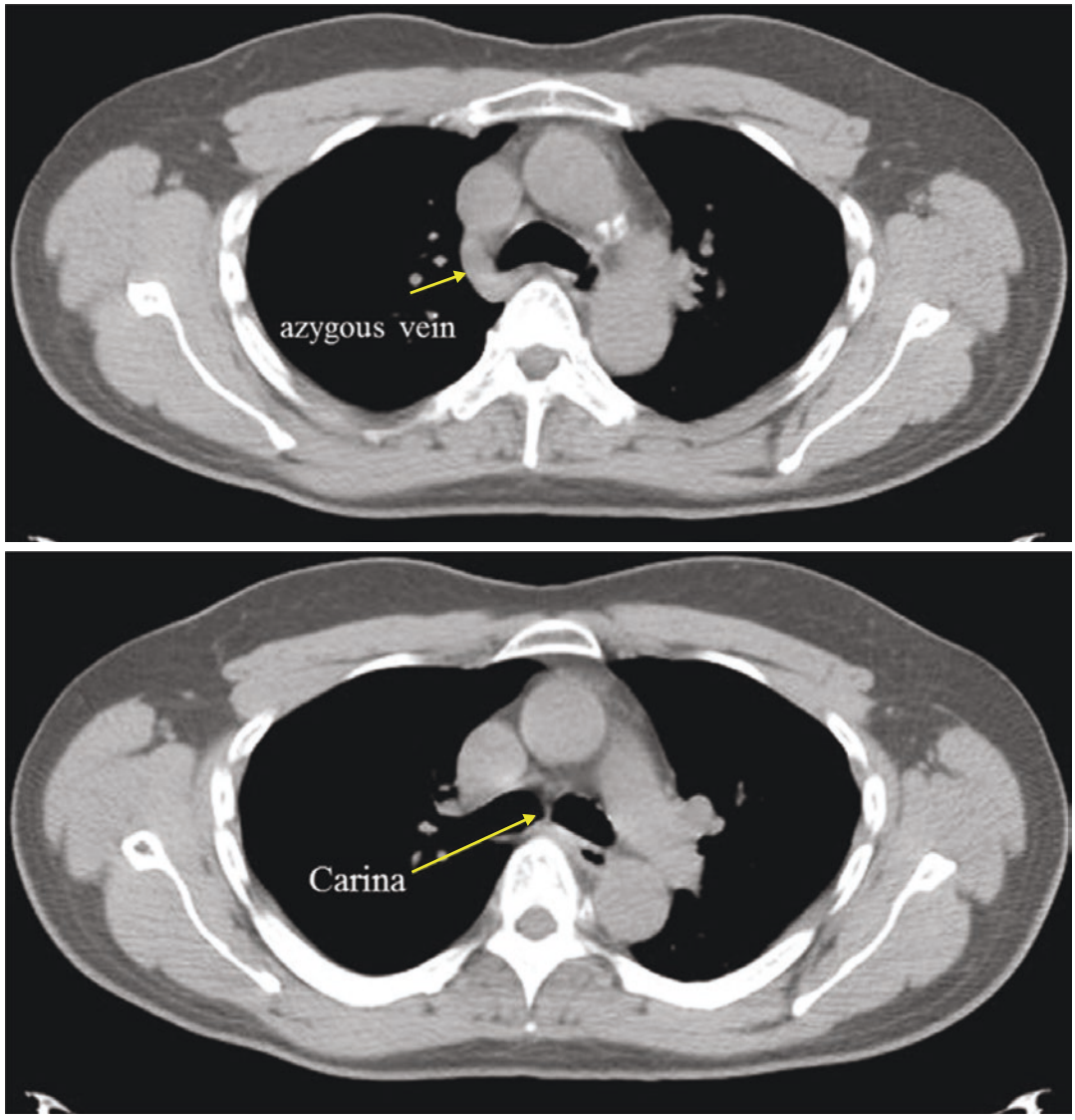
azygous vein
Carina

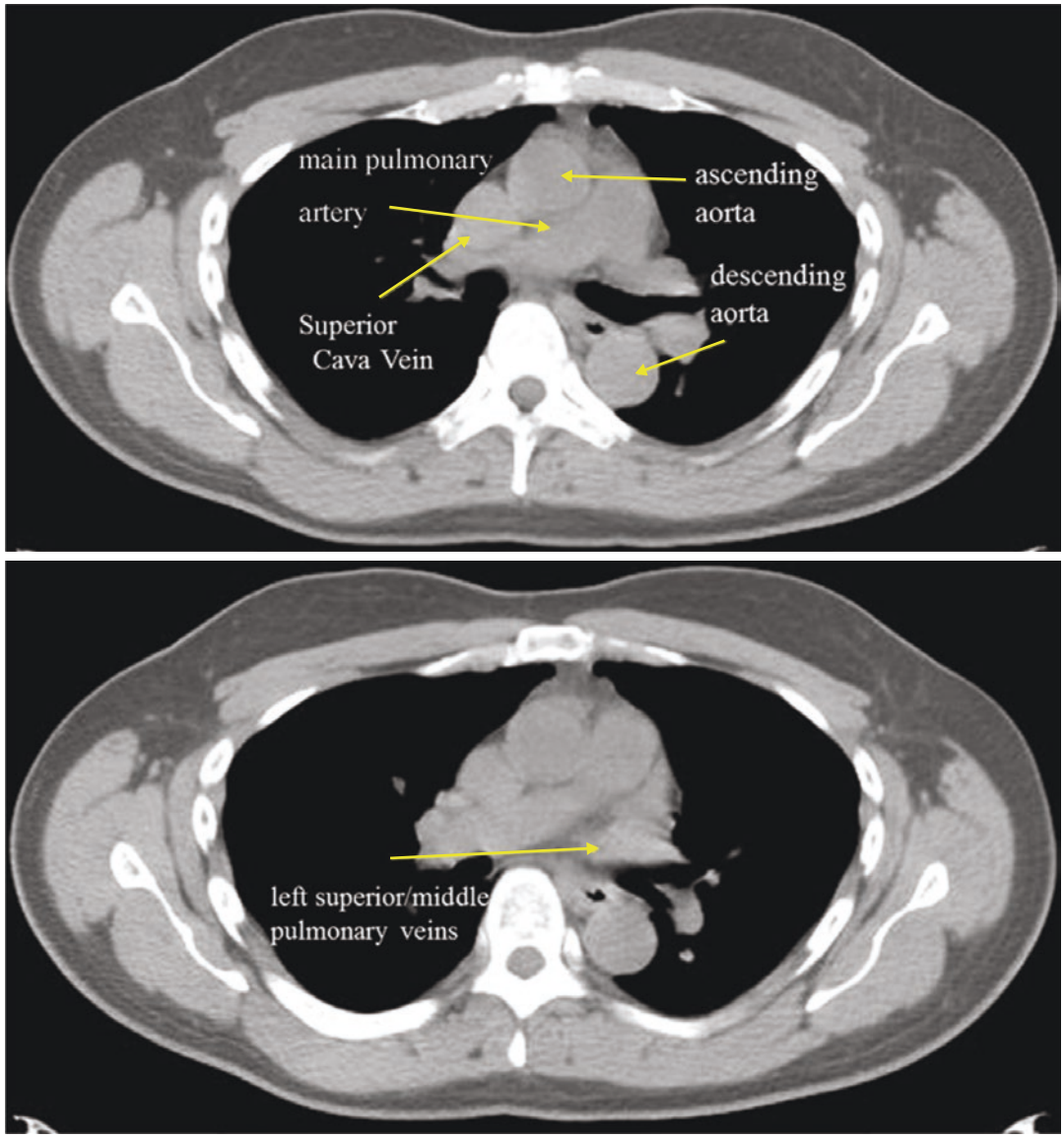
main pulmonary
artery
ascending
aorta
descending
aorta
Superior
Cava Vein
left superior/middle
pulmonary veins

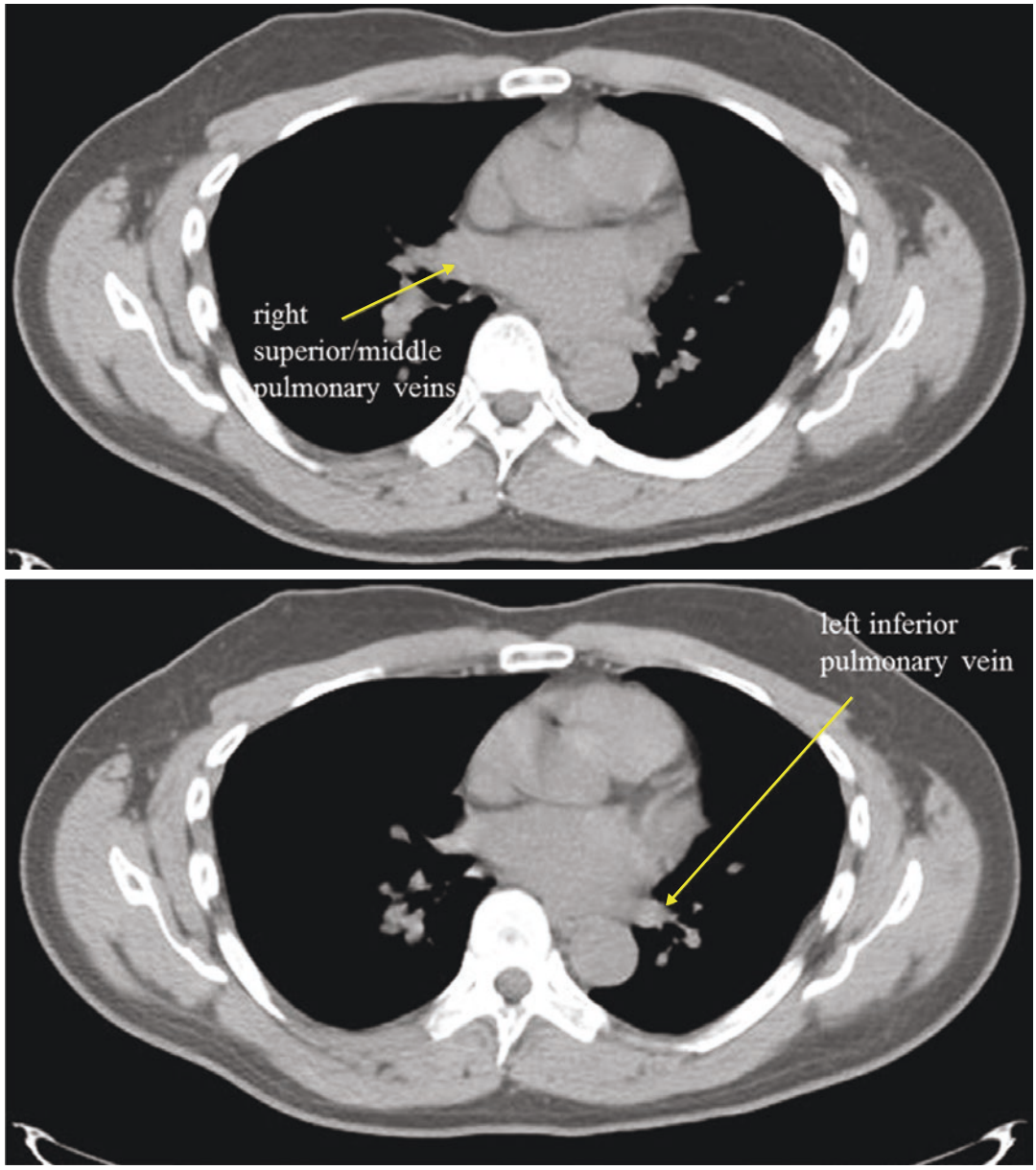
right
superior/middle
pulmonary veins
left inferior
pulmonary vein

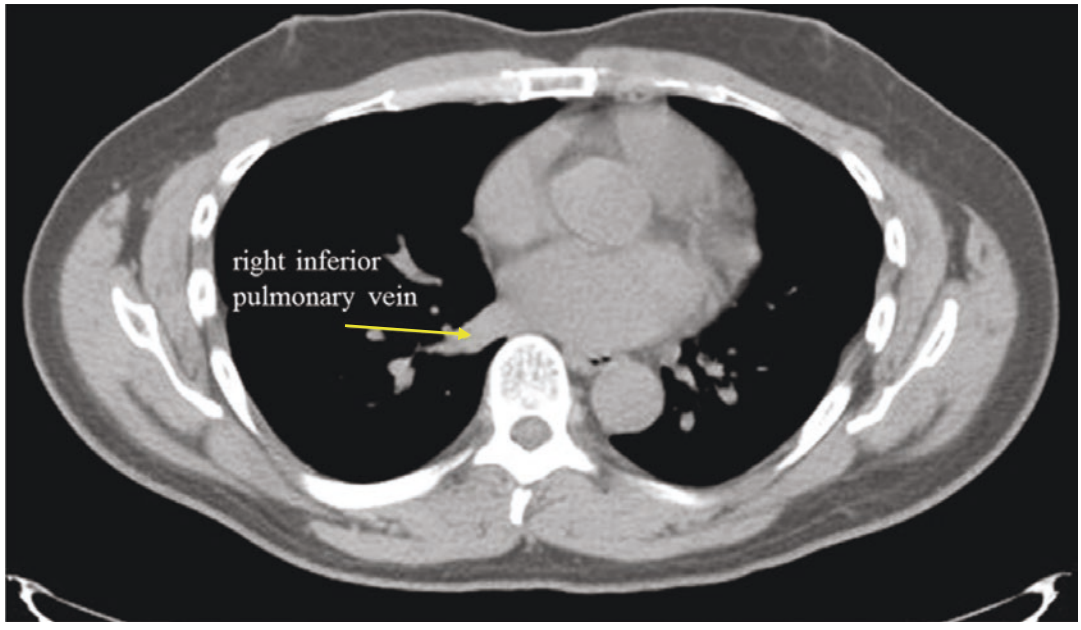
right inferior
pulmonary vein

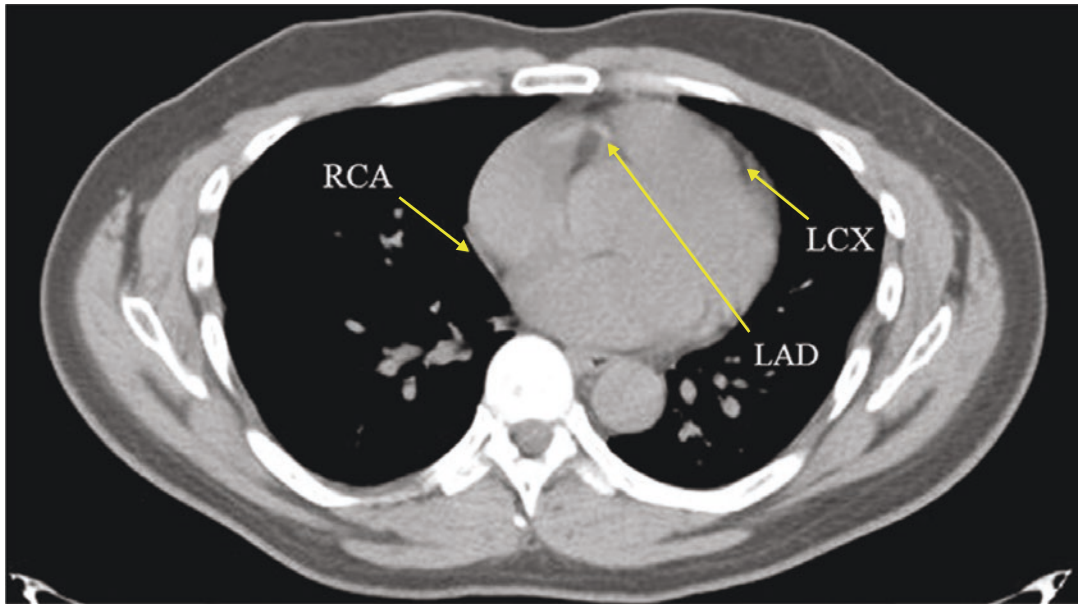
RCA
LCX
LAD

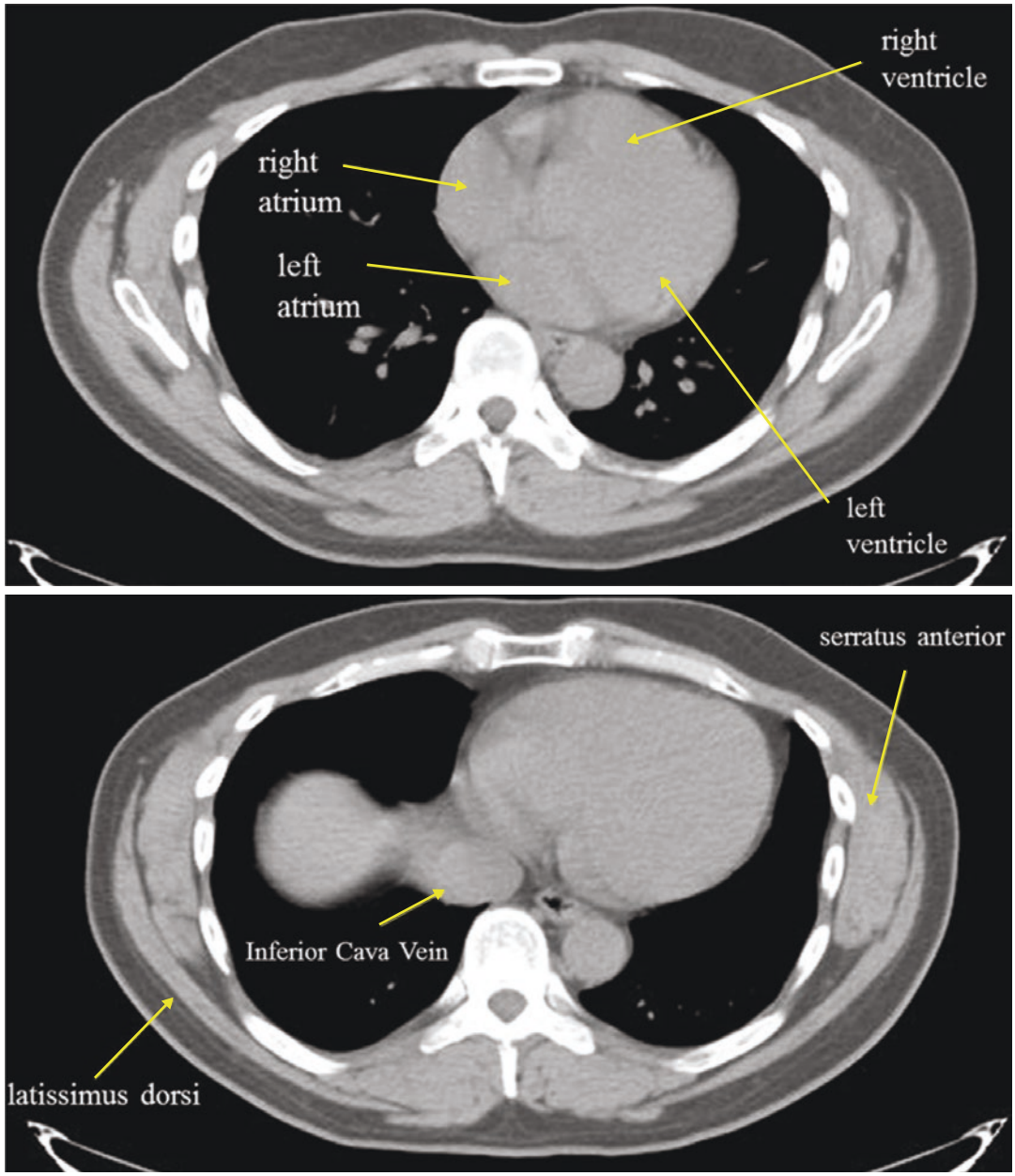
right
ventricle
right
atrium
left
atrium
left
ventricle
serratus anterior
Inferior Cava Vein
latissimus dorsi

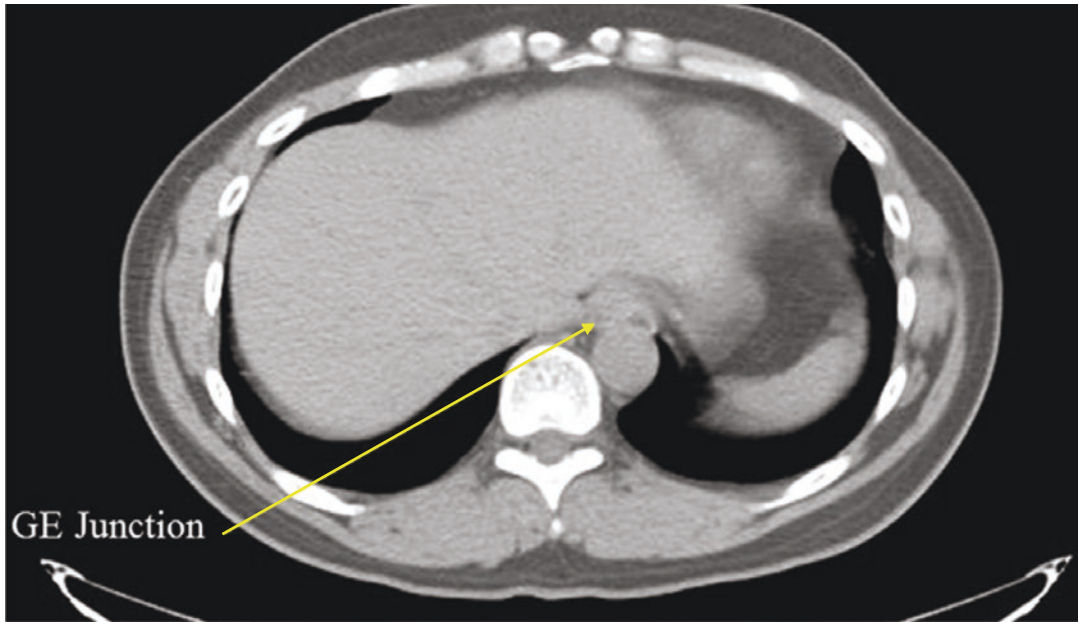
GE Junction

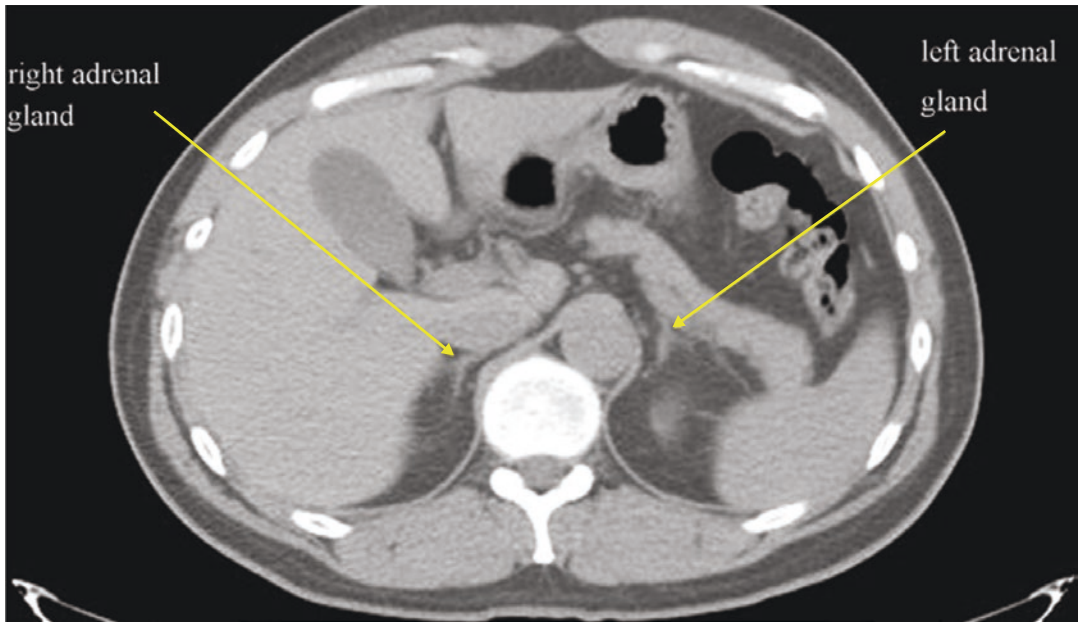
right adrenal gland
left adrenal gland

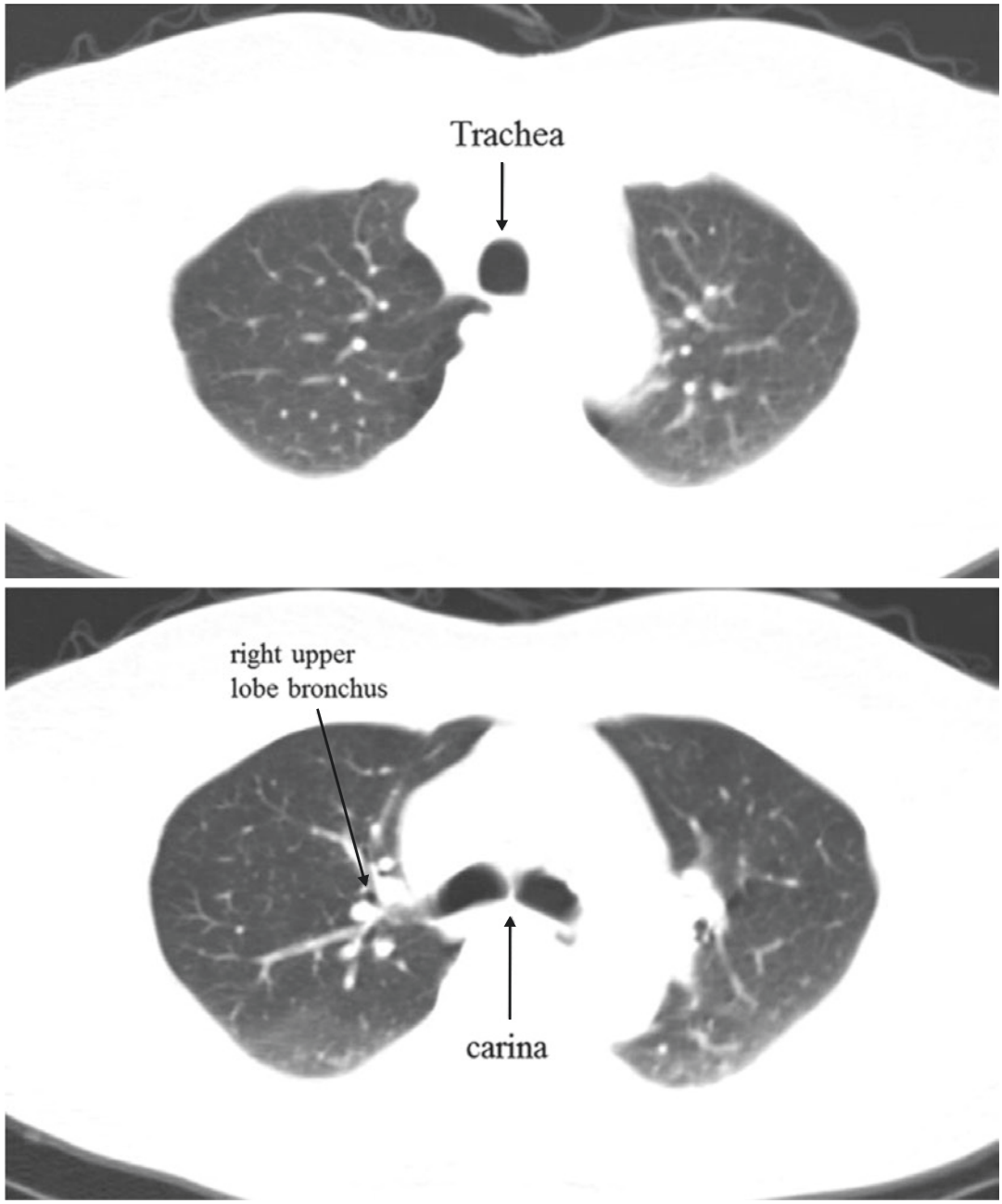
Trachea
right upper
lobe bronchus
carina

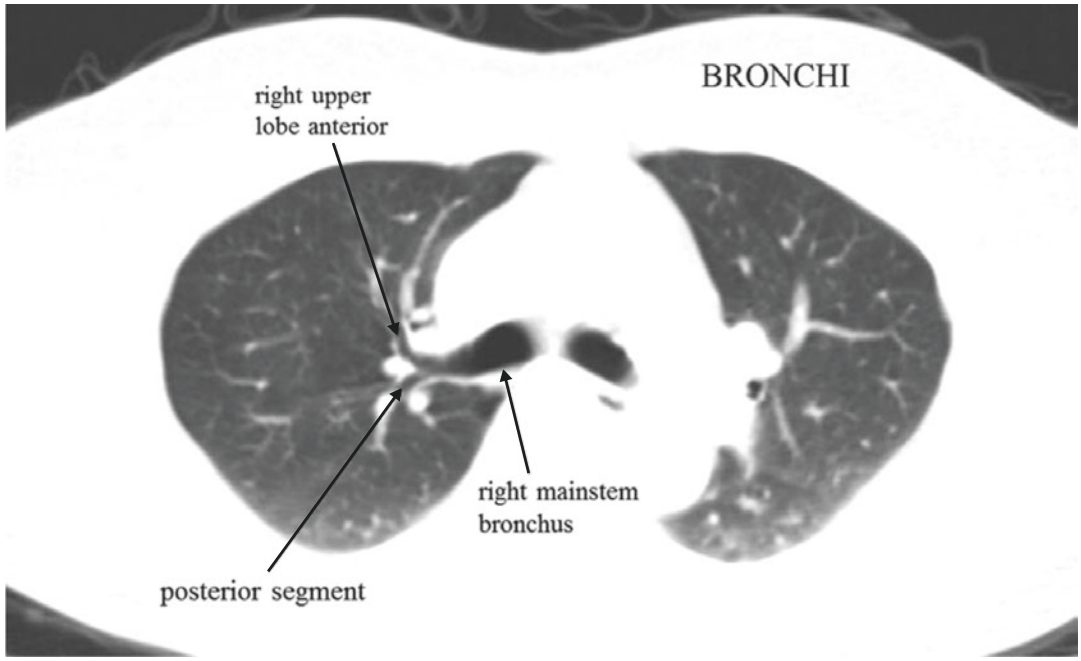
BRONCHI
right upper
lobe anterior
right mainstem
bronchus
posterior segment

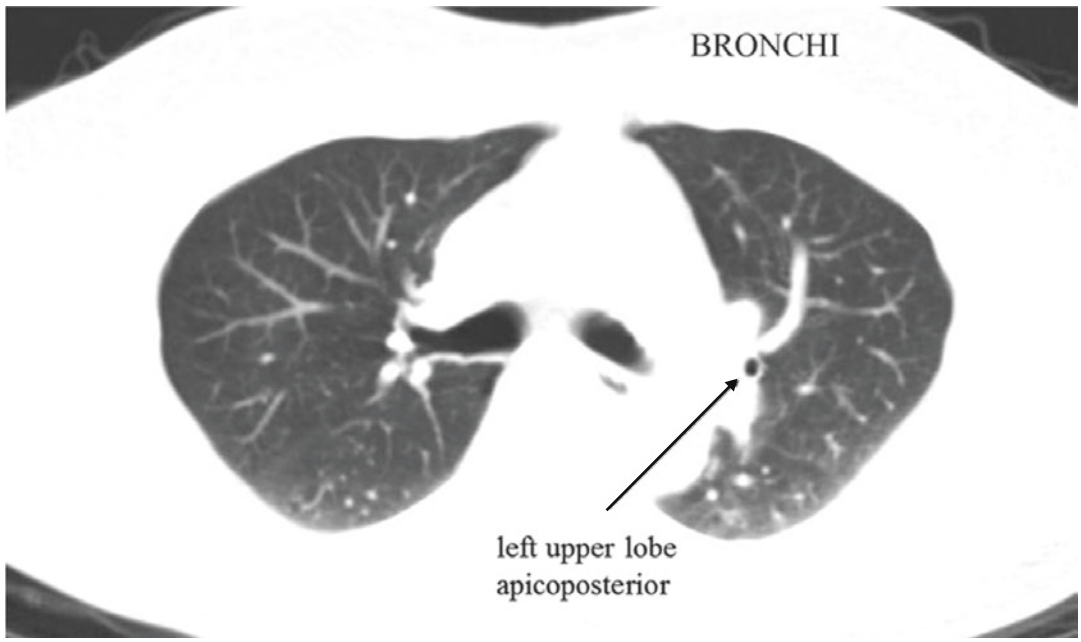
BRONCHI
left upper lobe
apicoposterior

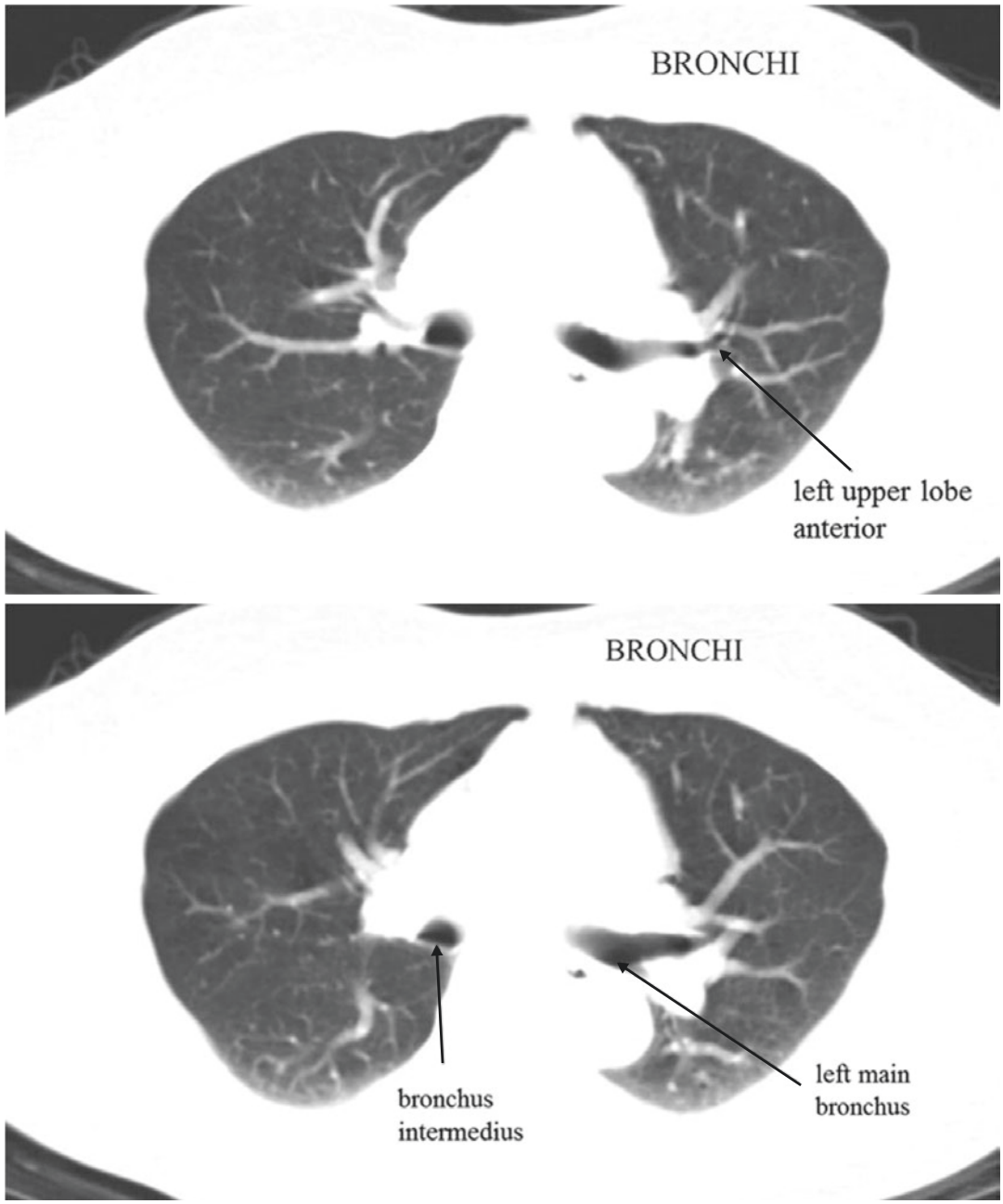
BRONCHI
left upper lobe
anterior
BRONCHI
bronchus
intermedius
left main
bronchus

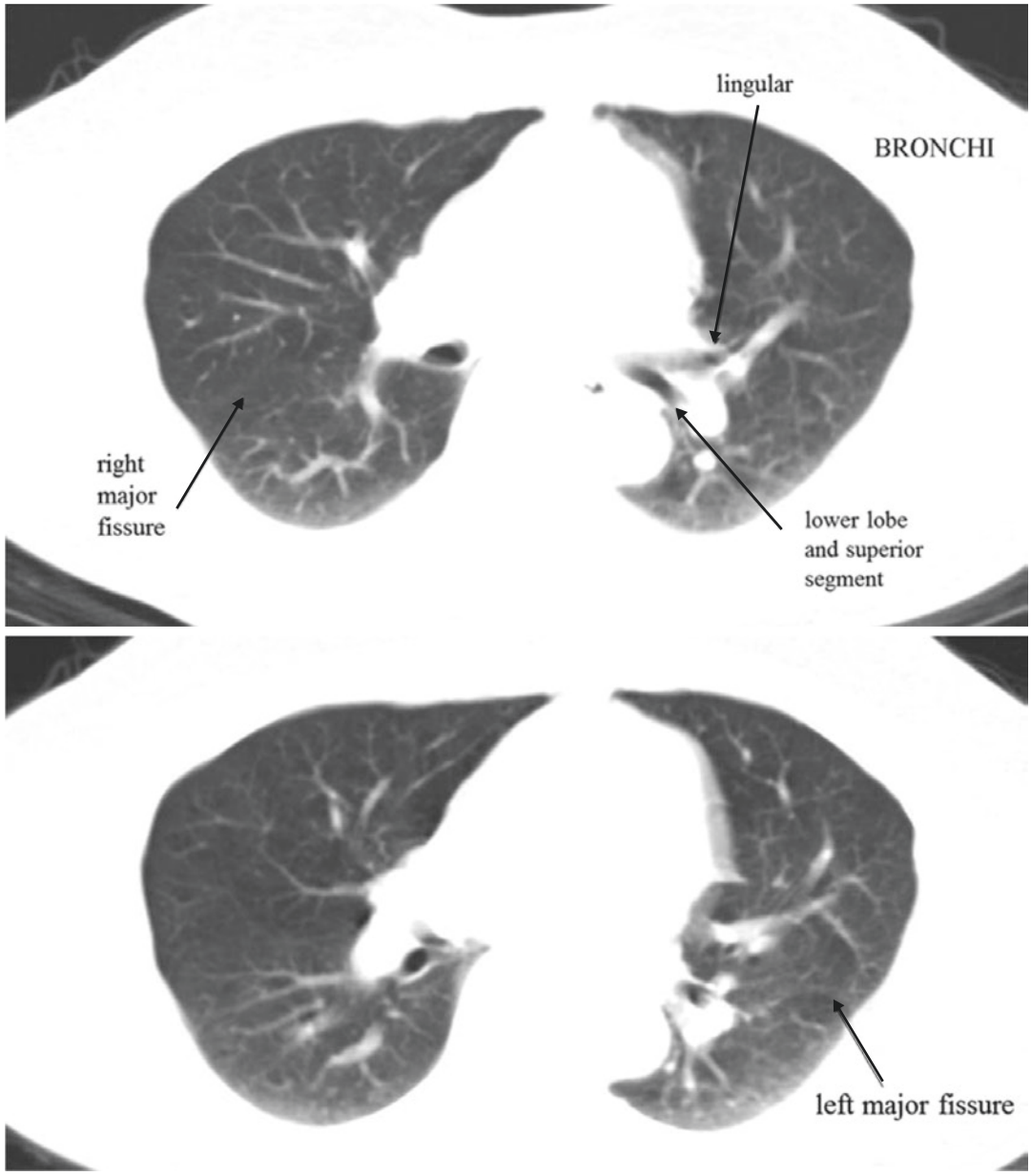
lingular
BRONCHI
right
major
fissure
lower lobe
and superior
segment
left major fissure

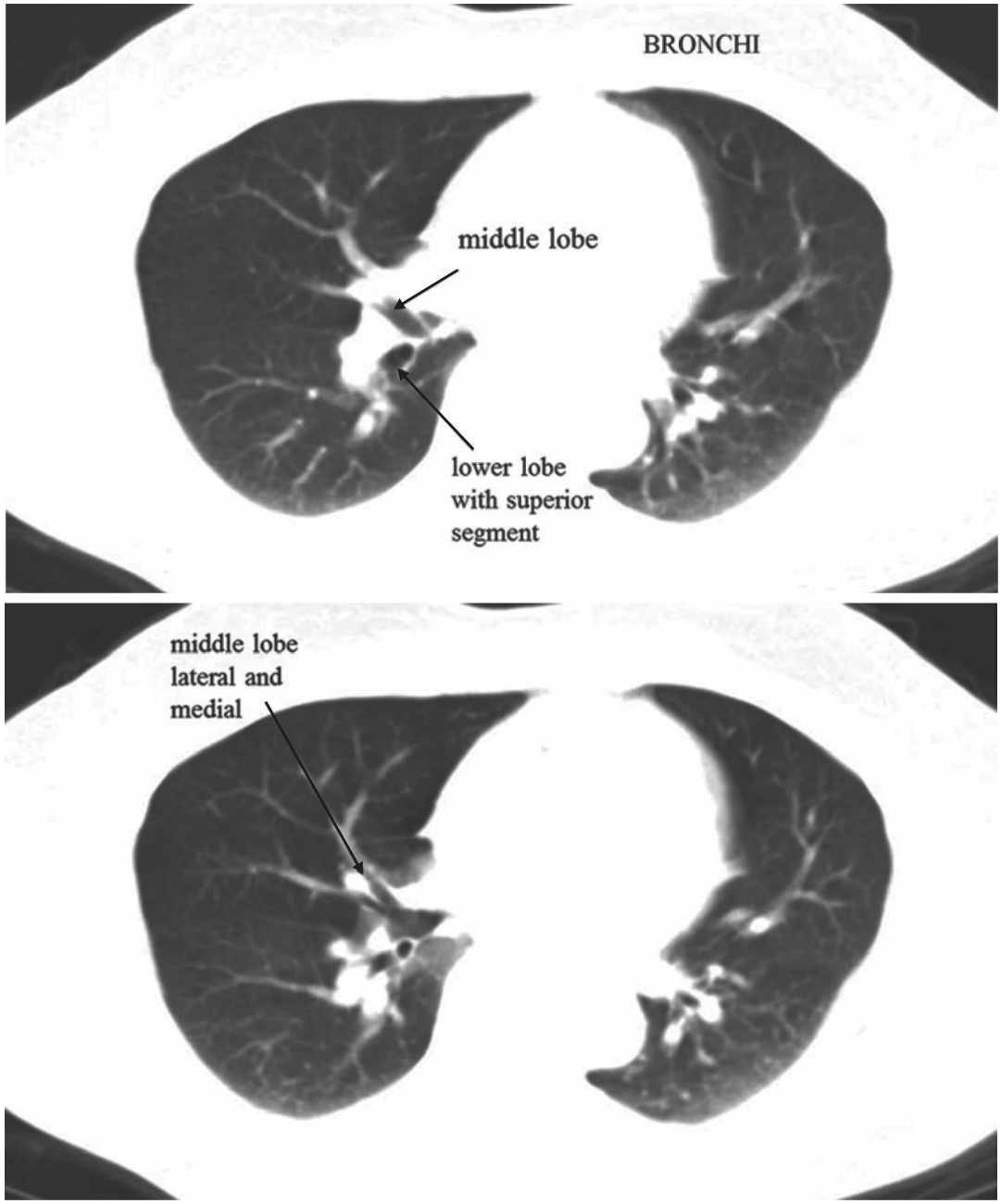
BRONCHI
middle lobe
lower lobe
with superior
segment
middle lobe
lateral and
medial

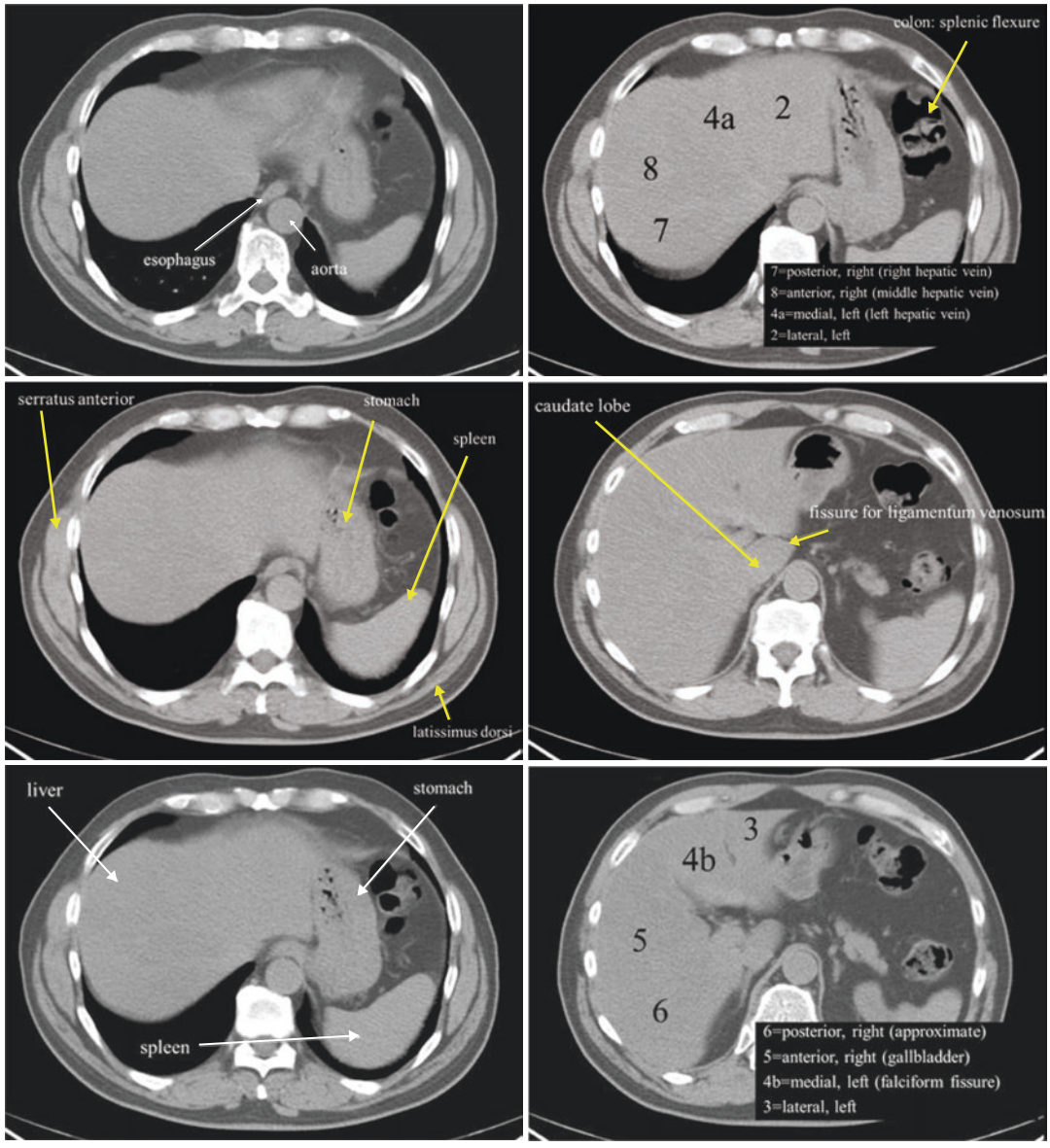
esophagus
aorta
colon: splenic flexure
4a
2
8
7
7=posterior, right (right hepatic vein)
8=anterior, right (middle hepatic vein)
4a=medial, left (left hepatic vein)
2=lateral, left
serratus anterior
stomach
spleen
latissimus dorsi
caudate lobe
fissure for ligamentum venosum
liver
stomach
spleen
3
4b
5
6
6=posterior, right (approximate)
5=anterior, right (gallbladder)
4b=medial, left (falciform fissure)
3=lateral, left

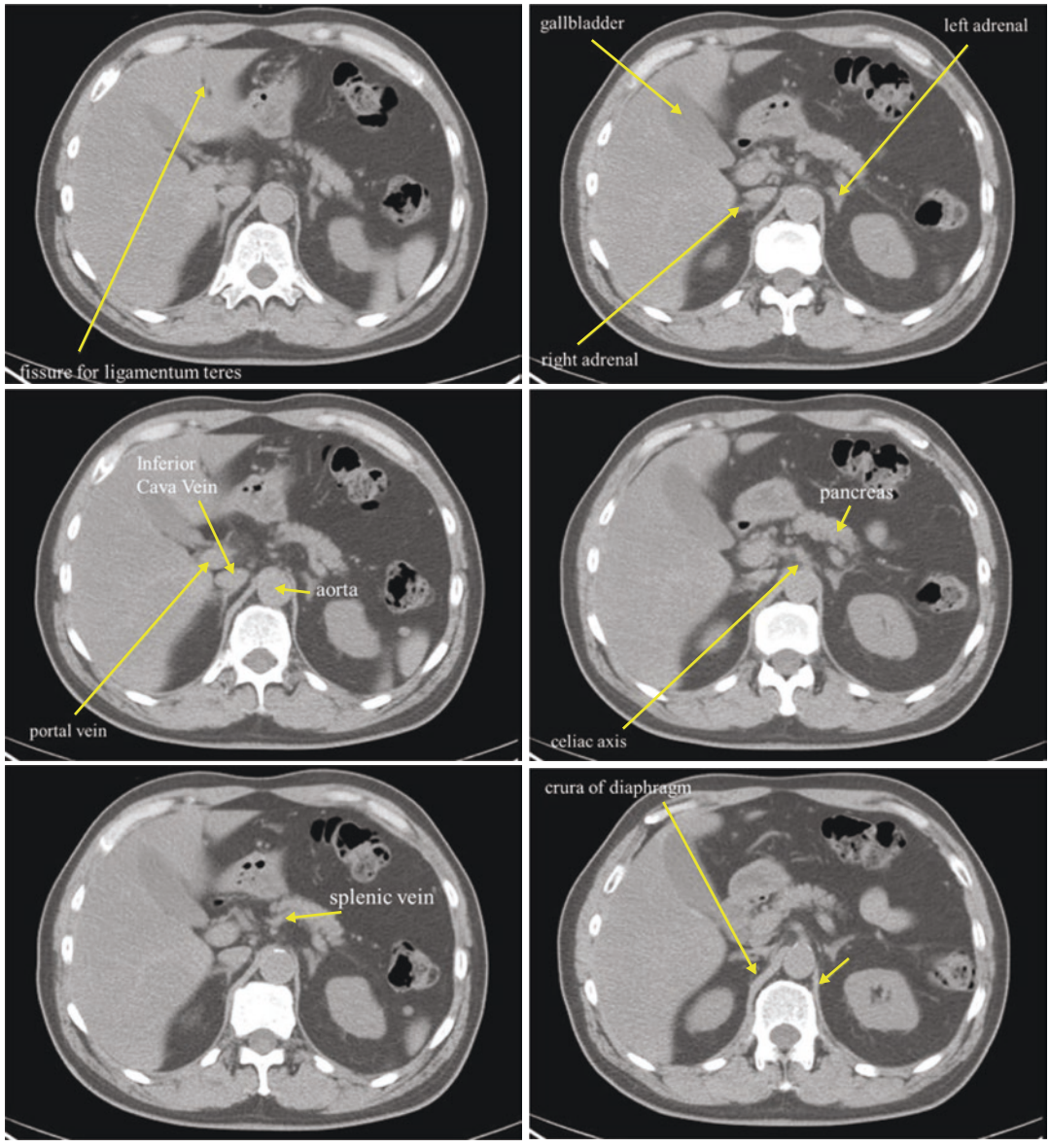
fissure for ligamentum teres
gallbladder
left adrenal
right adrenal
Inferior
Cava Vein
aorta
portal vein
pancreas
celiac axis
splenic vein
crura of diaphragm

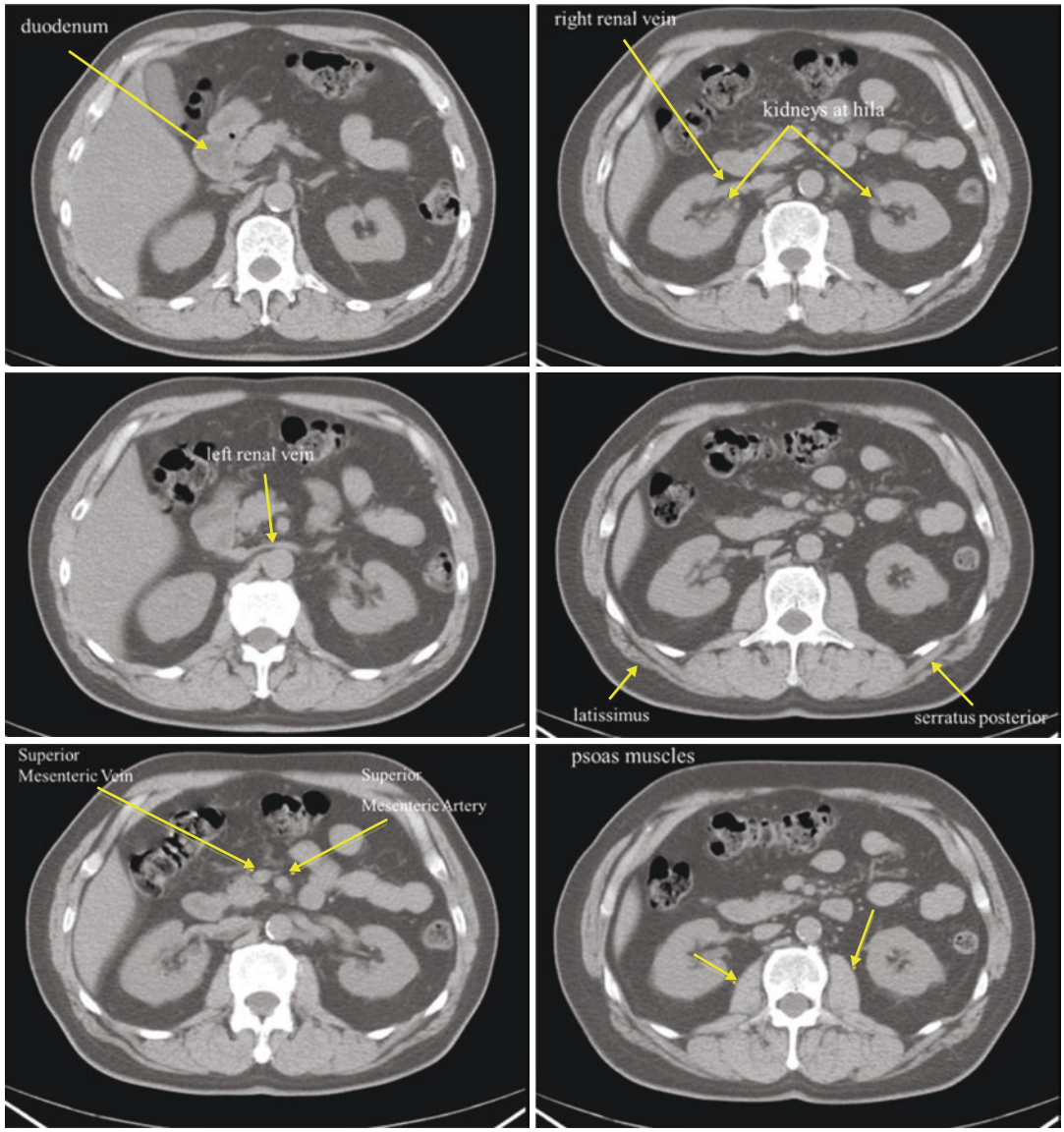
duodenum
right renal vein
kidneys at hila
left renal vein
latissimus
serratus posterior
Superior
Mesenteric Vein
Superior
Mesenteric Artery
psoas muscles

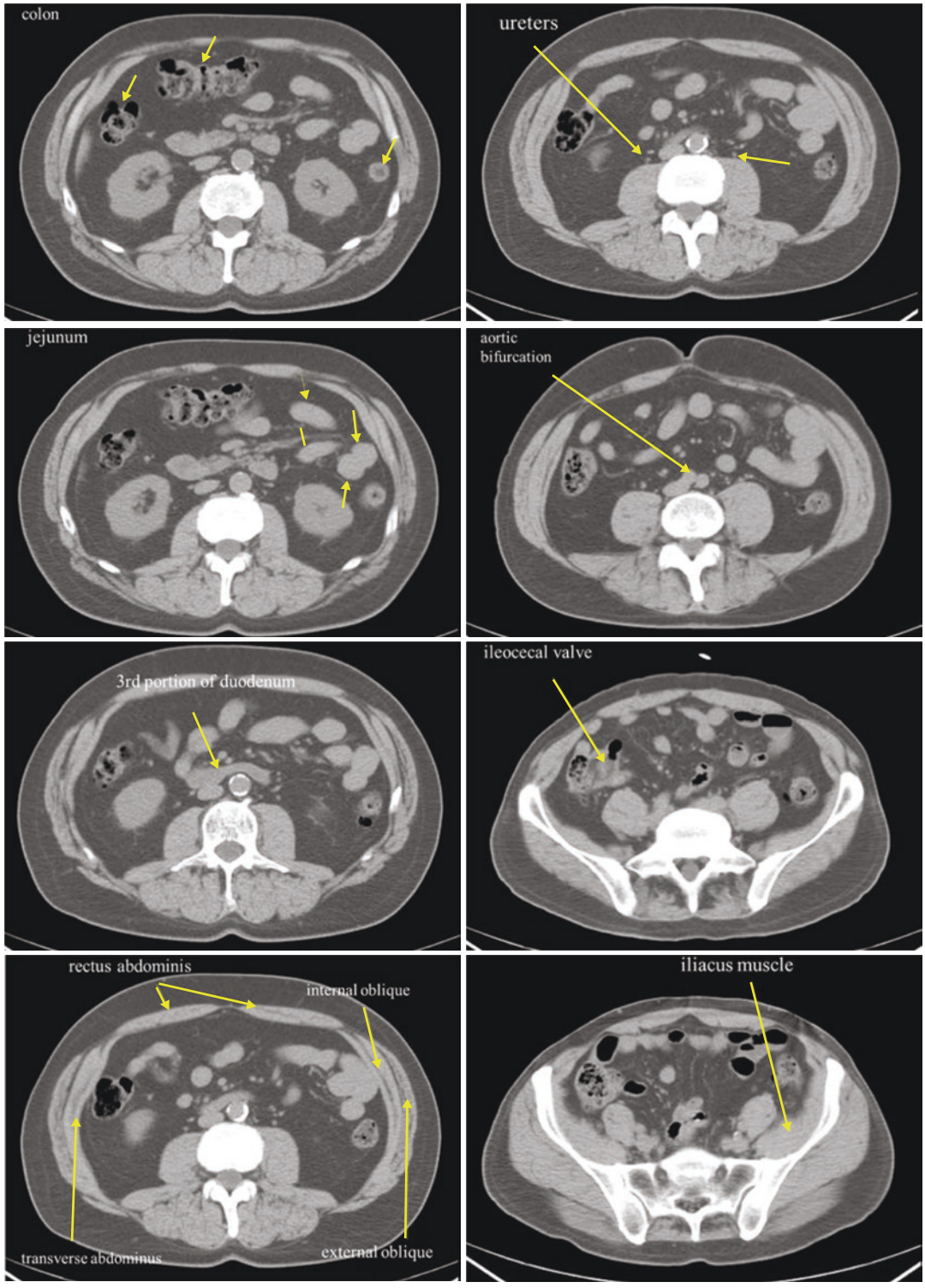
colon
ureters
jejunum
aortic
bifurcation
3rd portion of duodenum
ileocecal valve
rectus abdominis
internal oblique
transverse abdominus
external oblique
iliacus muscle

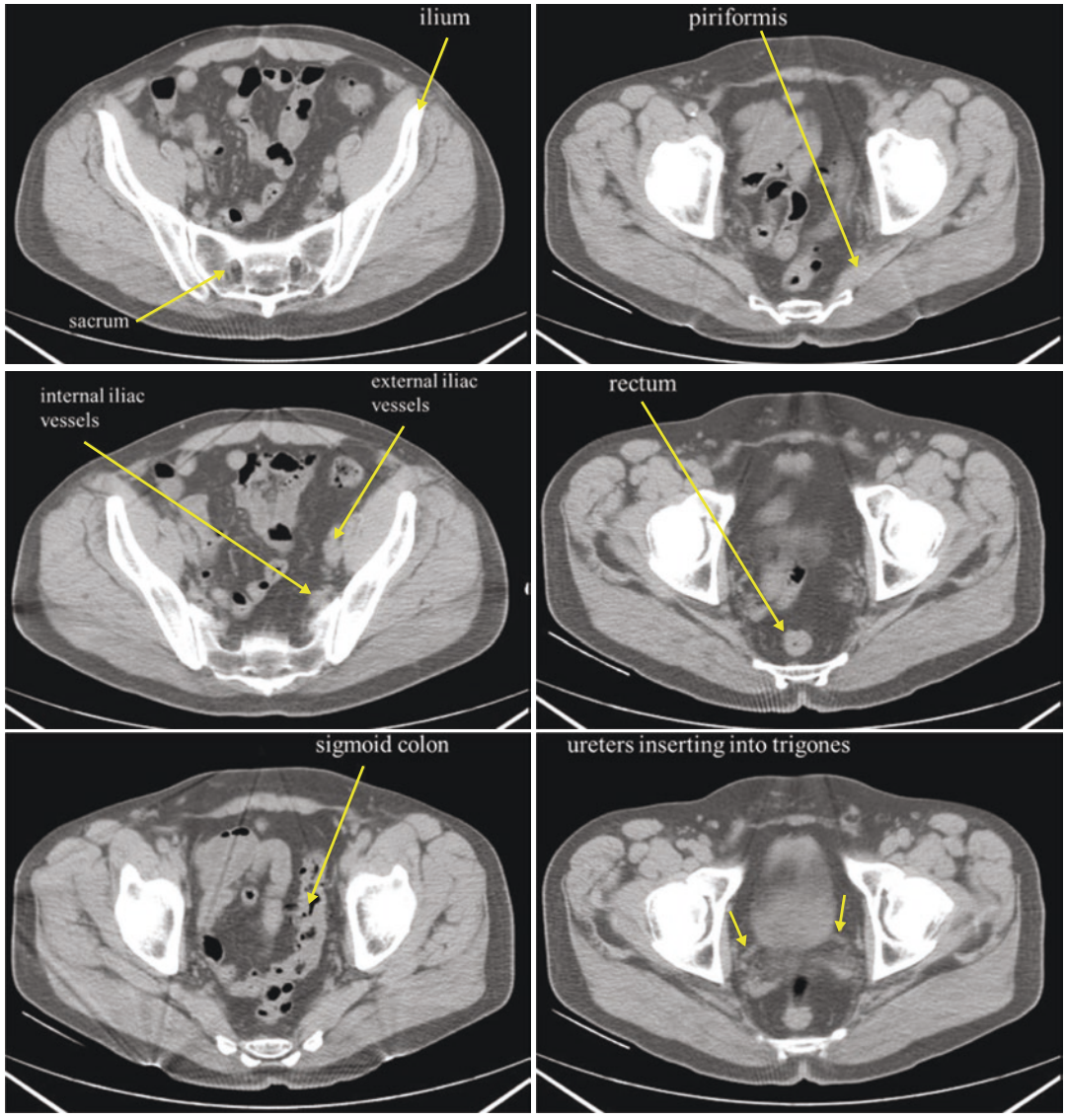
ilium
sacrum
piriformis
internal iliac vessels
external iliac vessels
rectum
sigmoid colon
ureters inserting into trigones

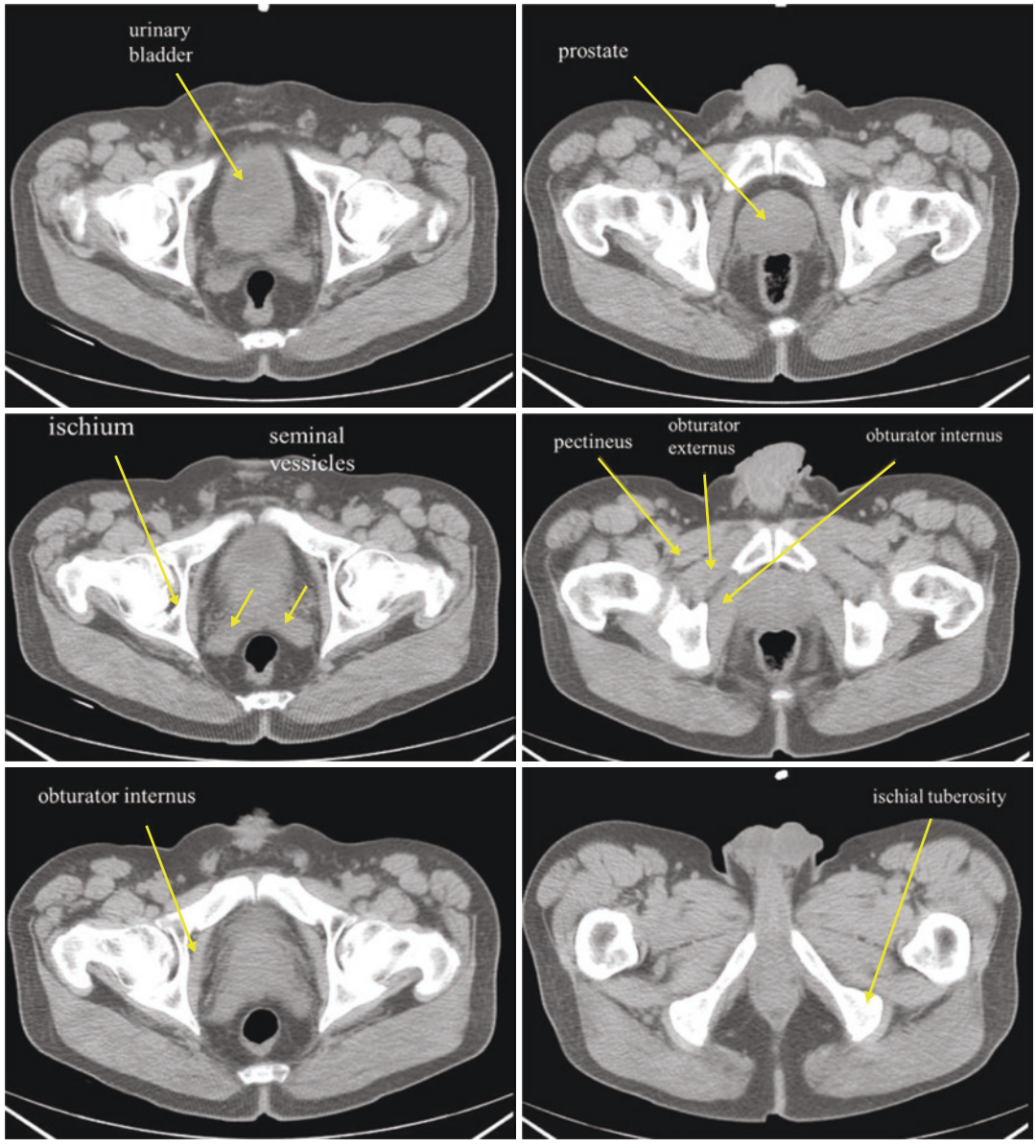
urinary bladder
prostate
ischium
seminal vessicles
pectineus
obturator externus
obturator internus
obturator internus
ischial tuberosity

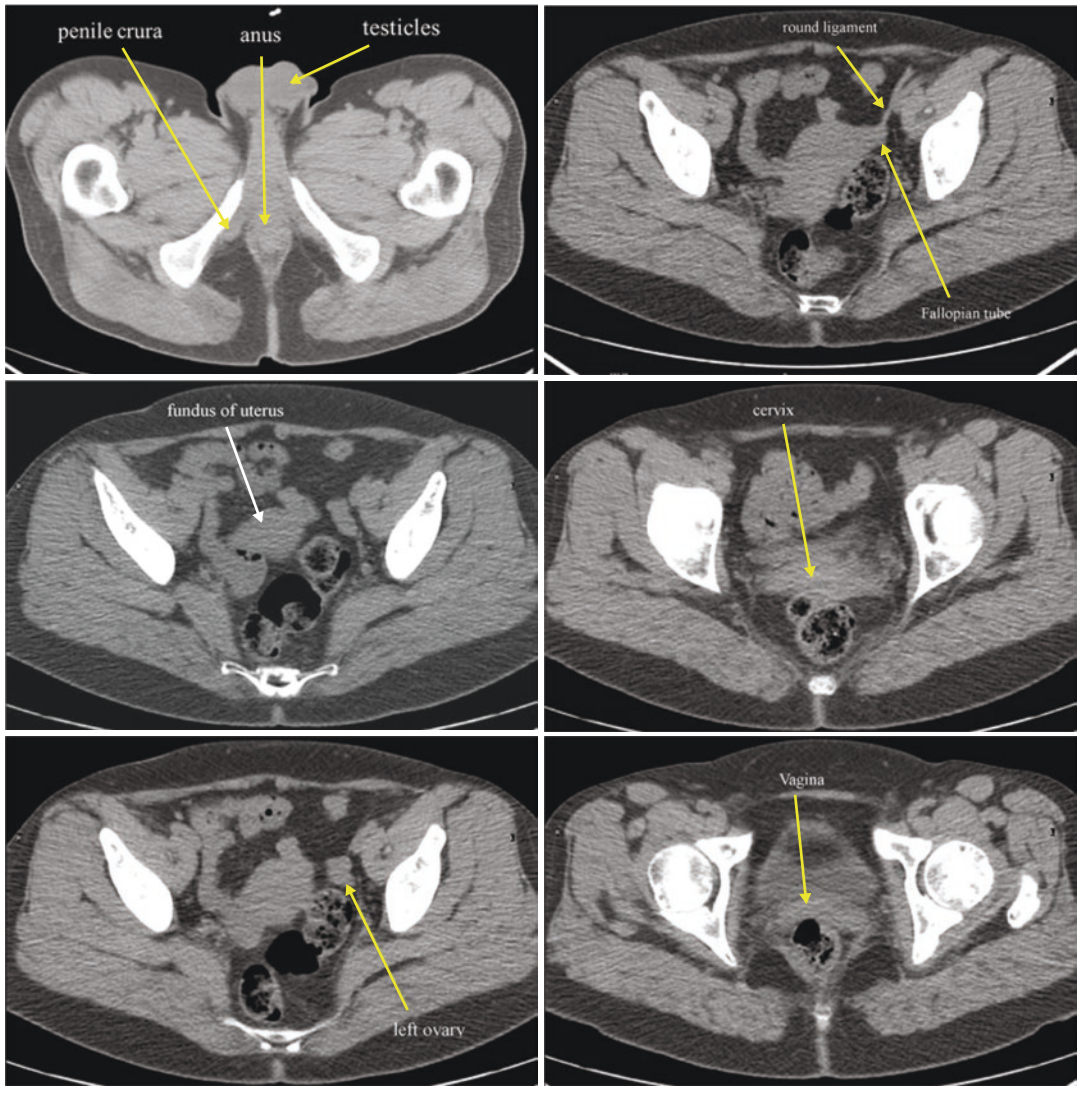
penile crura
anus
testicles
round ligament
Fallopian tube
fundus of uterus
cervix
left ovary
Vagina

Normal Anatomy Full Dose Contrast Enhanced CT

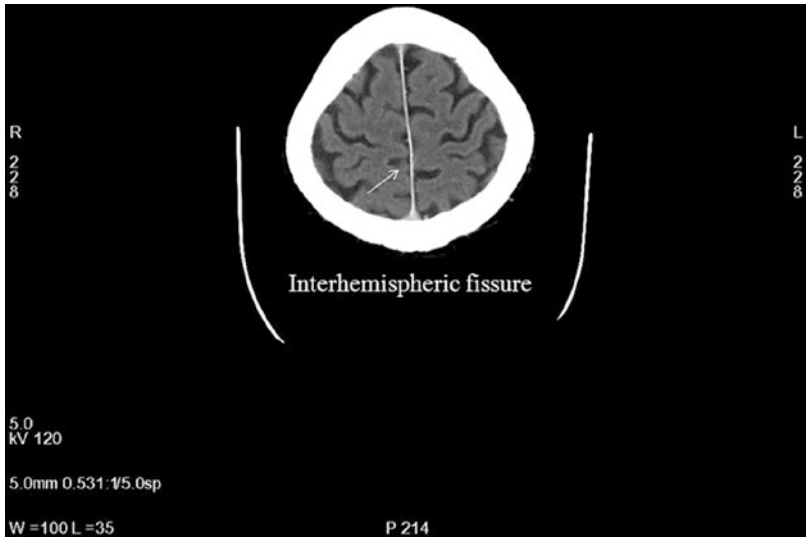

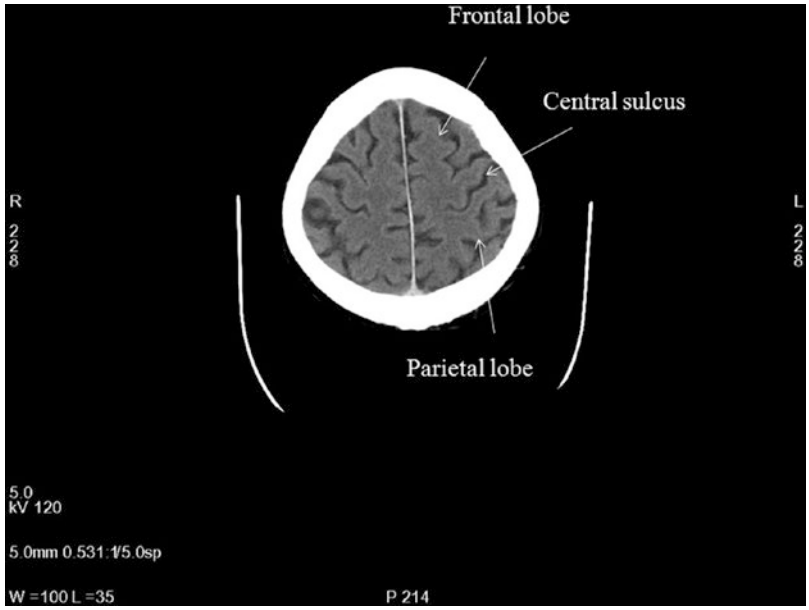

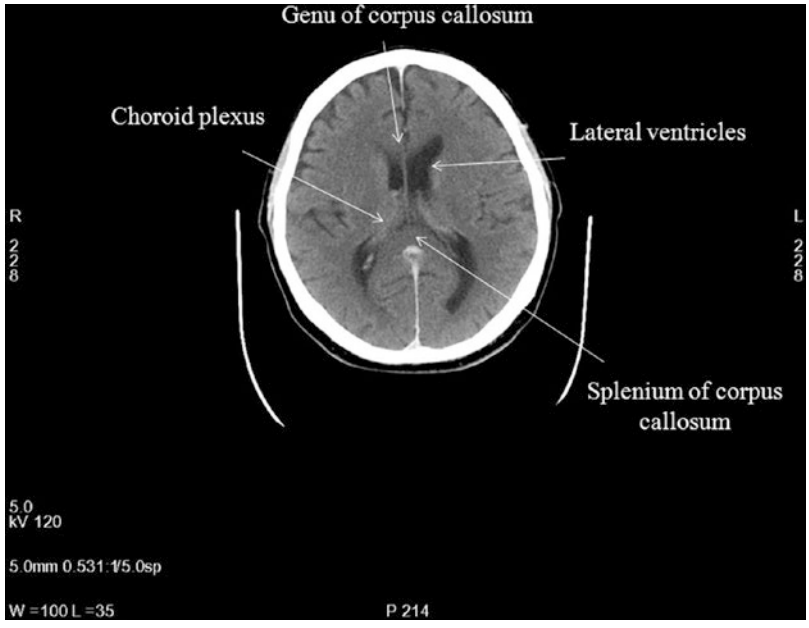
Genu of corpus callosum
Choroid plexus
Lateral ventricles
R
L
Splenium of corpus callosum
5.0
kV 120
5.0mm 0.531:1/5.0sp
W =100 L =35
P 214

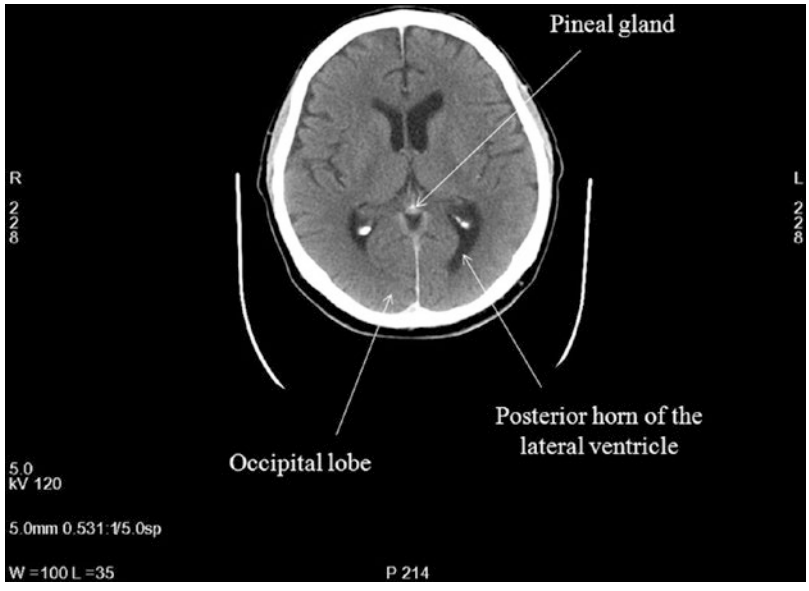
Pineal gland
R
L
Posterior horn of the lateral ventricle
Occipital lobe
5.0
kV 120
5.0mm 0.531:1/5.0sp
W =100 L =35
P 214

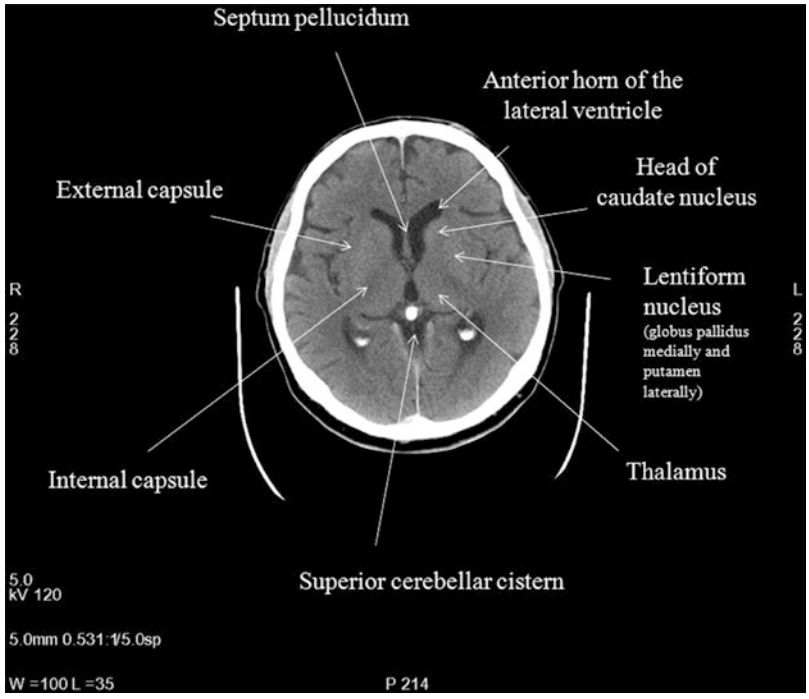
Septum pellucidum
Anterior horn of the lateral ventricle
Head of caudate nucleus
External capsule
Lentiform nucleus
(globus pallidus medially and putamen laterally)
R
L
Internal capsule
Thalamus
Superior cerebellar cistern
5.0
kV 120
5.0mm 0.531:1/5.0sp
W =100 L =35
P 214

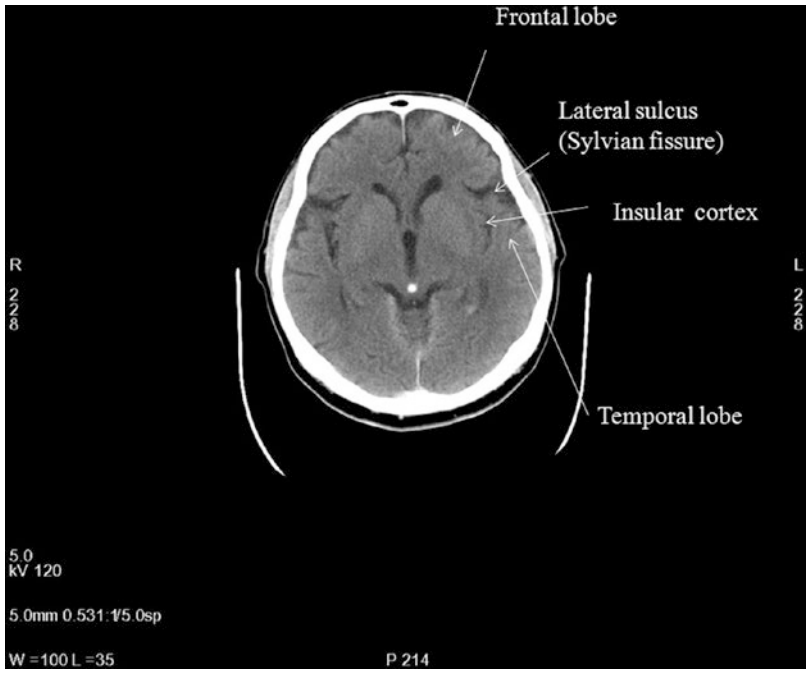
Frontal lobe
Lateral sulcus
(Sylvian fissure)
Insular cortex
R
L
Temporal lobe
5.0
kV 120
5.0mm 0.531:1/5.0sp
W =100 L =35
P 214

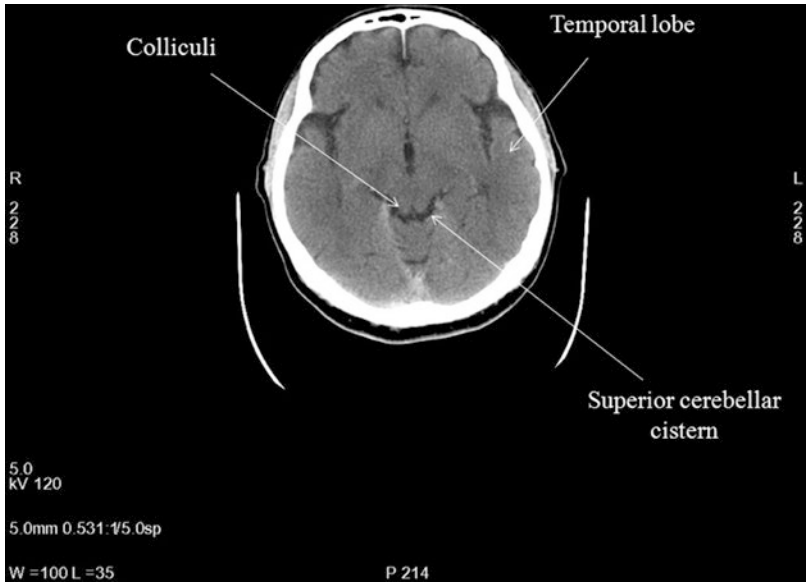
Colliculi
Temporal lobe
Superior cerebellar cistern
R
L
5.0
kV 120
5.0mm 0.531:1/5.0sp
W =100 L =35
P 214

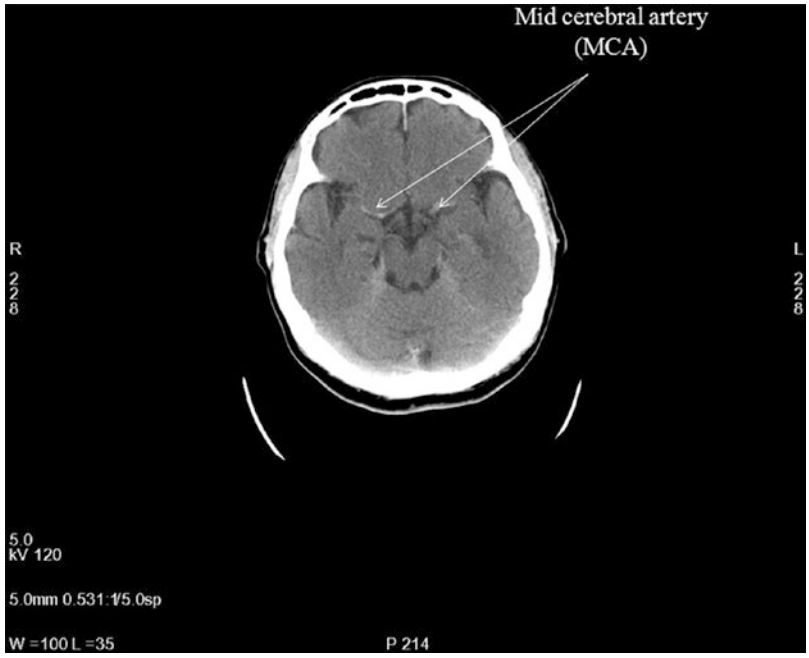
Mid cerebral artery (MCA)
R
L
5.0
kV 120
5.0mm 0.531:1/5.0sp
W =100 L =35
P 214

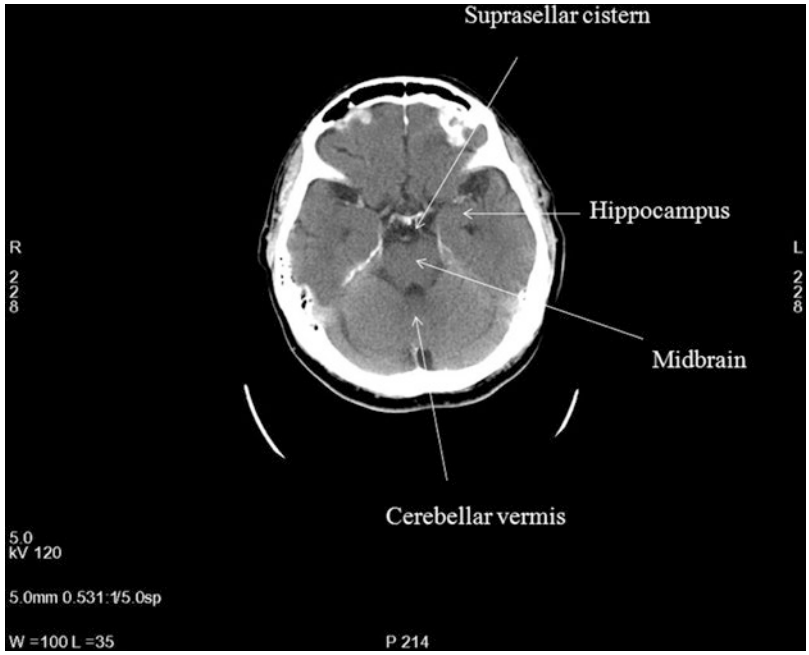
Suprasellar cistern
Hippocampus
Midbrain
Cerebellar vermis
R
L
5.0
kV 120
5.0mm 0.531:1/5.0sp
W =100 L =35
P 214

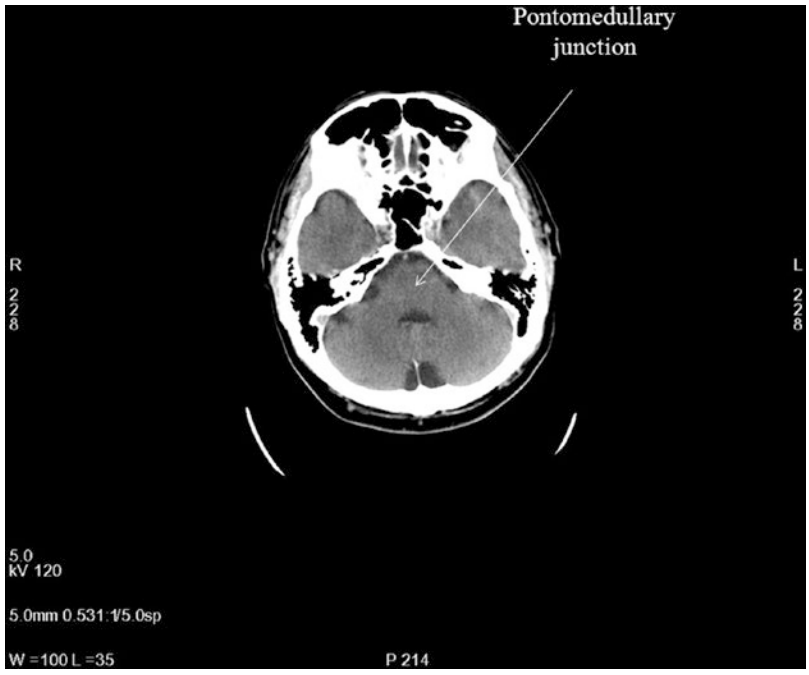
Pontomedullary
junction
R
L
5.0
kV 120
5.0mm 0.531:1/5.0sp
W =100 L =35
P 214

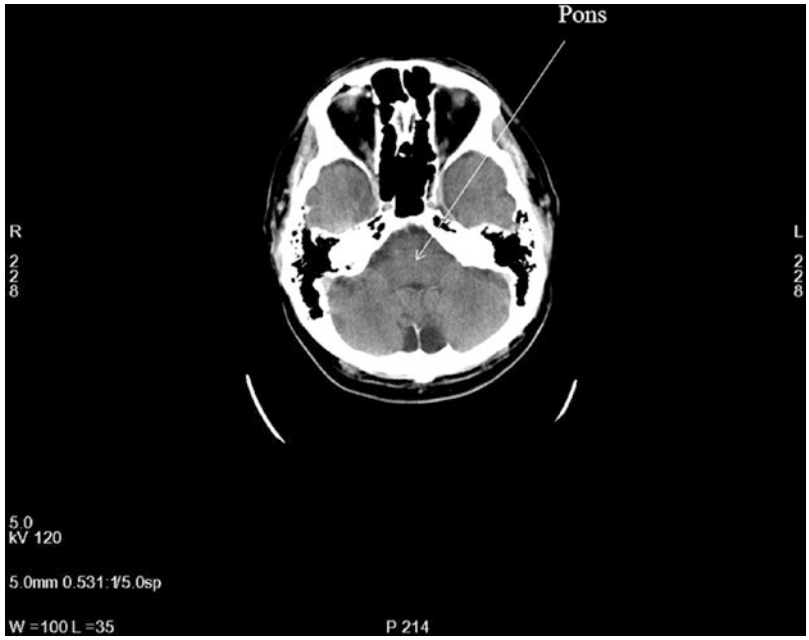
Pons
R
L
2
2
8
5.0
kV 120
5.0mm 0.531:1/5.0sp
W =100 L =35
P 214

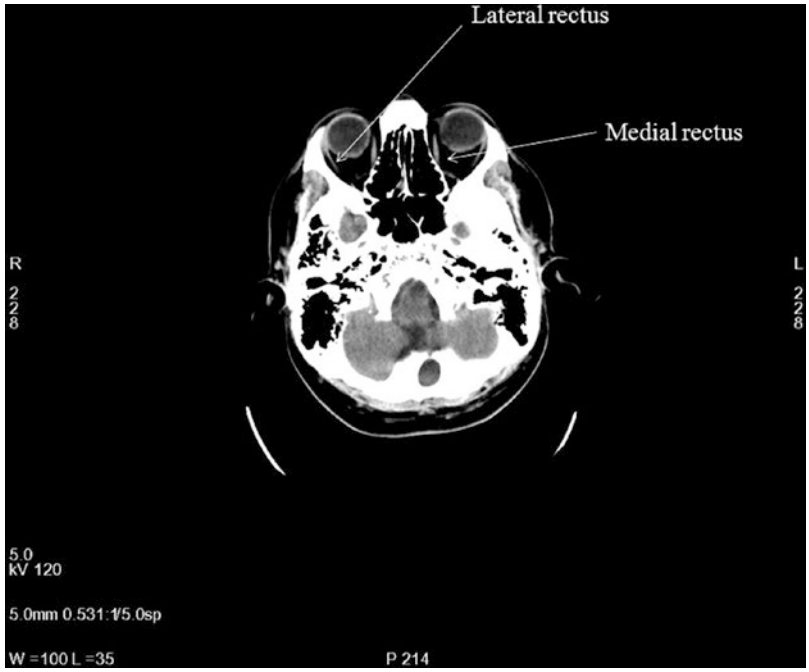
Lateral rectus
Medial rectus
R
L
2
2
8
5.0
kV 120
5.0mm 0.531:1/5.0sp
W =100 L =35
P 214

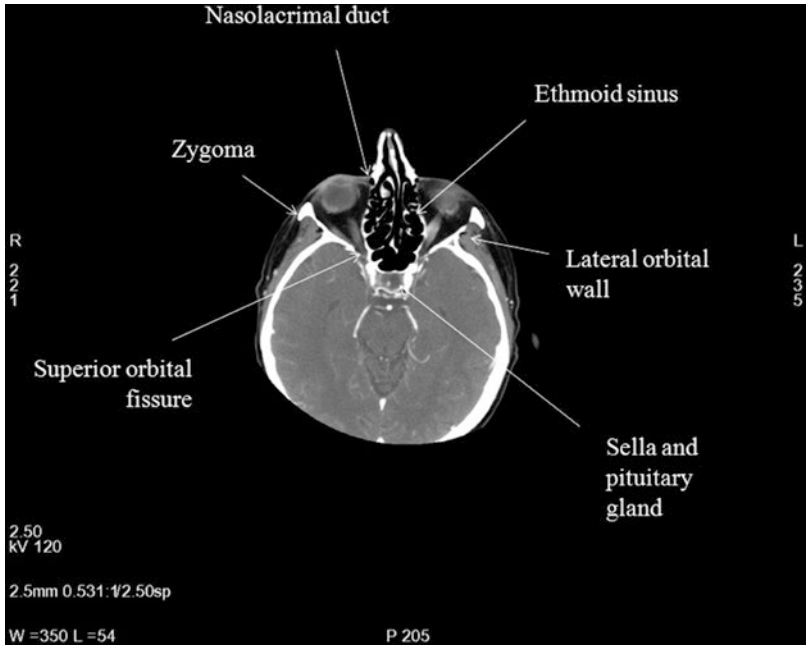
Nasolacrimal duct
Ethmoid sinus
Zygoma
Lateral orbital wall
Superior orbital fissure
Sella and pituitary gland
R
L
2.50
kV 120
2.5mm 0.531:1/2.50sp
W =350 L =54
P 205

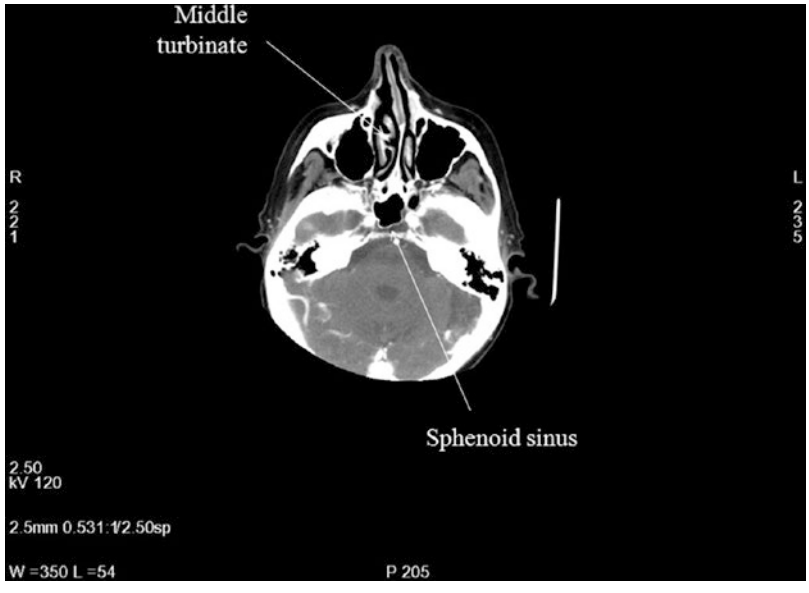
Middle turbinate
Sphenoid sinus
R
L
2.50
kV 120
2.5mm 0.531:1/2.50sp
W =350 L =54
P 205

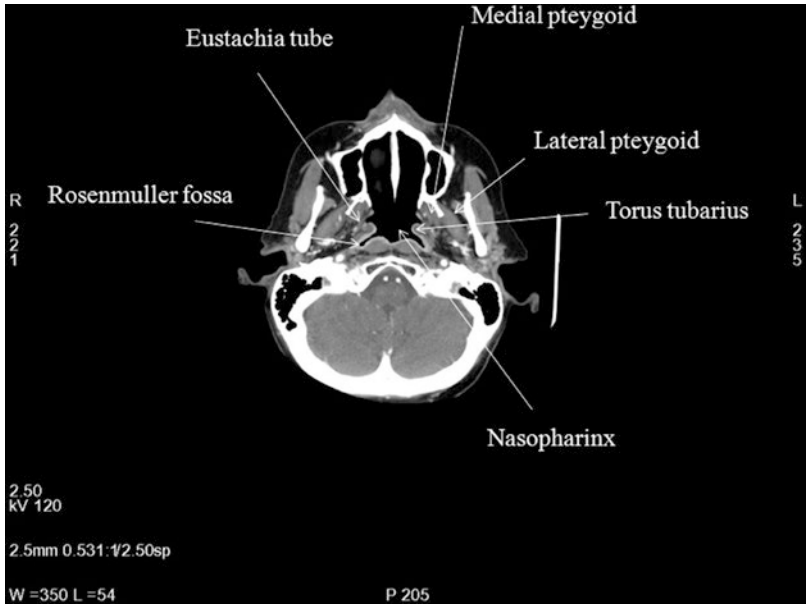
Eustachia tube
Medial pteygoid
Lateral pteygoid
Rosenmuller fossa
Torus tubarius
Nasopharinx
R
L
2.50
kV 120
2.5mm 0.531:1/2.50sp
W =350 L =54
P 205

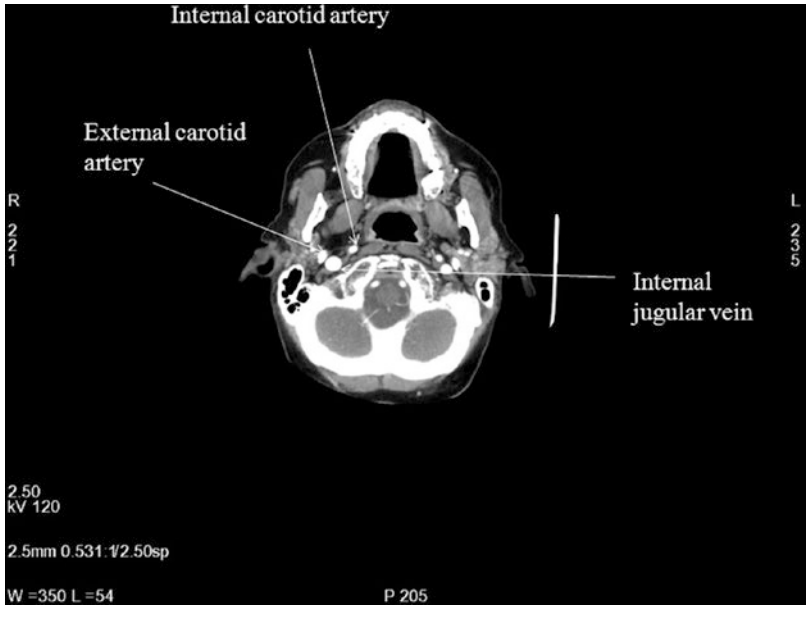
Internal carotid artery
External carotid artery
Internal jugular vein
R
L
2.50
kV 120
2.5mm 0.531:1/2.50sp
W =350 L =54
P 205

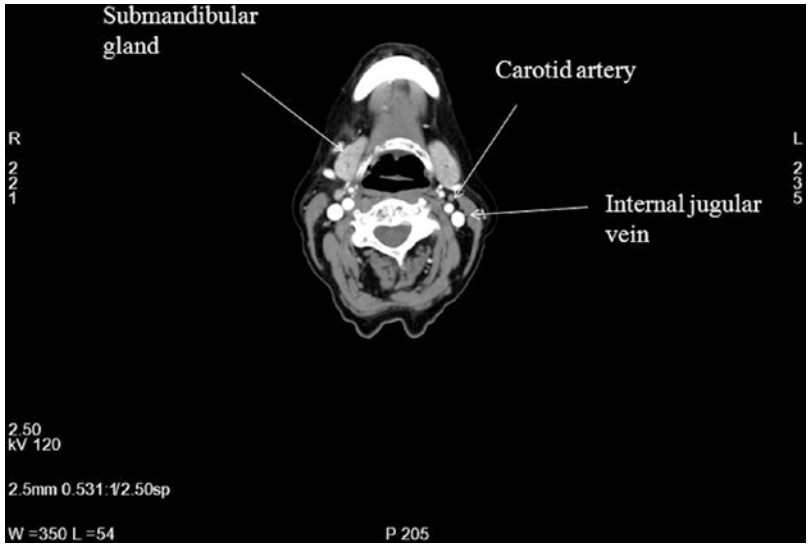
Submandibular gland
Carotid artery
Internal jugular vein
R
L
2.50
kV 120
2.5mm 0.531:1/2.50sp
W =350 L =54
P 205

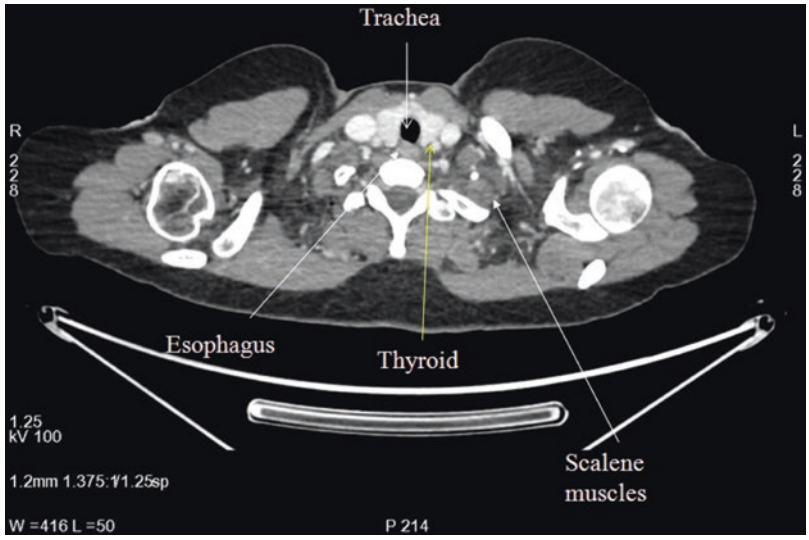
Trachea
Esophagus
Thyroid
Scalene muscles
R
L
1.25
kV 100
1.2mm 1.375:1/1.25sp
W =416 L =50
P 214

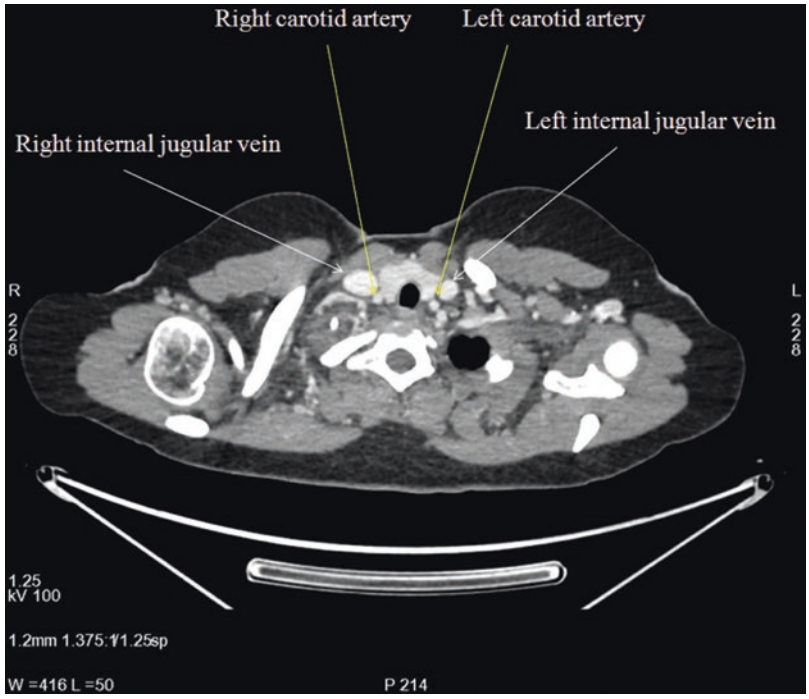
Right carotid artery
Left carotid artery
Left internal jugular vein
Right internal jugular vein
R
L
1.25
kV 100
1.2mm 1.375:1/1.25sp
W =416 L =50
P 214

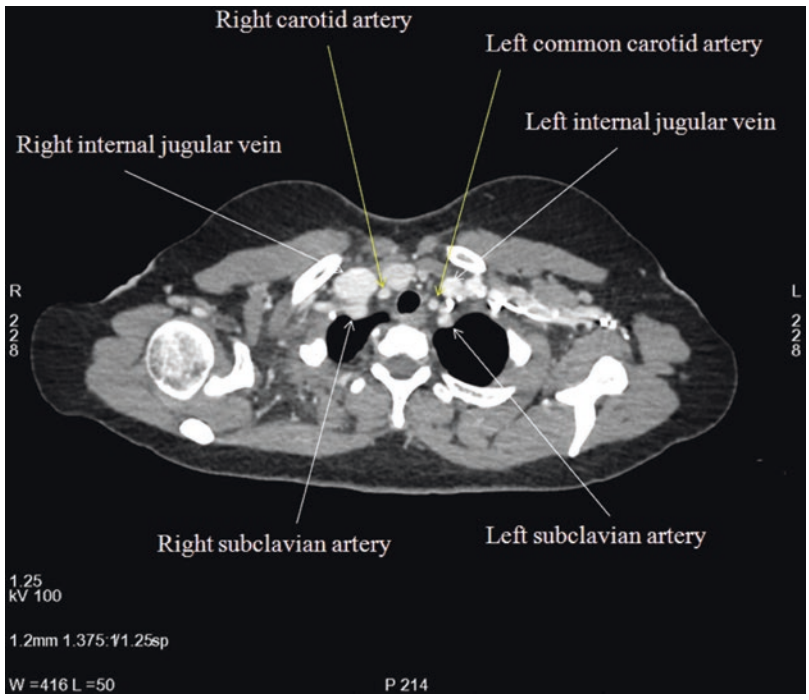
Right carotid artery
Left common carotid artery
Left internal jugular vein
Right internal jugular vein
R
L
Right subclavian artery
Left subclavian artery
1.25
kV 100
1.2mm 1.375:1/1.25sp
W =416 L =50
P 214

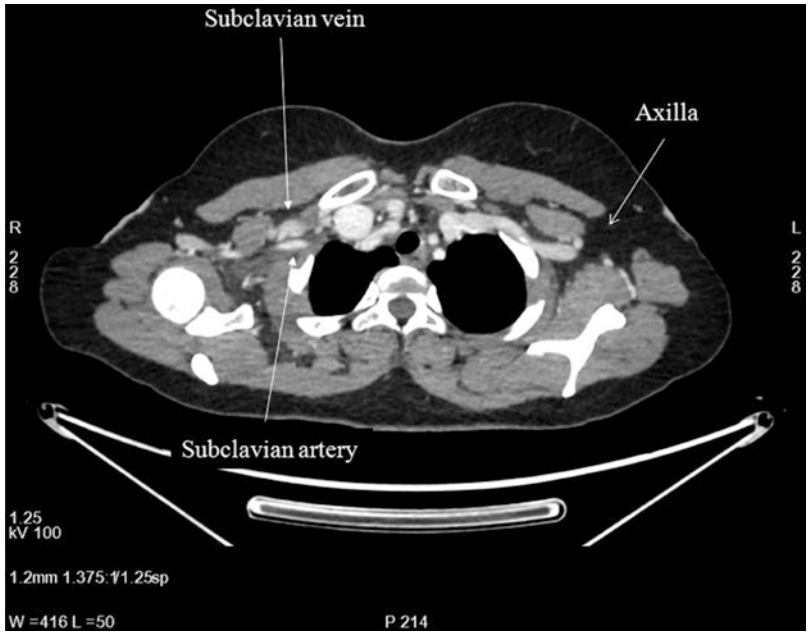
Subclavian vein
Axilla
Subclavian artery
R
L
1.25
kV 100
1.2mm 1.375:1/1.25sp
W =416 L =50
P 214

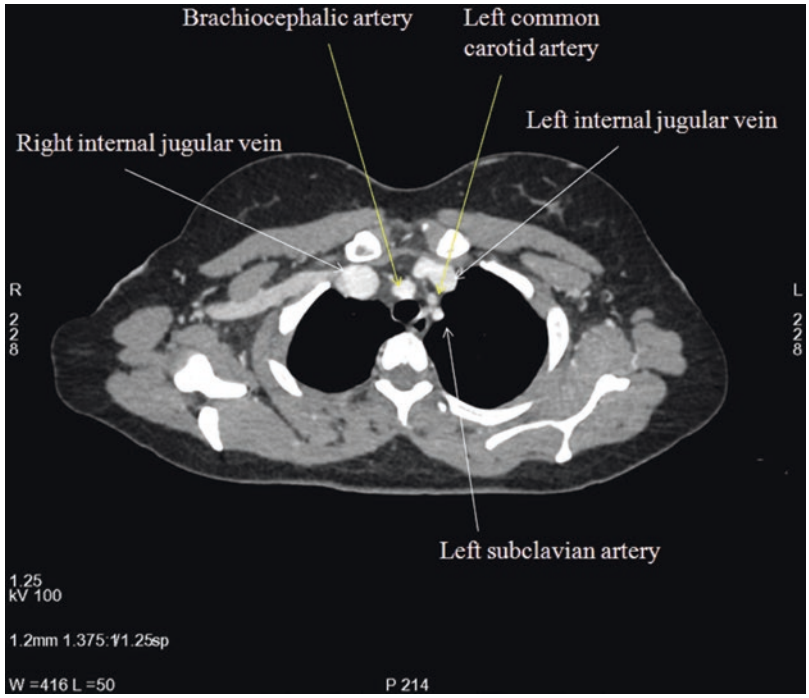
Brachiocephalic artery
Left common carotid artery
Left internal jugular vein
Right internal jugular vein
Left subclavian artery
R
L
1.25
kV 100
1.2mm 1.375:1/1.25sp
W =416 L =50
P 214

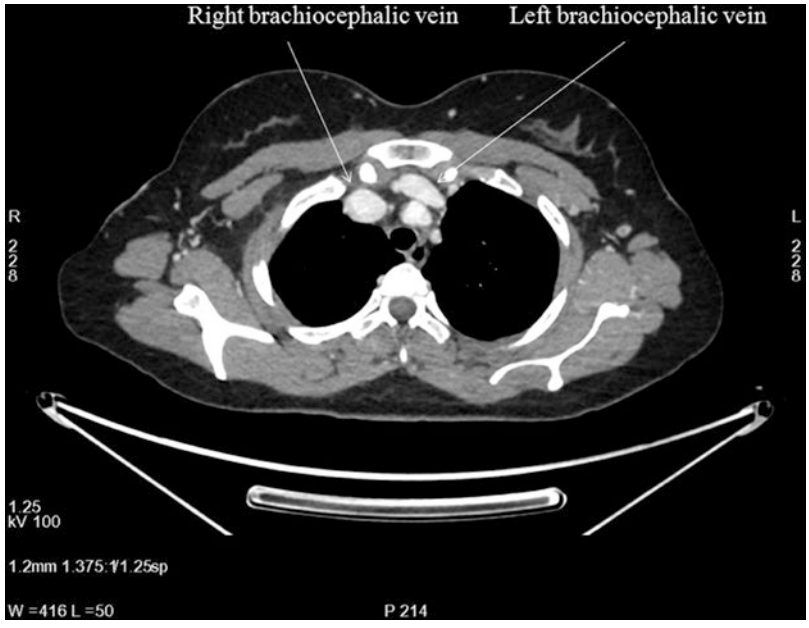
Right brachiocephalic vein
Left brachiocephalic vein
R
L
2
2
8
1.25
kV 100
1.2mm 1.375:1/1.25sp
W =416 L =50
P 214

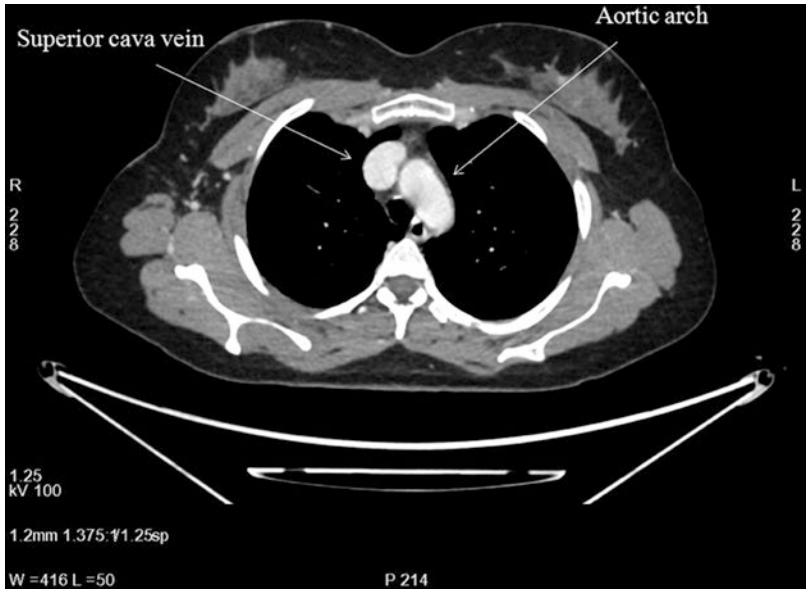
Superior cava vein
Aortic arch
R
L
2
2
8
1.25
kV 100
1.2mm 1.375:1/1.25sp
W =416 L =50
P 214

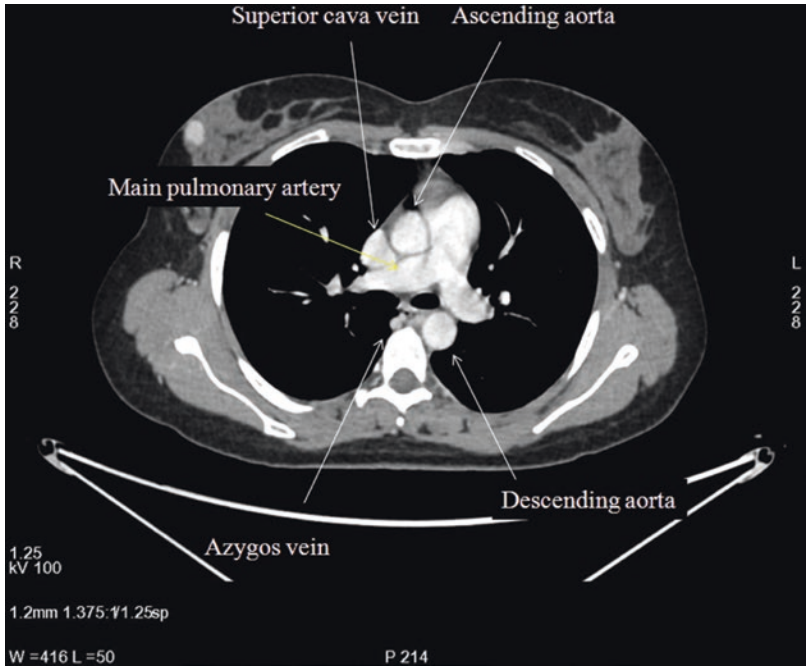
Superior cava vein
Ascending aorta
Main pulmonary artery
R
228
L
228
Descending aorta
Azygos vein
1.25
kV 100
1.2mm 1.375:1/1.25sp
W =416 L =50
P 214

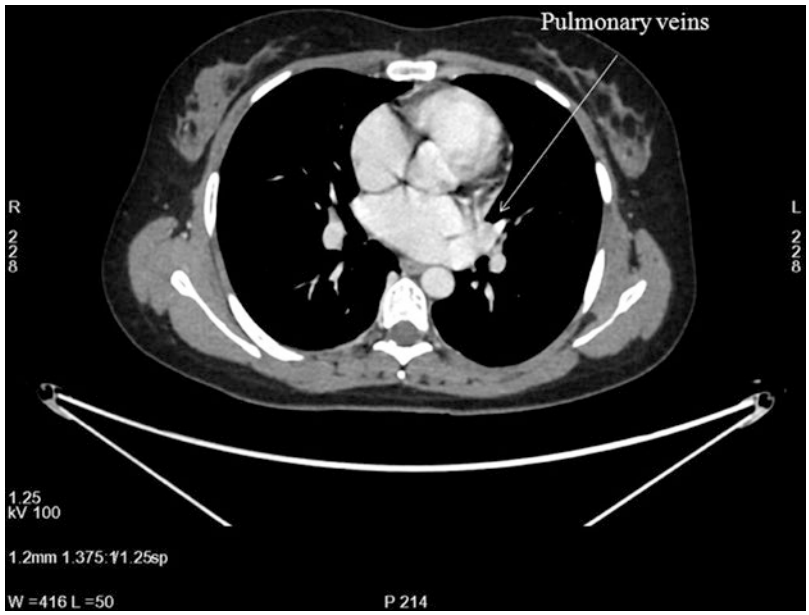
Pulmonary veins
R
228
L
228
1.25
kV 100
1.2mm 1.375:1/1.25sp
W =416 L =50
P 214

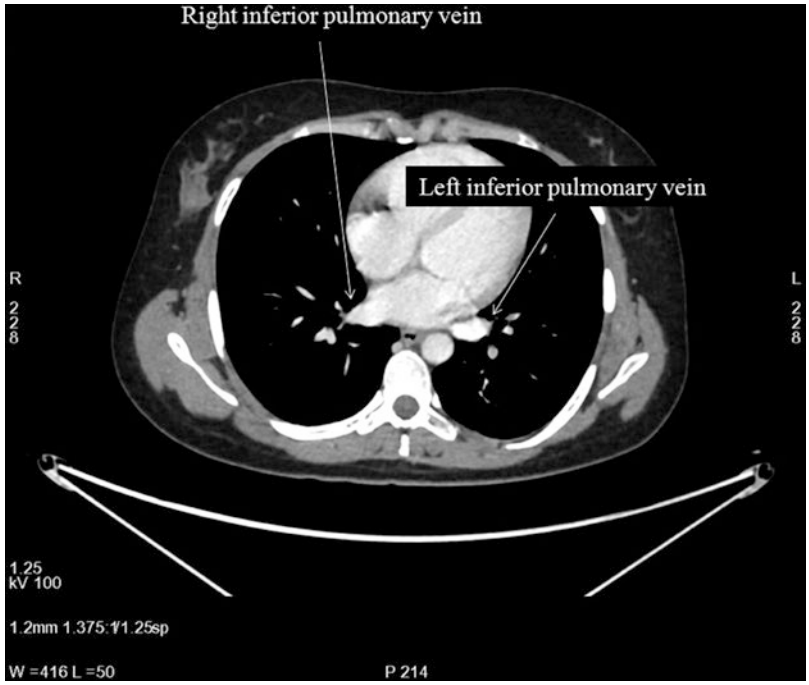
Right inferior pulmonary vein
Left inferior pulmonary vein
R
L
1.25
kV 100
1.2mm 1.375:1 1.25sp
W =416 L =50
P 214

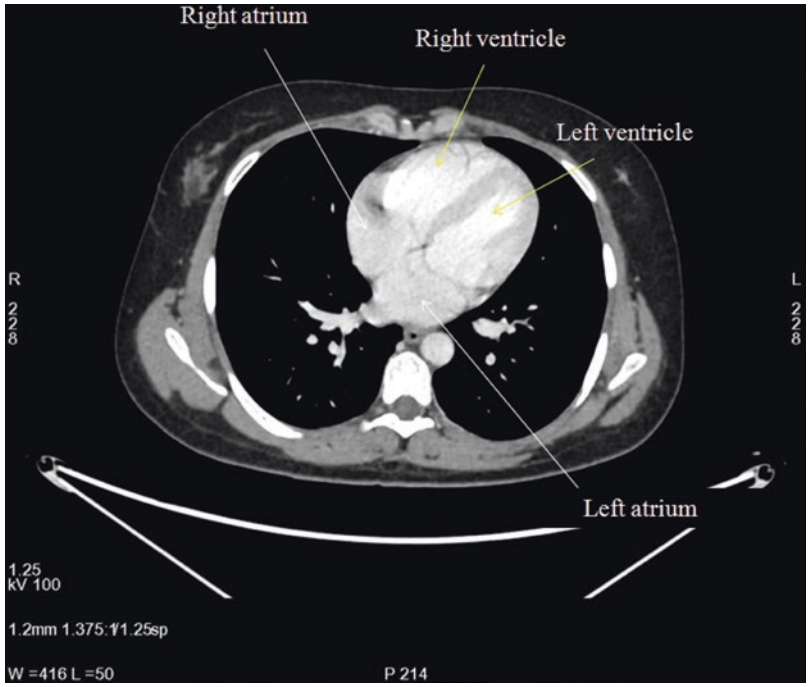
Right atrium
Right ventricle
Left ventricle
Left atrium
R
L
1.25
kV 100
1.2mm 1.375:1 1.25sp
W =416 L =50
P 214

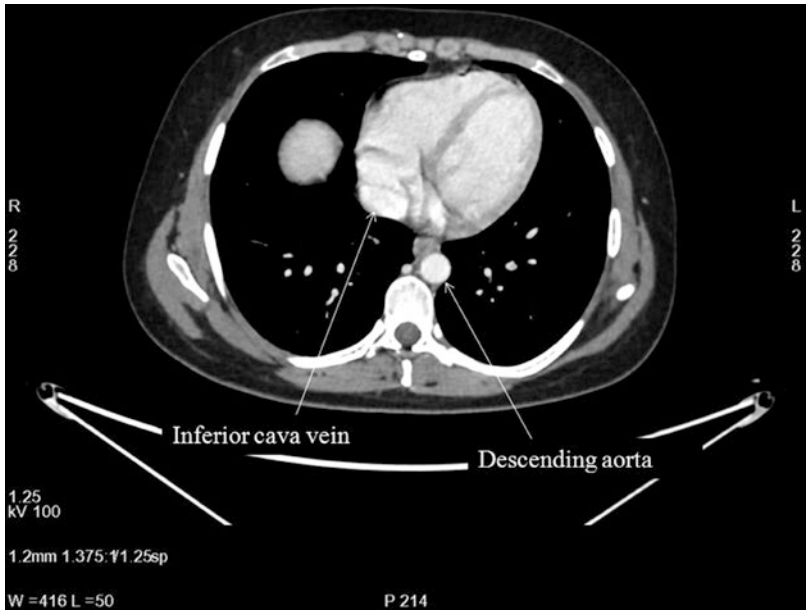
R
L
Inferior cava vein
Descending aorta
1.25
kV 100
1.2mm 1.375:1 1.25sp
W =416 L =50
P 214

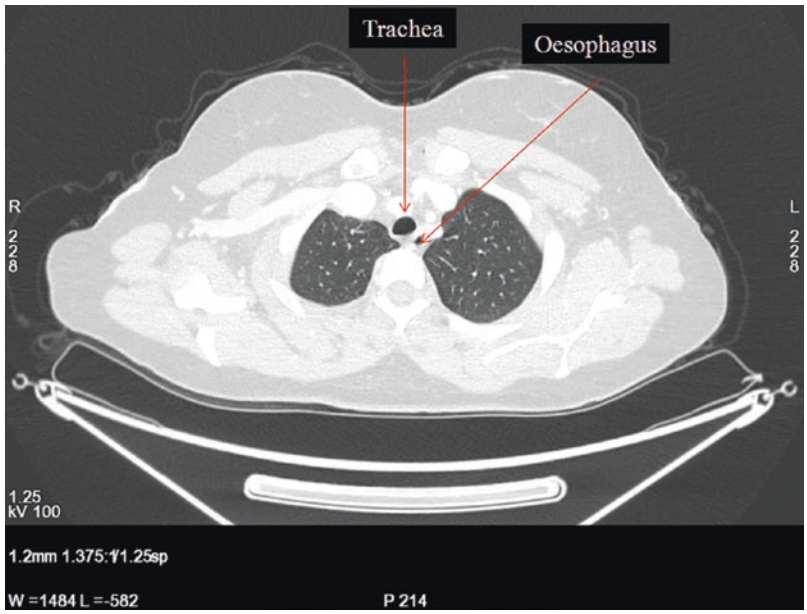
Trachea
Oesophagus
R
L
1.25
kV 100
1.2mm 1.375:1 1.25sp
W =1484 L =-582
P 214

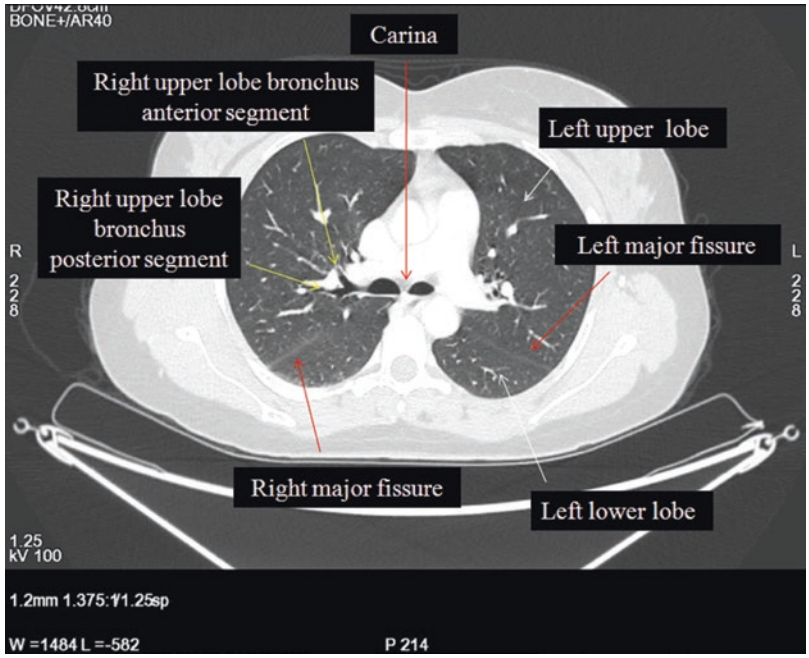
BONE+/AR40
Carina
Right upper lobe bronchus anterior segment
Left upper lobe
Right upper lobe bronchus posterior segment
Left major fissure
R
L
Right major fissure
Left lower lobe
1.25
kV 100
1.2mm 1.375:1/1.25sp
W =1484 L =-582
P 214

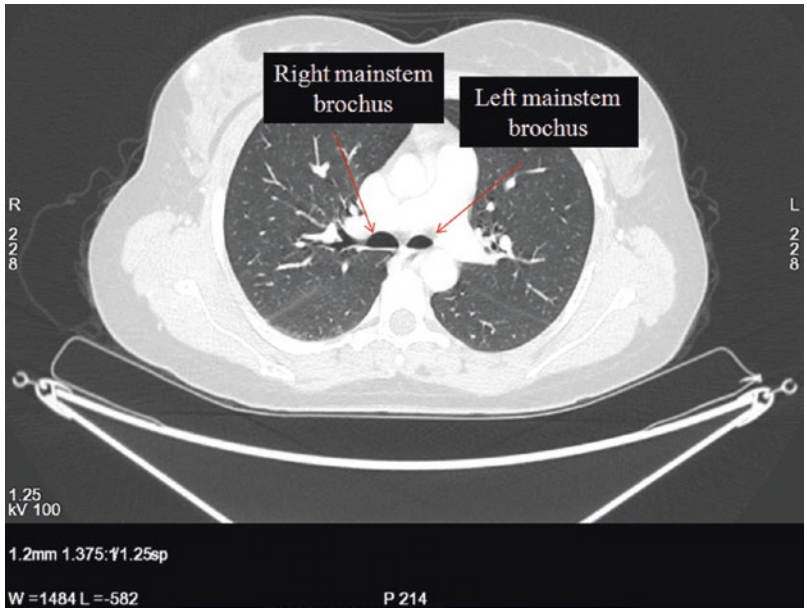
Right mainstem brochus
Left mainstem brochus
R
L
1.25
kV 100
1.2mm 1.375:1/1.25sp
W =1484 L =-582
P 214

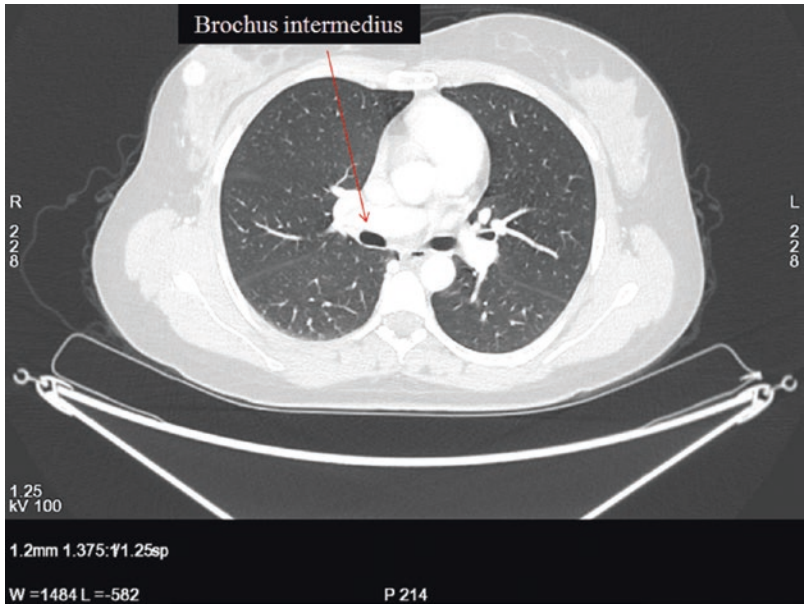
Brochus intermedius
R
L
1.25
kV 100
1.2mm 1.375:1/1.25sp
W =1484 L =-582
P 214

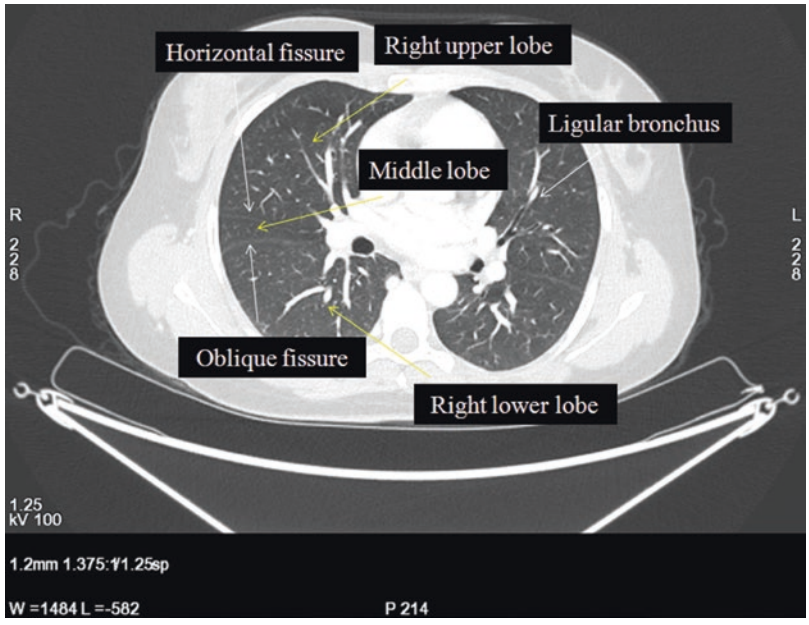
Horizontal fissure
Right upper lobe
Ligular bronchus
Middle lobe
Oblique fissure
Right lower lobe
R
L
1.25
kV 100
1.2mm 1.375:1/1.25sp
W =1484 L =-582
P 214

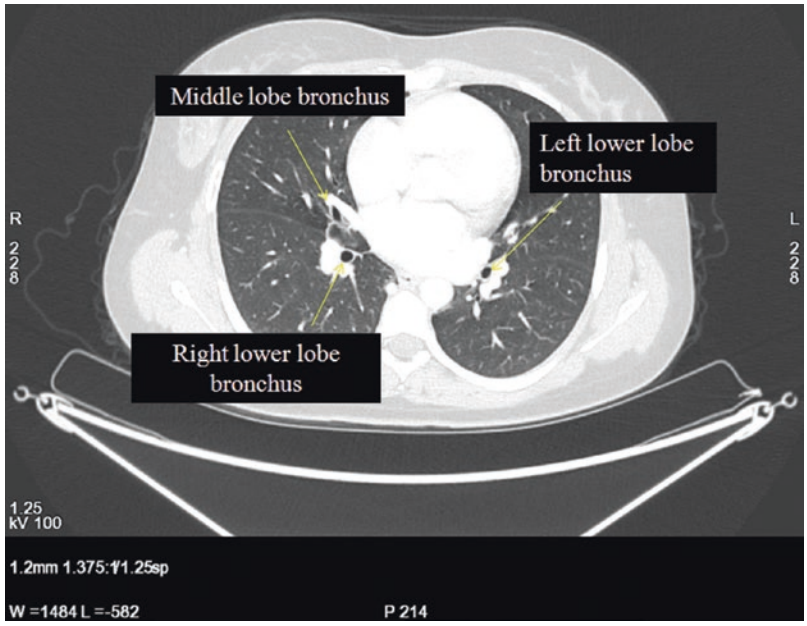
Middle lobe bronchus
Left lower lobe bronchus
Right lower lobe bronchus
R
L
1.25
kV 100
1.2mm 1.375:1 1.25sp
W =1484 L =-582
P 214

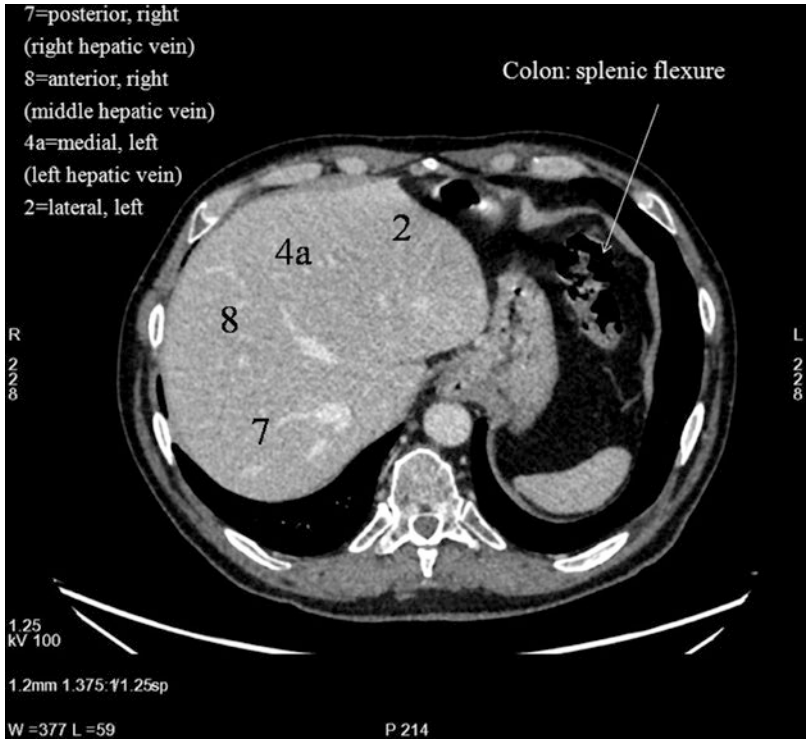
7=posterior, right
(right hepatic vein)
8=anterior, right
(middle hepatic vein)
4a=medial, left
(left hepatic vein)
2=lateral, left
Colon: splenic flexure
2
4a
8
7
R
L
1.25
kV 100
1.2mm 1.375:1 1.25sp
W =377 L =59
P 214

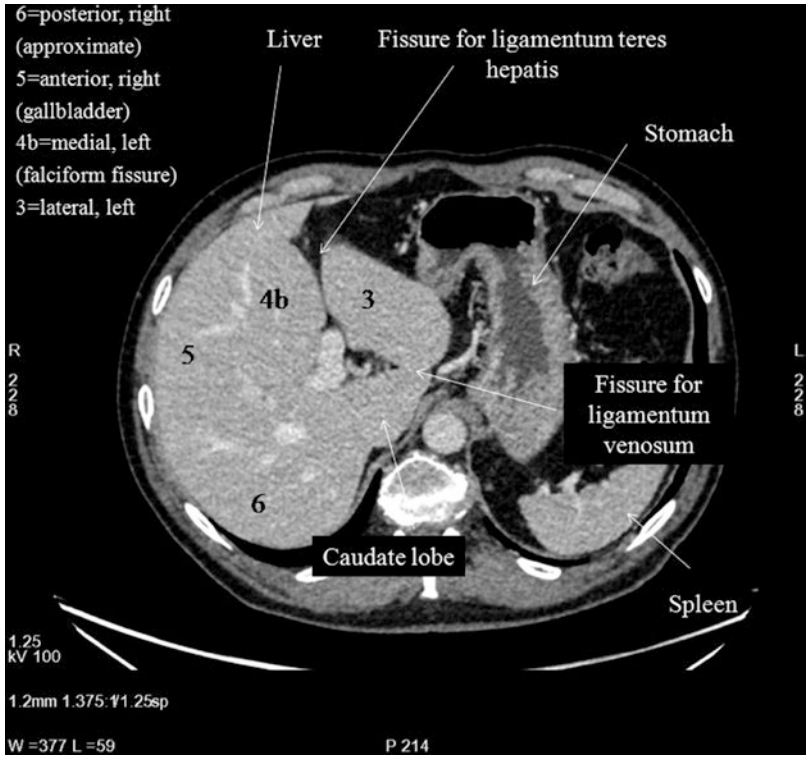
6=posterior, right
(approximate)
5=anterior, right
(gallbladder)
4b=medial, left
(falciform fissure)
3=lateral, left
Liver
Fissure for ligamentum teres hepatis
Stomach
4b
3
5
Fissure for ligamentum venosum
6
Caudate lobe
Spleen
R
L
1.25
kV 100
1.2mm 1.375:1/1.25sp
W =377 L =59
P 214

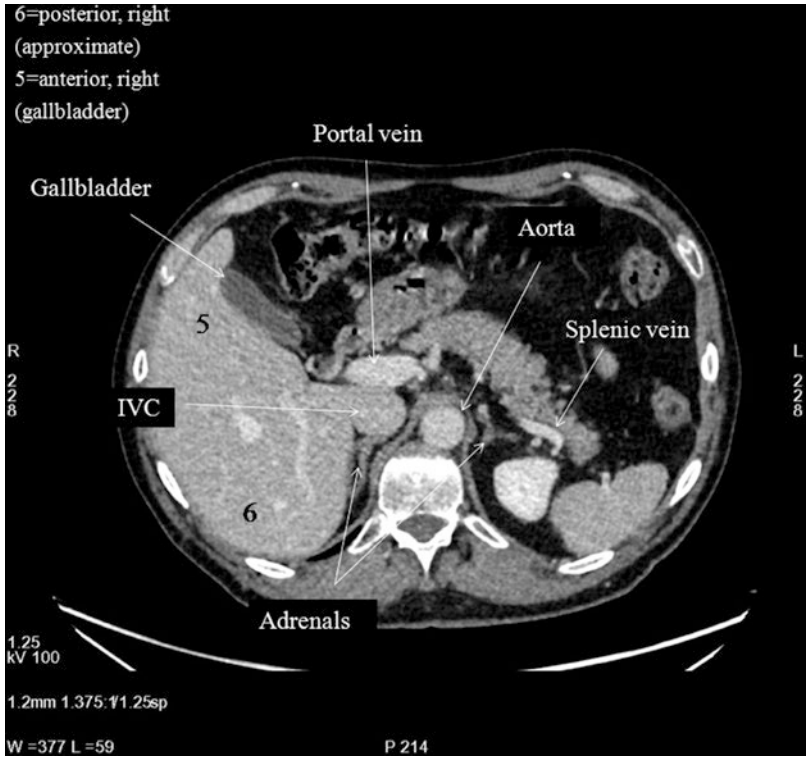
6=posterior, right
(approximate)
5=anterior, right
(gallbladder)
Portal vein
Gallbladder
Aorta
5
Splenic vein
IVC
6
Adrenals
R
L
1.25
kV 100
1.2mm 1.375:1/1.25sp
W =377 L =59
P 214

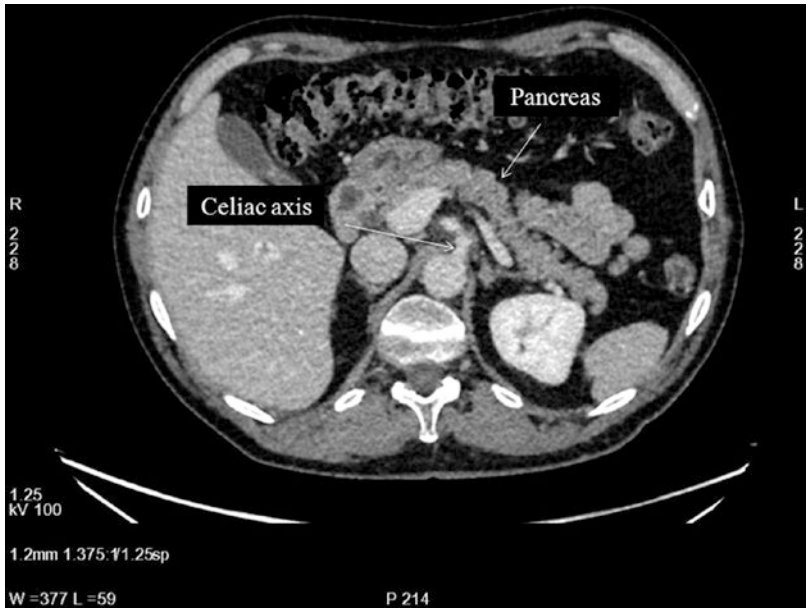
Pancreas
Celiac axis
R
L
1.25
kV 100
1.2mm 1.375:1/1.25sp
W =377 L =59
P 214

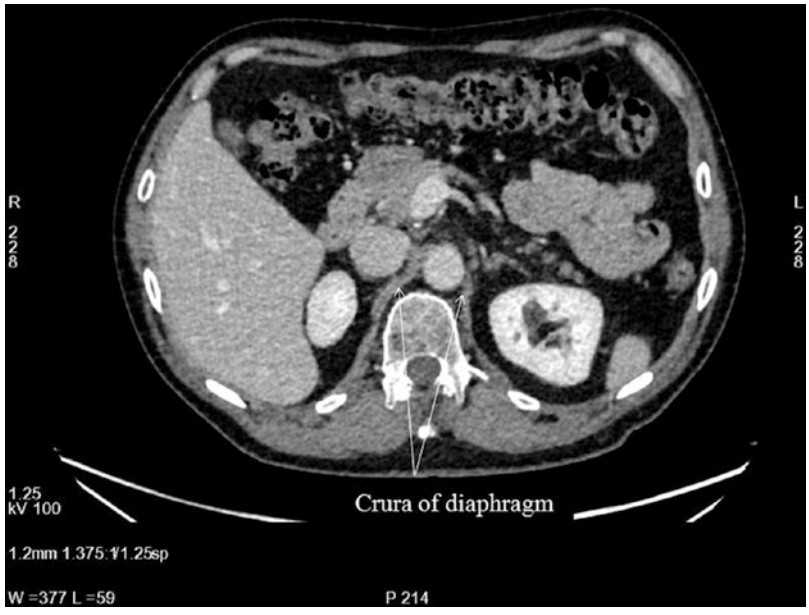
R
L
1.25
kV 100
Crura of diaphragm
1.2mm 1.375:1/1.25sp
W =377 L =59
P 214

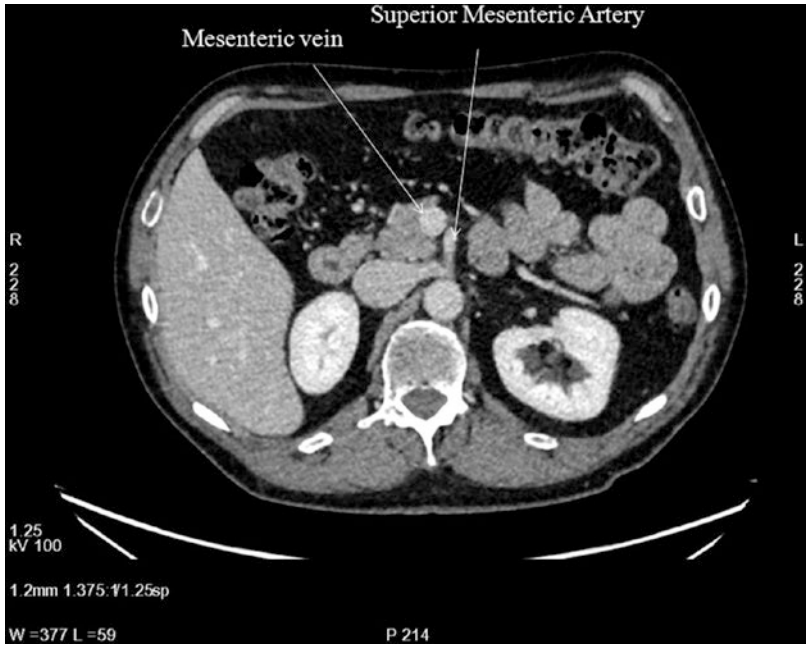
Superior Mesenteric Artery
Mesenteric vein
R
L
1.25
kV 100
1.2mm 1.375:1/1.25sp
W =377 L =59
P 214

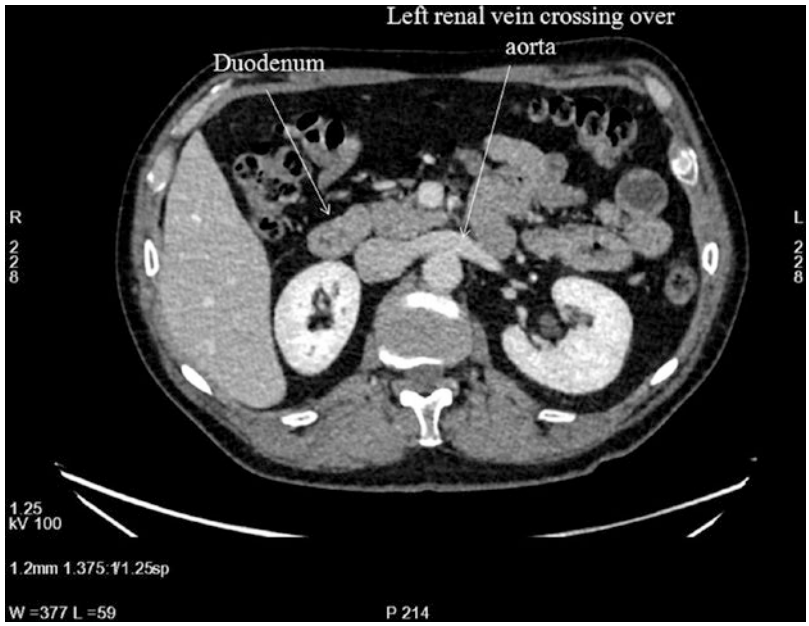
Left renal vein crossing over
aorta
Duodenum
R
L
1.25
kV 100
1.2mm 1.375:1/1.25sp
W =377 L =59
P 214

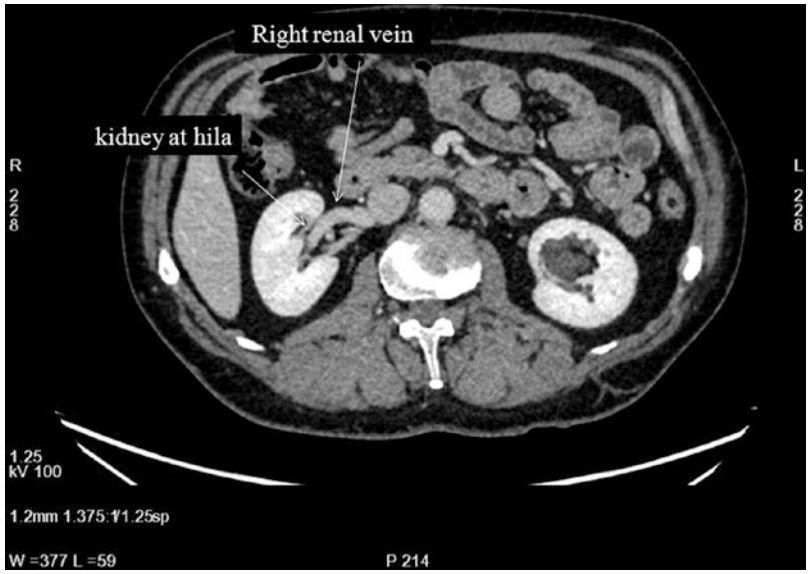
Right renal vein
kidney at hila
R
L
1.25
kV 100
1.2mm 1.375:1/1.25sp
W =377 L =59
P 214

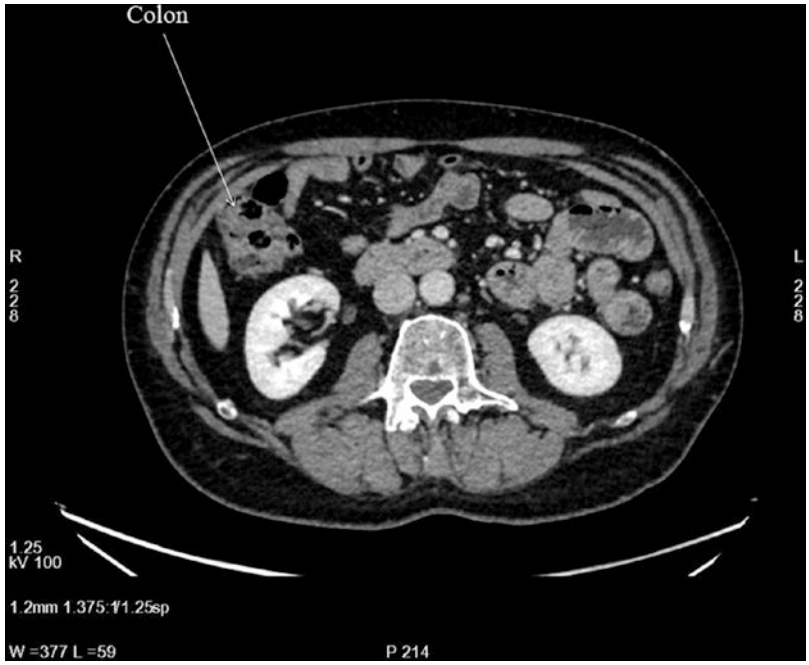
Colon
R
L
1.25
kV 100
1.2mm 1.375:1/1.25sp
W =377 L =59
P 214

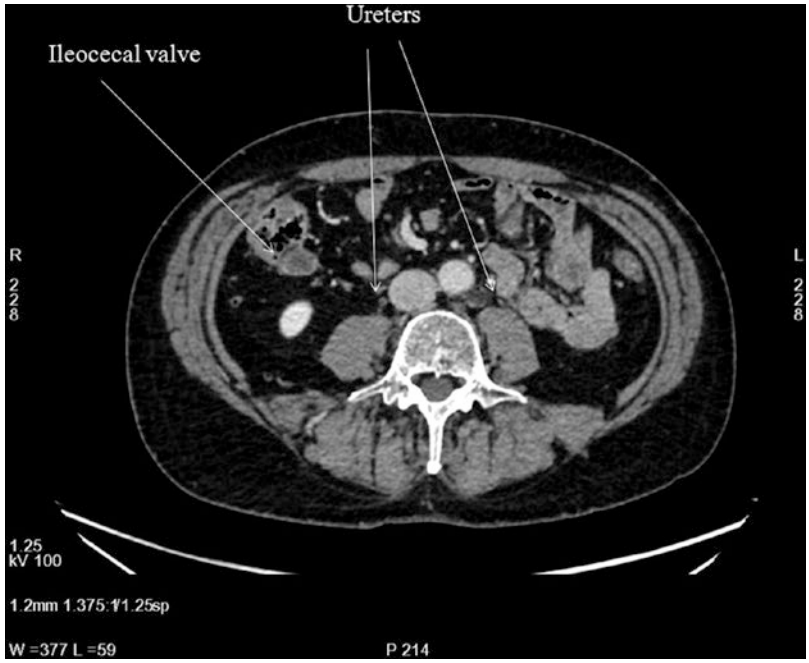
Ureters
Ileocecal valve
R
L
1.25
kV 100
1.2mm 1.375:1/1.25sp
W =377 L =59
P 214

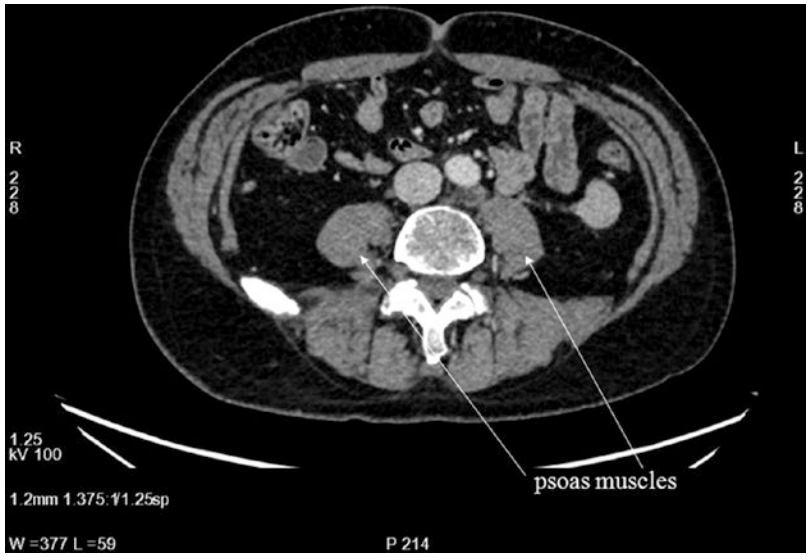
R
L
1.25
kV 100
psoas muscles
1.2mm 1.375:1/1.25sp
W =377 L =59
P 214

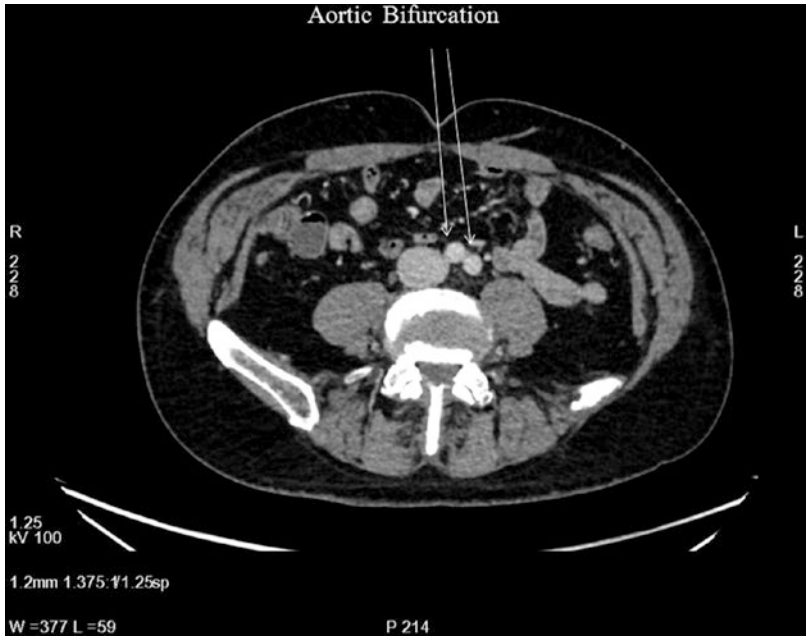
Aortic Bifurcation
R
L
1.25
kV 100
1.2mm 1.375:1/1.25sp
W =377 L =59
P 214

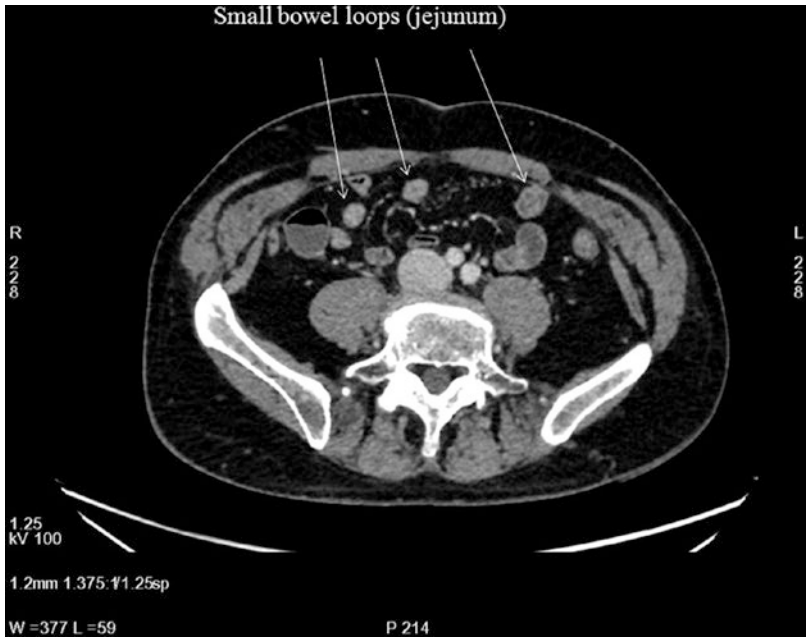
Small bowel loops (jejunum)
R
L
1.25
kV 100
1.2mm 1.375:1/1.25sp
W =377 L =59
P 214

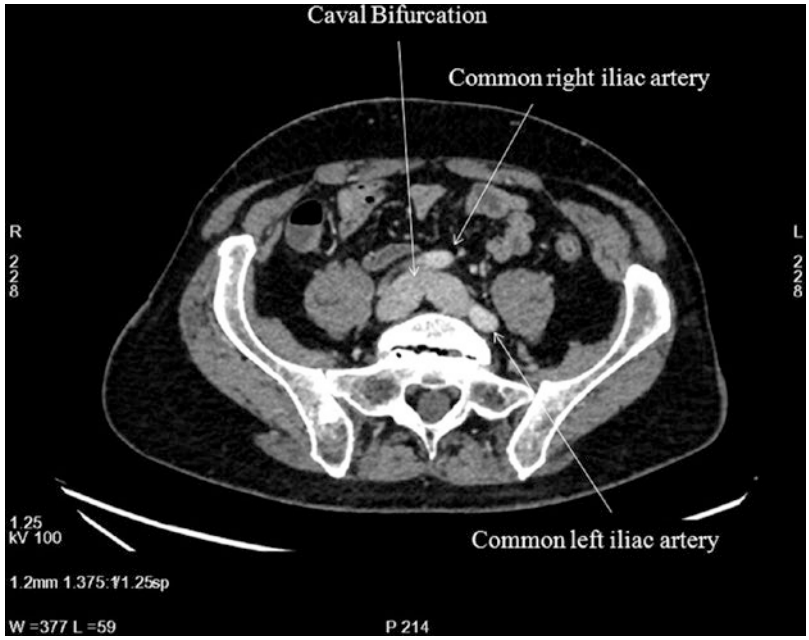
Caval Bifurcation
Common right iliac artery
Common left iliac artery
R
L
1.25
kV 100
1.2mm 1.375:1 1.25sp
W =377 L =59
P 214

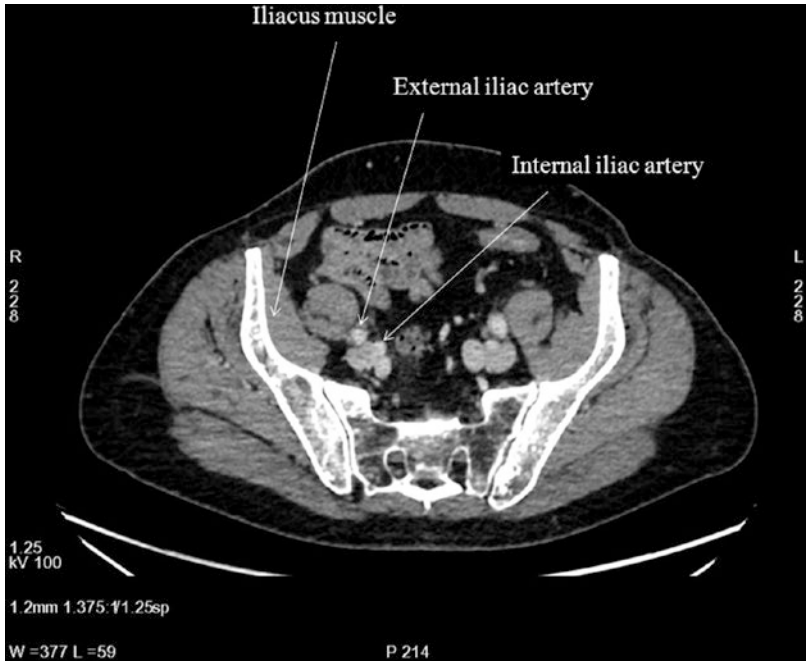
Iliacus muscle
External iliac artery
Internal iliac artery
R
L
1.25
kV 100
1.2mm 1.375:1 1.25sp
W =377 L =59
P 214

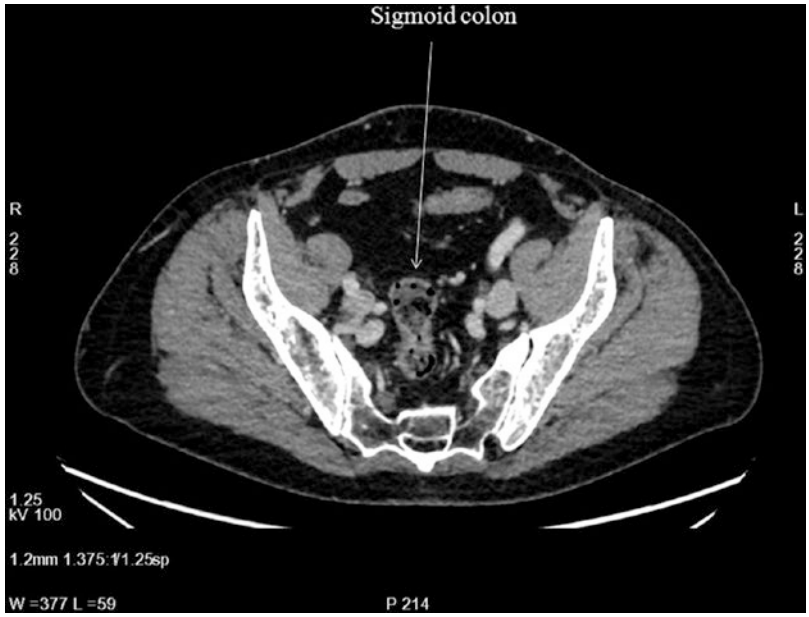
Sigmoid colon
R
L
1.25
kV 100
1.2mm 1.375:1/1.25sp
W =377 L =59
P 214

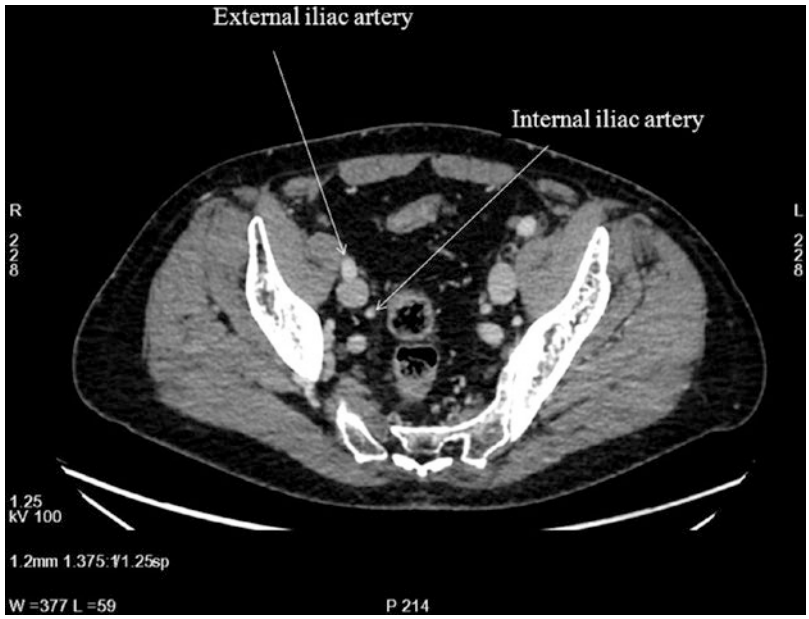
External iliac artery
Internal iliac artery
R
L
1.25
kV 100
1.2mm 1.375:1/1.25sp
W =377 L =59
P 214

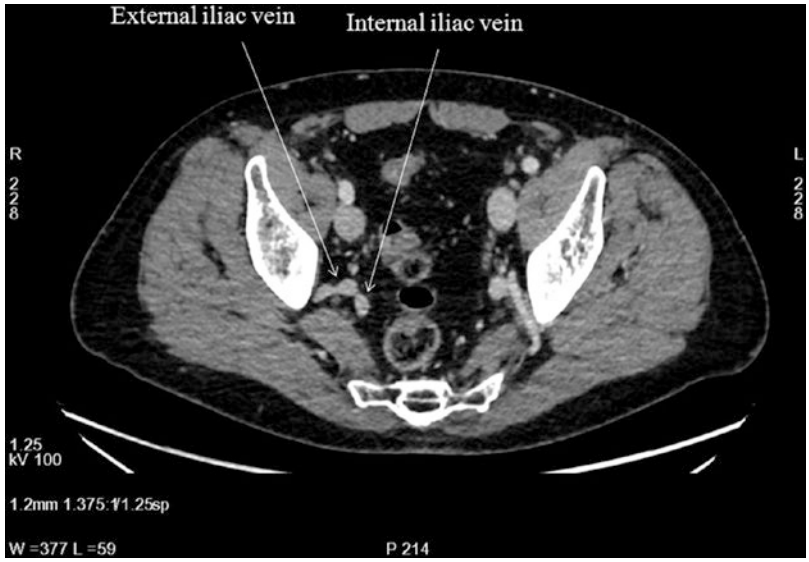
External iliac vein
Internal iliac vein
R
L
1.25
kV 100
1.2mm 1.375:1/1.25sp
W =377 L =59
P 214

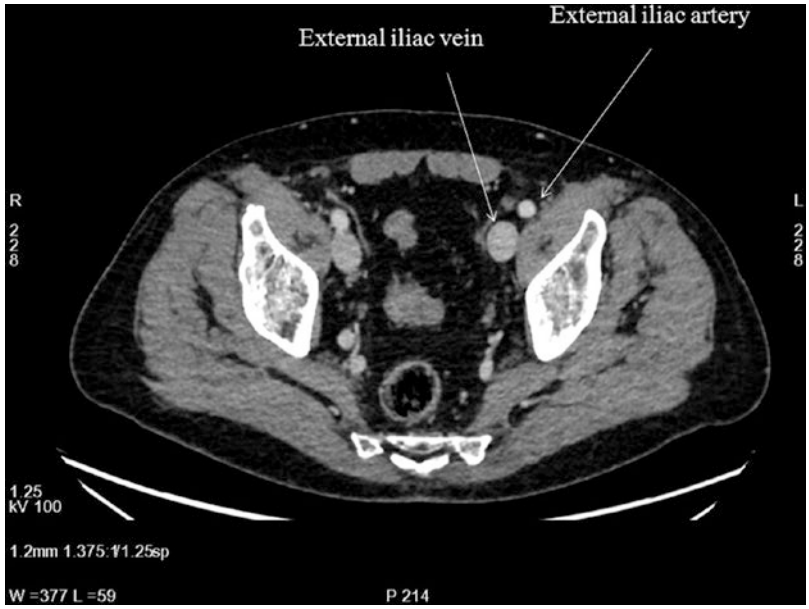
External iliac artery
External iliac vein
R
L
1.25
kV 100
1.2mm 1.375:1/1.25sp
W =377 L =59
P 214


Seminal Vescicles
R
L
1.25
kV 100
1.2mm 1.375:1 1.25sp
W =377 L =59
P 214


ureter inserting into trigone
R
L
1.25
kV 100
1.2mm 1.375:1 1.25sp
W =377 L =59
P 214

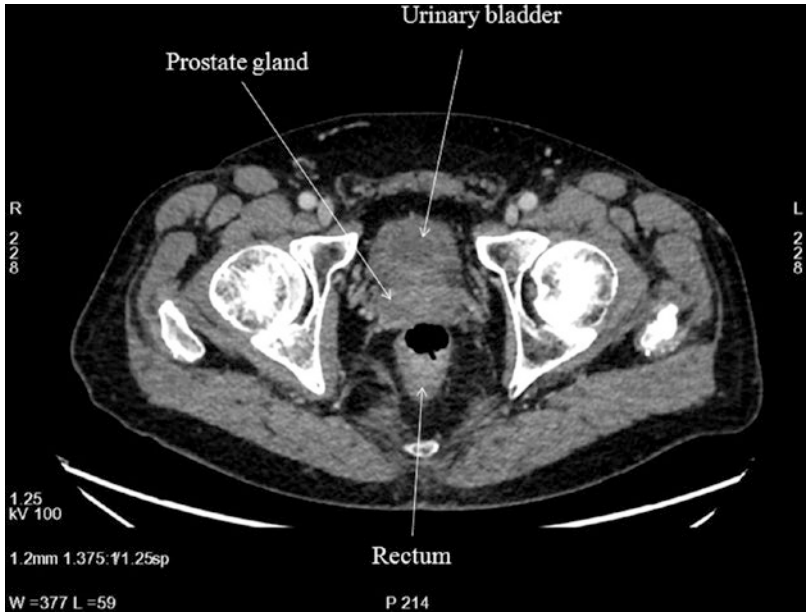
Urinary bladder
Prostate gland
R
L
Rectum
1.25
kV 100
1.2mm 1.375:1/1.25sp
W =377 L =59
P 214

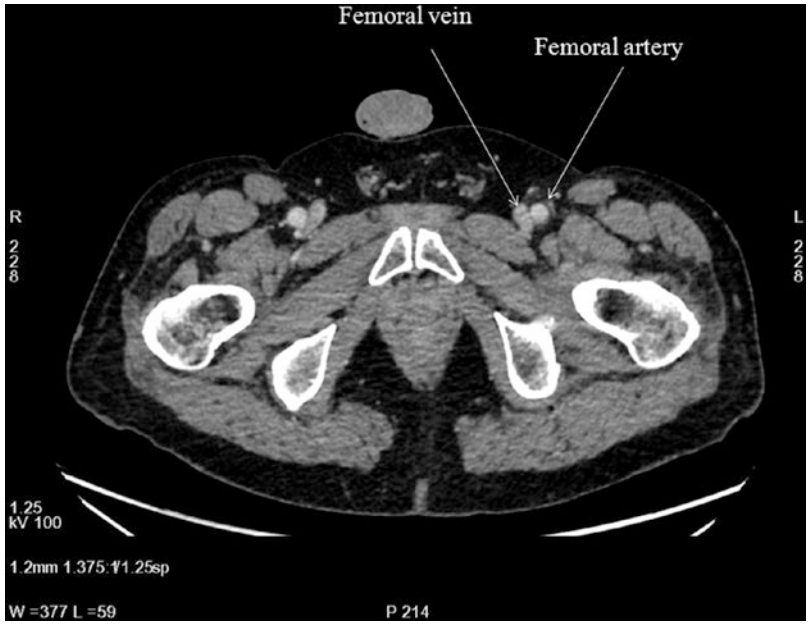
Femoral vein
Femoral artery
R
L
1.25
kV 100
1.2mm 1.375:1/1.25sp
W =377 L =59
P 214

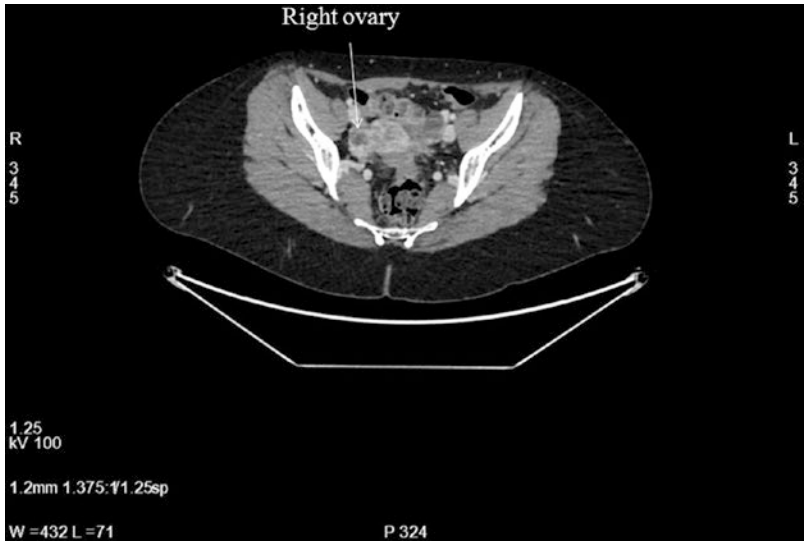
Right ovary
R
3
4
5
L
3
4
5
1.25
kV 100
1.2mm 1.375:1/1.25sp
W =432 L =71
P 324

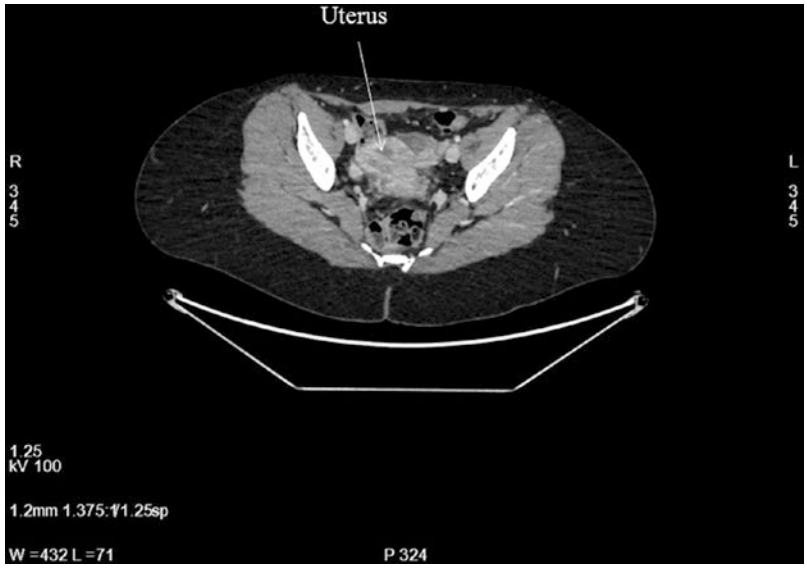
Uterus
R
3
4
5
L
3
4
5
1.25
kV 100
1.2mm 1.375:1/1.25sp
W =432 L =71
P 324

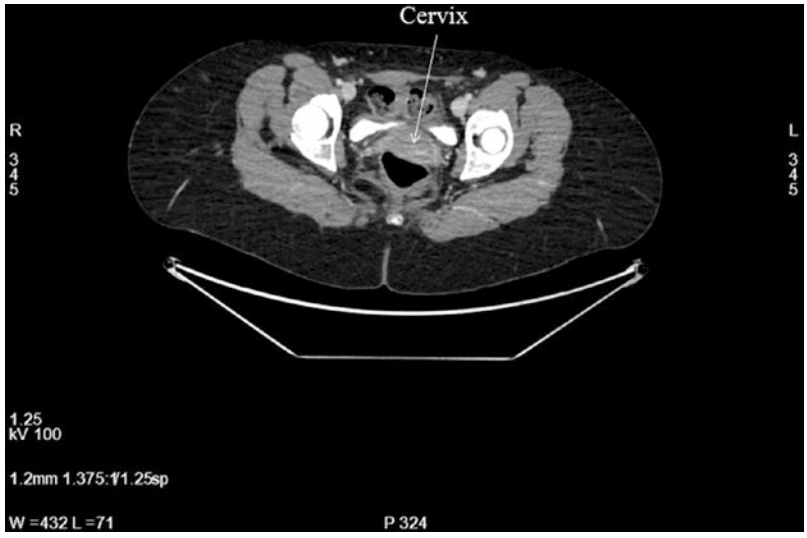
Cervix
R
3
4
5
L
3
4
5
1.25
kV 100
1.2mm 1.375:1/1.25sp
W =432 L =71
P 324

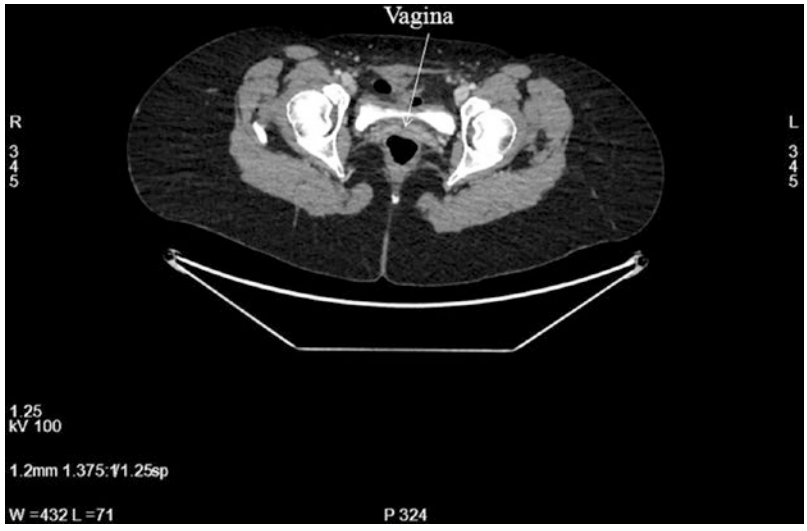
Vagina
R
3
4
5
L
3
4
5
1.25
kV 100
1.2mm 1.375:1/1.25sp
W =432 L =71
P 324

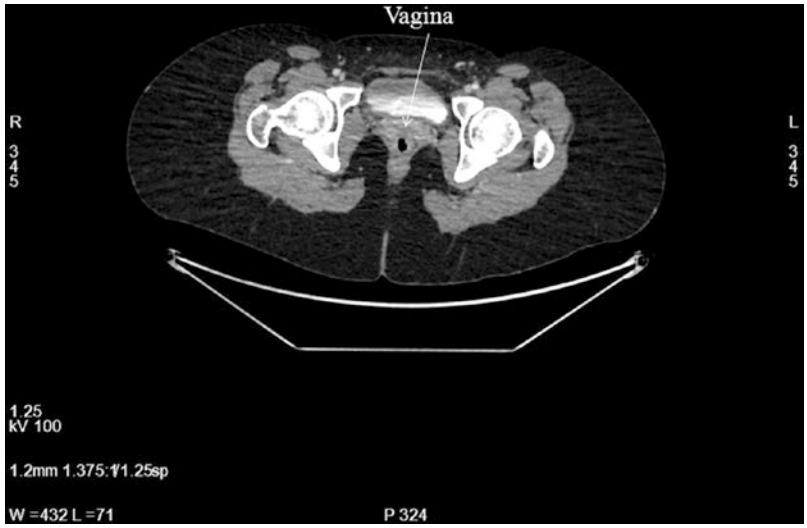
Vagina
R
3
4
5
L
3
4
5
1.25
kV 100
1.2mm 1.375:1/1.25sp
W =432 L =71
P 324

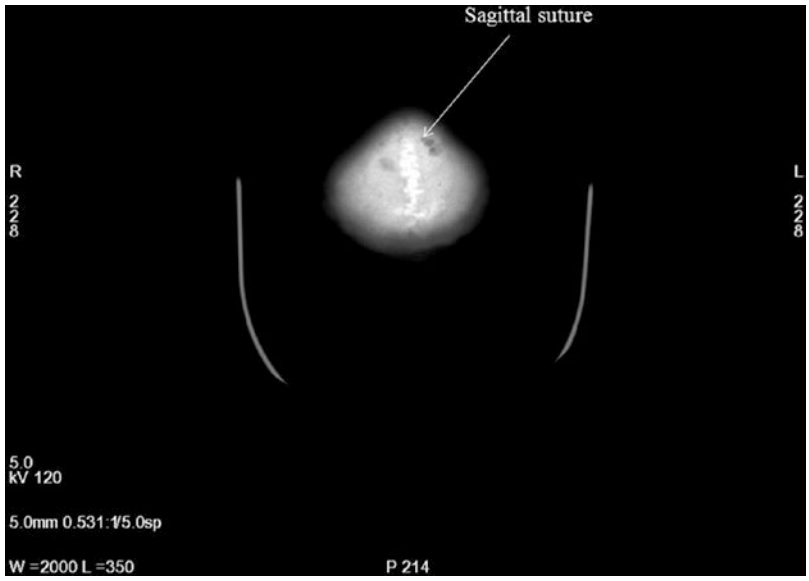
Sagittal suture
R
2
2
8
L
2
2
8
5.0
kV 120
5.0mm 0.531:1/5.0sp
W =2000 L =350
P 214

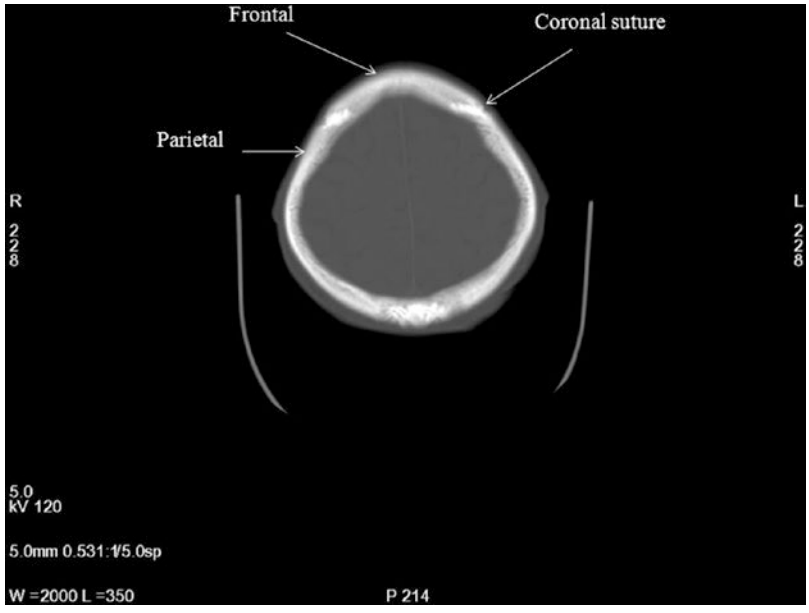
Frontal
Coronal suture
Parietal
R
L
5.0
kV 120
5.0mm 0.531:1/5.0sp
W =2000 L =350
P 214

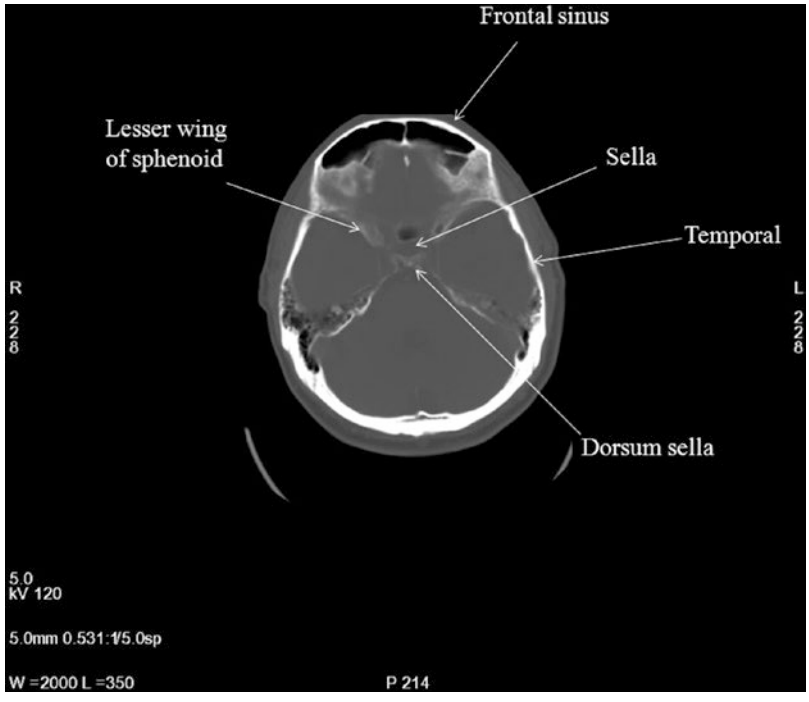
Frontal sinus
Lesser wing
of sphenoid
Sella
Temporal
R
L
Dorsum sella
5.0
kV 120
5.0mm 0.531:1/5.0sp
W =2000 L =350
P 214

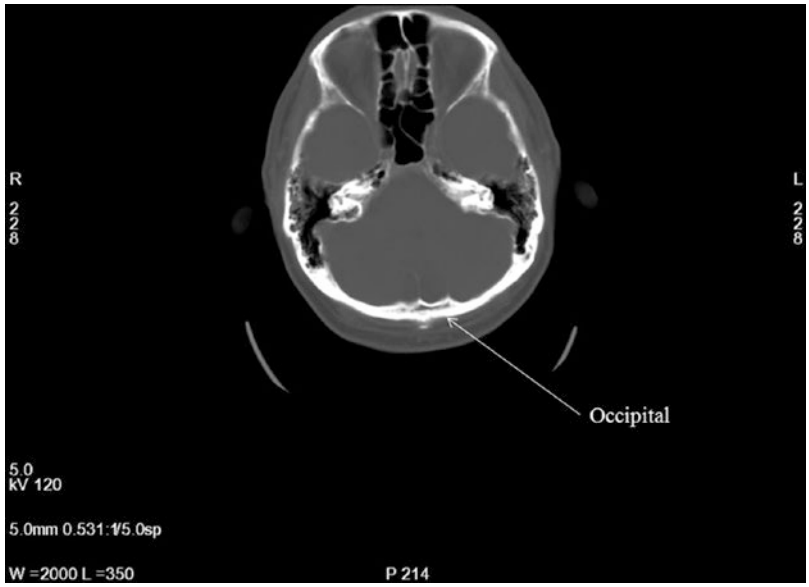
R
L
Occipital
5.0
kV 120
5.0mm 0.531:1/5.0sp
W =2000 L =350
P 214

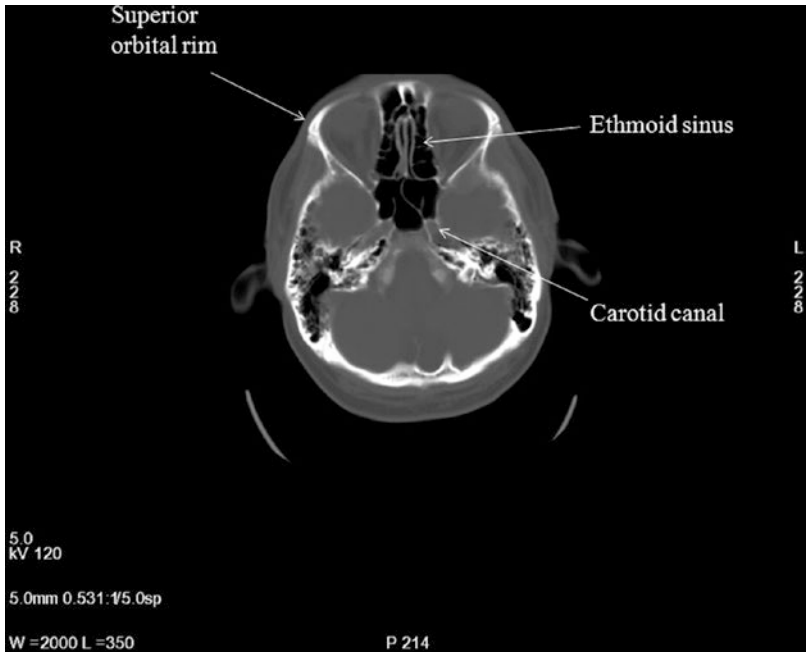
Superior
orbital rim
Ethmoid sinus
Carotid canal
R
L
5.0
kV 120
5.0mm 0.531:1/5.0sp
W =2000 L =350
P 214

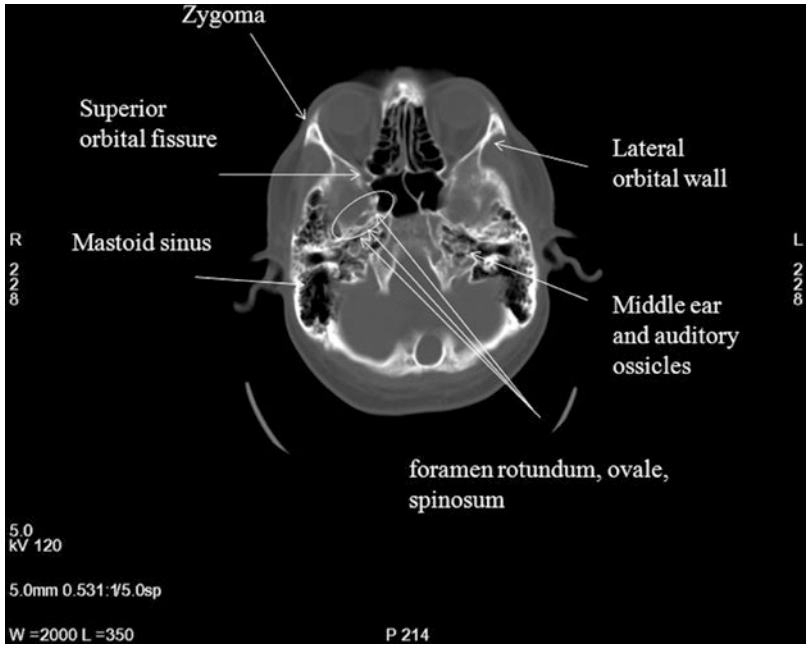
Zygoma
Superior orbital fissure
Lateral orbital wall
Mastoid sinus
Middle ear and auditory ossicles
foramen rotundum, ovale, spinosum
R
L
2 2 8
5.0
kV 120
5.0mm 0.531:1/5.0sp
W =2000 L =350
P 214

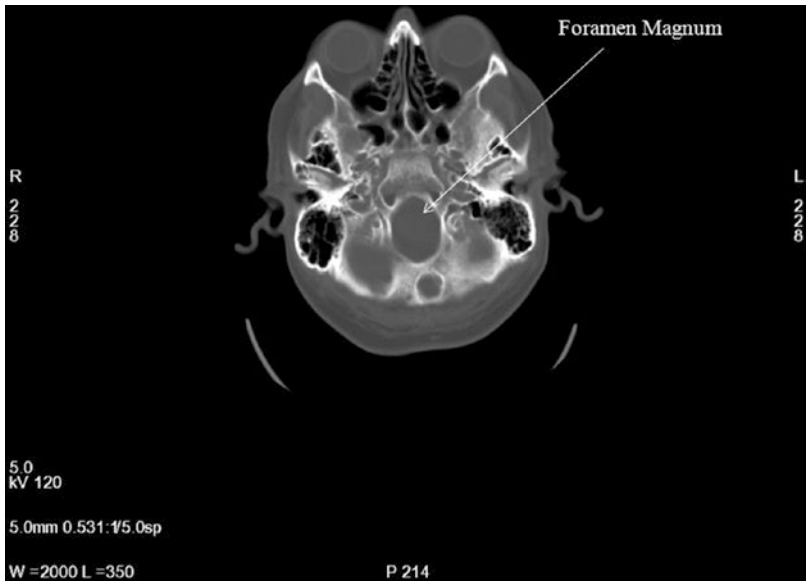
Foramen Magnum
R
L
2 2 8
5.0
kV 120
5.0mm 0.531:1/5.0sp
W =2000 L =350
P 214

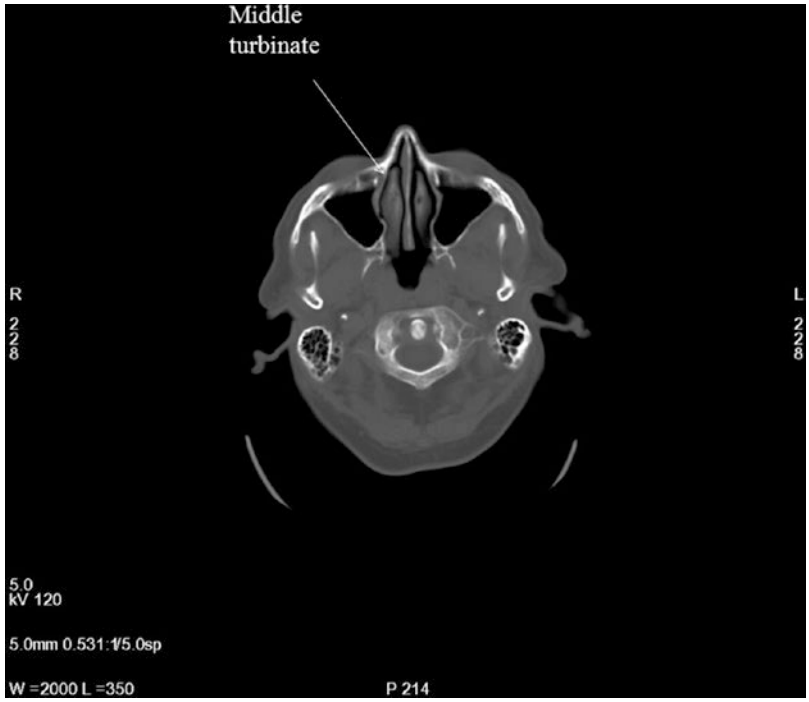
Middle
turbinate
R
L
5.0
kV 120
5.0mm 0.531:1/5.0sp
W =2000 L =350
P 214


Nasolacrimal duct
Zygomatic arch
R
L
5.0
kV 120
5.0mm 0.531:1/5.0sp
W =2000 L =350
P 214

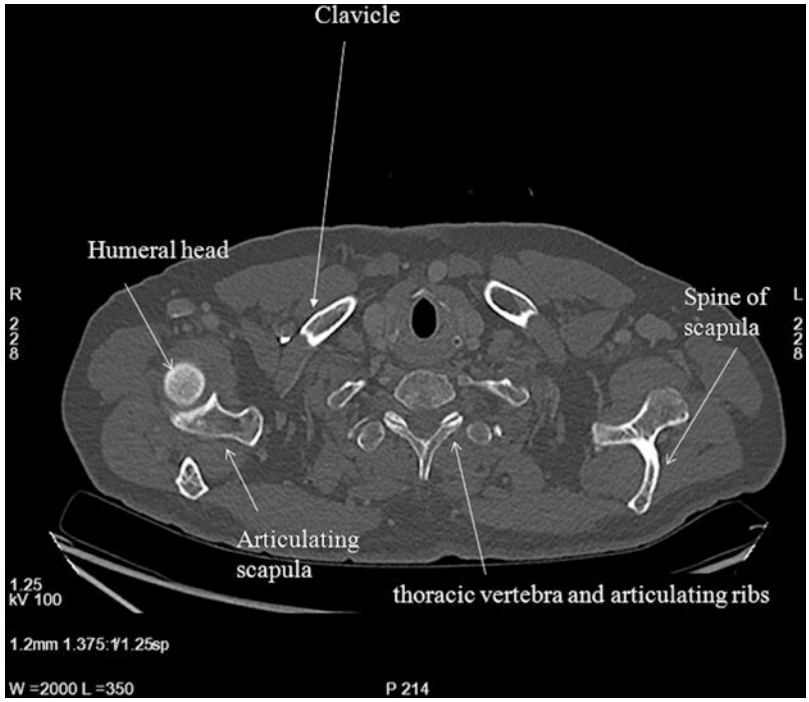
Clavicle
Humeral head
Spine of scapula
R
L
228
228
Articulating scapula
thoracic vertebra and articulating ribs
1.25
kV 100
1.2mm 1.375:1/1.25sp
W =2000 L =350
P 214

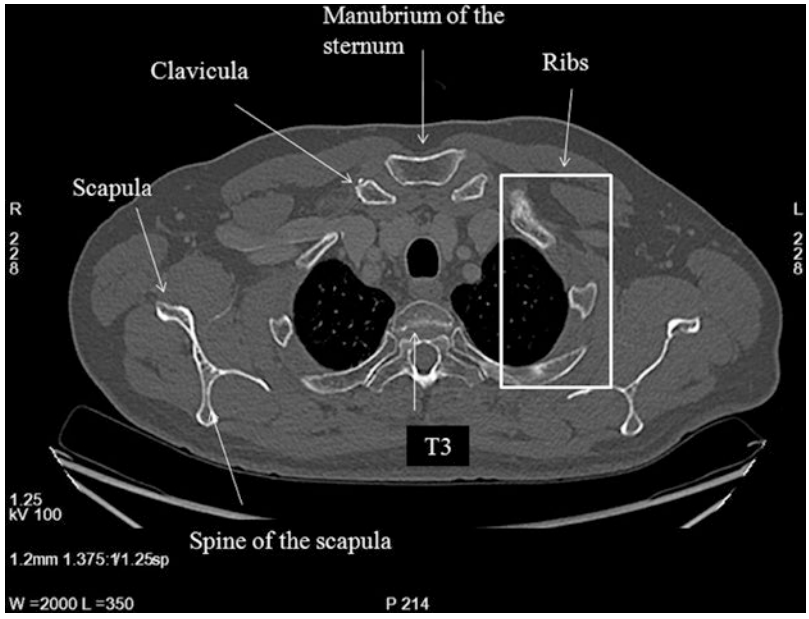
Manubrium of the sternum
Clavicula
Ribs
Scapula
R
L
228
228
T3
1.25
kV 100
Spine of the scapula
1.2mm 1.375:1/1.25sp
W =2000 L =350
P 214

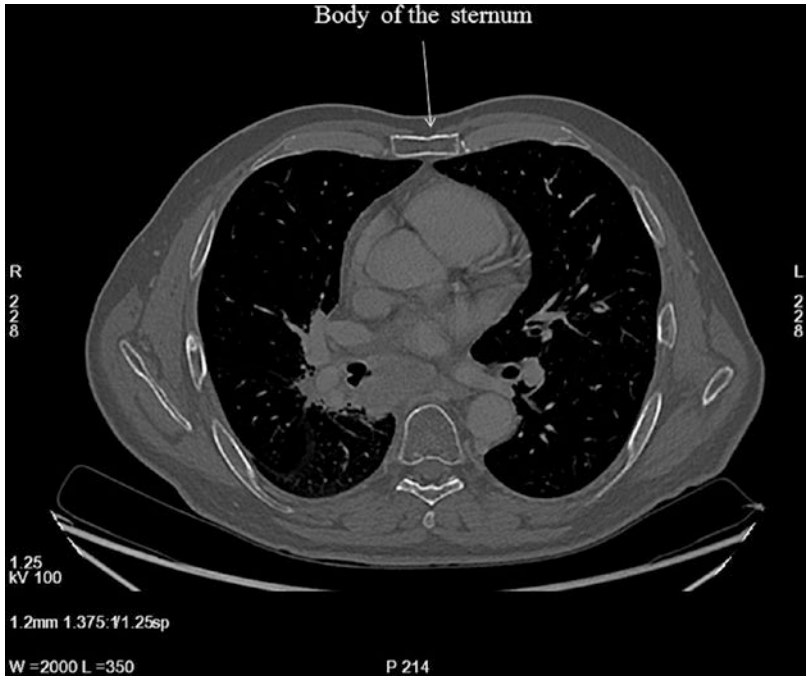
Body of the sternum
R
L
1.25
kV 100
1.2mm 1.375:1 1.25sp
W =2000 L =350
P 214

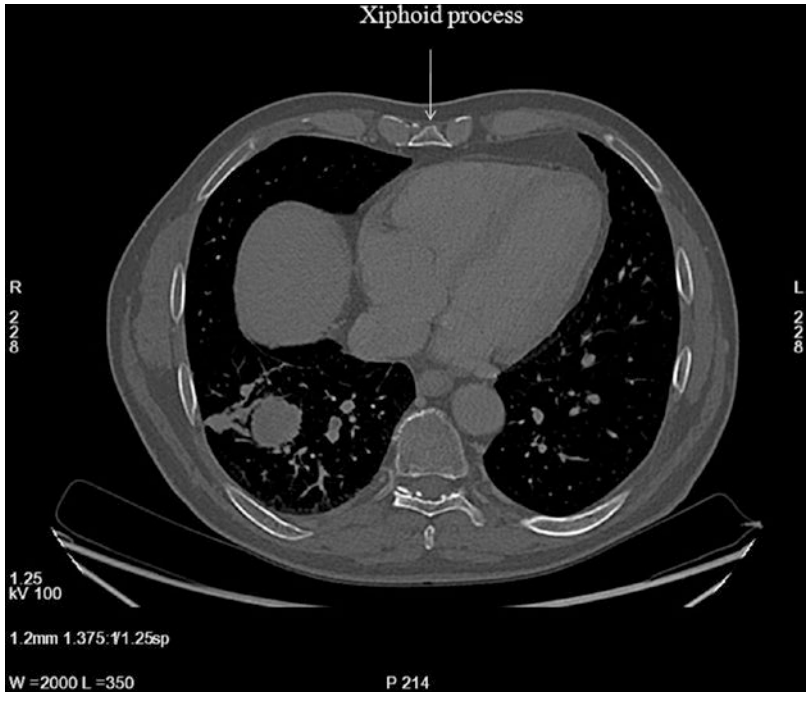
Xiphoid process
R
L
1.25
kV 100
1.2mm 1.375:1 1.25sp
W =2000 L =350
P 214

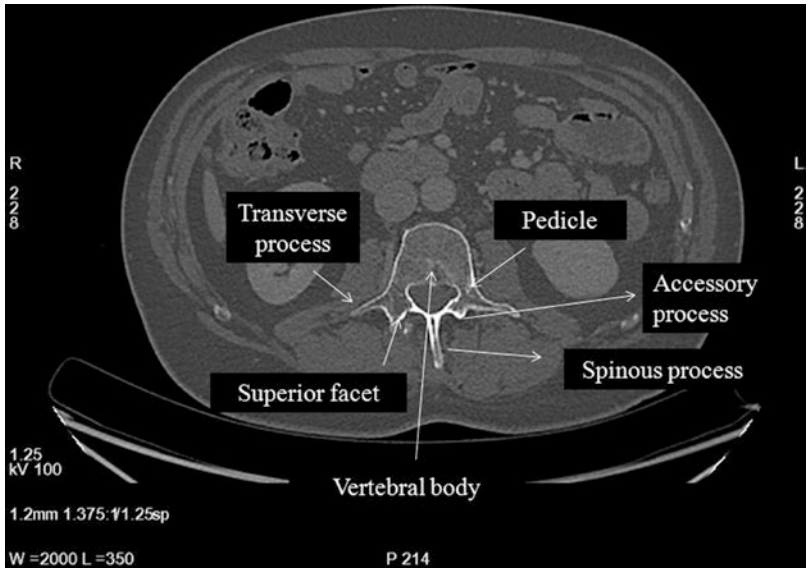
R
2
2
8
L
2
2
8
Transverse process
Pedicle
Accessory process
Spinous process
Superior facet
Vertebral body
1.25
kV 100
1.2mm 1.375:1 1.25sp
W =2000 L =350
P 214

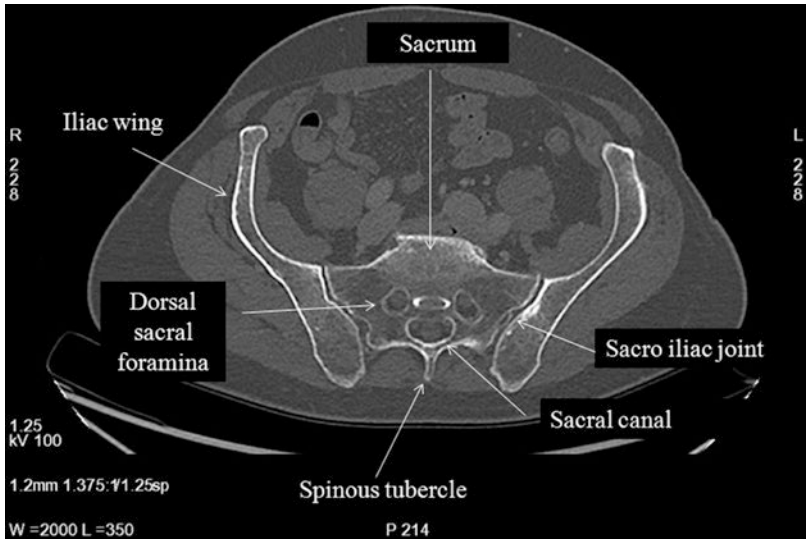
Sacrum
Iliac wing
R
2
2
8
L
2
2
8
Dorsal sacral foramina
Sacro iliac joint
Sacral canal
Spinous tubercle
1.25
kV 100
1.2mm 1.375:1 1.25sp
W =2000 L =350
P 214

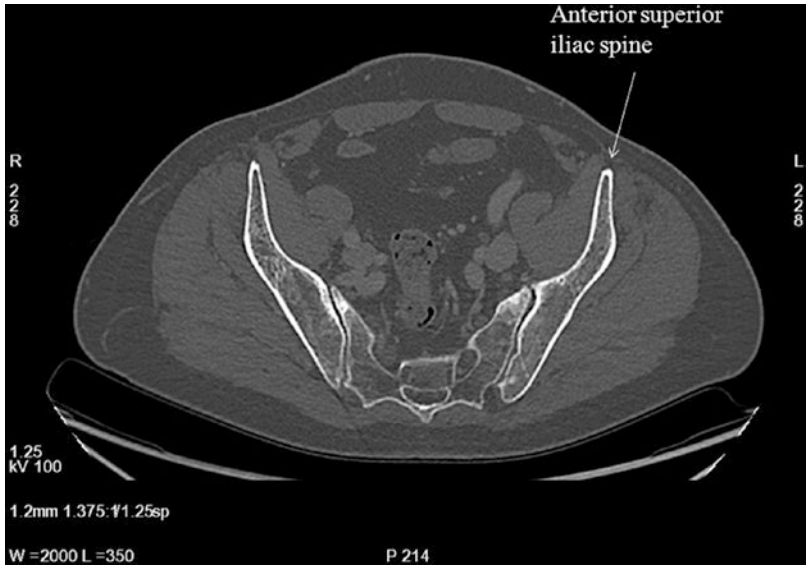
Anterior superior
iliac spine
R
L
1.25
kV 100
1.2mm 1.375:1 1.25sp
W =2000 L =350
P 214

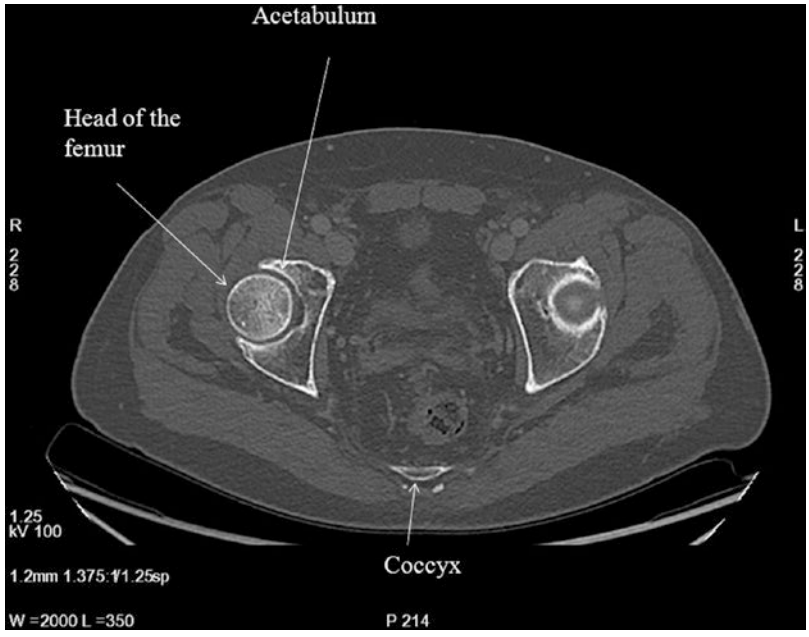
Acetabulum
Head of the
femur
R
L
1.25
kV 100
1.2mm 1.375:1 1.25sp
Coccyx
W =2000 L =350
P 214

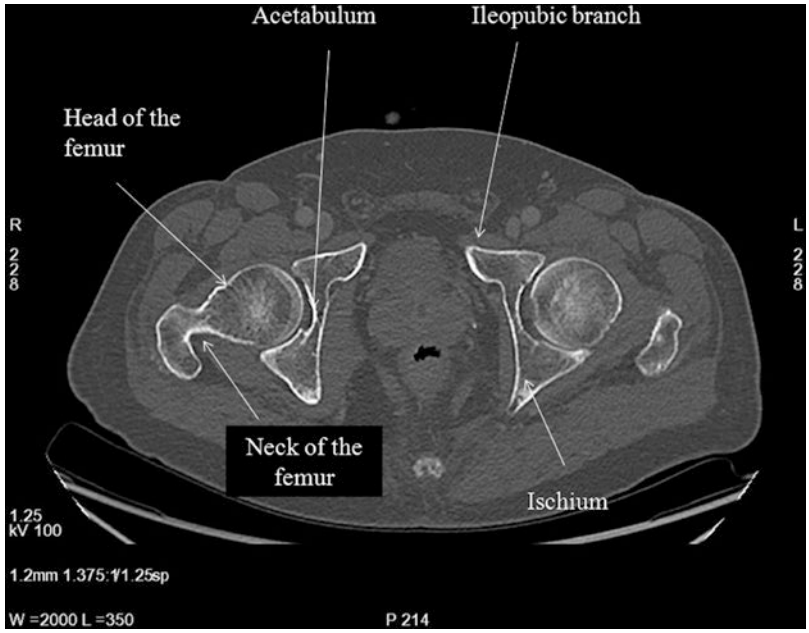
Acetabulum
Ileopubic branch
Head of the femur
Neck of the femur
Ischium
R
L
1.25
kV 100
1.2mm 1.375:1/1.25sp
W =2000 L =350
P 214

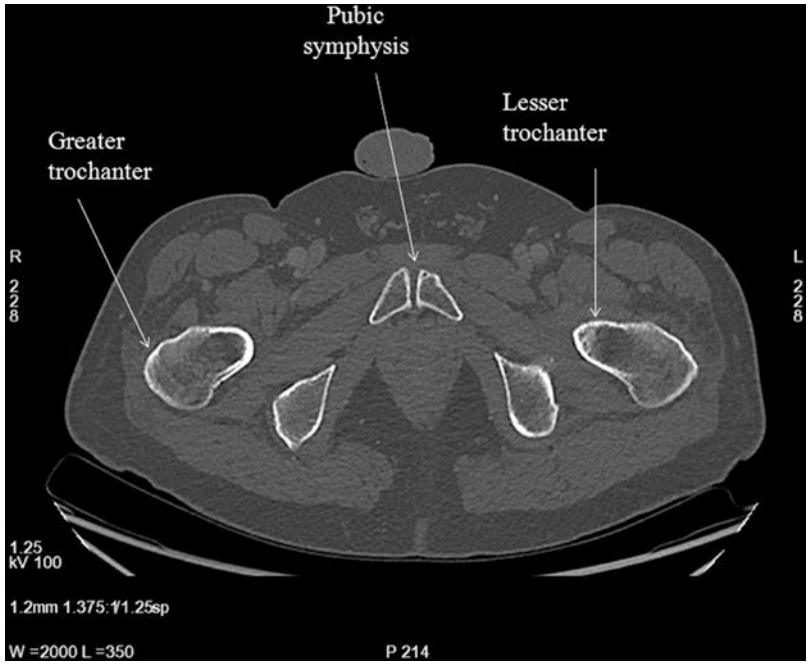
Pubic symphysis
Lesser trochanter
Greater trochanter
R
L
1.25
kV 100
1.2mm 1.375:1/1.25sp
W =2000 L =350
P 214

Head and Neck

2

Cristina Nanni, Stefano Fanti, and Lucia Zanoni

C. Nanni (✉) · S. Fanti · L. Zanoni
Department of Nuclear Medicine, IRCCS Azienda Ospedaliera-Universitaria di Bologna, Bologna, Italy
e-mail: cristina.nanni@aosp.bo.it; stefano.fanti@aosp.bo.it; lucia.zanoni@aosp.bo.it

C. Nanni et al. (eds.), *Radiology for PET/CT Reporting*,
https://doi.org/10.1007/978-3-030-87641-8_2

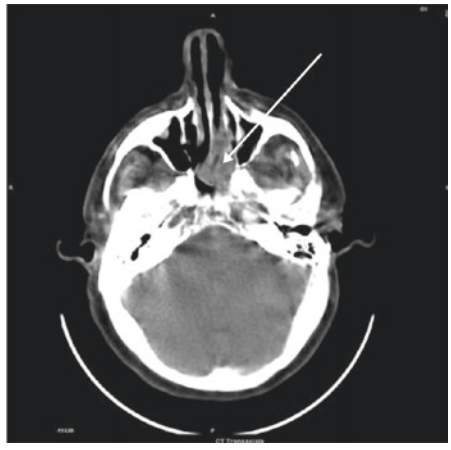

Fig. 2.1 Asymmetry of the respiratory mucosa causing unilateral obstruction, consistent with new formation of pathological tissue

Intestinal-Type Adenocarcinoma of the Respiratory Mucosa

It can originate in the respiratory epithelium or the underlying mucoserous glands. There is a well-known occupational risk after prolonged exposure (frequently decades), particularly among woodworkers and leather workers. The most common symptoms of ITACs are unilateral obstruction, rhinorrhea, and epistaxis.

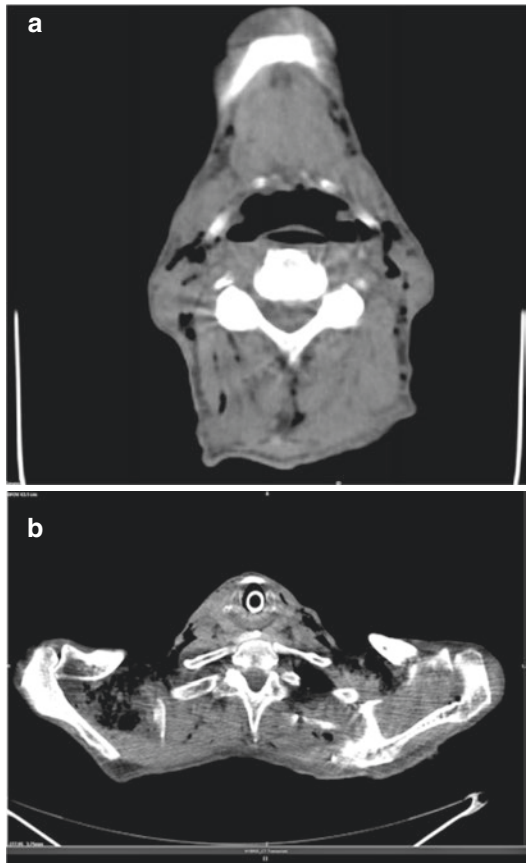

Fig. 2.2 (**a**, **b**) Dark linear/ovoid areas in the subcutaneous region of the neck and clavicular region bilaterally, consistent with air in the soft tissue

Subcutaneous Emphysema

Gas or air is present in the subcutaneous layer of the skin. It usually occurs on the chest, neck, and face, where it is able to travel from the chest cavity along the fascia. Causes of subcutaneous emphysema can be divided into air arising internally (pneumothorax, pneumomediastinum, pulmonary interstitial emphysema, perforated hollow viscus in the neck, fistula tract), air introduced externally (penetrating trauma, surgery, percutaneous intervention), and air produced de novo.

Air in the soft tissues is seen as dark linear or ovoid areas. It is also possible to find the exact spot from which air is entering the soft tissues.

Thorax

3

Cristina Nanni, Stefano Fanti, Lucia Zanoni, Rita Golfieri, Stefano Brocchi, Nicolò Brandi, and Anna Parmeggiani

C. Nanni (✉) · S. Fanti · L. Zanoni
Department of Nuclear Medicine, IRCCS Azienda Ospedaliera-Universitaria di Bologna, Bologna, Italy
e-mail: cristina.nanni@aosp.bo.it; stefano.fanti@aosp.bo.it; lucia.zanoni@aosp.bo.it

R. Golfieri · S. Brocchi
Department of Radiology, IRCCS Azienda Ospedaliera-Universitaria di Bologna, Bologna, Italy
e-mail: rita.golfieri@unibo.it; stefano.brocchi@aosp.bo.it

N. Brandi · A. Parmeggiani
University of Bologna, Bologna, Italy
e-mail:nicolo.brandi@studio.unibo.it; anna.parmeggiani2@studio.unibo.it

C. Nanni et al. (eds.), *Radiology for PET/CT Reporting*,
https://doi.org/10.1007/978-3-030-87641-8_3

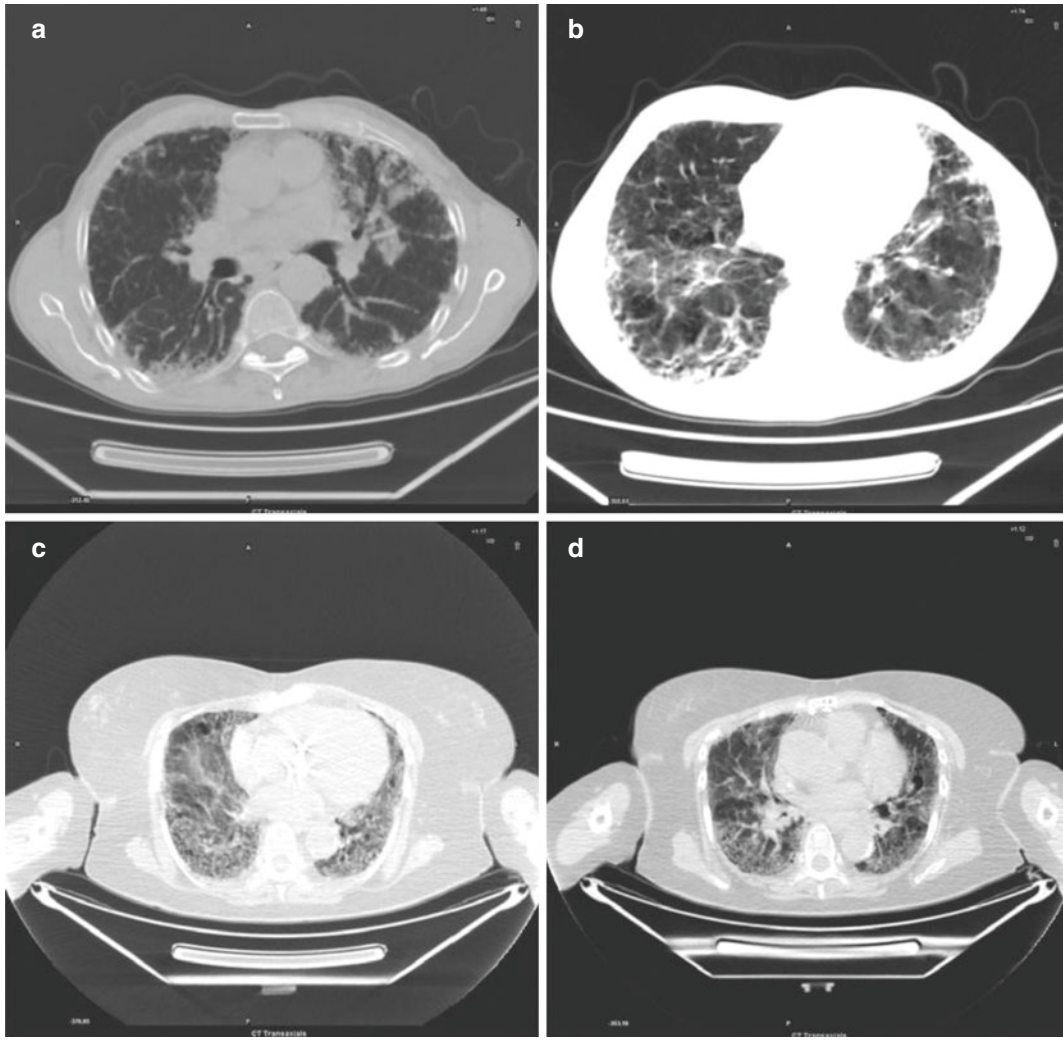

Fig. 3.1 (**a**–**d**) Interstitial distortion in both lungs, most evident in the lingula and less evident in lower dorsal lobes

Idiopathic Pulmonary Fibrosis (IPF)

Idiopathic pulmonary fibrosis (IPF) is a chronic progressive pulmonary disease of unknown etiology. It is primarily diagnosed on the basis of clinical, physiologic, and radiologic criteria. In its International Consensus statement, the American Thoracic Society defines IPF as a specific chronic interstitial pneumonia that is limited to the lung and that has the histological appearance of usual interstitial pneumonia (UIP) on open or thoracoscopic biopsy.

CT manifestations of IPF consist of symmetric bilateral reticulation, architectural distortion, and honeycombing involving mainly the subpleural lung regions and lower lobes. The active stage of the disease, which is characterized by active alveolitis and hazy ground-glass opacifications, is potentially reversible and potentially amenable to treatment, unlike end-stage disease, characterized by honeycombing without ground-glass attenuation in typical distribution, which is irreversible. In 50% of cases, the CT findings may mimic those of other interstitial lung diseases being relatively non-specific.

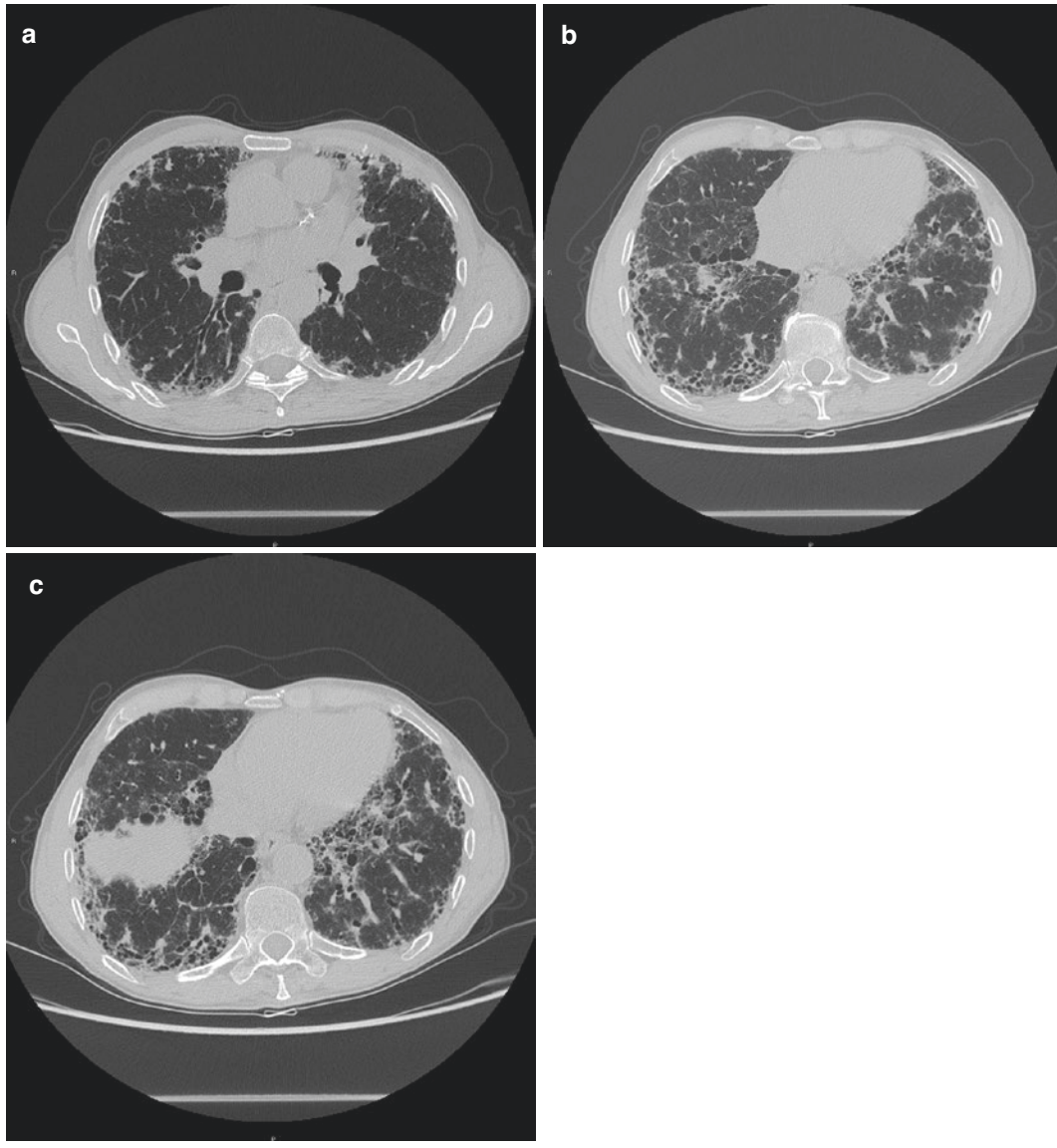

Fig. 3.2 (**a**–**c**) Axial high resolution CT images showing the typical features of Idiopathic Pulmonary Fibrosis (IPF), in particular honeycombing cysts, reticular septal thickening, architectural distortion with predominance of subpleural and posterior basal regions

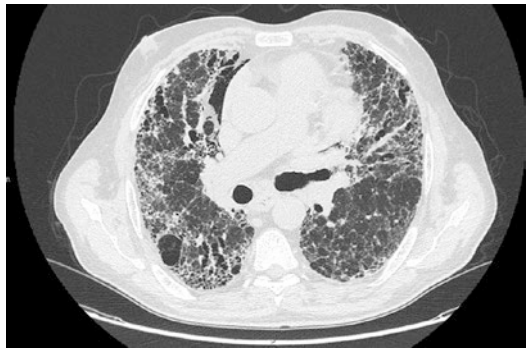

Fig. 3.3 Axial high resolution CT image showing the typical features of Idiopathic pulmonary fibrosis (IPF), in particular honeycombing cysts, reticular septal thickening, architectural distortion with predominance of subpleural and posterior basal regions

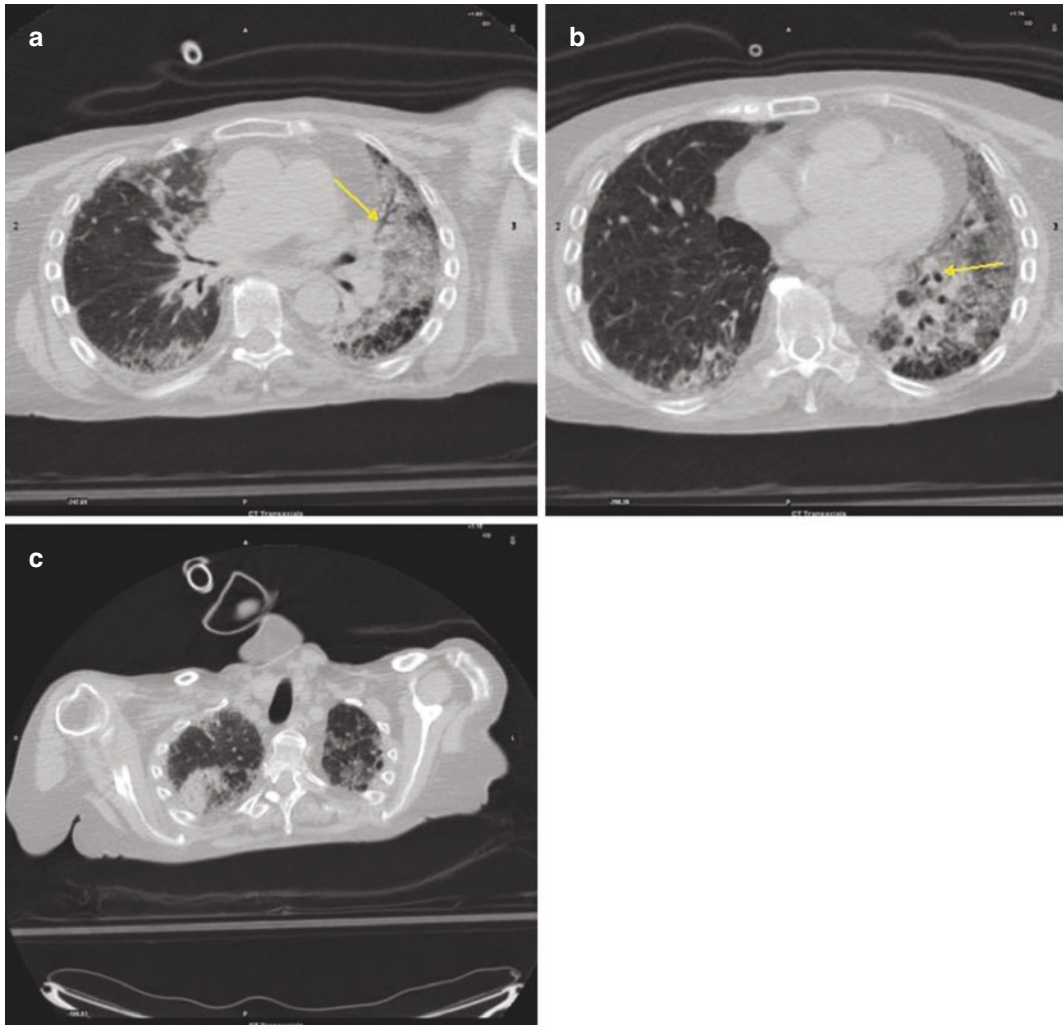

Fig. 3.4 (**a**–**c**) Basal (**a**), middle pulmonary (**b**) and apical peripheral architectural distortion resulting from fibrosis and producing traction bronchiectasis (arrows)

Usual Interstitial Pneumonia (UIP)

It is one of the most common interstitial lung diseases. It shows typically an apicobasal gradient with predominantly basal and peripheral reticular pattern with honeycombing and traction bronchiectases (a very good differentiating feature from patients with non-specific interstitial pneumonia (NSIP) and concurrent emphysema). Architectural distortion, meaning lung fibrosis, is often prominent. In cases of more advanced fibrosis, lobar volume loss is seen. Cross-sectional imaging also reveals heterogeneous, with areas of fibrosis alternating with areas of normal lung, indeed it is often patchy. The term idiopathic pulmonary fibrosis (IPF) is now applied solely to the clinical syndrome associated with the morphologic pattern of UIP.

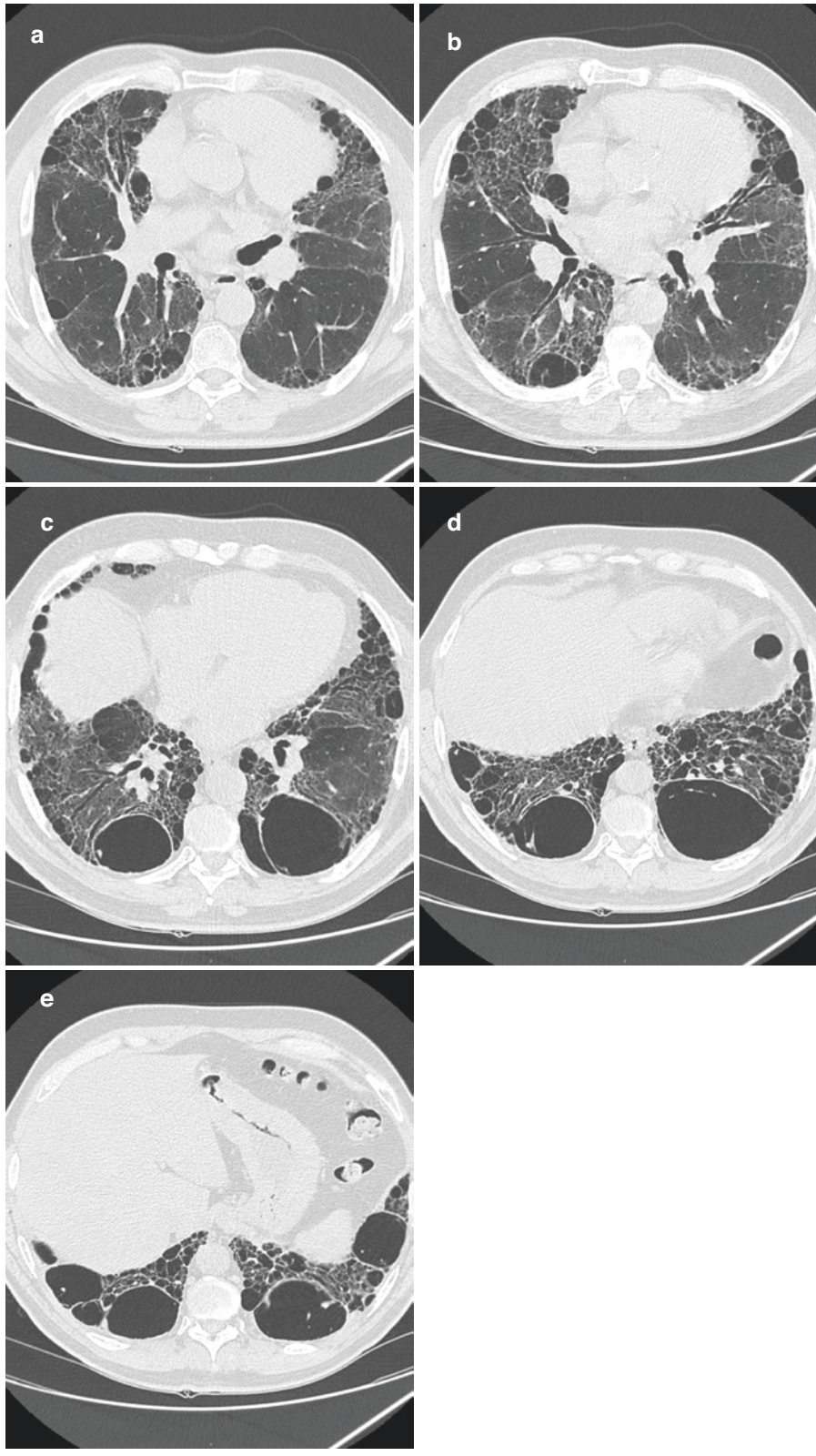

Fig. 3.5 (**a**–**e**) Axial CT images on lung window setting showing a severe reticular interstitial pattern with periferical architectural distorsion resulting from fibrosis and traction bronchiectasis

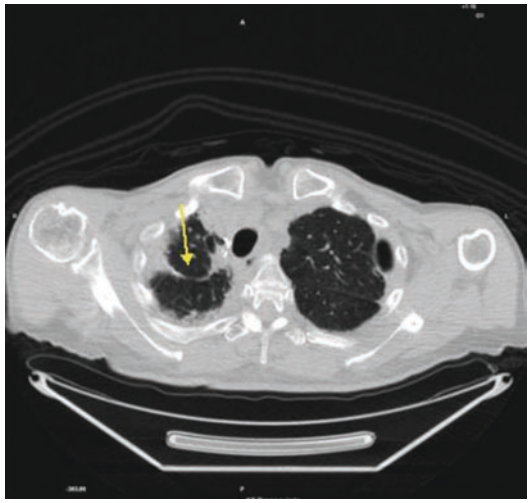

Fig. 3.6 Fibrotic area in the right apical lung connected to the pleura (arrow)

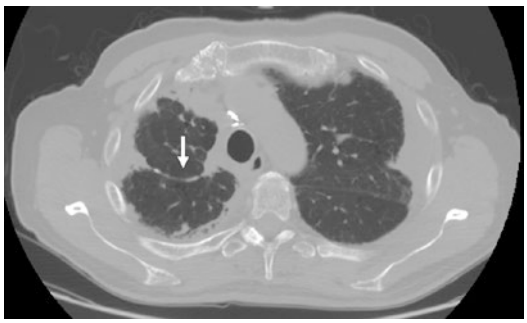

Fig. 3.7 Axial CT image with lung window showing fibrotic area in the right apical lung connected to the pleura (white arrow)

Right Superior Lobectomy Scarring

Pulmonary scarring usually occurs after surgery. At CT there are fibrotic areas connected to the pleura and an expansion of the residual lung parenchyma. Surgical clips may appear as small hyperdense dots.

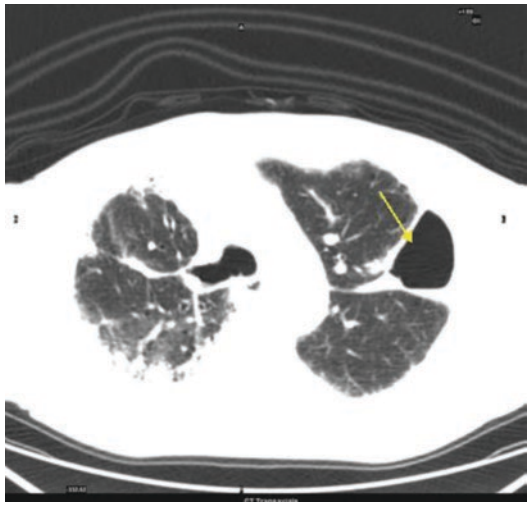

Fig. 3.8 Abnormal collection of air or gas in the pleural space that separates the lung from the chest wall

Fig. 3.9 Axial High Resolution CT image showing abnormal collection of air in the pleural space that separates the right lung from the chest wall with the consequent pulmonary parenchyma compression

Pneumothorax

Abnormal collection of air or gas in the pleural space that separates the lung from the chest wall. Complication of medical or surgical intervention. CT shows even the smallest pneumothorax. Air-density (blackness) is the same inside and outside the chest. A compressed lung segment can be also noted.

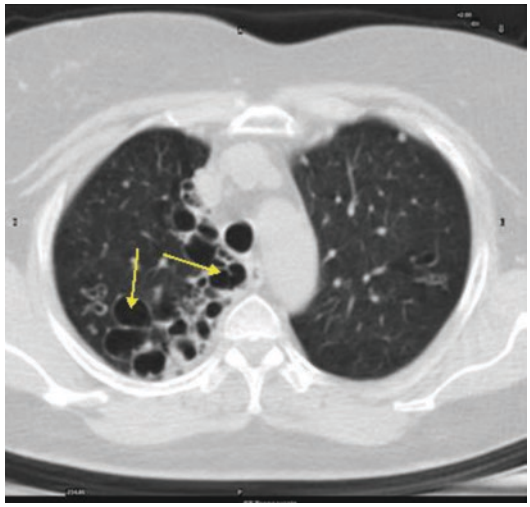

Fig. 3.10 Right pulmonary bronchiectasis (arrows)

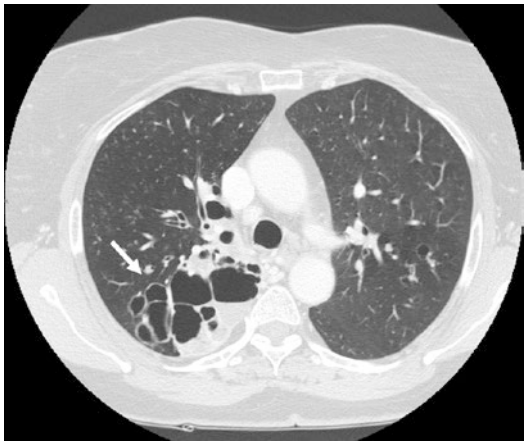

Fig. 3.11 Axial High Resolution CT image showing right pulmonary bronchiectasis (white arrow)

Bronchiectasis

Dilated airways (tram lines) with a signet ring appearance with a luminal diameter >1.5 times that of the adjacent vessel in cross section or by grapelike clusters in case of mire severity. Other findings can be thickening of the bronchial walls due to peribronchial fibrosis, obstruction of airways (opacification and air trapping), and consolidation.

On the contrary, *bulla* generally has no definable wall thickness and no accompanying vessels.

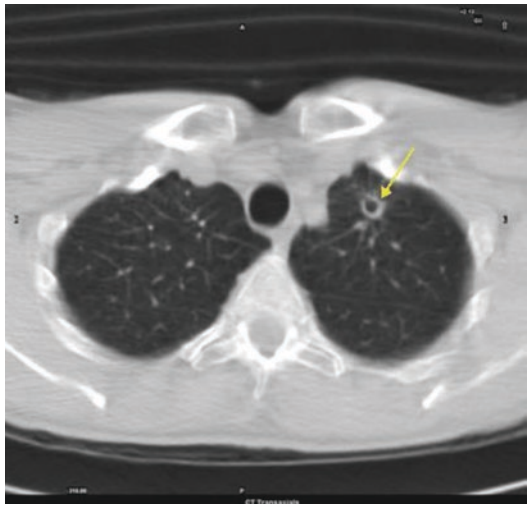

Fig. 3.12 Left pulmonary nodular cavitated lesion (arrow)

Fig. 3.13 Axial CT image showing a mycotic cavitated lesion surrounded by a ground-glass opacity

Mycotic Lung Infection

Fungal infection occurs following the inhalation of spores, after the inhalation of conidia, or by the reactivation of a latent infection. When the process is recovering, a nodular lesion usually surrounded by a ground-glass opacity or halo, and cavitated, can be found. Air crescent sign can be detected in which crescentic air space separates the cavity from the fungus ball.

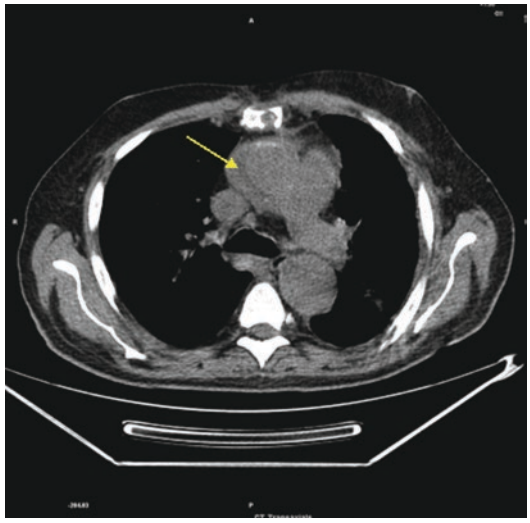

Fig. 3.14 A low-attenuation fluid collection adjacent to the ascending aorta (arrow)

Para-Aortic Arch Abscess

Aortic infections are uncommon clinical manifestations but are associated with high rates of morbidity and mortality. Ultrasound and CT allow direct visual access to deep infections with less invasiveness than traditional open techniques. Large, saccular fluid collections can be discovered around the aorta. Abscess may cause persistent sepsis, fistula formation, and an increased need for surgery.

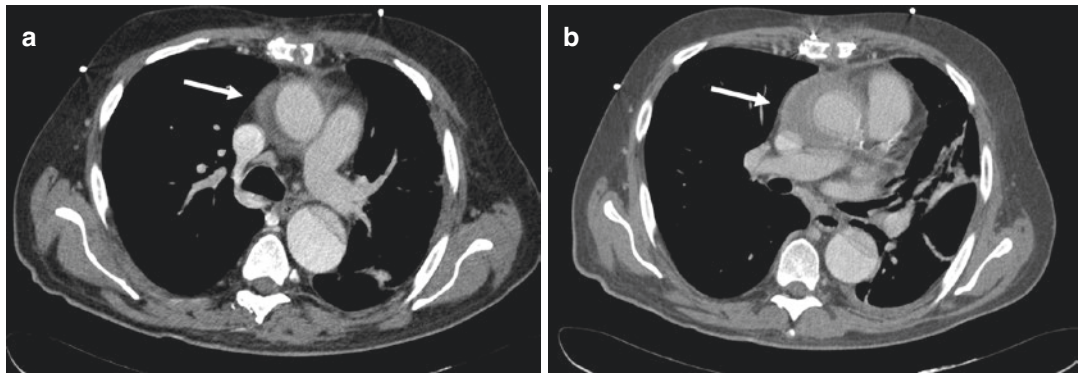

Fig. 3.15 (**a**, **b**) Axial post contrast CT images on mediastinal window setting showing a low-attenuation fluid collection adjacent to the ascending aorta (arrow)

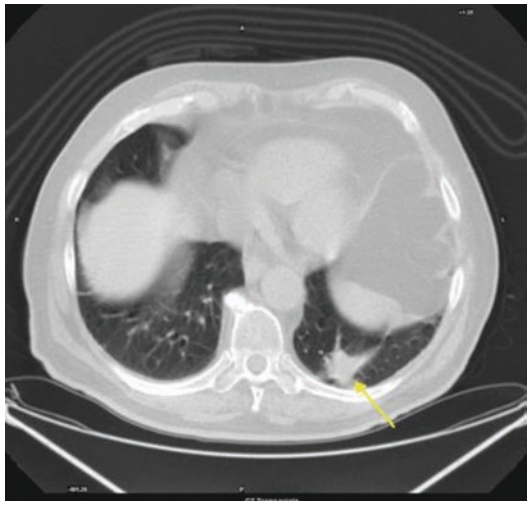

Fig. 3.16 Patient affected by secondary lung lesion from colon cancer underwent left inferior lobe nodulectomy

Postsurgical Lung Changes

Lung changes occur after surgery. Fibrotic areas generally connected to the pleura and surgical clips may appear at CT images.

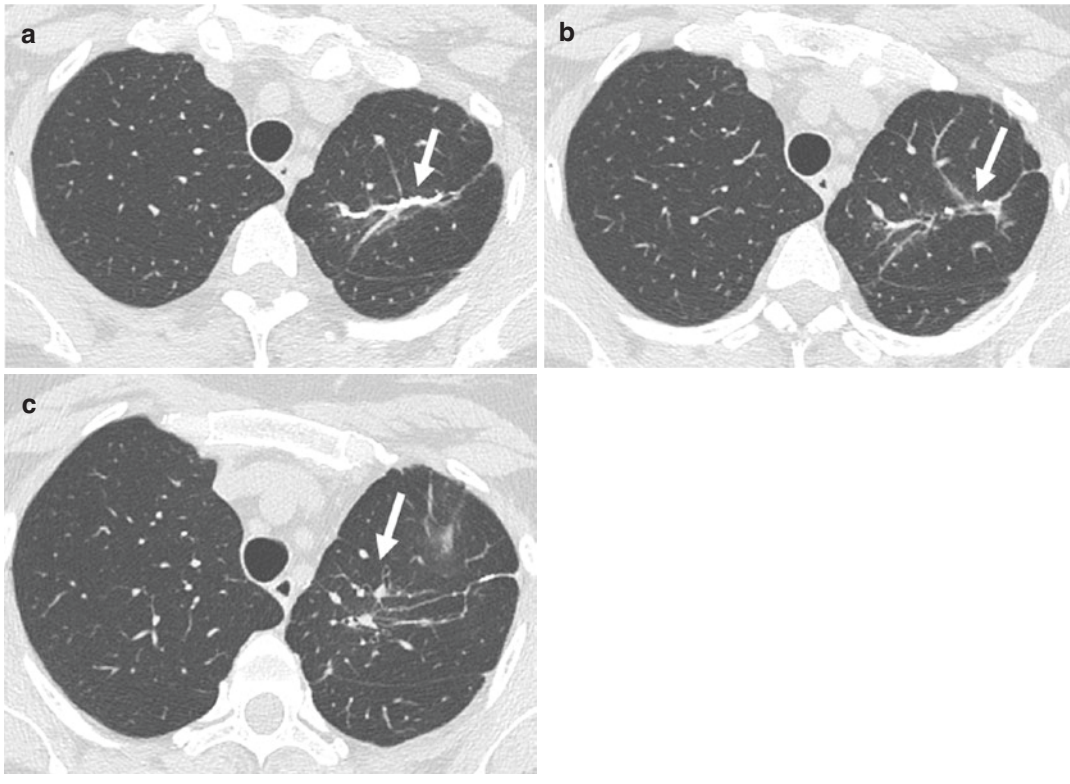

Fig. 3.17 (**a**–**c**) Axial CT images showing fibrotic area in the right apical lung connected to the pleura with surgical clips appearing as small hyperdense dots

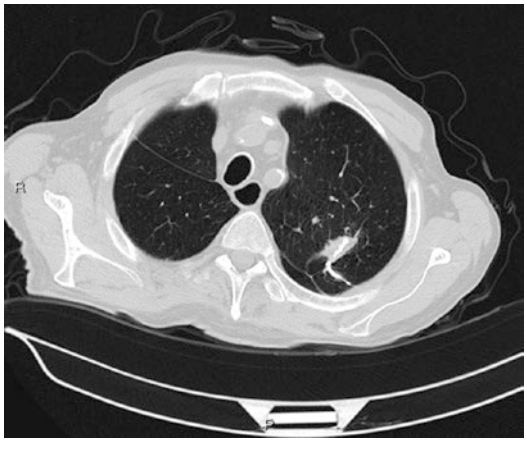

Fig. 3.18 Axial CT image showing fibrotic area in the right apical lung connected to the pleura with surgical clips appearing as small hyperdense dots

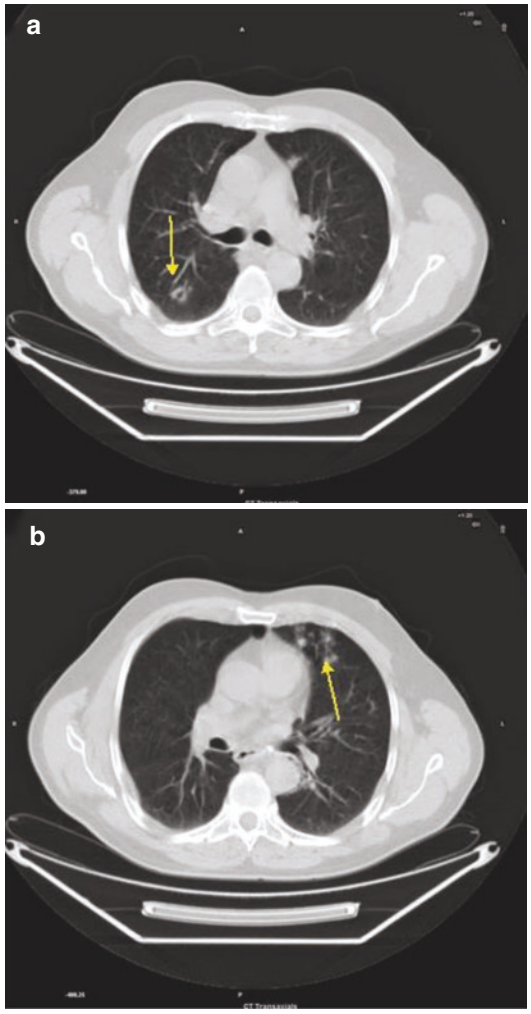

Fig. 3.19 Bronchiolar dilatation (**a**, arrow), and bronchiolar luminal impaction (**b**, arrow)

Peribronchial Inflammation

Direct CT signs of bronchiolar disease include bronchiolar wall thickening, bronchiolar dilatation, and bronchiolar luminal impaction. Indirect signs include subsegmental atelectasis and air trapping.

Fig. 3.20 Axial CT image showing signs of bronchiolar disease including bronchiolar wall thickening, bronchiolar dilatation, and bronchiolar luminal impaction

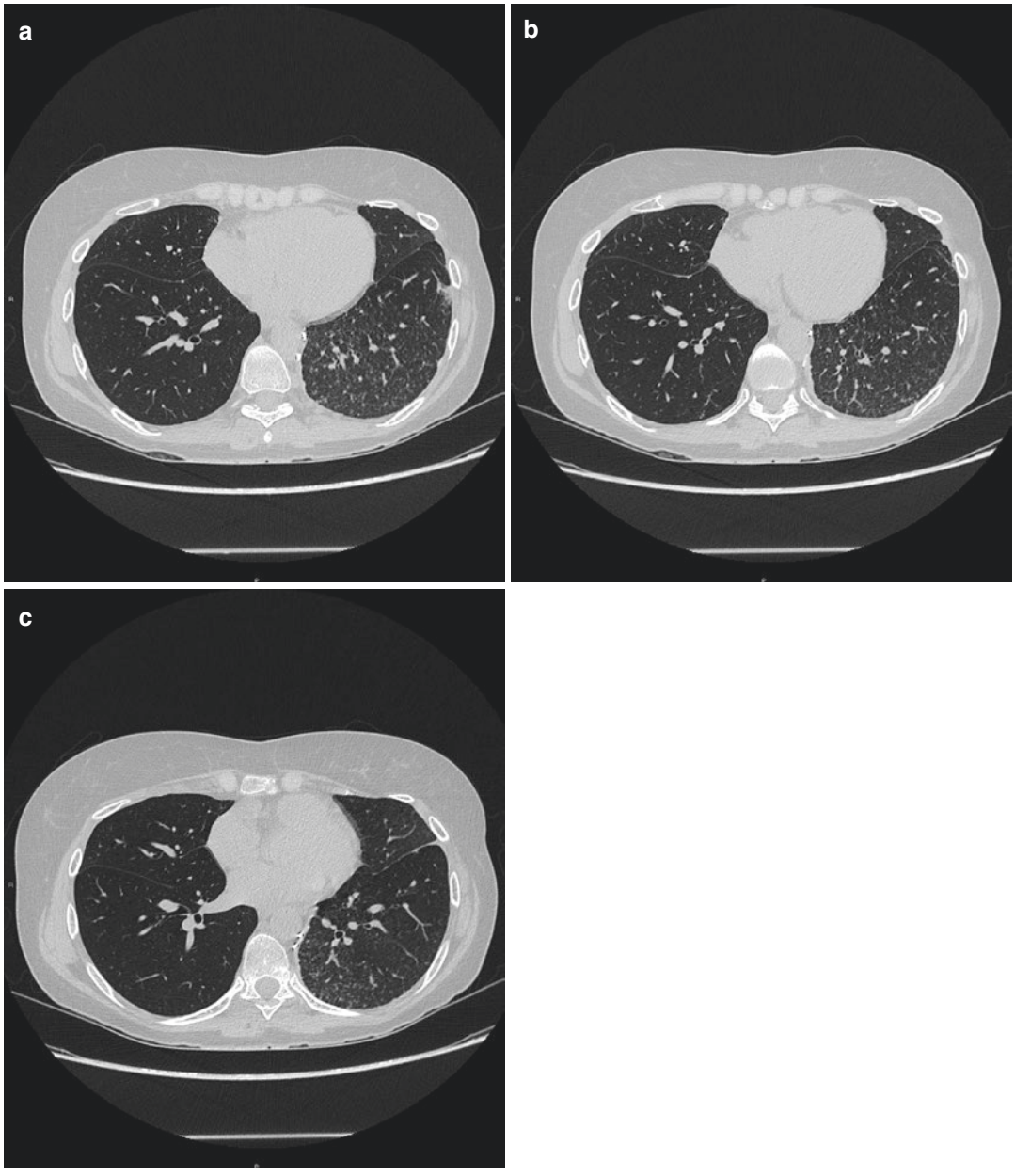

Fig. 3.21 (**a**–**c**) Axial CT images showing signs of bronchiolar disease including tree in bud

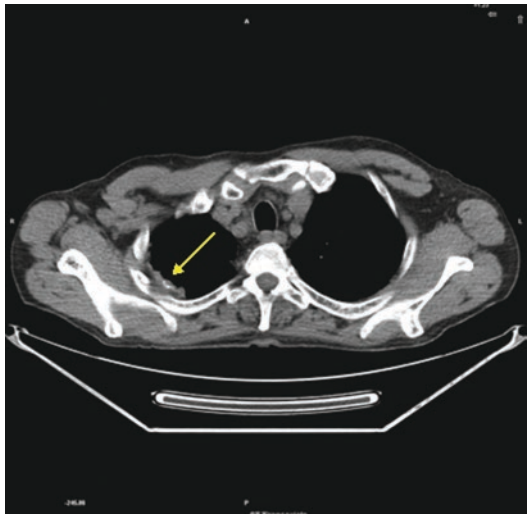

Fig. 3.22 Right apical and calcified pleural plaque caused by asbestos exposure (arrow)

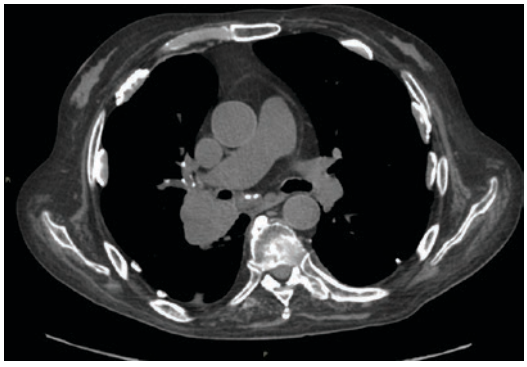

Fig. 3.23 Axial CT image showing bilateral calcified pleural plaque caused by asbestos exposure

Asbestosis Pleural Plaques

Circumscribed pleural plaques are the most common manifestation of asbestos exposure and comprise discrete areas of white or yellow thickening on the parietal pleura. They are frequently bilateral and symmetric and occur particularly on the posterolateral chest wall between the fifth and eighth ribs, over the mediastinal pleura, and on the dome of the diaphragm. Histological examination reveals plaques to be acellular, with a "basket-weave" pattern of hyalinized collagen strands. They are covered by a single layer of normal mesothelial cells on the pleural surface.

Pleural plaques typically develop 20–30 years after exposure, and their incidence increases with longer duration of exposure. They are found in as many as 50% of asbestos-exposed workers but may also occur after low-dose exposures. The total surface area of pleural plaques measured via CT does not appear to be related to cumulative asbestos exposure.

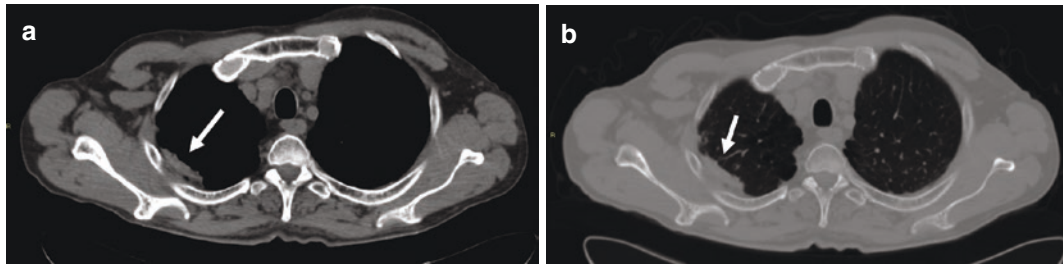

Fig. 3.24 (**a**, **b**) Axial CT images showing a pleural plaque caused by asbestos exposure (white arrow) both on mediastinal window (**a**) and lung window (**b**) setting

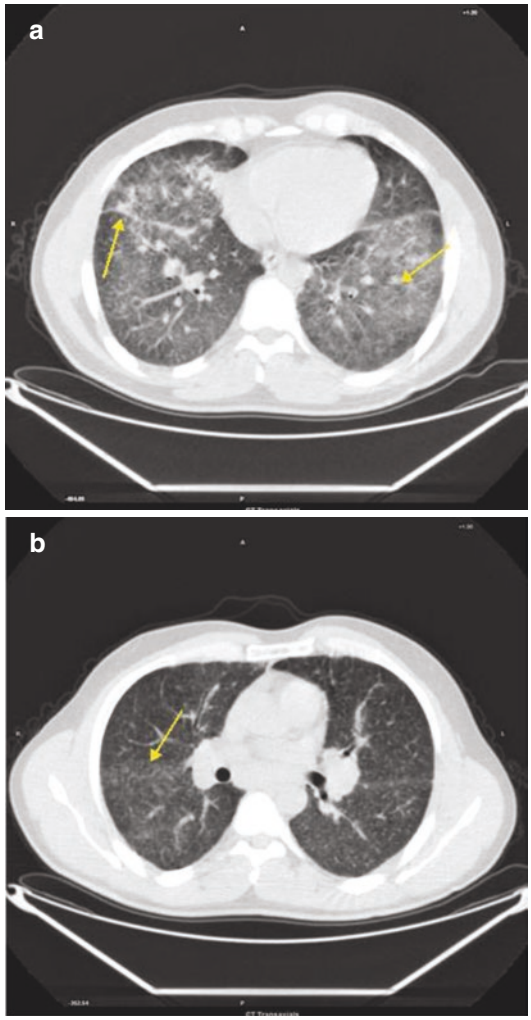

Fig. 3.25 (**a**, **b**) Multiple small nodules in a peribronchovascular distribution along with irregular thickening of the interstitium (**a**, **b**, arrows)

Pulmonary Sarcoidosis

Systemic disorder of unknown cause is characterized by the presence of noncaseating granulomas and the proliferation of epithelioid cells. Pulmonary infiltrates are typically represented by nodules, interstitial thickening, and fibrosis. Multiple small nodules in a peribronchovascular distribution along with irregular thickening of the interstitium are typical CT findings of sarcoidosis.

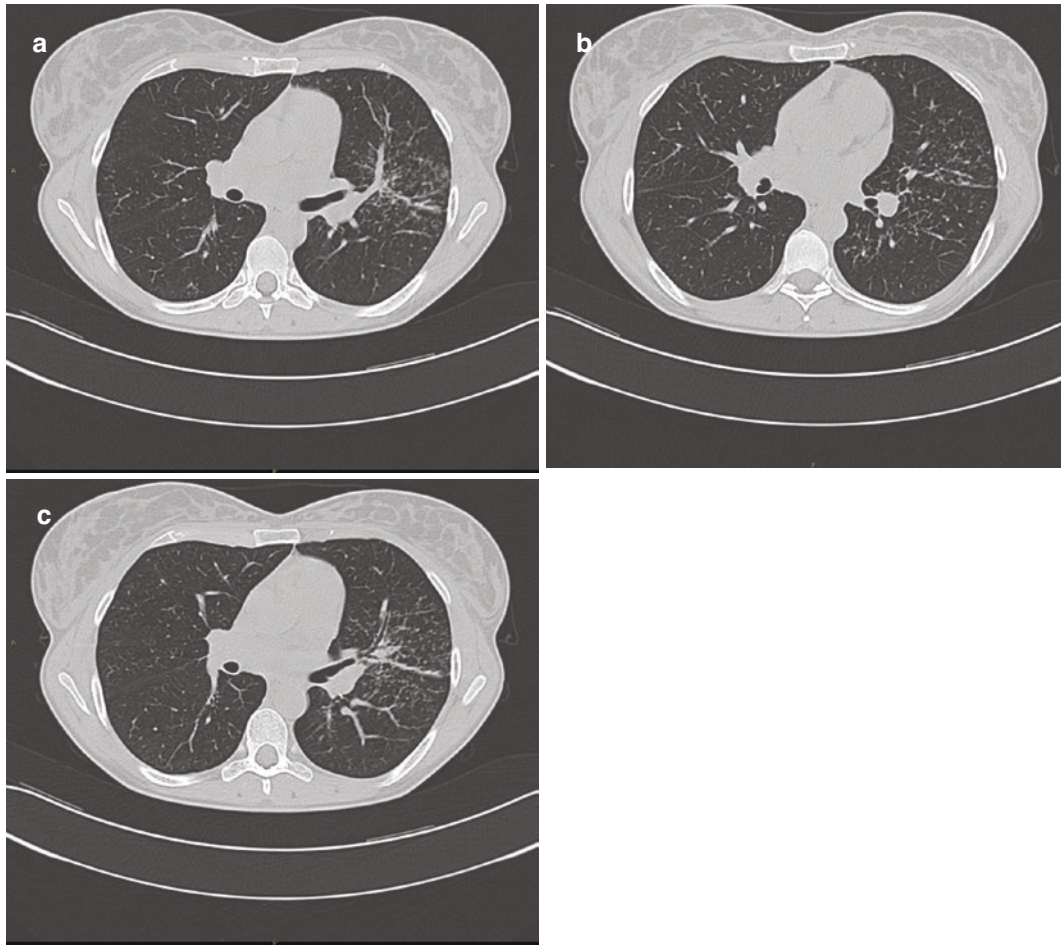

Fig. 3.26 (**a**–**c**) Axial CT images showing multiple small nodules in a peribronchovascular distribution along with irregular thickening of the interstitium

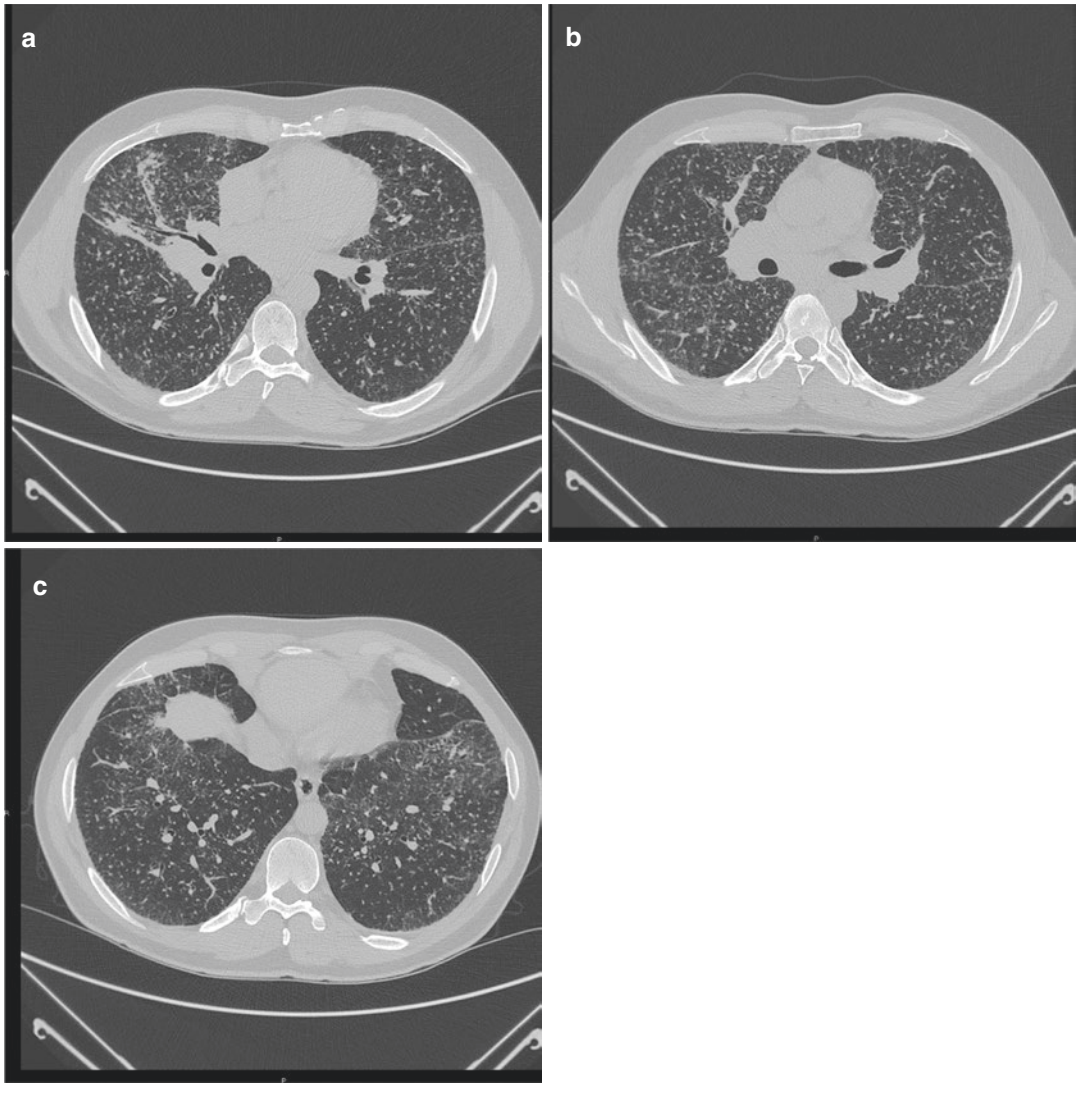

Fig. 3.27 (**a**–**c**) Axial CT images on lung window setting showing multiple small nodules in a peribronchovascular distribution along with irregular thickening of the interstitium of both lungs

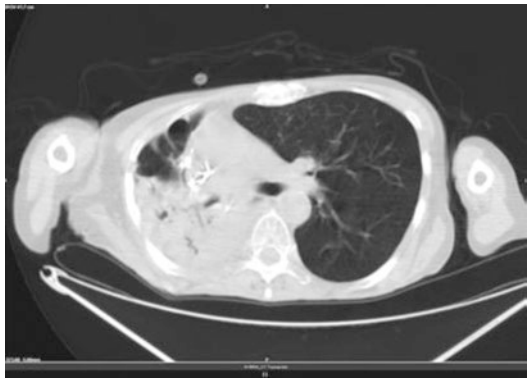

Fig. 3.28 History of right superior lobectomy for adenocarcinoma without radiation treatment (FDG avid). Extensive consolidation of the right inferior lobe parenchyma with mediastinal retraction

Klebsiella Pneumonia

Klebsiella pneumonia is a form of bacterial pneumonia associated with *Klebsiella pneumoniae*. Common CT findings in patients with acute Klebsiella pneumonia are ground-glass attenuation, consolidation, and intralobular reticular opacity. They can be mainly found in the lung periphery and in both sides of the lungs. Often they are associated with pleural effusion (>50%).

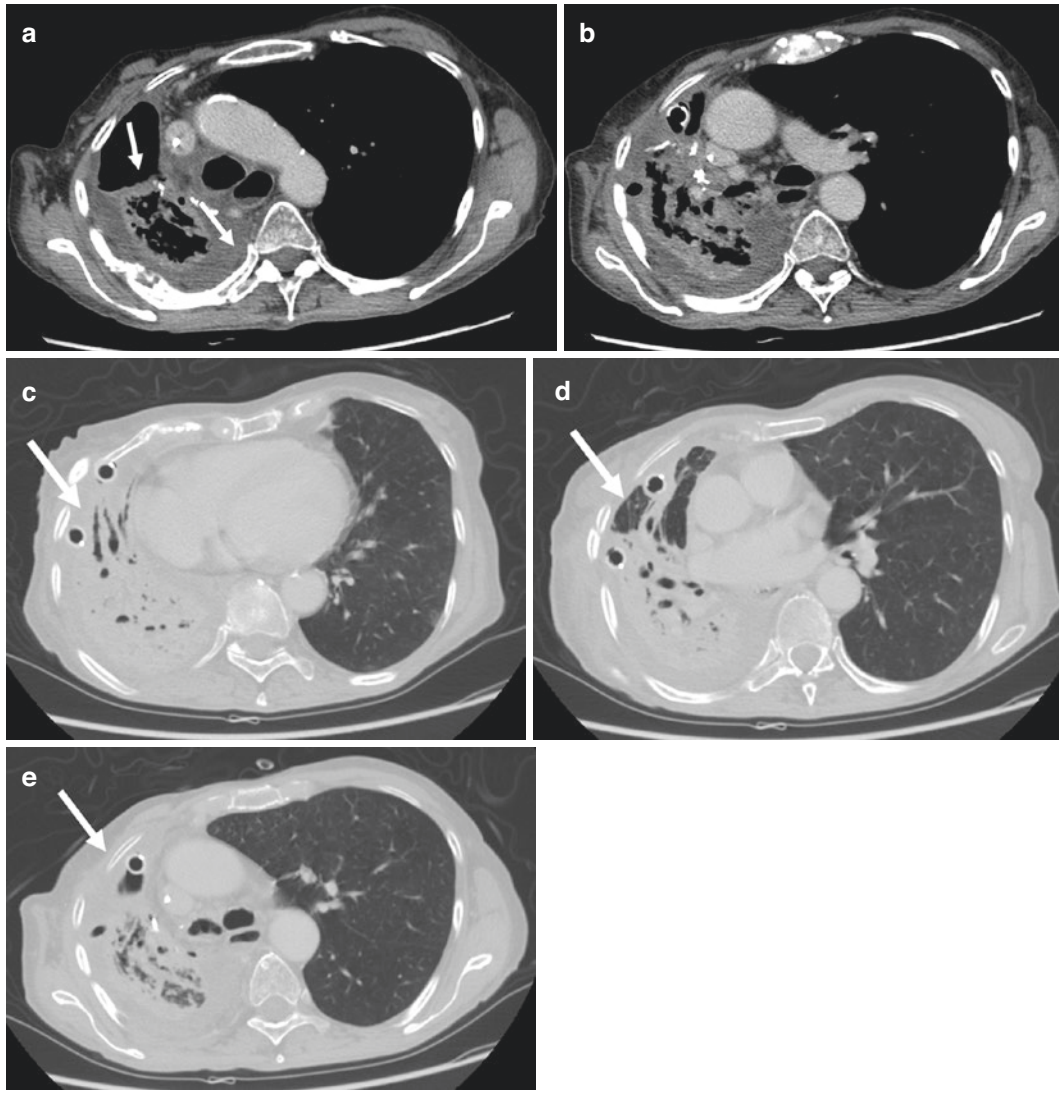

Fig. 3.29 (**a**–**e**) Axial CT images in portal venous phase with mediastinic window of a patient with history of right superior lobectomy for adenocarcinoma without radiation treatment (FDG avid). Note the atelectasis of part of the residual right lung parenchyma (white arrow) and the dorsal-basal right pleural effusion (white arrow tip)

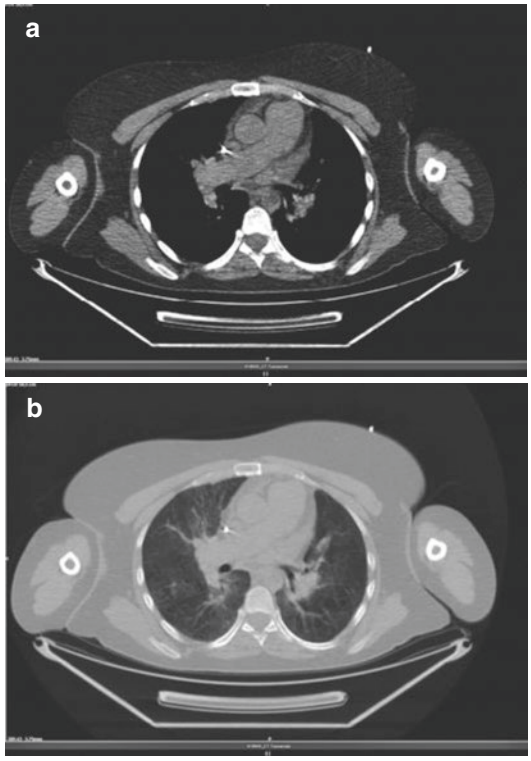

Fig. 3.30 (**a**, **b**) Central pulmonary artery dilatation

Pulmonary Hypertension

Pulmonary arterial hypertension may be idiopathic or arise in association with chronic pulmonary thromboembolism (caused by tumor cells, parasitic material, or foreign material), parenchymal lung disease, liver disease, vasculitis, human immunodeficiency virus infection, or a left-to-right cardiac shunt. Features of pulmonary arterial hypertension that may be seen at CT are markedly enlarged pulmonary arteries with tiny branching smaller vessels, abrupt narrowing or tapering of peripheral pulmonary vessels, right ventricular hypertrophy, enlarged chambers of the right heart, dilated bronchial arteries, and a mosaic pattern of attenuation due to variable lung perfusion.

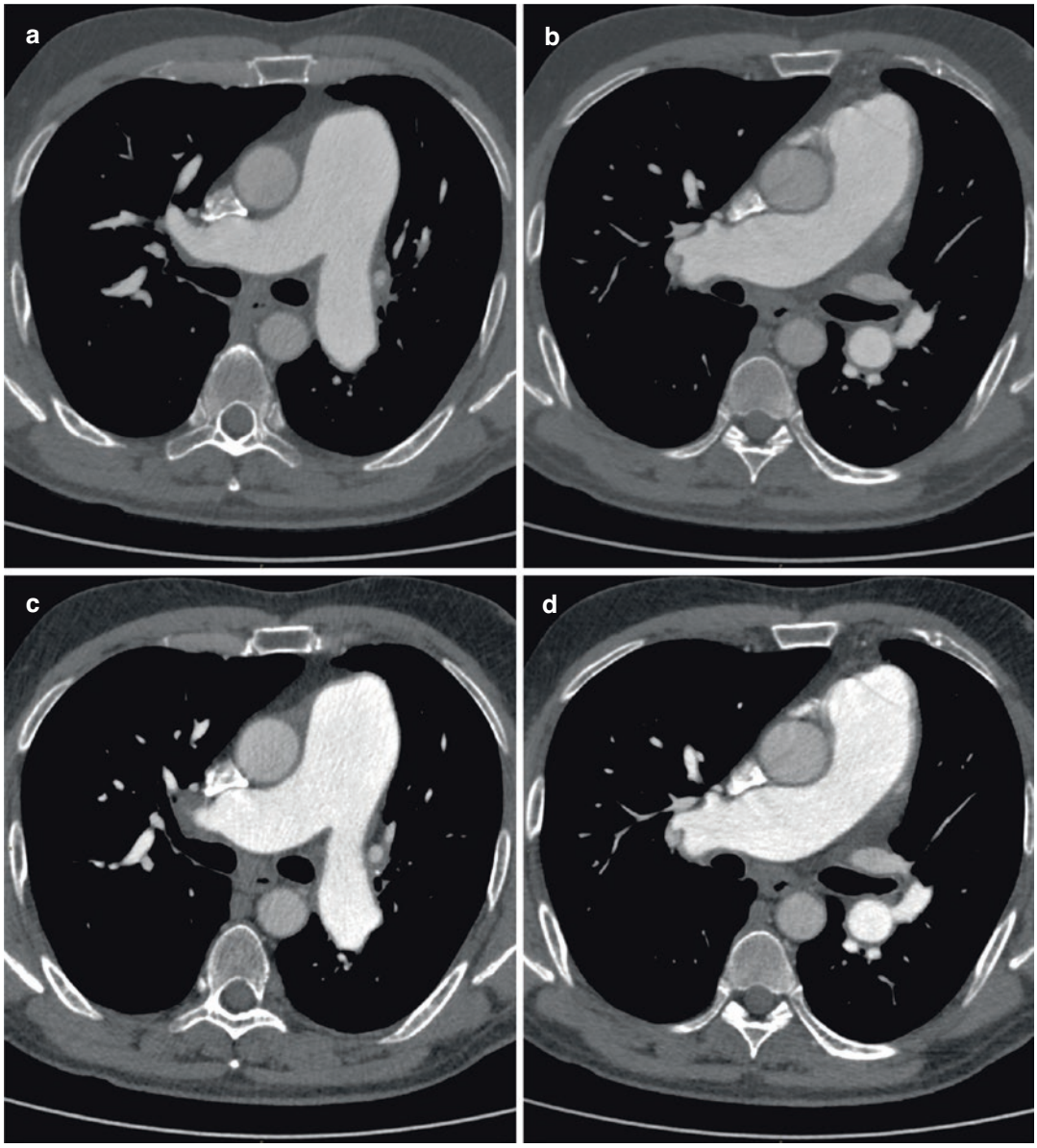

Fig. 3.31 (**a**–**d**) Pulmonary artery dilatation, mediastinal window

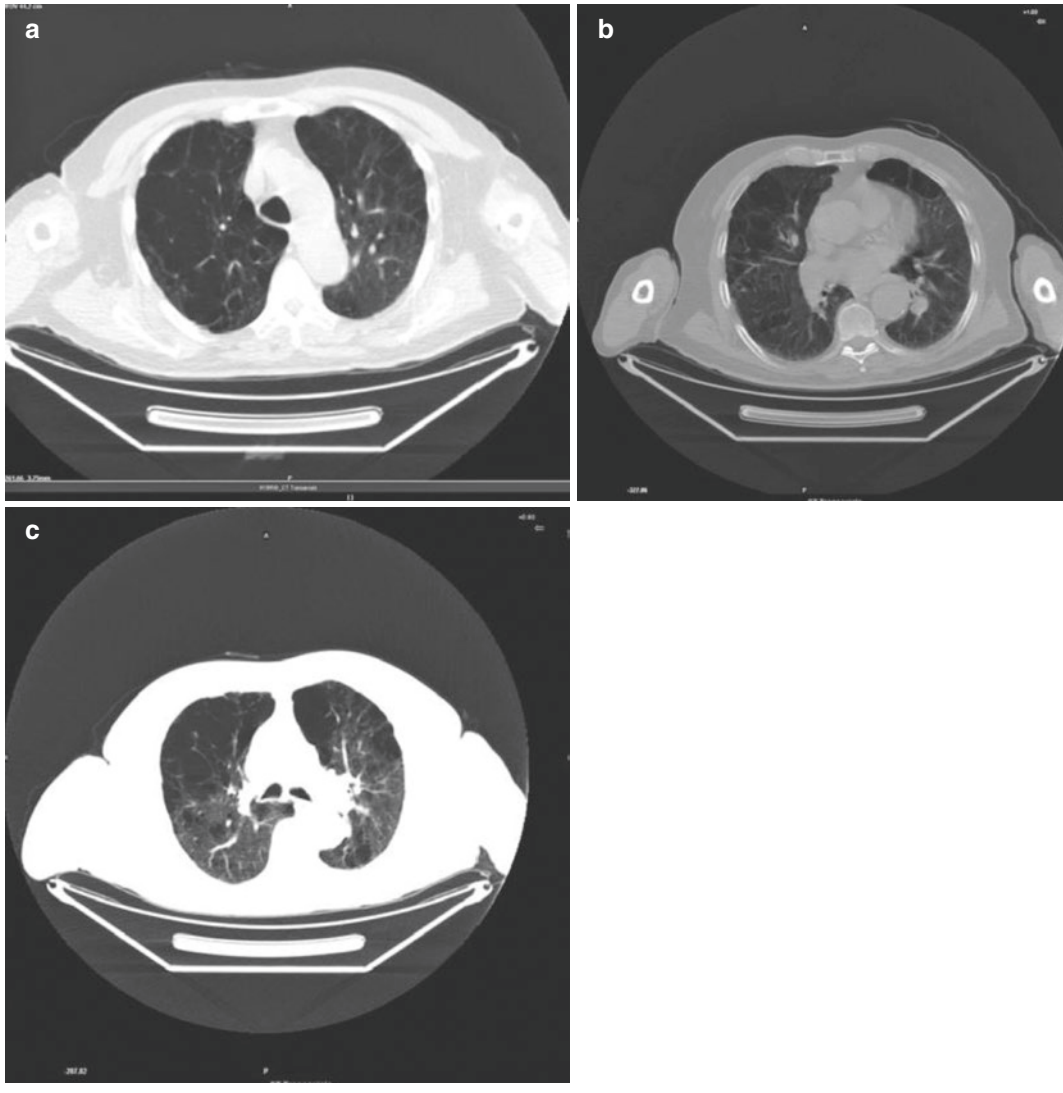

Fig. 3.32 (**a**–**c**) Mosaic patterns of attenuation due to variable lung perfusion

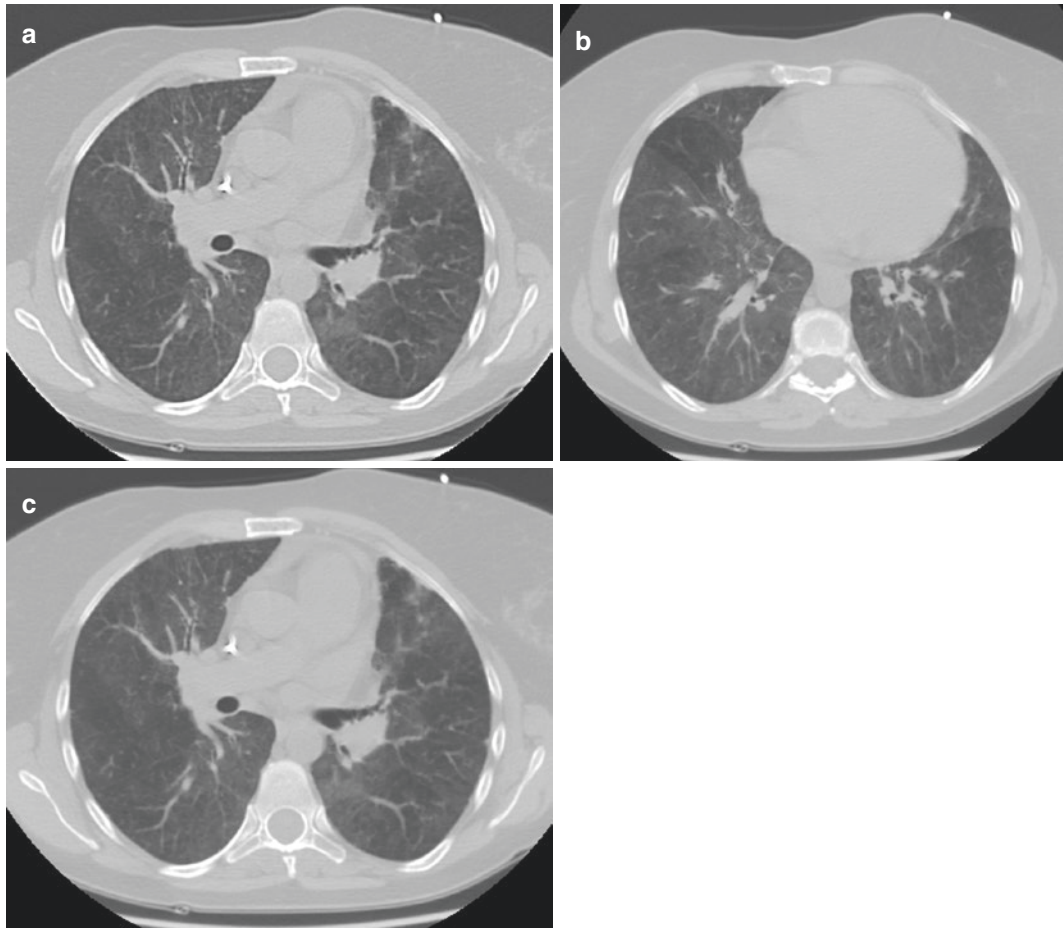

Fig. 3.33 (**a**–**c**) Axial CT images on lung window setting showing mosaic patterns of attenuation due to variable lung perfusion (lung window)

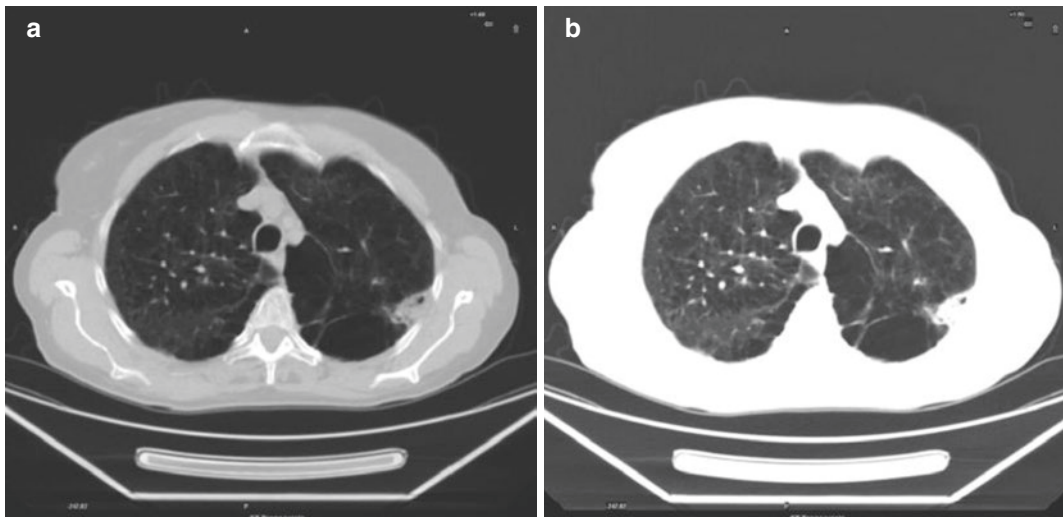

Fig. 3.34 (**a**, **b**) Mosaic pattern of attenuation (**a** intermediate mediastinal-lung window; **b** lung window)

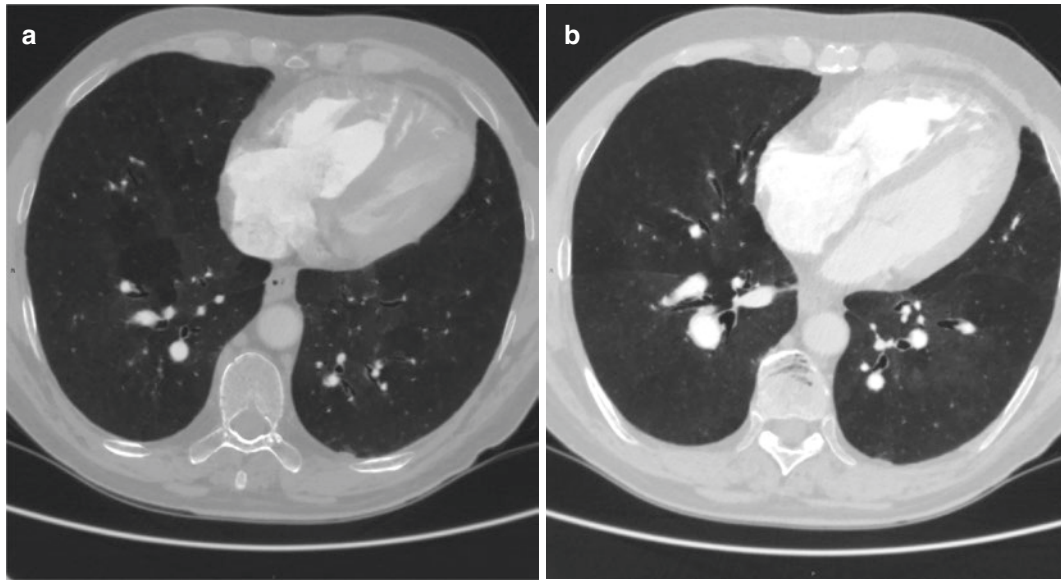

Fig. 3.35 (**a**, **b**) Mosaic pattern of attenuation

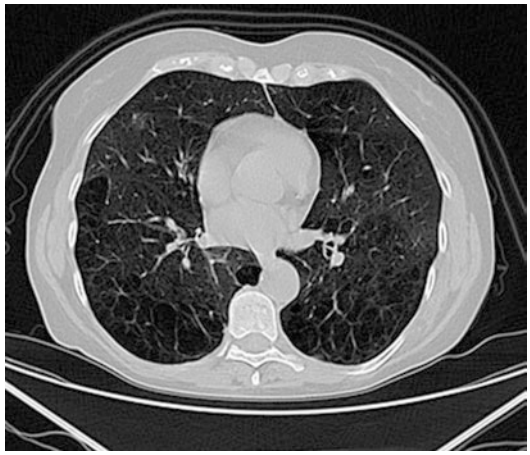

Fig. 3.36 Small air-density areas mainly concentrated adjacent to the pleural surfaces

Paraseptal Emphysema

Paraseptal emphysema affects the peripheral parts of the secondary pulmonary lobule and is usually located adjacent to the pleural surfaces and pleural fissures. The affected lobules are almost always subpleural and demonstrate small focal air-density areas up to 10 mm in size. The emphysematous spaces are not bounded by any visible wall. It is also associated with smoking and can lead to the formation of focal air-density areas larger than 10 mm called as *subpleural bullae or blebs* and *spontaneous pneumothorax*.

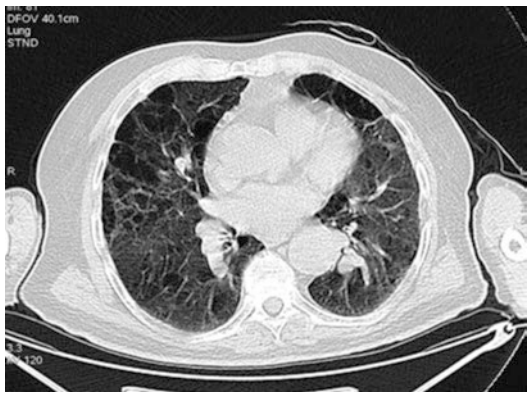

Fig. 3.37 Another pattern of emphysematous spaces in both lungs

Fig. 3.38 Axial CT image on lung window setting showing multiple bilateral air-density areas, mainly concentrated adjacent to the pleural surfaces in both lungs

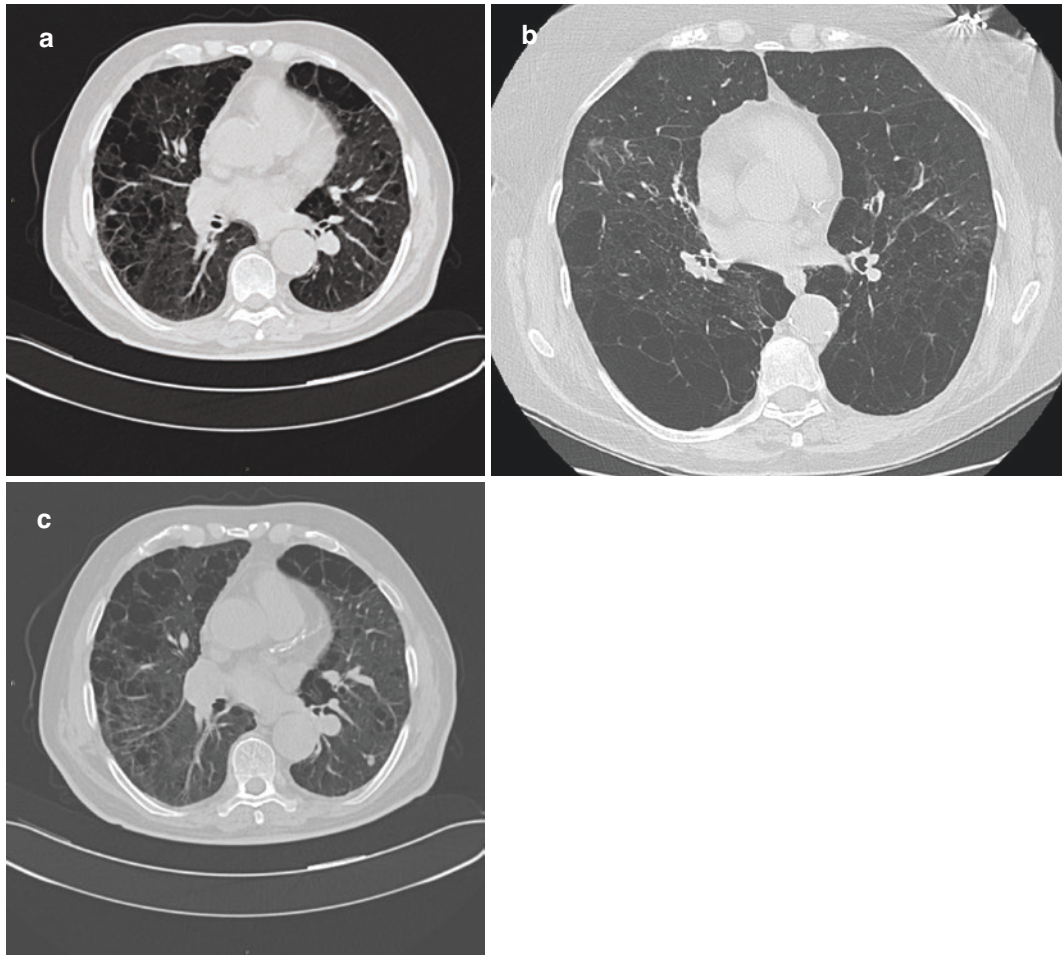

Fig. 3.39 (**a**–**c**) Axial CT image on lung window setting showing multiple bilateral air-density areas, mainly concentrated adjacent to the pleural surfaces in both lungs

Fig. 3.40 Small air-density areas near the center of secondary pulmonary lobules (arrow)

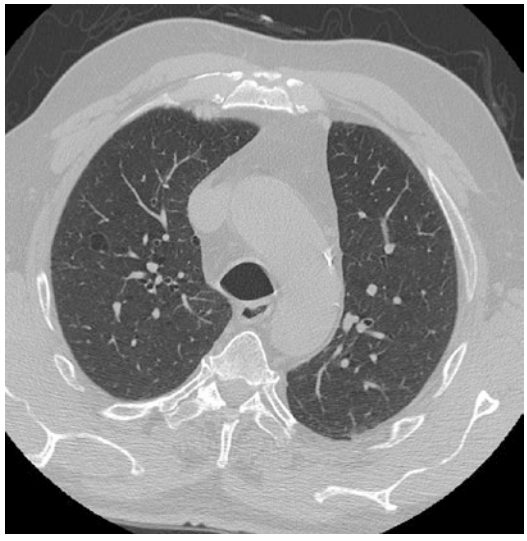

Fig. 3.41 Axial CT image on lung window setting showing small air-density area near the center of secondary pulmonary lobules

Centrilobular Emphysema

Small, round areas of low-attenuation, several millimeters in diameter, grouped near the center of secondary pulmonary lobules, with no detectable walls in many cases.

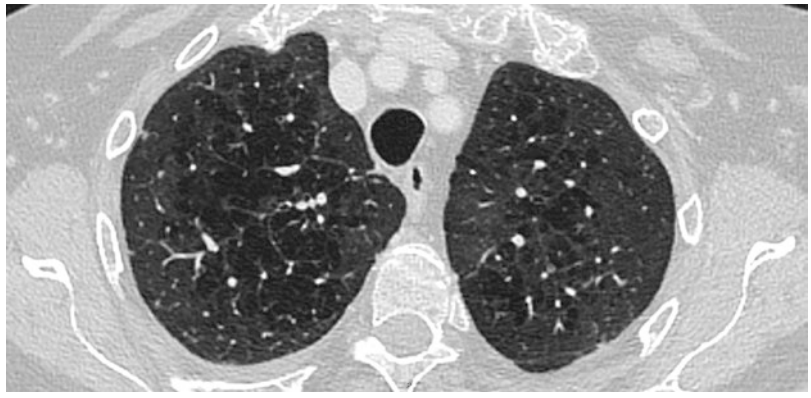

Fig. 3.42 Axial CT images on lung window setting showing small air-density areas near the center of secondary pulmonary lobules of both pulmonary apexes

Fig. 3.43 Small calcified nodule (arrow)

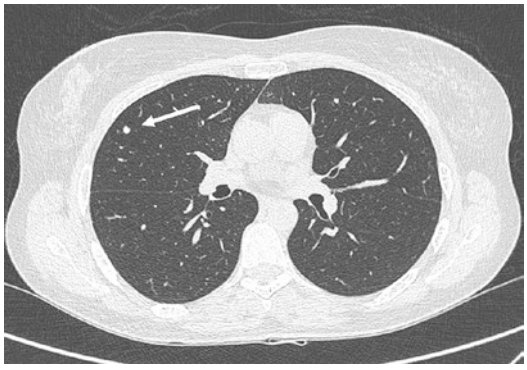

Fig. 3.44 Axial CT image in lung window showing small calcified nodule

Silicosis

Silicosis is an occupational lung disease caused by the inhalation of crystalline silicon dioxide (silica). The most common is *simple chronic silicosis* which results from exposure to low amounts of silica between 2 and 10 years. Multiple small nodules are usually upper lobe predominant and accompanied by calcifications. Hilar and mediastinal lymphadenopathy may precede the appearance of parenchymal nodular lesions. It is common to find calcification of lymph nodes that typically occurs at the periphery of the node. An eggshell calcification pattern is highly suggestive of silicosis.

Chronic silicosis can be complicated by silicotic conglomerates. In this case, CT features are focal soft-tissue masses, often with irregular or ill-defined margins and calcifications, surrounded by areas of emphysematous change.

On the contrary, acute silicosis results from exposure to very large amounts of silica dust over a period of less than 2 years and presents as alveolar silicoproteinosis. It is mainly characterized by numerous bilateral centrilobular nodular ground-glass opacities, multifocal patchy ground-glass opacities, and consolidation.

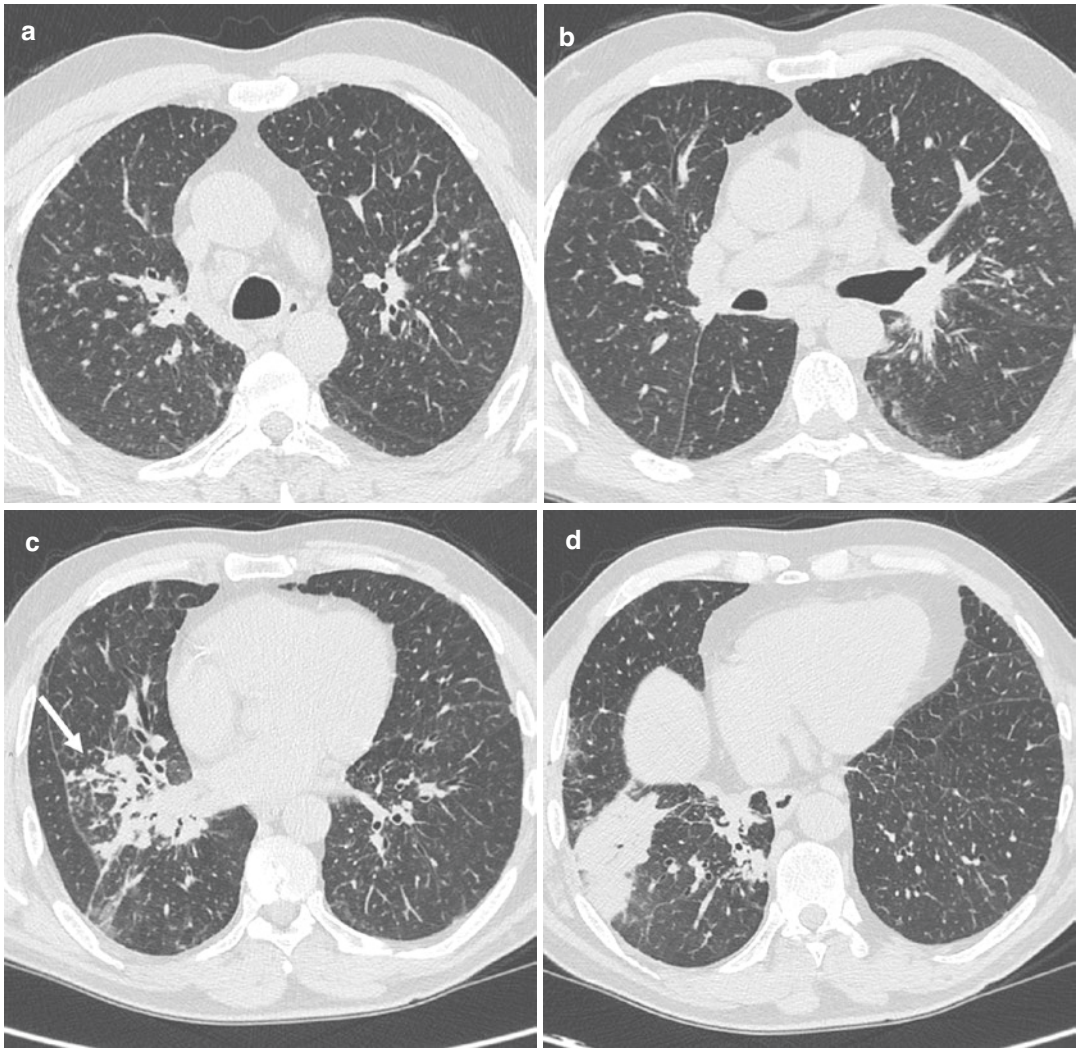

Fig. 3.45 (**a**–**d**) Axial CT images on lung window setting showing focal soft-tissue masses (white arrow), often with irregular or ill-defined margins and calcifications, surrounded by areas of emphysematous change

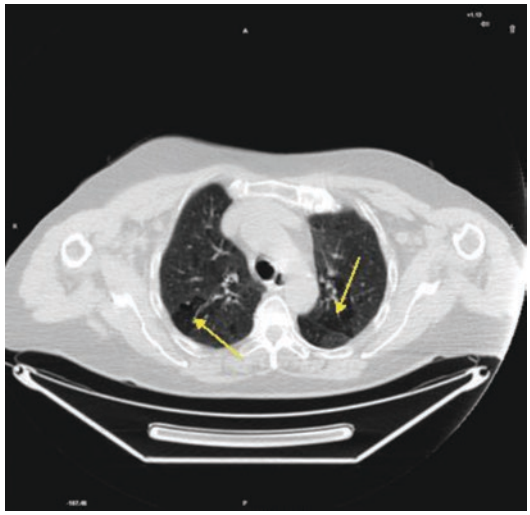

Fig. 3.46 Bilateral mosaic attenuation deriving from small airways disease and producing areas with decreased attenuation due to air trapping (arrows)

Fig. 3.47 Axial CT image in lung window showing mosaic pattern of attenuation due to variable lung perfusion (white arrows)

Lung Mosaic Attenuation

Mosaic attenuation of lung on CT can be grouped into three different categories:

- Small Airways Disease: Regional air trapping and hypoxic vasoconstriction will appear as decreased size and number of vessels and decreased attenuation in the affected regions in comparison to areas of normally ventilated lung. Decreased attenuation and/or increased volume of affected areas will persist on end-expiratory images.
- Small Vessel Disease: Also known as "mosaic perfusion," obliteration of small vessels gives the affected areas a decreased attenuation in comparison to normally perfused lung. There will be no air trapping on end-expiratory images.
- Infiltrative Disease: Patchy infiltration of the interstitium and/or partial filling of airspaces with fluid, cells, or fibrosis will increase attenuation in affected areas. The vessel size will be uniform and there will be no air trapping.

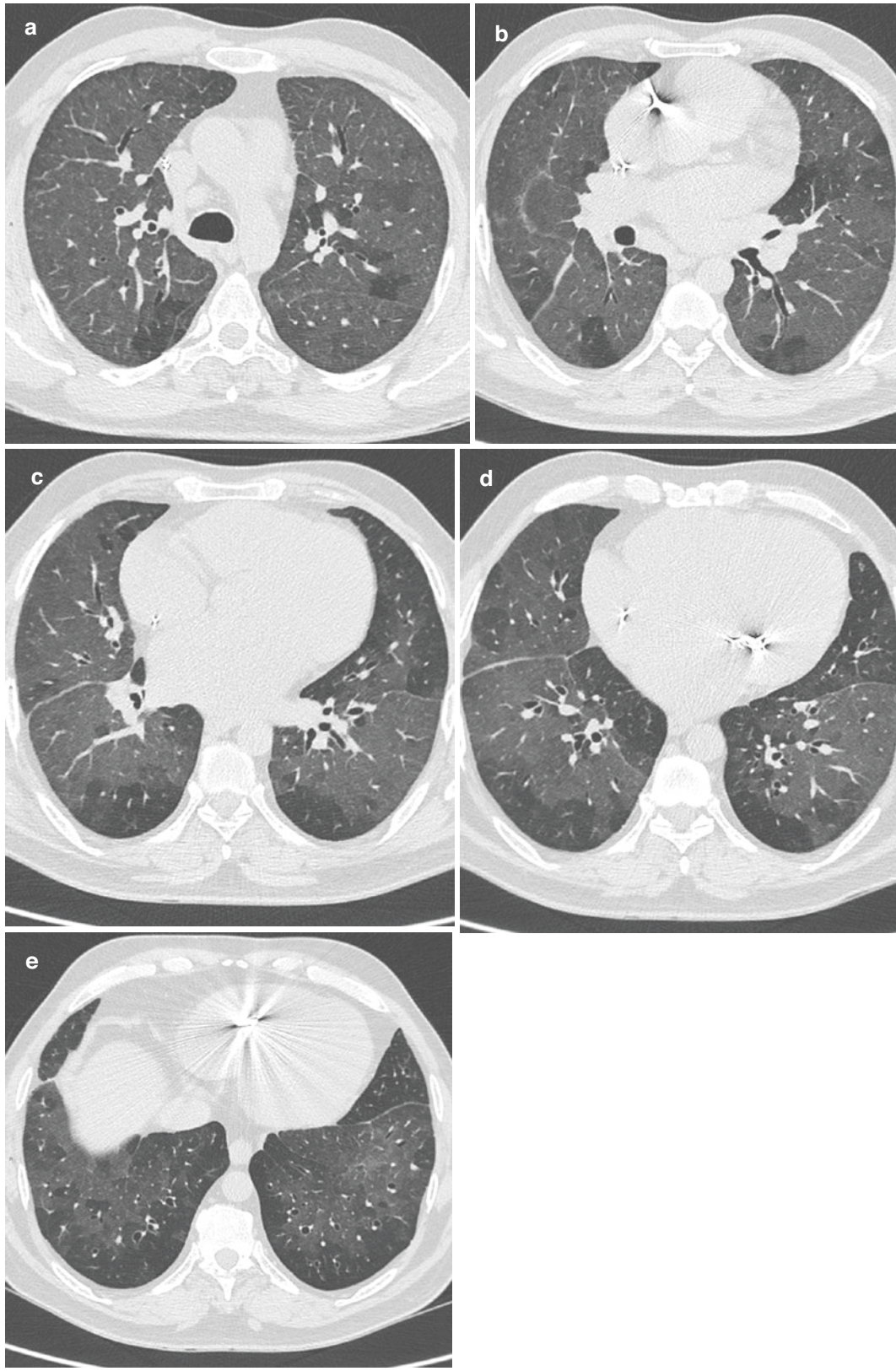

Fig. 3.48 (**a**–**e**) Axial CT images on lung window setting showing mosaic pattern of attenuation due to variable lung perfusion

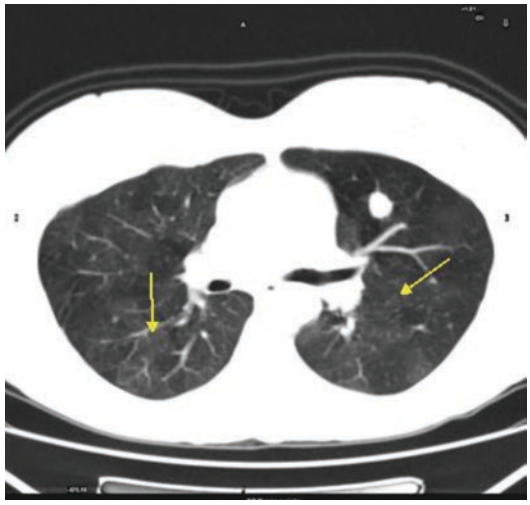

Fig. 3.49 Bilateral mosaic attenuation deriving from infiltrative disease and producing areas with increased attenuation due to partial filling of airspaces with fluid (arrows)

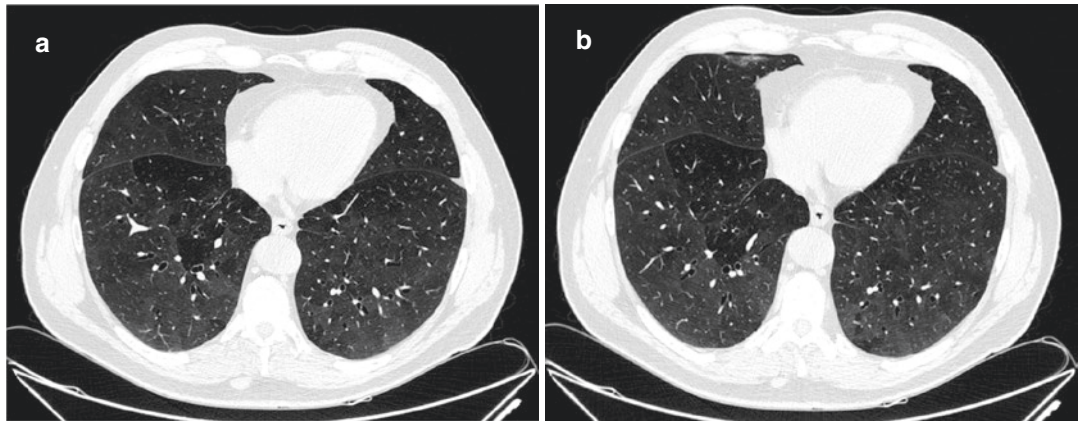

Fig. 3.50 (**a**, **b**) Axial CT images on lung window setting showing mosaic pattern of attenuation due to variable lung perfusion

Fig. 3.51 Lung architectural distortion and interlobular septal thickening (arrow)

Fig. 3.52 Lung architectural distortion (arrow)

Irregular Interstitial Thickening

CT scans can find reversible aspects like ground glass, nodular aspects, and irregular linear opacities. Other irreversible findings are lung architectural distortion, interlobular septal thickening, and cystic air spaces. There are two prevalent CT patterns of attenuation: a reticular pattern and a nodular pattern.

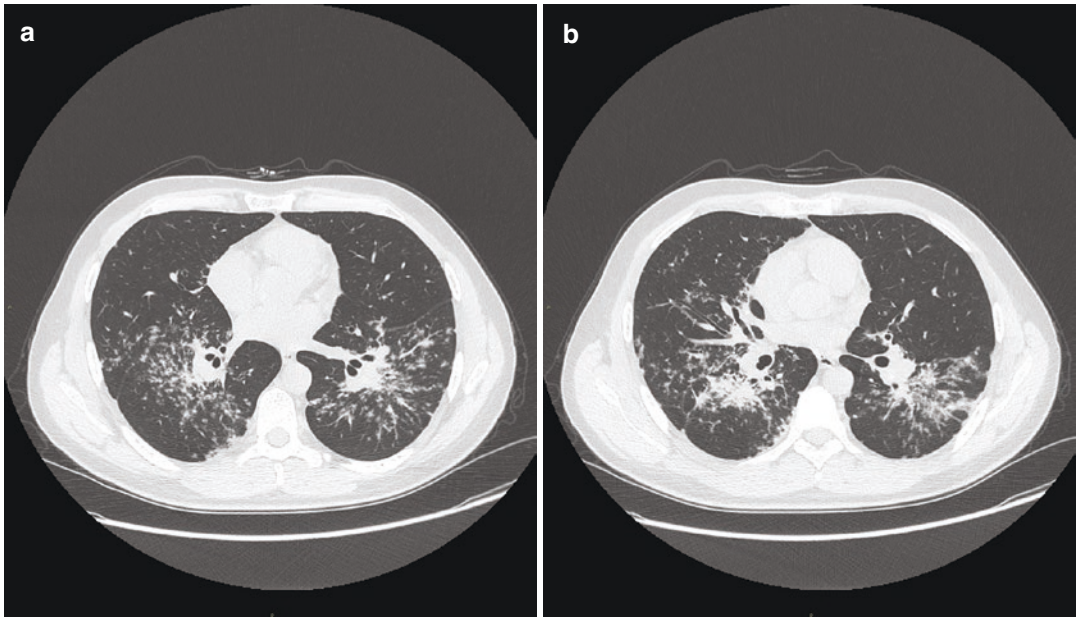

Fig. 3.53 (**a**, **b**) Axial CT images showing multiple small nodules in a peribronchovascular distribution along with irregular thickening of the interstitium. This is typical of reticular sarcoidosis pattern

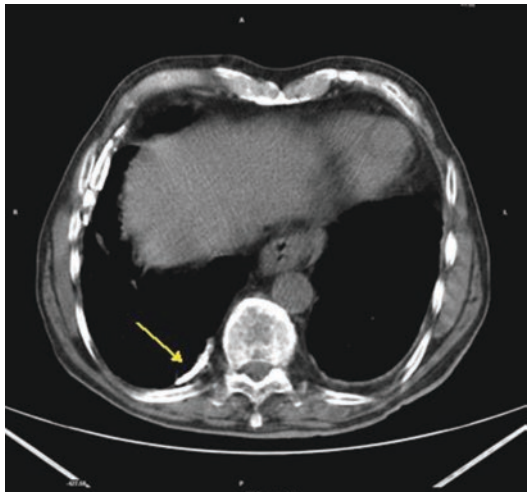

Fig. 3.54 Right pleural thickening and calcification (arrow)

Fibrothorax

A fibrothorax is characterized by smooth symmetric pleural thickening that may be calcified. The mediastinal pleura is usually spared. There is usually marked volume loss in the affected hemithorax with changes seen extending towards the hilum. The combination may give a characteristic "dot in box" appearance, subpleural nodules, and thickening on the interlobar fissures; pleural effusion(s); hilar and mediastinal nodal enlargement; and relatively little destruction of overall lung architecture.

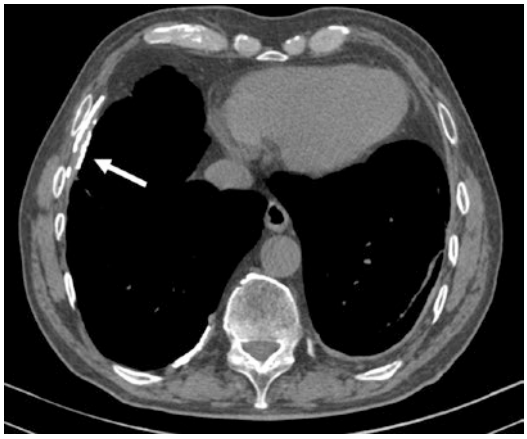

Fig. 3.55 Axial CT image on mediastinal window setting in portal venous phase showing right pleural thickening and calcification (white arrow)

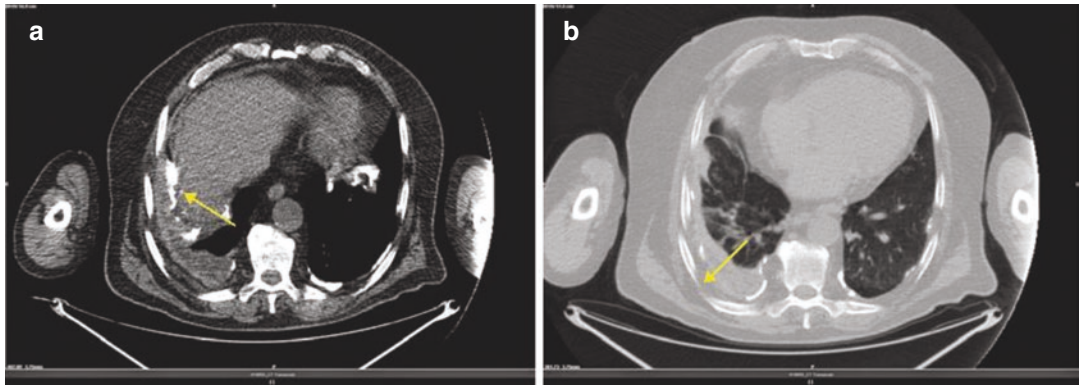

Fig. 3.56 (**a**, **b**) Bilateral pleural thickening and calcification (**a**, arrow) associated with right pleural effusion (**b**, arrow)

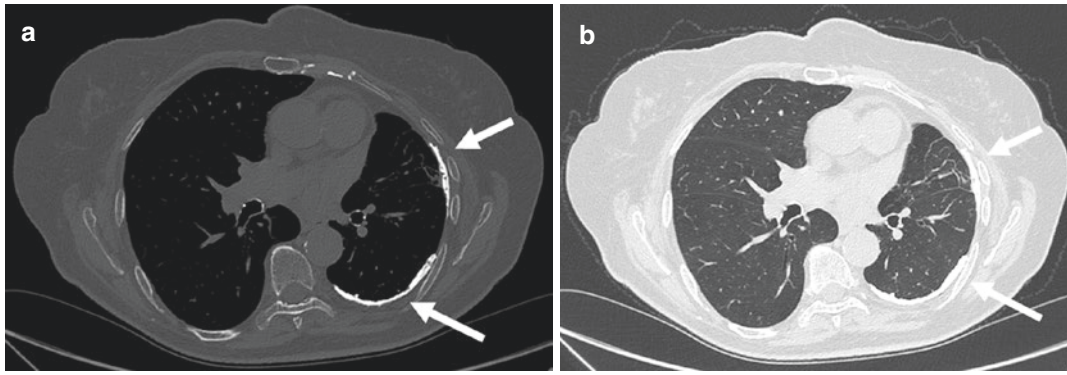

Fig. 3.57 (**a**, **b**) Axial CT images showing left pleural thickening and calcification (white arrows) both on mediastinal and lung window settings

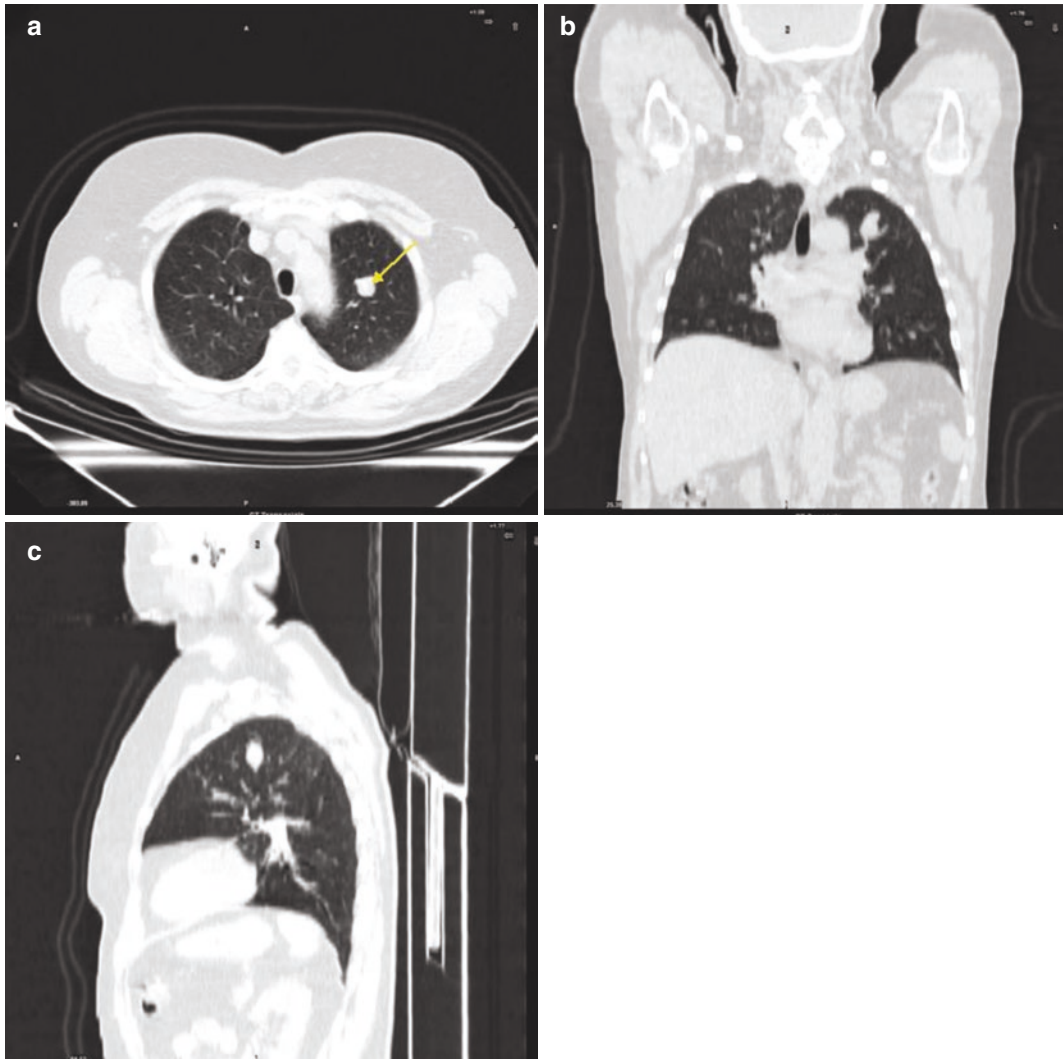

Fig. 3.58 (**a**–**c**) Solitary pulmonary nodule in the apical segment of the left superior lobe (axial-**a**; coronal-**b**; sagittal views). A tiny typical popcorn calcification is hardly seen in the center (arrow)

Pulmonary Hamartoma

CT can detect intralesional fat and calcification. The reported prevalence of calcification (popcorn) in hamartomas on CT varies from 5% to 50%, while fat may be identified in up to 50% of hamartomas at CT. The fat components may be localized or generalized within the nodule. Fat can be recognized by comparing it to subcutaneous fat and will typically have a Hounsfield measurement of −40 to −120 HU. Presence of fat in a well-circumscribed solitary pulmonary nodule which does not demonstrate significant growth is essentially pathognomonic of a pulmonary hamartoma, and no further investigations are required. Fat can only be identified in 60% of lesions. Thin section CT is therefore essential to avoid missing small foci of fat. Calcification is typically dispersed in the form of multiple clumps throughout the lesion in a popcorn configuration.

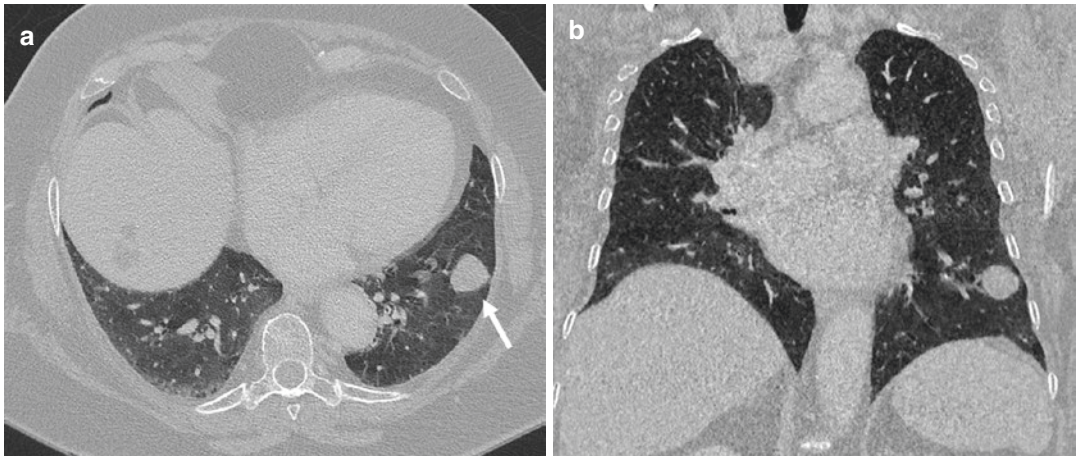

Fig. 3.59 (**a**, **b**) Axial (**a**), and coronal (**b**) CT images of a solitary pulmonary nodule in the left inferior lobe consistent with hamartoma

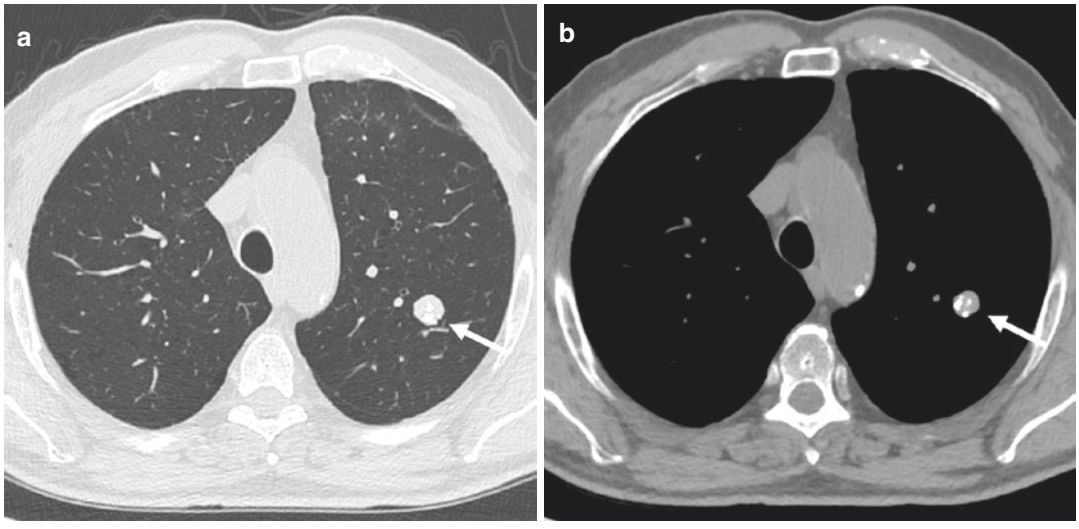

Fig. 3.60 (**a**, **b**) Axial CT images of a solitary pulmonary nodule in the apical segment of the left superior lobe, both on lung (**a**) and mediastinal window (**b**) settings; tiny typical pop-corn calcifications are recognizable in the center (white arrow)

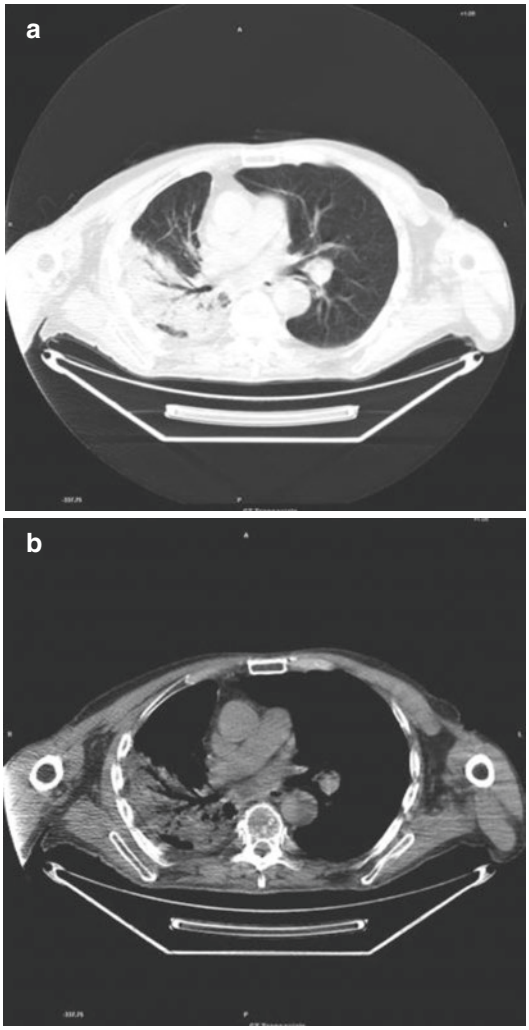

Fig. 3.61 Lung window (**a**) and mediastinal window (**b**) of the right lung showing the typical linear appearance of radiation pneumonitis in a patient previously treated with radiotherapy. Little shift of the mediastinum can be also seen

Radiation Pneumonitis

CT findings can be divided in acute or chronic radiation pneumonitis. Typical characteristics are volume loss; shift of the mediastinum; and linear appearance.

CT findings in acute radiation pneumonitis are homogeneous slight increase in attenuation and patchy non-uniform discrete consolidation.

CT findings in chronic radiation pneumonitis are solid consolidation (radiation fibrosis) and bronchiectasis (stabilized by 1 year after therapy).

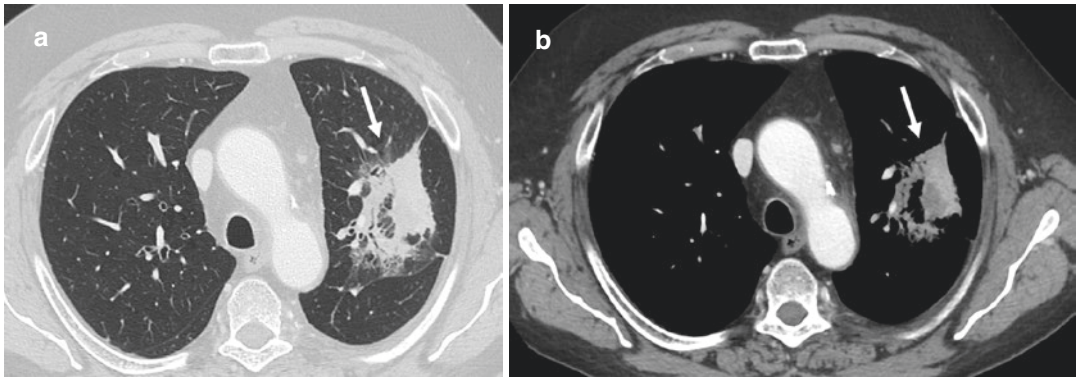

Fig. 3.62 (**a**, **b**) Axial CT images on lung (**a**) and mediastinal in portal venous phase (**b**) window settings showing the typical linear appearance of radiation pneumonitis in a patient previously treated with radiotherapy (white arrows)

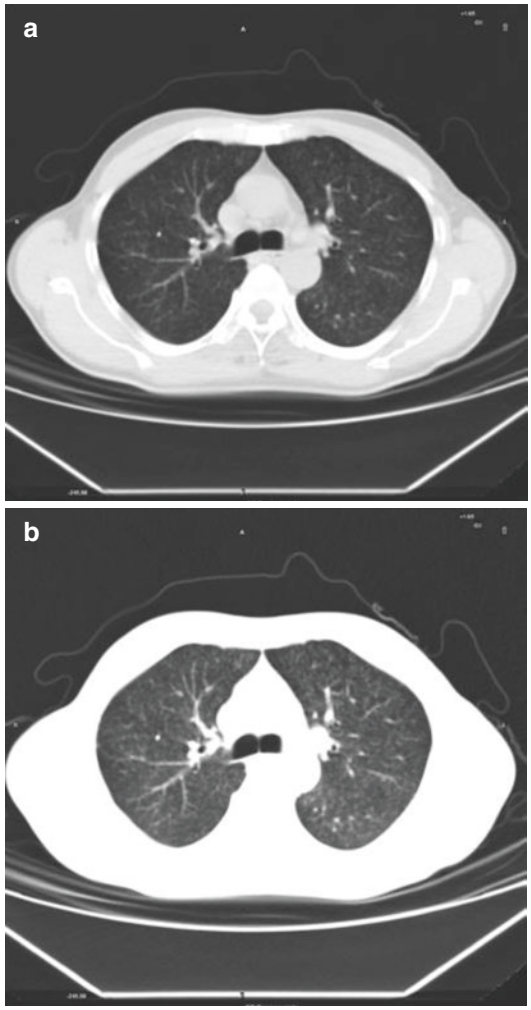

Fig. 3.63 (**a**, **b**) Innumerable bilateral pulmonary micronodules (mediastinal-**a** and lung-**b** window)

Miliary Pulmonary Tuberculosis

The CT findings consist of innumerable, subcentimetric diameter micronodules (1–4 mm) randomly distributed throughout both lungs. Thickening of interlobular septa and fine intralobular networks is frequently evident. Diffuse or localized ground-glass opacity is sometimes seen. Calcified mediastinal nodes are usually present.

Fig. 3.64 Axial High Resolution CT images showing innumerable bilateral pulmonary micronodules with random distribution

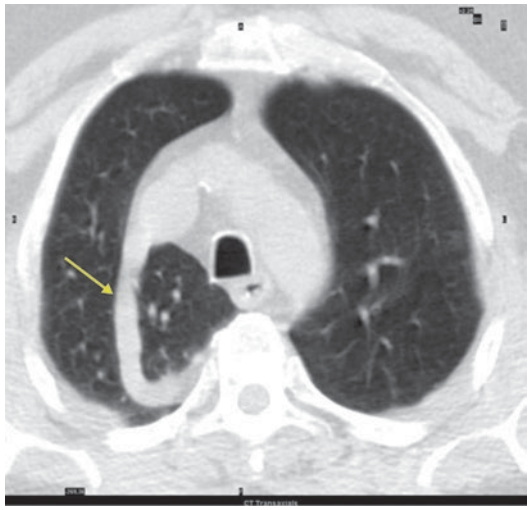

Fig. 3.65 Abnormally located azygos vein (arrow) which creates an accessory fissure in the right upper lobe

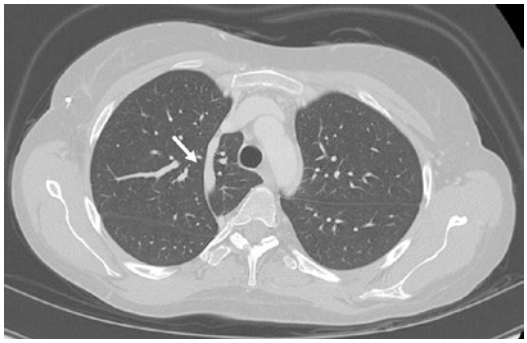

Fig. 3.66 Axial High Resolution CT image showing abnormally located azygos vein (white arrow) which creates an accessory fissure in the right upper lobe

Accessory Azygos Lobe

It is a rare congenital variation of the upper lobe of the right lung; it has no bronchi, veins, and arteries of its own. CT shows the azygos fissure and abnormally located azygos vein. It develops when the apical bronchus grows superiorly medial to the arch of the azygos vein instead of lateral to it. Anatomy of azygos lobe is clinically important during thoracic surgical procedures. Cases of spontaneous pneumothorax have been reported.

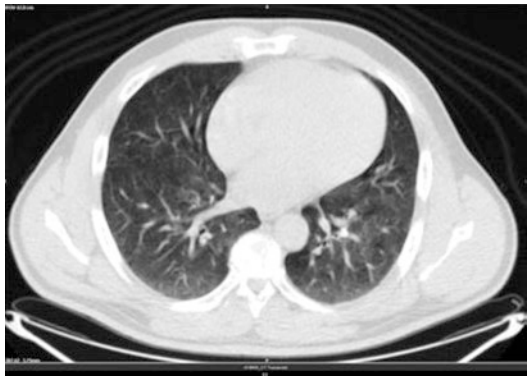

Fig. 3.67 Patchy pattern of ground-glass attenuation, more prominent in the left lung

Respiratory Bronchiolitis

It is a common incidental finding in heavy cigarettes smokers. The use of a CT window level of 700 HU and a window width of 1000–1500 HU is recommended, because these settings provide the best depiction of airways and lung parenchyma. It probably represents a non-specific reaction of lung tissue to certain inhaled irritants and is usually asymptomatic. The various forms of bronchiolitis generally result in one of three predominant CT patterns: nodules and branching lines, ground-glass attenuation and consolidation, or low-attenuation and mosaic perfusion. The presence of ground-glass opacity (increased lung opacity that does not obscure underlying vessels) probably reflects the cellular exudate present within respiratory bronchioles and adjacent alveolar ducts and sacs, as well as the thickening of the peribronchial and alveolar interstitium. The patchy distribution of opacities is typical of the segmental distribution of respiratory bronchiolitis usually demonstrated by pathologic examination. The centrilobular distribution of opacities in some lung regions corresponds to the known bronchiolocentricity of respiratory bronchiolitis; in addition, parenchymal micronodules have been reported in asymptomatic smokers.

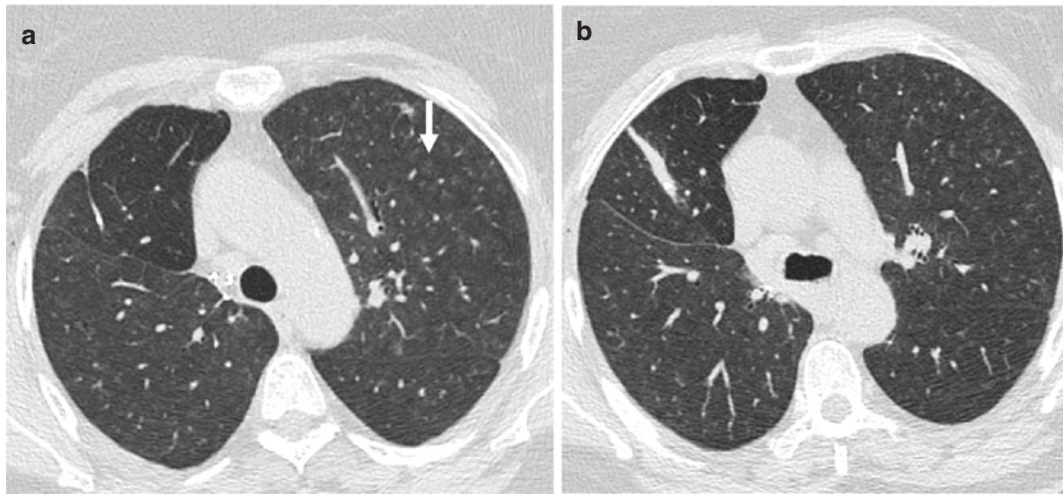

Fig. 3.68 (**a**, **b**) Axial High Resolution CT images showing multiple bilateral "ground glass" opacities, consistent with respiratory bronchiolitis (white arrows)

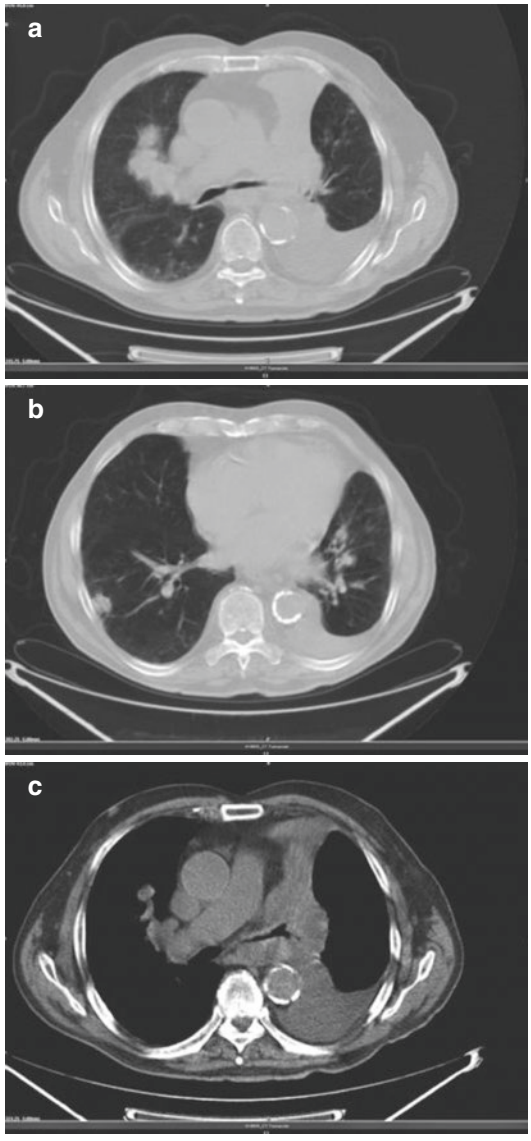

Fig. 3.69 (**a**–**c**) Large lymphadenopathy in left pulmonary hilum and subcarinal. This last one presents large central necrotic area and left superior bronchial compression causing atelectasis of LSL. Other pulmonary and hilar lymph nodes can be seen

Pulmonary Lymphoma

There can be multiple lymphoma findings: nodules less than 1 cm, mass or mass-like consolidation greater than 1 cm with or without cavitations or bronchograms, masses of pleural origin, atelectasis, pleural effusions, and hilar or mediastinal lymphadenopathies. These features can mimic pulmonary hematogenous metastases.

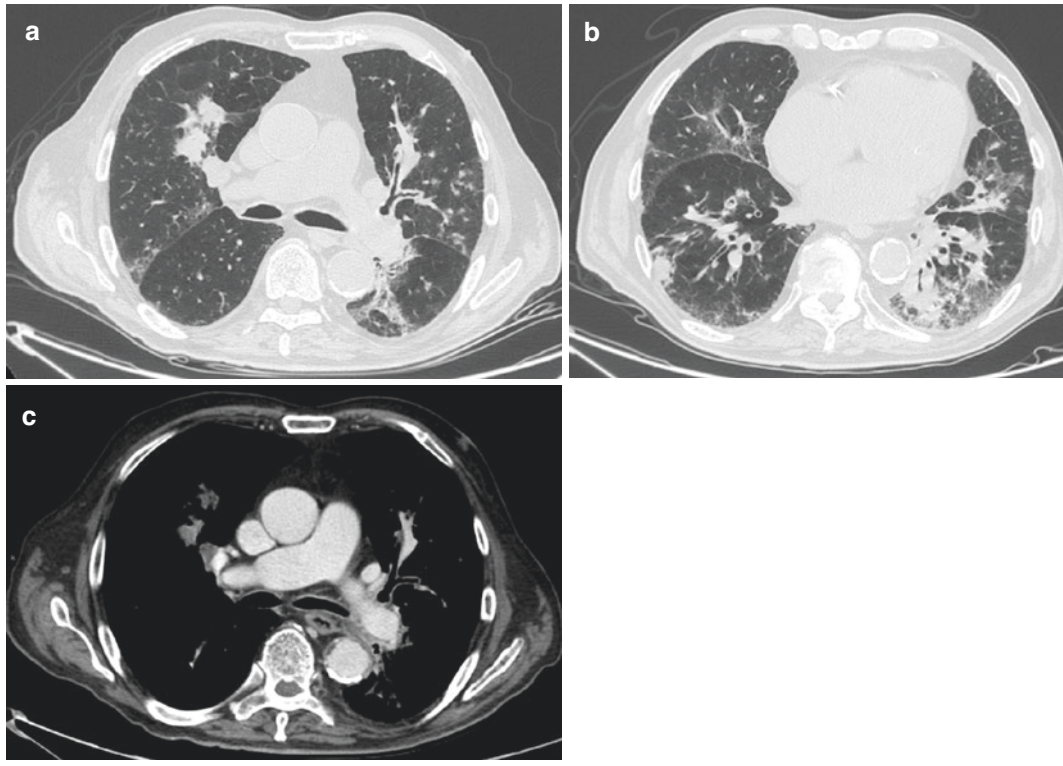

Fig. 3.70 (**a**–**c**) Axial High Resolution CT images (**a**, **b**) and axial venous phase CT image (**c**) showing large lymphadenopathy in left pulmonary

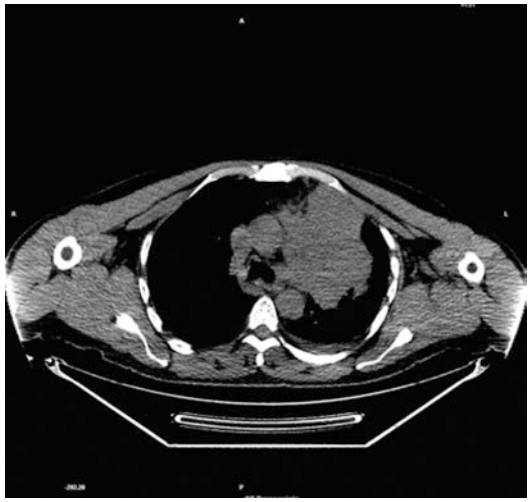

Fig. 3.71 Solid, inhomogeneous, undefined mass, measuring 10 × 11 cm, which involves the left superior lobe, the lingula and, in small part, the anterior basal segment of the left inferior lobe. The mass infiltrates the pleura, the pericardium, and the mediastinum, and there is no clear distinction with the main and the left pulmonary artery, the left main bronchus, and the subcarinal region

Lung Cancer

Lung cancer T-staging is best done with CT to determine the local extent and to look for satellite nodules. The primary tumor should be measured by using lung window settings in two dimensions: the maximum long axis and the largest diameter perpendicular to the long axis.

Although PET however is of great value in N- and M-staging, CT alone remains unsatisfactory for detecting hilar (N1) and mediastinal (N2 and N3) lymph node metastases and for chest wall involvement (T3) or mediastinal invasion (T4).

Parietal pleural involvement in lung cancer results either from neoplastic spread across the pleural cavity from visceral pleural sites along pleural of the malignant process or from the attachment of exfoliated cells from the visceral pleura. *Visceral pleural metastasis* in lung cancer is related to pulmonary artery invasion and embolization. Adenocarcinoma of the lung has a typical peripheral location and spreads by contiguity; moreover it commonly invades the vasculature; therefore, it is the most common histo-type to involve the pleura.

The CT appearances of pleural metastases are generally non-specific and may be indistinguishable from mesothelioma. Certain features, such as circumferential thickening, fissural involvement, and contraction of the hemithorax, are more in favor of mesothelioma.

Pleural effusion is the most common radiological manifestation of pleural metastases, and malignancy is the most common cause of a massive pleural effusion.

Patients with malignant effusions can show findings similar to those with *empyema* (previous sclerotherapy may be a confounding factor). Empyema shows parietal pleural thickening, thickening of the extrapleural subcostal tissues, and increased attenuation of extrapleural fat. Patients with transudative effusions have none of the above findings. Other causes of pleural effusion are lymphangitic carcinomatosis and benign asbestos pleural effusion. A malignant pleural effusion is expected to be stable or to progress, whereas a non-malignant effusion to be stable or to regress over time.

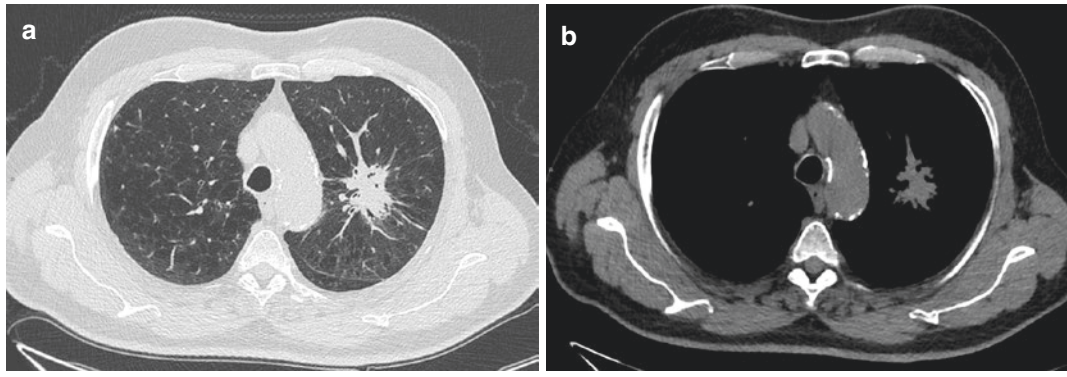

Fig. 3.72 (**a**, **b**) Axial High Resolution CT image (**a**) and axial CT imagine with mediastinal window showing a solid mass, with irregular margins and pleural connecting striae, which involves the left lung

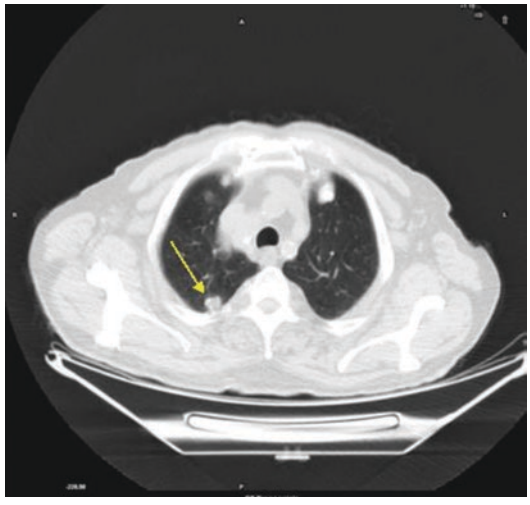

Fig. 3.73 Subpleural solitary pulmonary nodule in the right upper lobe with irregular margins (arrow) suspicious for cancer

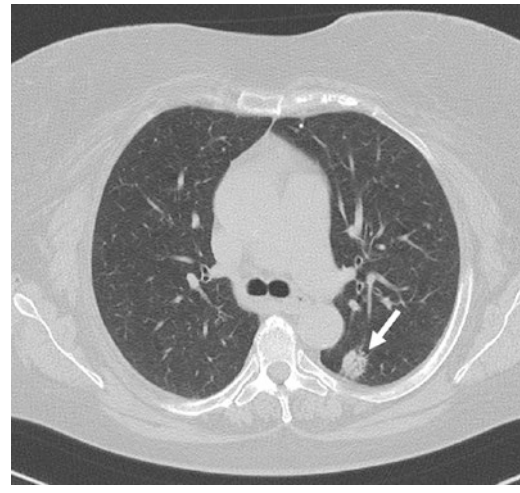

Fig. 3.74 Axial High Resolution CT image showing subpleural solitary pulmonary nodule in the left lung with irregular margins (white arrow) suspicious for cancer

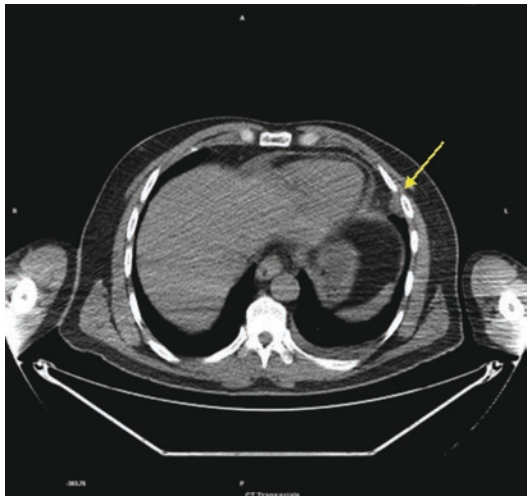

Fig. 3.75 Left pleural thickening

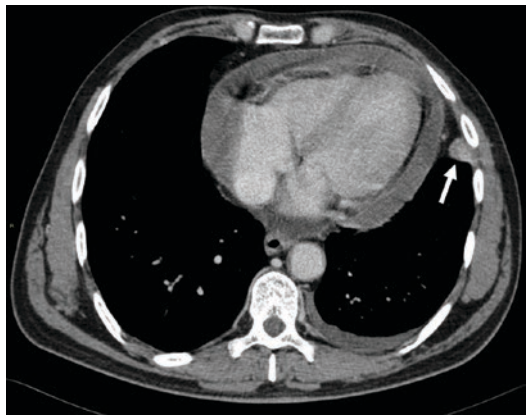

Fig. 3.76 Axial venous phase CT image showing a left pleural thickening (white arrow) consistent with malignant pleural and/or subpleural lesion. In addition: left pleural and significant pericardial effusion

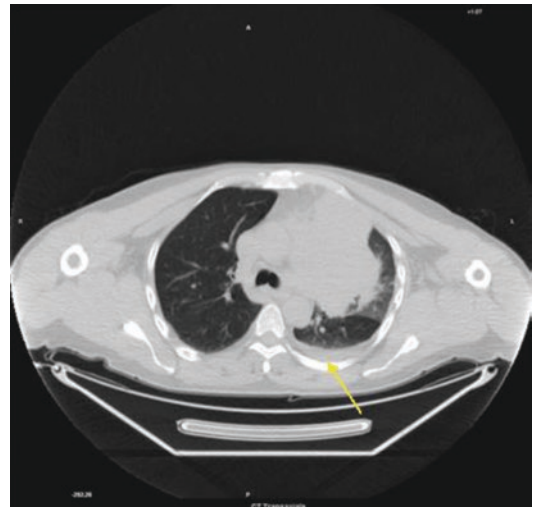

Fig. 3.77 Mild left pleural effusion (arrow)

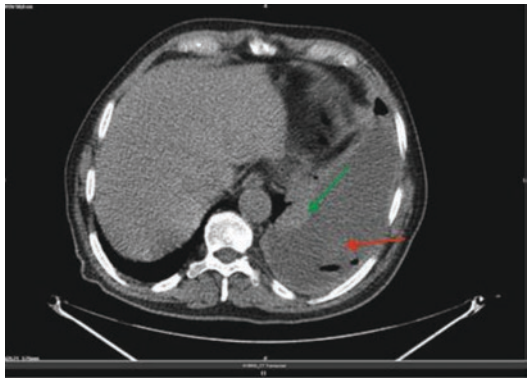

Fig. 3.78 Right basal pleural thickening (green arrow) and pleural effusion (red arrow) consistent with mesothelioma

Fig. 3.79 Axial venous phase CT image showing right irregular pleural thickening involving both parietal and visceral pleurae

Pleural Mesothelioma

Malignant pleural mesothelioma (MPM) is a rare and usually fatal neoplasm that is increasing in frequency. It is associated with exposure to asbestos. The clinical signs and symptoms are nonspecific. CT scan shows diffuse, irregular pleural thickening involving both parietal and visceral pleurae. Pleural effusion is present and lung is markedly contracted. An extensive irregularly lobulated bulky and pleural-based mass associated with pleural plaques is usually detected.

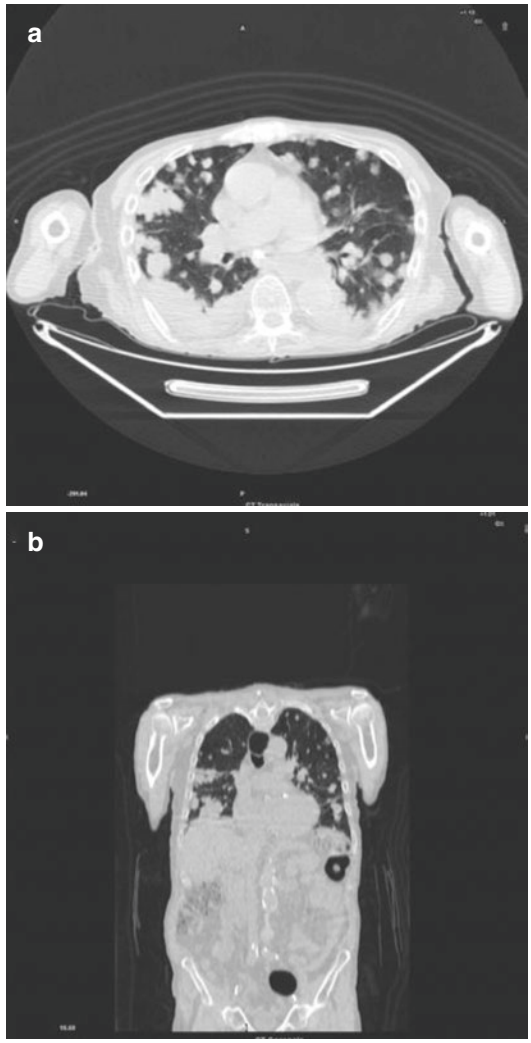

Fig. 3.80 (**a**-axial; **b**-coronal) Multiple bilateral pleuro-pulmonary lesions

Lung Metastases

Typical radiologic findings of diffused pulmonary metastases include multiple peripherally located round variable-sized nodules (hematogenous metastasis) and diffuse thickening of the interstitium (lymphangitic carcinomatosis).

Atypical findings include cavitation, calcification, hemorrhage around the metastatic nodules, pneumothorax, air-space pattern, tumor embolism, endobronchial metastasis, solitary mass, dilated vessels within a mass, and sterilized metastasis.

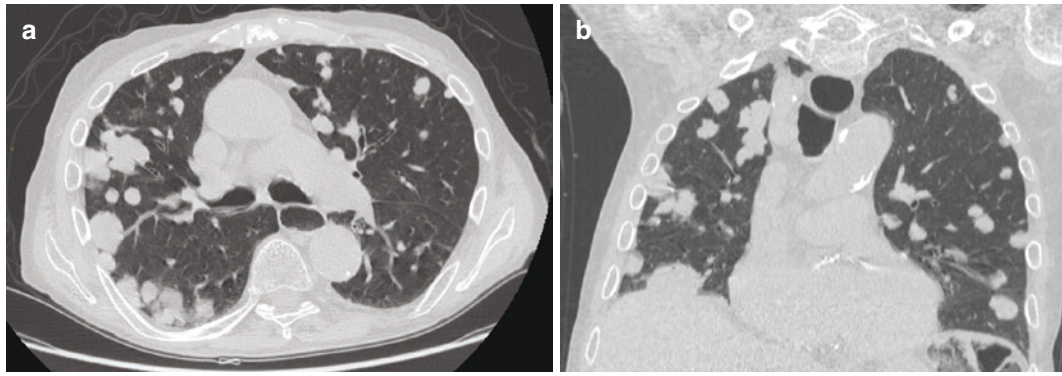

Fig. 3.81 (**a**, **b**) Axial (**a**) and coronal (**b**) High Resolution CT images showing multiple bilateral pleuro-pulmonary lesions

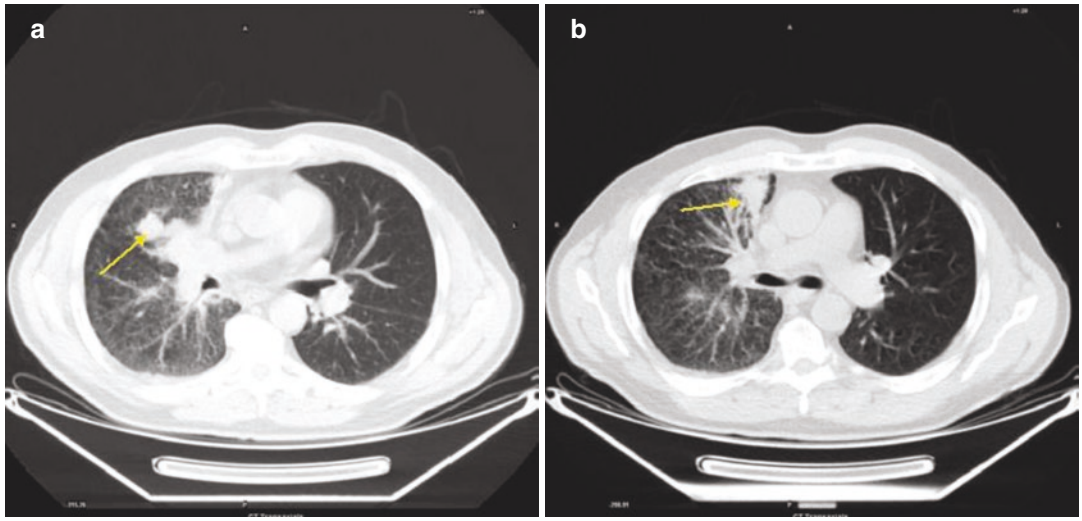

Fig. 3.82 Right pulmonary nodular (**a**) and irregular (**b**) septal thickening (arrows)

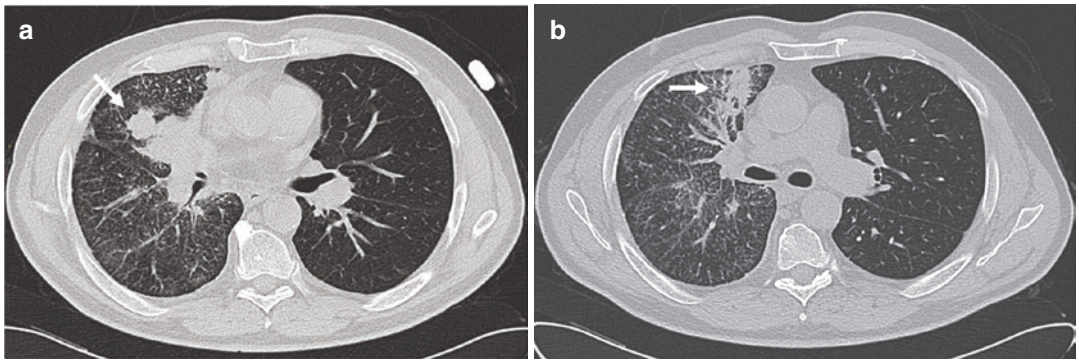

Fig. 3.83 (**a**, **b**) Axial High Resolution CT images showing a right pulmonary nodule (**a**) and irregular (**b**) septal thickening (white arrows)

Fig. 3.84 Bilateral irregular interlobular septal thickening

Carcinomatous Lymphangitis

It results from hematogenous spread to the lung, with subsequent invasion of interstitium and lymphatics. Typically the manifestation is that of interlobular septal thickening most often nodular and irregular, although smooth thickening may also sometimes be seen.

Focal or unilateral abnormalities are present in 50% of patients, hilar lymphadenopathy in 50%, pleural effusion due to pleuritic carcinomatosis in more than 50% of patients.

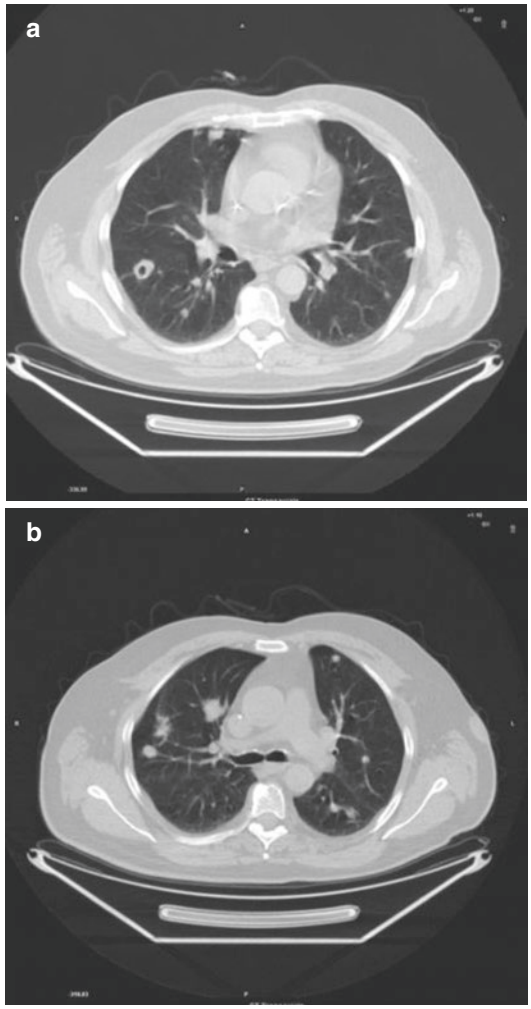

Fig. 3.85 (**a**, **b**) Multiple bilateral rounded lung nodules in a patient treated for colorectal cancer. One nodule in the right lung presents with air-space consolidation. Most of the nodules appear in contact with a pulmonary vessel

Lung Metastases in Colon Cancer

CT findings include multiple well-circumscribed, rounded, soft-tissue attenuated, variable-sized nodules (more often in the periphery of the lung) and diffuse thickening of interstitium. A prominent pulmonary vessel has frequently been noted heading into a metastasis, called as feeding vessel sign. CT aspects to evaluate are margin of nodule, the hemorrhagic phenomenon related to metastatic nodule, calcification, cavitation, small metastatic nodules in the lobules, lymphangitic carcinomatosis, tumor emboli, and pleural metastases. The air-space consolidation is often seen in cases of metastases from gastrointestinal tract malignancies.

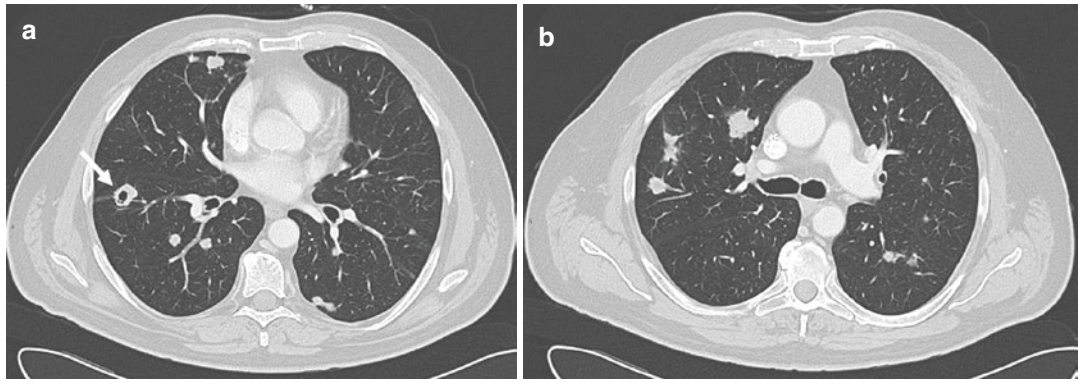

Fig. 3.86 (**a**, **b**) Axial High Resolution CT images showing multiple bilateral rounded lung nodules in a patient treated for colorectal cancer. One nodule in the right lung presents with air-space consolidation (white arrow). Most of the nodules appear in contact with a pulmonary vessel (feeding vessel sign)

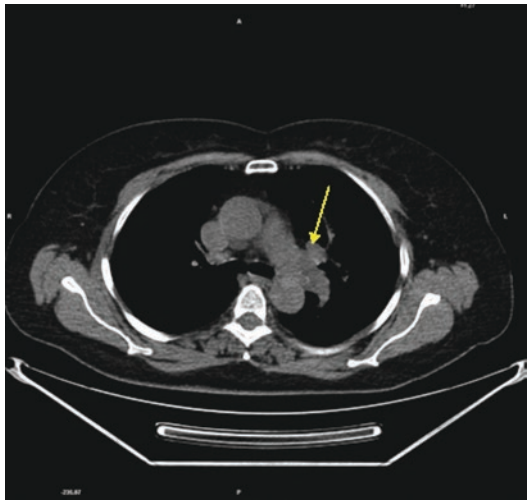

Fig. 3.87 Abnormal soft tissue surrounding the left pulmonary artery (arrow)

Fig. 3.88 Axial arterial phase CT image showing abnormal soft tissue surrounding the left pulmonary artery (white arrow)

Left Pulmonary Artery Angiosarcoma

Pulmonary artery sarcoma is a rare malignancy arising from the mesenchymal cells of the intima of the pulmonary artery. The diagnosis is often delayed due to the non-specific symptoms, mimicking pulmonary embolism, as well as its relatively slow growth. The presentation depends on the degree of pulmonary artery obstruction. The sarcoma may involve the main pulmonary trunk and may extend into both of the main pulmonary arteries. These patients may have evidence of severe right heart failure. CT scans may detect a soft-tissue density located in or around the pulmonary arteries.

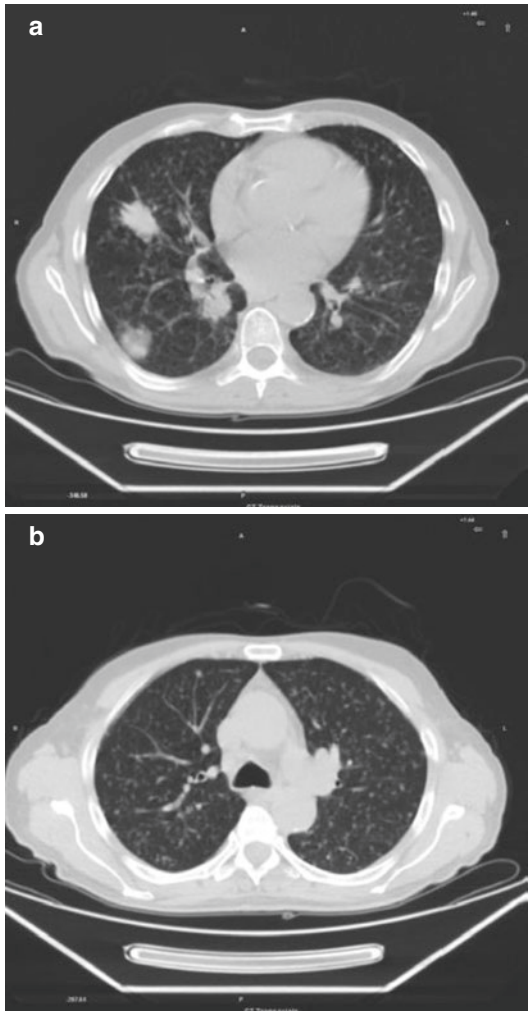

Miliary Pulmonary Metastases

Uncommon form of pulmonary metastases. Most commonly due to thyroid cancer, renal cell carcinoma, and melanoma. Typical appearance of a "Snowstorm."

Fig. 3.89 (**a**, **b**) Multiple small 2–3 mm nodules throughout both lungs

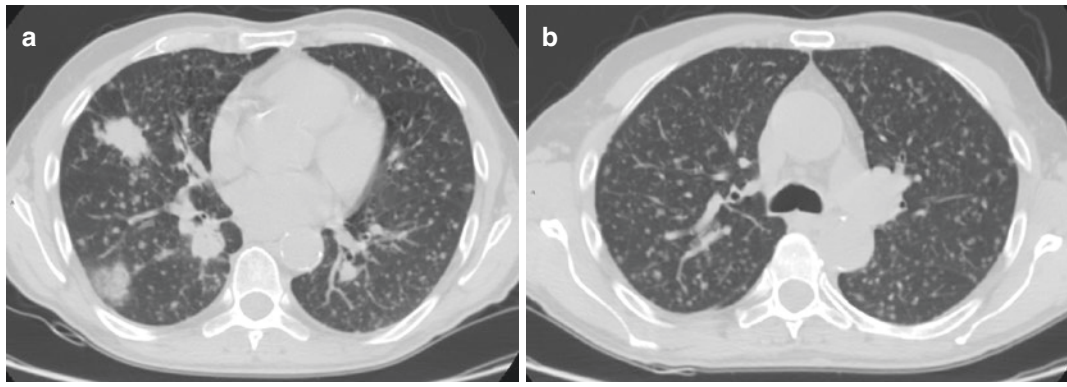

Fig. 3.90 (**a**, **b**) Axial CT images with lung window showing multiple small 2–3 mm nodules throughout both lungs with random distribution

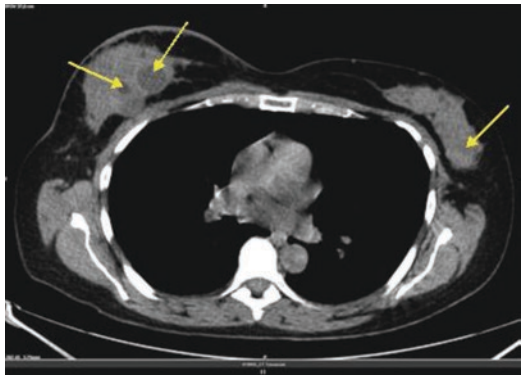

Fig. 3.91 Inhomogeneous glandular parenchyma with multiple rounded hypodense lesions in both breasts (arrows)

Fig. 3.92 Axial venous phase CT image showing inhomogeneous glandular parenchyma with multiple hyperdense lesions left breast

Carcinomatous Mastitis

It is a relatively uncommon but aggressive form of invasive breast carcinoma representing 1–4% of all breast cancers, typically occurring in the fourth to fifth decades. The invasive ductal carcinoma tends to be the most common histological type. It displays the same symptoms that may occur with inflammation, like breast warmth, redness involving more than one-third of the breast, thickening (edema/swelling) of the skin of the breast, and ridging of the skin of the breast. Systemic symptoms such as fever are absent which helps somewhat differentiate from mastitis.

Inflammatory breast carcinoma (IBC) is a T4 tumor according to the standard TNM staging classification of breast cancer. The advanced stage of IBC, along with the tendency to grow and spread quickly, makes it difficult to treat successfully. Standard imaging findings using mammography and sonography have been largely described. CT should be reviewed for focal masses, architectural distortion, asymmetric density, and calcifications associated with the typical clinical features.

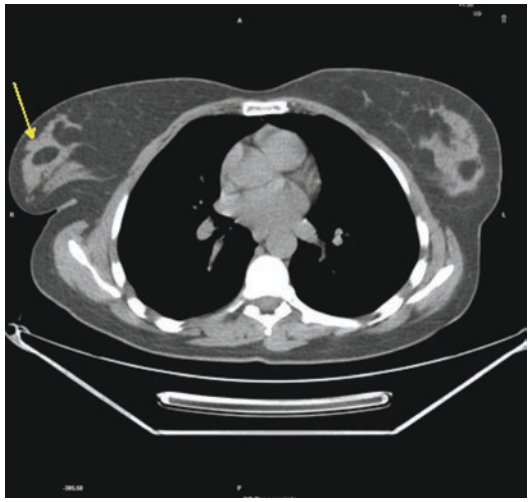

Fig. 3.93 Small ovoid right breast mass (arrow) consistent with malignancy

Lobular Breast Carcinoma

Invasive lobular carcinoma (ILC), sometimes called infiltrating lobular carcinoma, is the second most common type of breast cancer after invasive ductal carcinoma.

The shape of the incidental enhancing breast lesion was described as a round, ovoid, lobulated, and irregular mass or non-mass (in this case CE administration is necessary). The margin of the incidental breast lesion is usually described as well circumscribed, irregular, and spiculated.

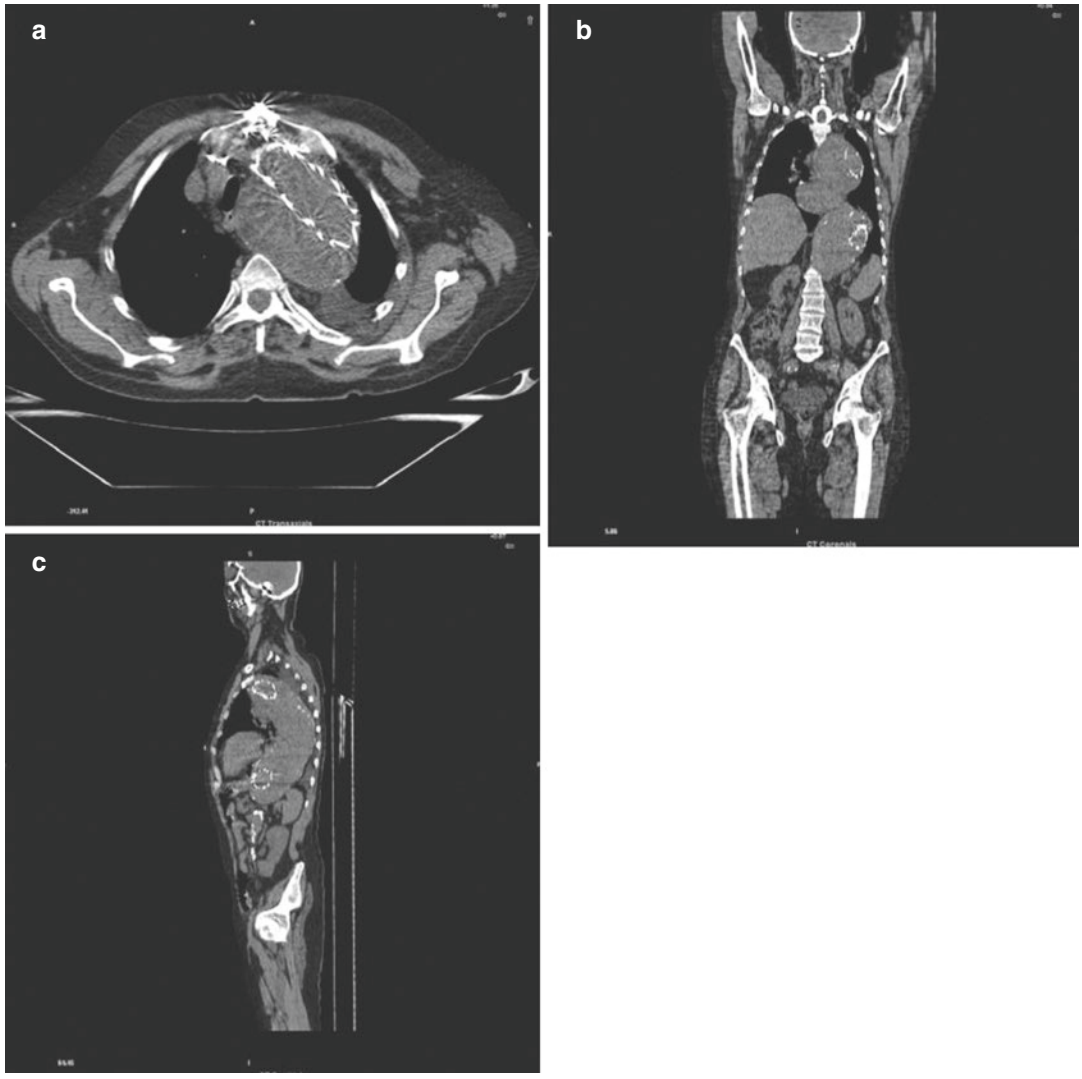

Fig. 3.94 (**a**–**c**) Aortic aneurysm seen in axial-**a**, coronal-**b**, and sagittal-**c** views, in a patient affected by Marfan syndrome

Aorta Disease in Marfan Syndrome

Marfan syndrome is an inherited multisystemic connective tissue disease that is caused by a mutation of the fibrillin-1 gene. It may affect various systems, including the cardiovascular, musculoskeletal, central nervous, pulmonary, ocular, and integumentary systems. Potential cardiovascular manifestations include annuloaortic ectasia with or without aortic valve insufficiency, aortic aneurysm, aortic dissection, mitral valve prolapse, and pulmonary artery dilatation.

Compared with atherosclerotic aneurysms, the aortic aneurysms seen in Marfan syndrome rarely show intimal calcification or atherosclerotic thrombosis, and they occur commonly and develop more rapidly in younger patients. They are caused by the weakening of the connective tissue (cystic medial degeneration).

Fig. 3.95 Rounded, soft-tissue density mass in the anterior mediastinum in keeping with thymoma (arrow)

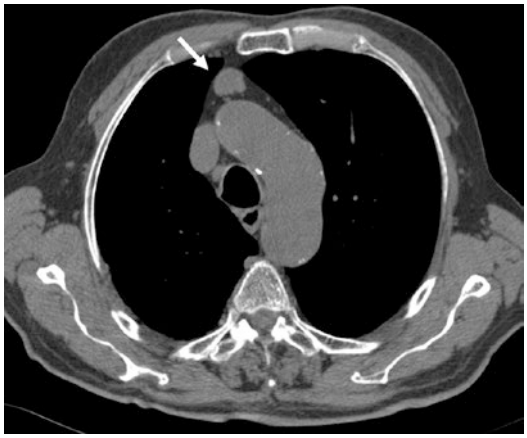

Fig. 3.96 Axial CT image with mediastinal window, showing a rounded, soft tissue-density mass in the anterior mediastinum in keeping with thymoma (white arrow)

Thymoma

Normal thymic tissue has a triangular density in the anterior mediastinum. Thymus should be <1.8 cm up to 20 years and <1 cm after 20 years when fatty involution occurs. Thymoma is the most common anterior mediastinal mass representing a solid or more rarely cystic, lymphoepithelial tumor of the thymus. On non-contrast CT scans, thymomas usually appear as soft-tissue density masses equal in attenuation to muscle (40–60 HU). Five percent may contain curvilinear or amorphous calcification. Features of malignancy are absence of fat planes and invasion of adjacent structures.

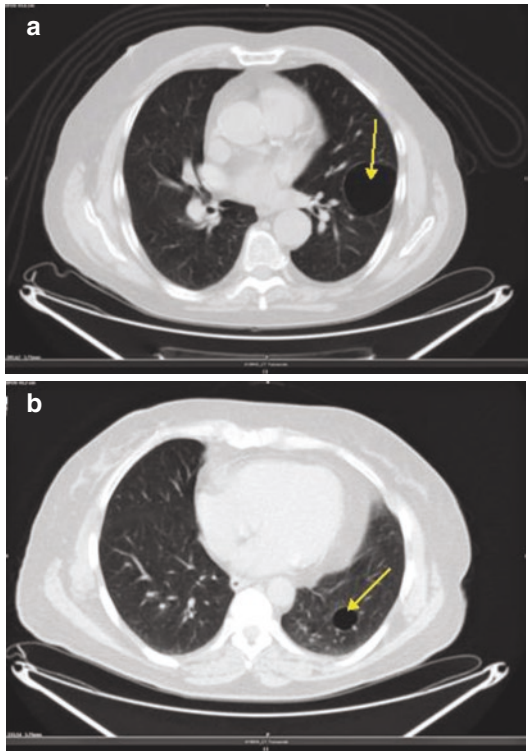

Fig. 3.97 (**a**, **b**) Examples of bulla in the left lung: the larger one is perifissural, whereas the other one is smaller and in the left lower lobe (arrows)

Emphysematous Bulla

A round, focal air space, 1 cm or more in diameter. It is demarcated by a thin epithelialized wall which is usually no greater than 1 mm in thickness. Walls may be formed by pleura, septa, or compressed lung tissue. Bulla is seen more in upper lobes, tends to trap air, and may become larger on expiration.

An emphysema characterized by the presence of bullae is called *Bullous emphysema*.

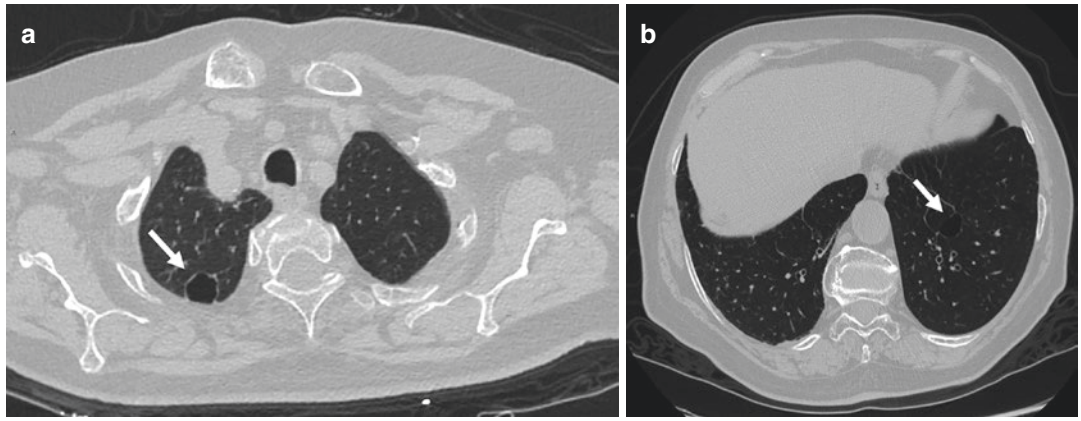

Fig. 3.98 (**a**, **b**) Axial High Resolution CT images showing a peri-fissural enphysematous bulla in the upper right lobe (**a**) and a centro-lobular enphysematous bulla in the left lower lobe (**b**) (white arrows)

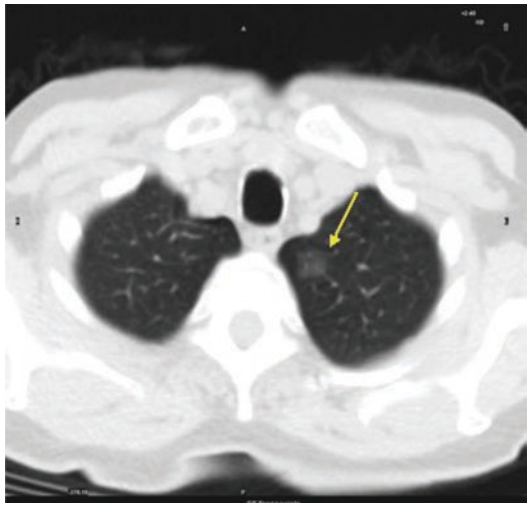

Fig. 3.99 Focal area of increased attenuation in the apical segment of the left upper lobe (arrow)

Fig. 3.100 Axial High Resolution CT image showing a focal area of increased attenuation in the postero-lateral segment of the right lower lobe (white arrow)

Ground Glass

Focal or diffuse hazy area of increased attenuation of the lung which does not obscure vascular structures. It is like a "veil" across the lung parenchyma. Indicates a partial filling of air spaces by *exudate* or *transudate*, as well as interstitial thickening or partial collapse of lung alveoli. It can be found in acute lung diseases, as Pneumocystis pneumonia (PCP), Viral pneumonias, Acute interstitial pneumonia, Acute eosinophilic pneumonia, Hypersensitivity pneumonitis, or Early interstitial lung disease. Chronic states instead can be Hypersensitivity pneumonitis, Interstitial lung diseases (NSIP, DIP), Bronchoalveolar carcinoma, Alveolar proteinosis, and Sarcoidosis.

The persistence of nodular ground-glass opacity over time may be strongly suggestive of an early-stage malignancy, especially if the lesion increases in size or includes a solid component that increases in its extent. The more extensive is the solid portion of the lesion, the higher is the probability of malignancy and the poorer is the prognosis.

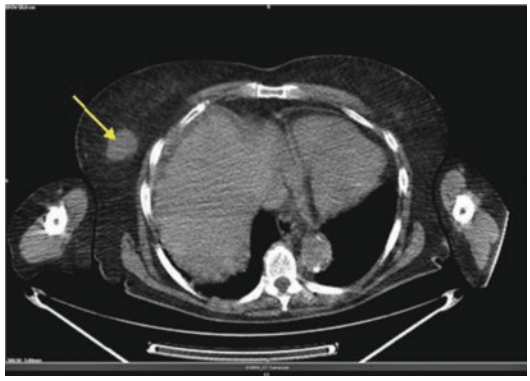

Fig. 3.101 Voluminous nodular mass in the right supero-external breast (arrow)

Fig. 3.102 Axial venous phase CT image showing a large, irregular, hyper-dense mass in the right supero-internal breast

Breast Cancer

Hypodense nodule, with indefinite margins. This finding should always require histological confirmation in order to exclude malignancy.

Irregular margins, irregular shape, and rim enhancement are the most highly predictive features for malignancy.

Atelectasis

Collapse or closure of the lung resulting in reduced or absent gas exchange. In acute atelectasis, the lung has recently collapsed and it is primarily notable only for airlessness. In chronic atelectasis, the affected area is often characterized by a complex mixture of airlessness, infection, widening of the bronchi (*bronchiectasis*), destruction, and scarring (fibrosis).

Rounded atelectasis: Localized, reversible form in subjacent peripheral tissue, often following pleural effusion and characterized by focal pleural scarring.

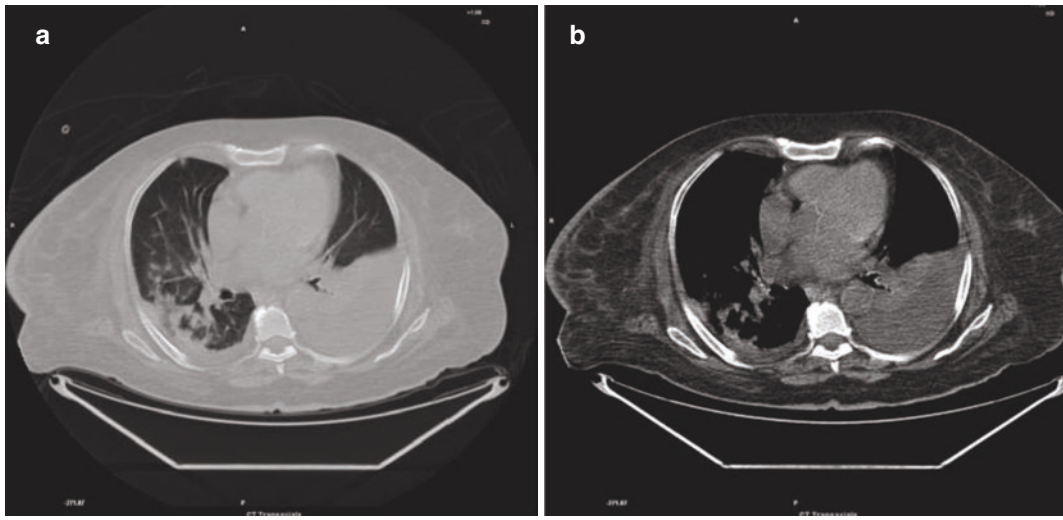

Fig. 3.103 (**a**, **b**) Atelectasis of the left inferior lobe

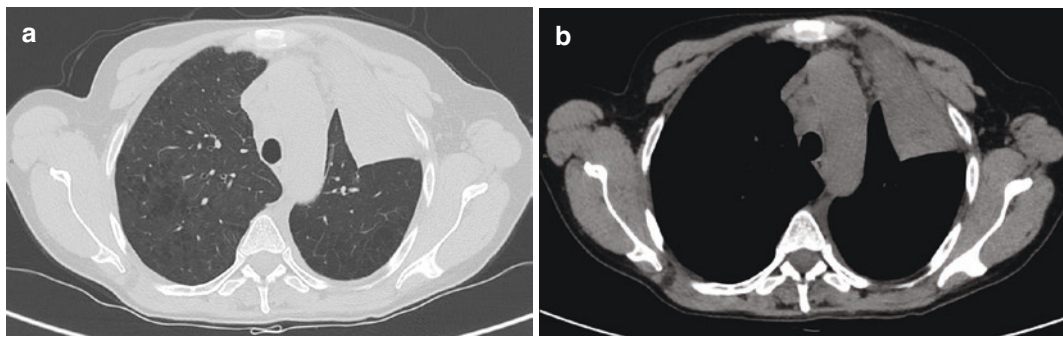

Fig. 3.104 (**a**, **b**) Axial High Resolution CT image (**a**) and axial CT image with mediastinal window (**b**) showing atelectasis of the anterior segment of left upper lobe

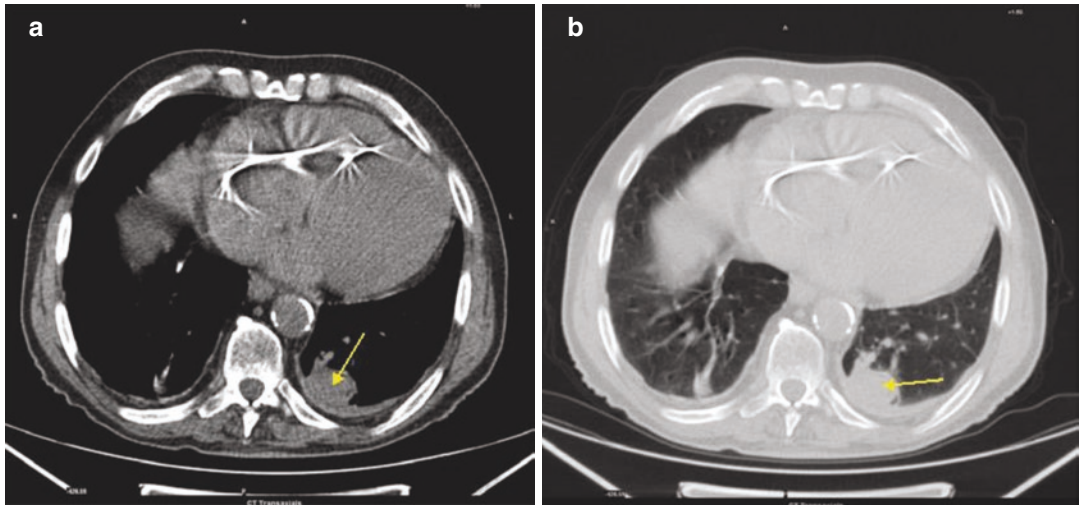

Fig. 3.105 (**a**, **b**) Rounded atelectasis of the left inferior lobe (arrows)

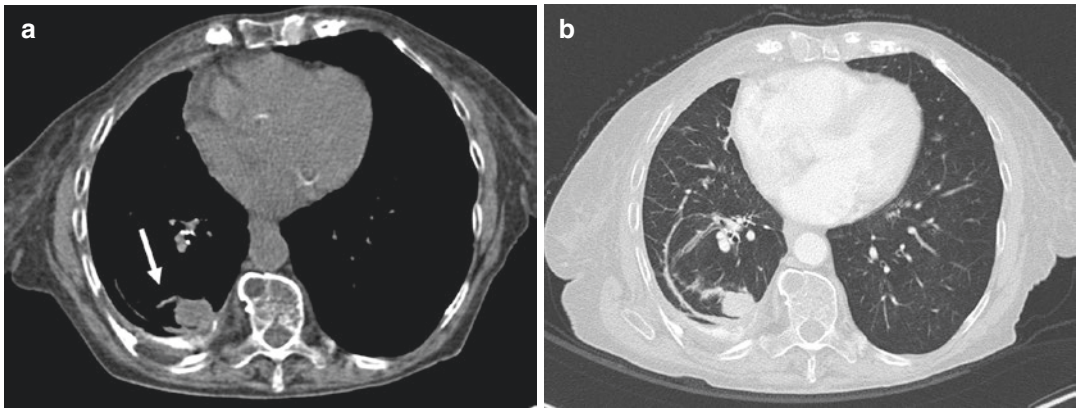

Fig. 3.106 (**a**, **b**) Axial CT images showing rounded atelectasis of the right inferior lobe (white arrows)

Fig. 3.107 Complete atelectasis of the left lung with severe component of pleural effusion. A more solid component is seen in the apical part with involvement of the left pulmonary hilum and lung base

Acinar Adenocarcinoma of the Lung

It is a histological subtype of gland-forming cancer diagnosed when cuboidal and/or columnar shaped malignant cells in the neoplastic tissue form acini and tubules. It is a common form of cancer occurring in the lung and prostate gland.

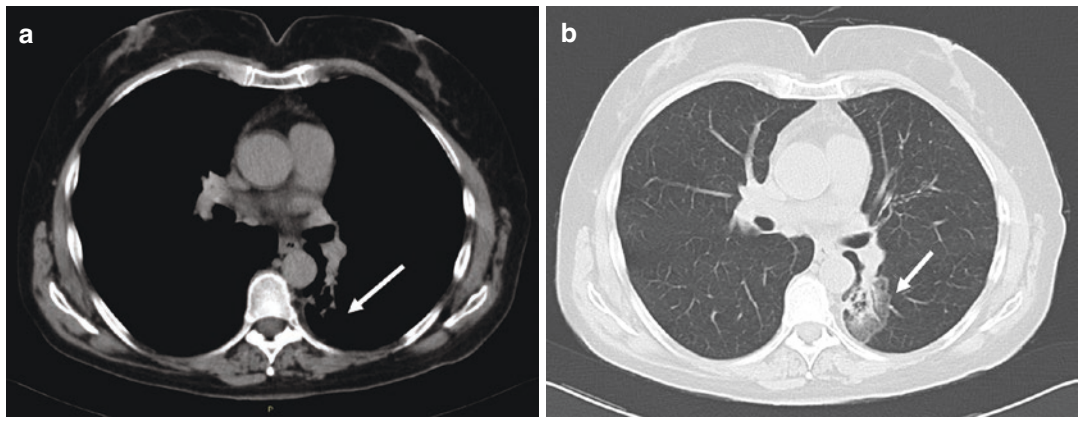

Fig. 3.108 (**a**, **b**) Axial CT images, respectively on mediastinal (**a**) and lung (**b**) window settings, showing a ground-glass area with a central more solid component compatible with acinar adenocarcinoma of the lung (white arrows)

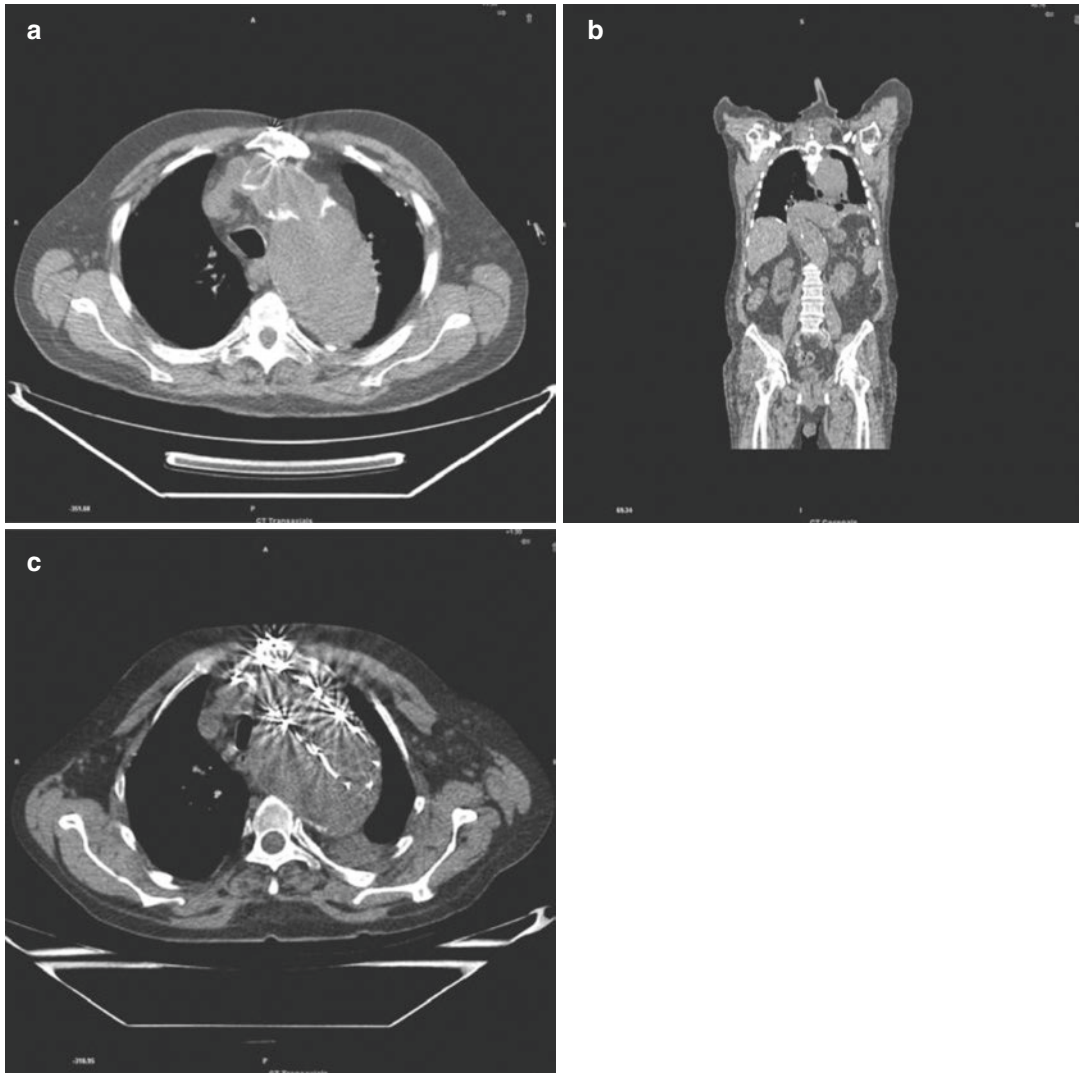

Fig. 3.109 (**a**–**c**) Patient affected by chronic aneurysmatic dissection of the thoracic aorta

Thoracic Artery Aneurysm

It is defined as a permanent abnormal dilatation of the thoracic aorta. The aortic diameter increases slightly with age; however the normal diameter of the mid-ascending aorta should always be less than 4 cm, and that of the descending aorta no more than 3 cm.

True aneurysms contain all three layers of the aortic wall (intima, media, and adventitia); on the contrary, false aneurysms have less than three layers and are contained by the adventitia or peri-adventitial tissues.

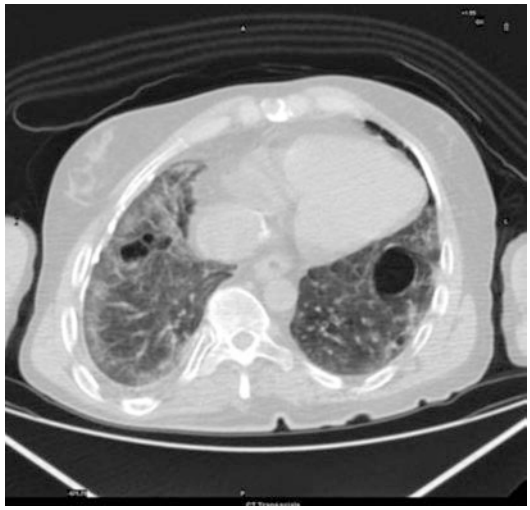

Fig. 3.110 Diffuse ground glass in the inferior lobes, more prominent in the right side, in keeping with interstitial lung disease with fibrotic evolution. Severe centrolobular and paraseptal emphysema with emphysematous bulla without focal active parenchymal lesions

Lung Fibrosis

Pulmonary fibrosis is the formation or development of excess fibrous connective tissue (fibrosis) in the lungs. It involves gradual exchange of normal lung parenchyma with fibrotic tissue. The replacement of normal lung with scar tissue causes irreversible decrease in oxygen diffusion capacity.

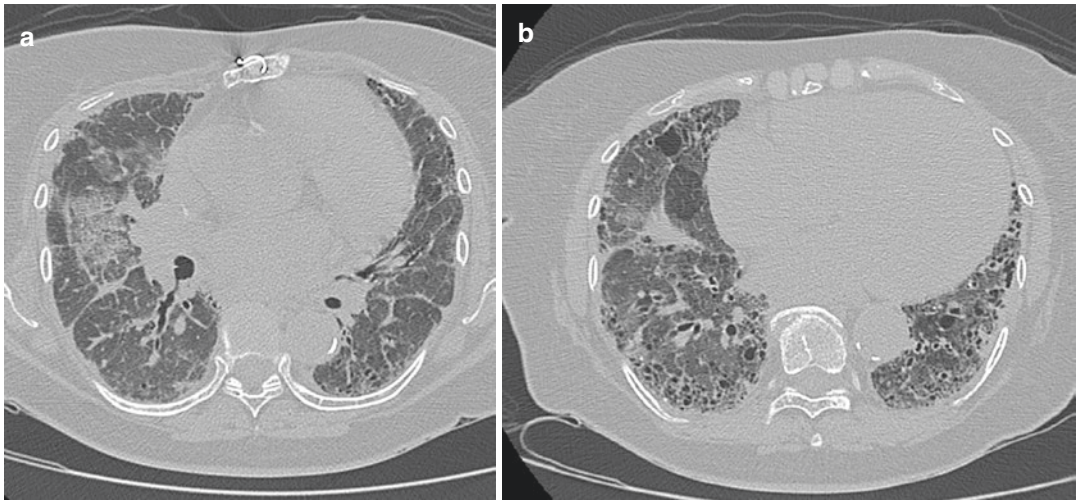

Fig. 3.111 (**a**, **b**) Axial CT images showing diffuse ground glass in the inferior lobes, more prominent in the right side, in keeping with interstitial lung disease with fibrotic evolution. Severe centro-lobular and para-septal emphysema with emphysematous bulla without focal active parenchymal lesions

Abdomen

4

Cristina Nanni, Stefano Fanti, Lucia Zanoni, Rita Golfieri, Cristina Mosconi, Anna Parmeggiani, and Nicolò Brandi

C. Nanni (✉) · S. Fanti · L. Zanoni
Department of Nuclear Medicine, IRCCS Azienda Ospedaliera-Universitaria di Bologna, Bologna, Italy
e-mail: cristina.nanni@aosp.bo.it; stefano.fanti@aosp.bo.it; lucia.zanoni@aosp.bo.it

R. Golfieri · C. Mosconi
Department of Radiology, IRCCS Azienda Ospedaliera-Universitaria di Bologna, Bologna, Italy
e-mail: rita.golfieri@unibo.it; cristina.mosconi@aosp.bo.it

A. Parmeggiani · N. Brandi
University of Bologna, Bologna, Italy
e-mail: anna.parmeggiani2@studio.unibo.it; nicolo.brandi@studio.unibo.it

C. Nanni et al. (eds.), *Radiology for PET/CT Reporting*,
https://doi.org/10.1007/978-3-030-87641-8_4

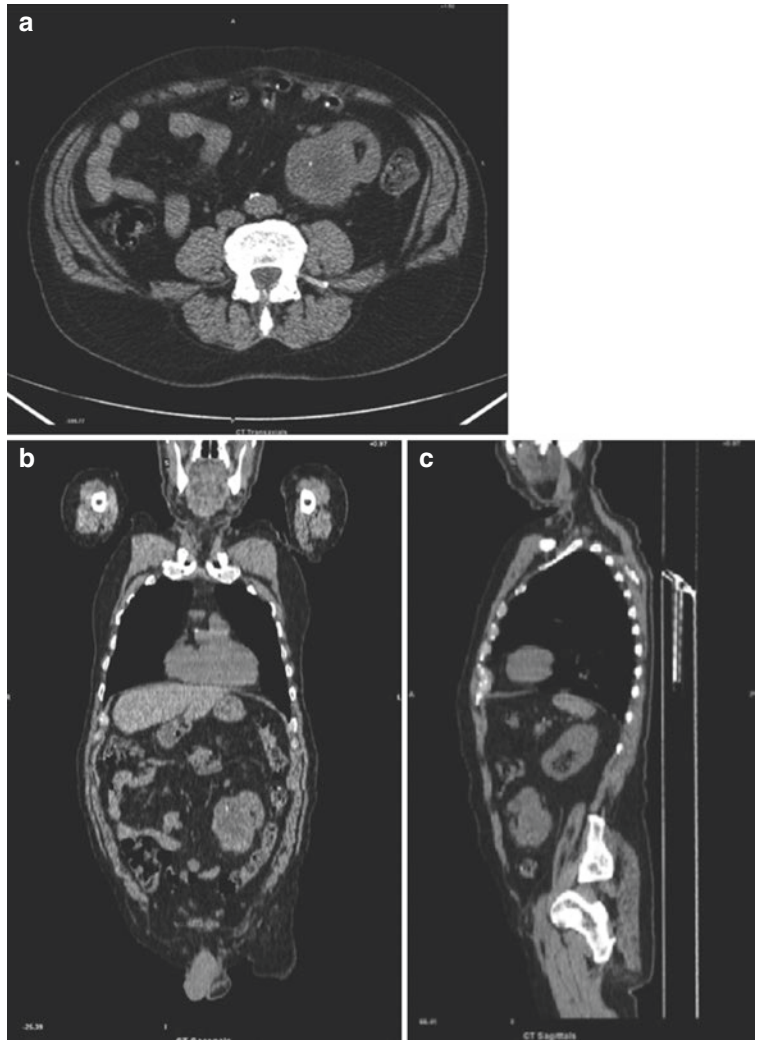

Fig. 4.1 (**a**–**c**) Ectopic right kidney in the left iliac fossa

Renal Ectopia or Ectopic Kidney

An ectopic kidney is a birth defect in which a kidney is located below, above, or on the opposite side of its usual position. It has an incidence of approximately 1/1000. Factors that may lead to an ectopic kidney include poor development of a kidney bud; a defect in the kidney tissue responsible for prompting the kidney to move to its usual position; genetic abnormalities; the mother being sick or being exposed to an agent, such as a drug or chemical, that causes birth defects. An ectopic kidney may not cause any symptoms and may function normally, even though it is not in its usual position. Possible complications of an ectopic kidney include problems with urine drainage from that kidney. Abnormal urine flow and the placement of the ectopic kidney can lead to various problems such as infection, stones, kidney damage, and injury from trauma. No treatment for an ectopic kidney is needed if urinary function is normal and no blockage of the urinary tract is present. Surgery or other treatment may be needed if there is an obstruction, reflux, or extensive damage to the kidney.

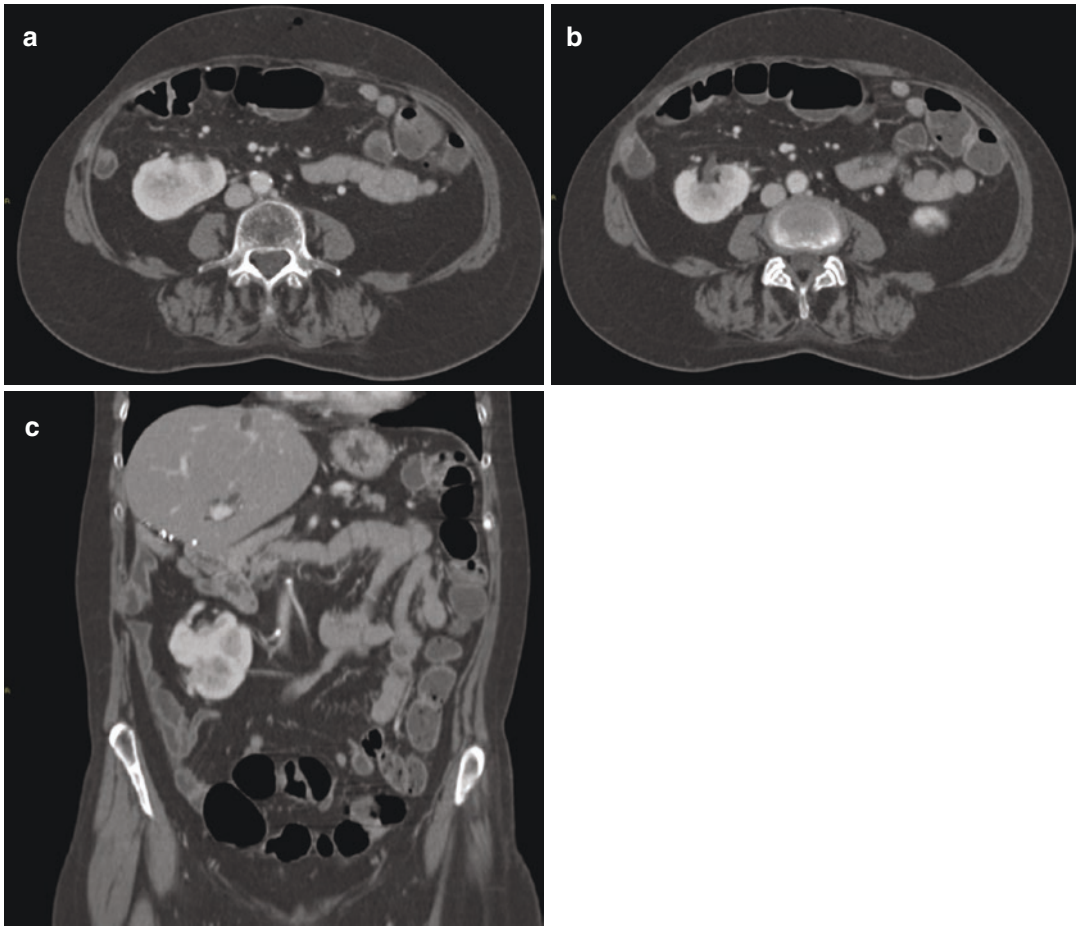

Fig. 4.2 Axial (**a**, **b**) and coronal (**c**) CT images showing ectopic right kidney in the right iliac fossa

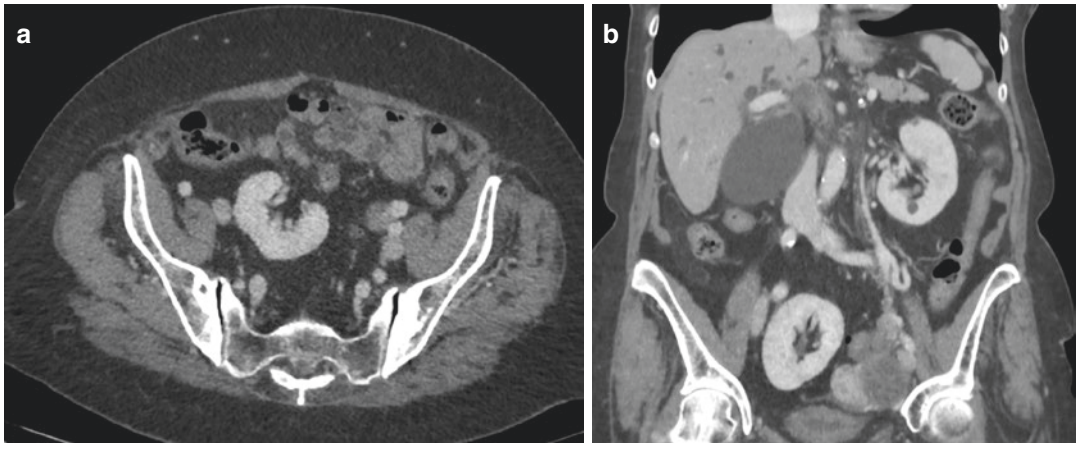

Fig. 4.3 Axial (**a**) and coronal (**b**) CT images showing ectopic right kidney in the right iliac fossa

Fig. 4.4 Stone in the left renal pelvis

Fig. 4.5 Axial CT image showing stone in the left renal pelvis

Renal Stone

Renal stones are dense and attenuate strongly. For stones greater than 3 mm, non-contrast CT examinations have a reported sensitivity and specificity of 97–100%. Both radiolucent and radiopaque stones can be identified. By utilizing computerized mapping techniques, uric acid stones with relatively low-attenuation values can be differentiated from struvite and calcium oxalate calculus stones. On the contrary, CT is unable to identify very rare pure matrix stones of mucoprotein and fibrin and Crixivan stones. It is not possible to provide direct physiologic information of the degree of obstruction in patients with kidney stone.

Polycystic Kidneys

Polycystic kidney disease (PKD) is a genetic disorder characterized by the growth of numerous cysts in the kidneys. There are inherited forms of PKD: the most common *autosomal dominant and* the rare *autosomal recessive PKD*. In CT examinations we find extensive cyst in both kidneys, with a few cysts in the liver as well (in about 40% of patients).

Bosniak Classification of Renal Cysts

The lesions in the renal parenchyma are usually divided into simple benign renal cysts and complex renal cysts. This classification is based on morphologic and enhancement characteristics with CT scanning. Category I: Benign simple cyst with a thin wall without septa, calcifications, or solid components with density of water. Category II: Benign cystic lesions in which there may be a few thin septa; the wall or septa may contain fine calcification or a short segment of slightly thickened calcification. This category also includes uniformly high attenuating lesions that are less than 3 cm in diameter, well marginated. Category IIF: These cysts, generally well marginated, may have multiple thin septa or minimal smooth thickening of the septa or wall, which may contain calcification that may also be thick and nodular. It also includes totally intrarenal high attenuating lesions that are more than 3 cm in diameter. Follow-up is requested to ascertain that they are nonmalignant. Measurable enhancement can be present in both category III and IV; therefore, ceCT would be necessary for differentiation. Category III: These are indeterminate cystic masses that have thickened irregular or smooth walls or septa. Approximately 40–60% are malignant (cystic renal cell carcinoma and multiloculated cystic renal cell carcinoma). On the contrary, hemorrhagic cysts, chronic infected cysts, and multiloculated cystic nephroma are benign. Category IV: These lesions (85–100% are malignant) have all the characteristics of category III cysts; in addition they contain enhancing soft-tissue components that are adjacent to and independent of the wall or septum.

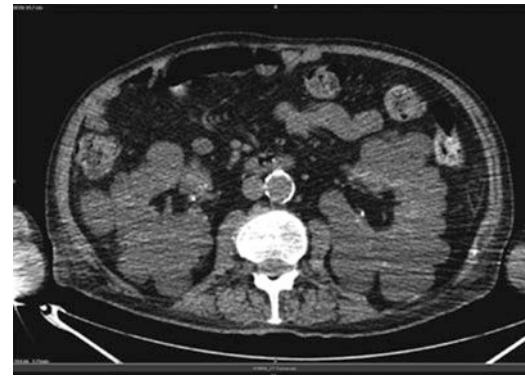

Fig. 4.6 Multiple cysts in the kidneys

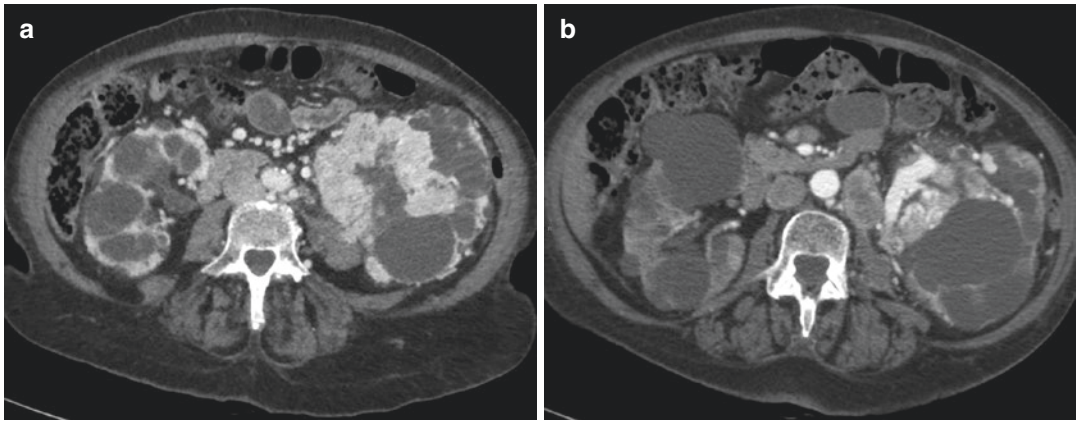

Fig. 4.7 Axial CT scan images acquired in arterial (**a**) and venous (**b**) phase of a patient with polycystic kidney disease, showing multiple cysts in the kidneys

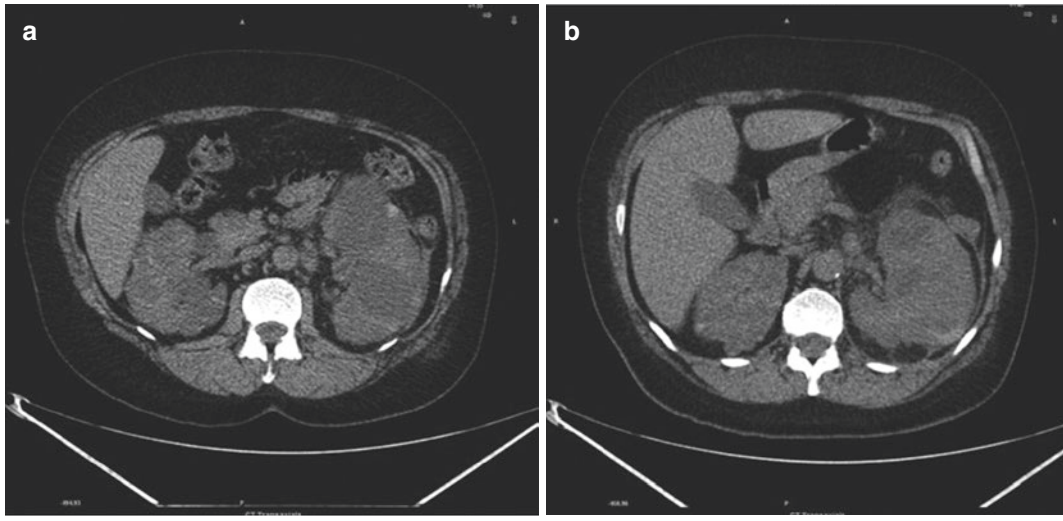

Fig. 4.8 (**a**, **b**) Polycystic kidney and left kidney inflammation

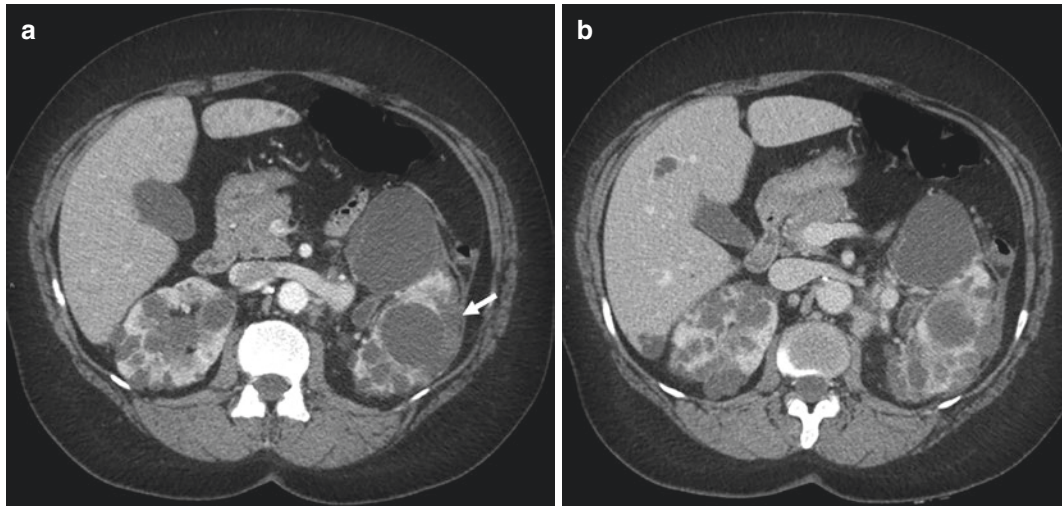

Fig. 4.9 Axial CT scan images (**a**, **b**) acquired in venous phase showing kidney policystosis complicated by left kidney infection, presenting as an area of reduced enhancement in the renal cortex (white arrow)

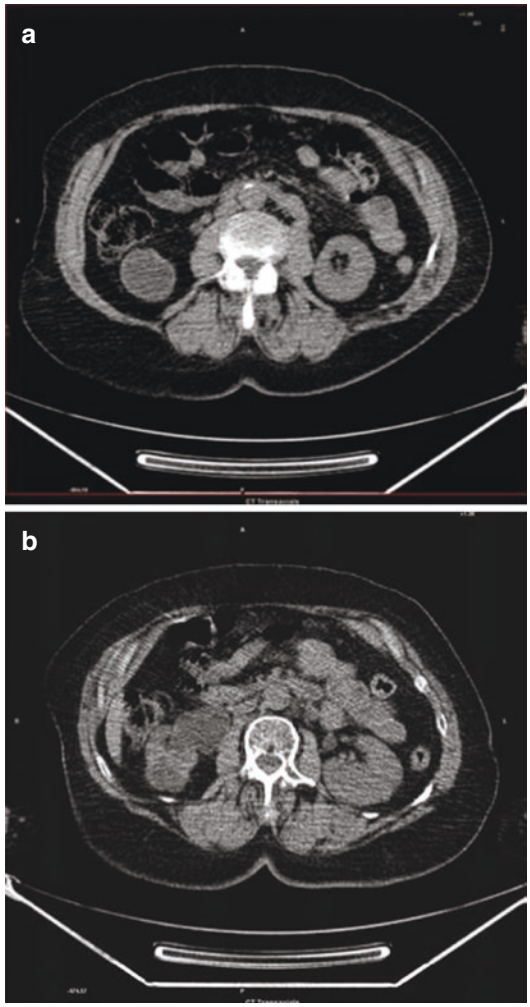

Fig. 4.10 (**a**, **b**) Hypo-attenuated mass in the right kidney

Renal Cancer

Kidney cancer originates in the kidney in two principal locations: most cancers in the renal tubule are renal cell carcinoma and clear cell adenocarcinoma; on the contrary, most cancers in the renal pelvis are transitional cell carcinoma. The primary limitation of CT is the characterization of hypo-attenuation in masses smaller than 8–10 mm. On initial non-enhanced CT scans, RCCs may appear as iso-attenuating, hypo-attenuating, or hyper-attenuating relative to the remainder of the kidney. Amorphous and internal calcification (less often rim like calcifications) may be present. It may also appear as a completely solid nodule.

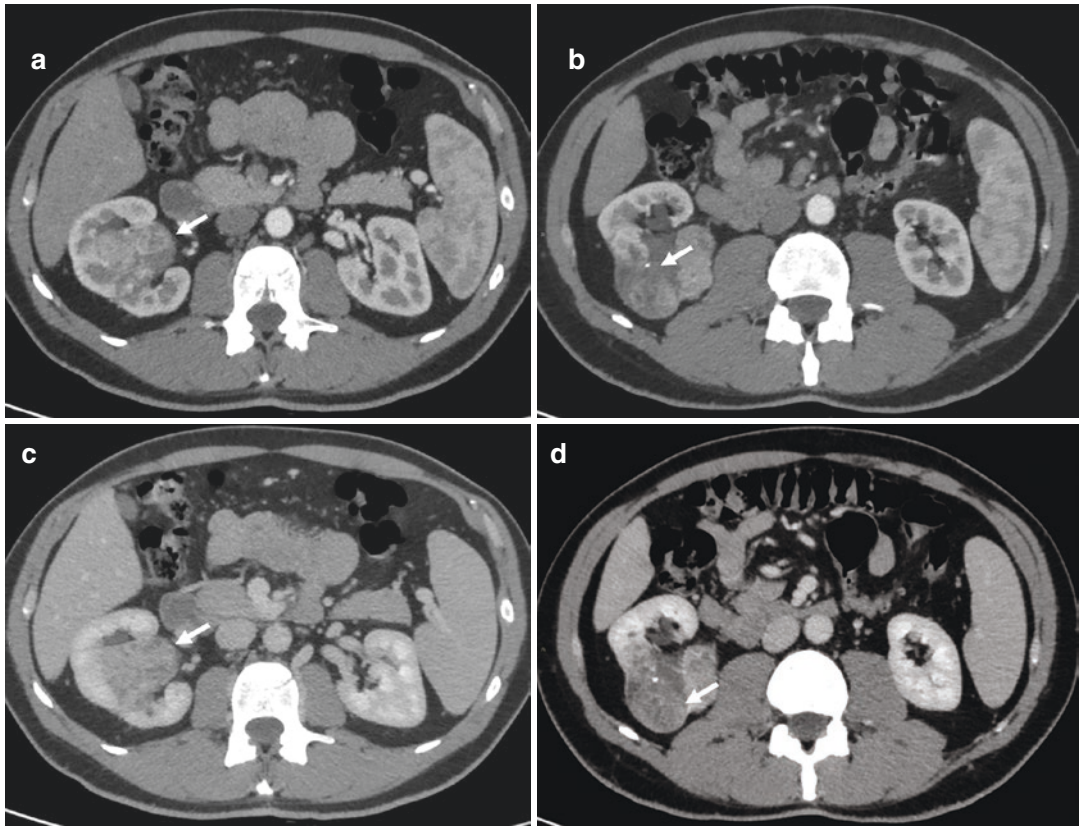

Fig. 4.11 Axial CT scan images both acquired in arterial phase (**a**, **b**) and venous phase (**c**, **d**) showing a renal cancer of the right kidney, characterized by irregular enhancement due to areas of necrosis (white arrows)

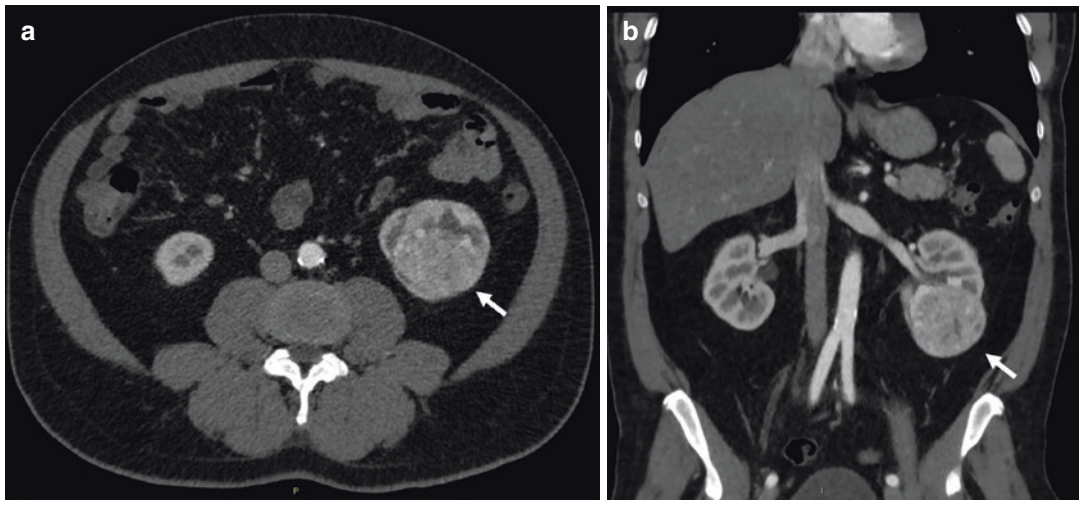

Fig. 4.12 Axial (**a**) and Coronal (**b**) CT scan images both acquired in arterial phase showing a renal cancer of the left kidney, characterized by irregular enhancement due to areas of necrosis (white arrows)

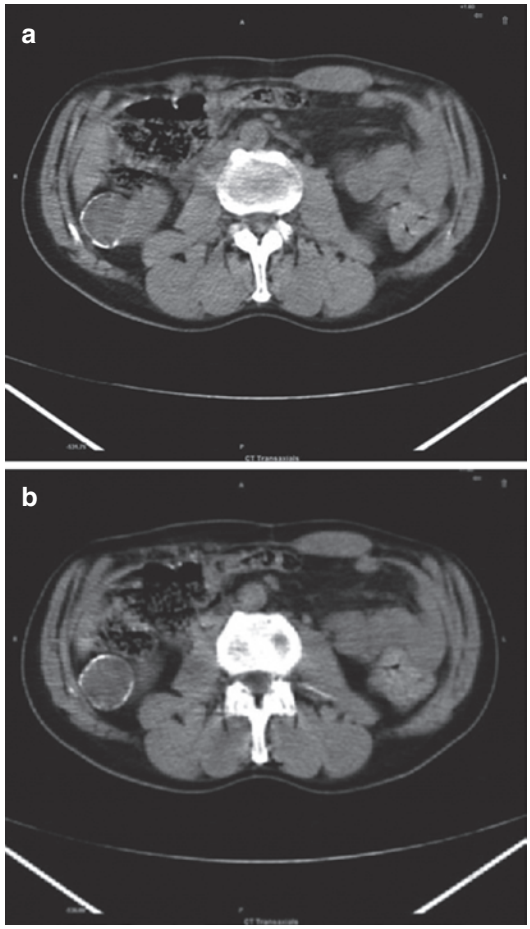

Fig. 4.13 (**a**, **b**) Homogeneous hypo-attenuated mass in the right kidney with a peripheral well-defined calcified rim

Oncocytoma

The imaging appearance of oncocytomas, which is a benign proximal tubular adenoma, is difficult to distinguish from malignant renal cell carcinoma. They are sharply demarcated lesions, solid cortical mass, often large at presentation. Usually if less than 3 cm they present homogeneous attenuation, if more than 3 cm heterogeneous attenuation. Perinephric fat stranding due to edema and calcifications may be present.

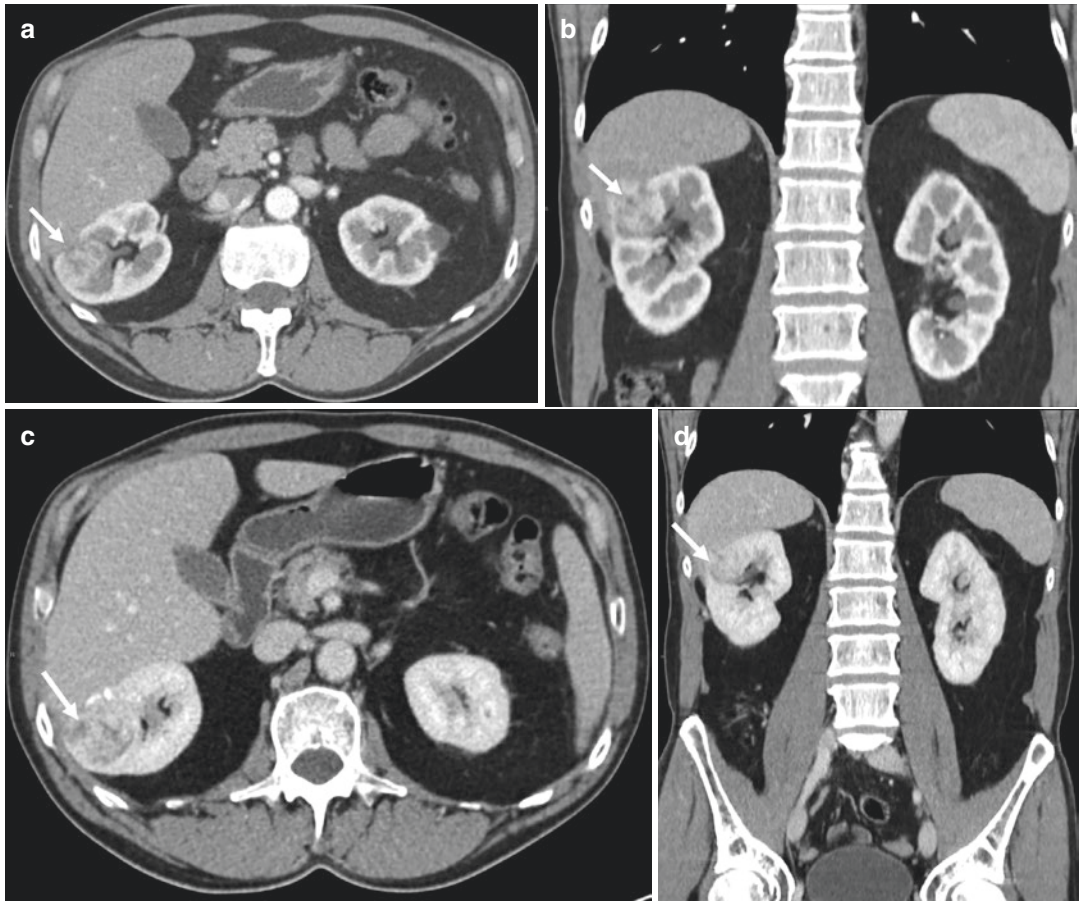

Fig. 4.14 Axial and Coronal CT scan images both acquired in arterial phase (**a**, **b**) and venous phase (**c**, **d**) showing a right-kidney oncocytoma (white arrows). Small oncocytomas may enhance homogeneously, but usually enhancement is heterogeneous and the mass is larger. A central stellate non-enhancing scar is seen in approximately a third of cases

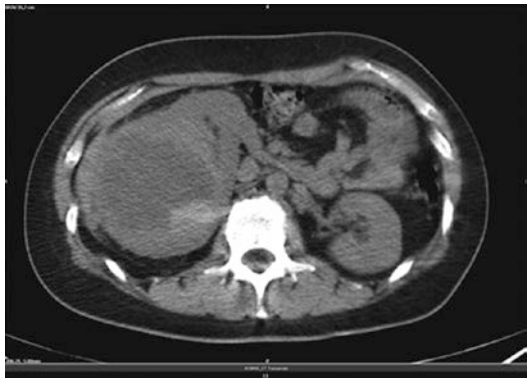

Fig. 4.15 Voluminous mass in the right enlarged kidney with inhomogeneous attenuation and central necrotic changes

Lymphoma of the Kidney

Typical patterns of renal lymphoma include multiple renal masses, solitary masses, diffuse infiltration, and invasion from contiguous retro-peritoneal disease. Atypical CT patterns may also be encountered and provide a diagnostic challenge. These include spontaneous hemorrhage, necrosis, heterogeneous attenuation, cystic transformation, and calcification.

CT accurately depicts renal involvement in most patients; it can also define the extrarenal extent of disease and provide comprehensive staging information. CT allows evaluation of the surrounding anatomic structures, including the perirenal space and retroperitoneum, which are commonly involved by lymphoma. Lesions can be solitary masses (10–20%) or multiple masses (60%). They are generally bilateral and present extension by contiguity (25–30%), diffuse infiltration (20%), or perirenal involvement (10%). Radiological findings frequently indicate renal involvement with multiple nodules (60%).

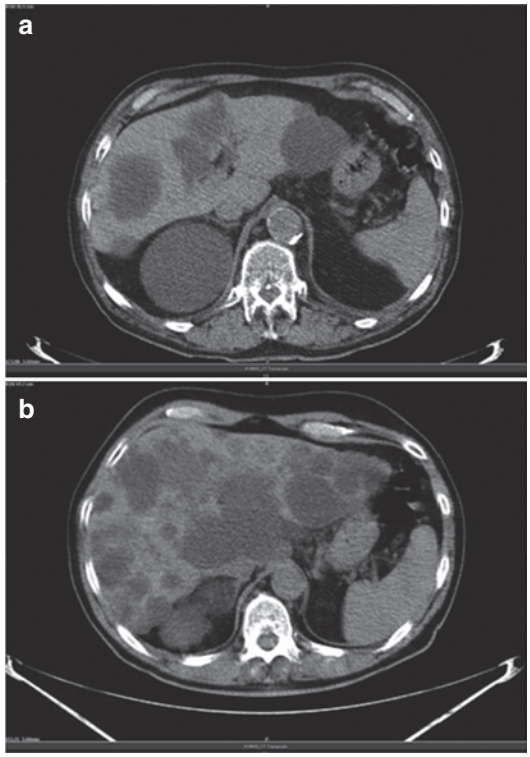

Fig. 4.16 (**a**, **b**) Multiple hepatic cysts

Fig. 4.17 Axial CT scan image acquired in venous phase showing multiple hepatic cysts

Hepatic Cysts

Hepatic cysts are divided in two categories: simple cysts—benign hepatic cyst, biliary hamartoma, Caroli disease, and autosomal polycystic liver disease—and complex cystic liver lesions. The features of this category are wall thickening or irregularity, septation, internal nodularity, enhancement, calcification, and hemorrhagic or proteinaceous contents. They may be further grouped as neoplastic, inflammatory, or infectious, and other miscellaneous entities.

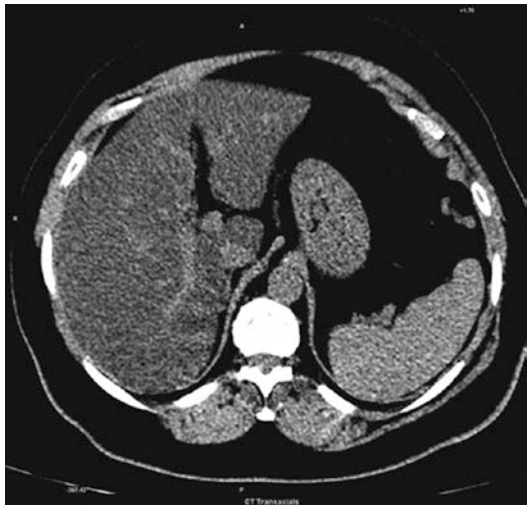

Fig. 4.18 Diffuse fat infiltration in the liver which shows evident lower attenuation than normal spleen

Non-alcoholic Fatty Liver Disease (NAFLD)

NAFLD is deposition of fat in the liver of a non-alcoholic subject, a condition which may progress to end-stage liver disease. Pathological changes are as follows:

1. Only fat deposition
2. Fat deposition + inflammation
3. Type I + advanced inflammation and ballooning degeneration
4. Type I + fibrosis and/or Mallory bodies and cirrhotic changes

CT scan findings in NAFLD are focal areas of fatty infiltration, with mean HU in liver less than that in spleen helps in diagnosis.

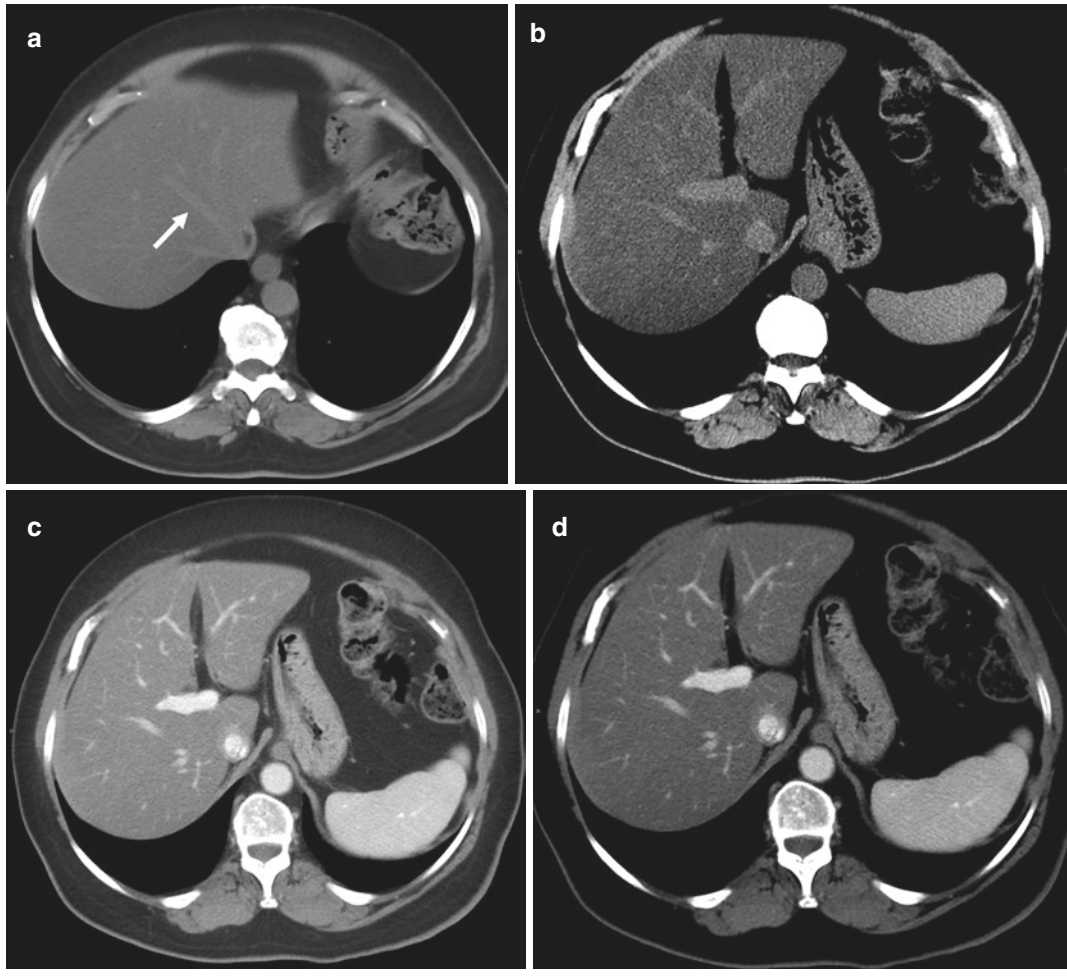

Fig. 4.19 Axial non-contrast CT scan images with abdomen (**a**) and liver (**b**) window showing diffuse fat infiltration in the liver. Even if contrast media hasn't been administred yet, sovrahepatic veins (white arrow) appear iper-attenuating compared to the adjacent liver parenchyma. Axial CT scan images acquired in venous phase with abdomen (**c**) and liver (**d**) window showing diffuse fat infiltration in the liver, with lower attenuation as compared to normal spleen

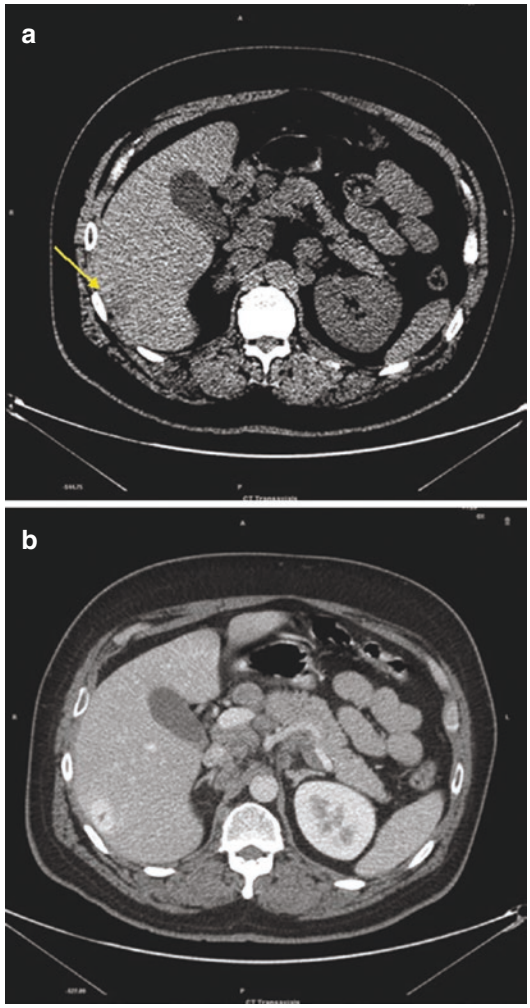

Fig. 4.20 Nodular area in the liver measuring 29 × 19 mm in keeping with FNH: slightly hypodense on low-dose CT (arrow) (**a**); hyperdense with central focal hypo density on both venous and late phase of diagnostic CT (**b**)

Focal Nodular Hyperplasia (FNH)

Focal nodular hyperplasia (FNH) is the second most common tumor of the liver, immediately after hepatic hemangioma. FNH is believed to occur as a result of a localized hepatocyte response to an underlying congenital arteriovenous malformation. It is a hyperplastic process in which all the normal liver constituents are present but in an abnormally organized pattern, with liver function tests usually within normal range. Central scar can be present. FNH is a benign-appearing homogeneous mass with attenuation similar to that of normal liver on non-enhanced scans; however, it enhances brightly and homogeneously on HAP scans. Lesions larger than 3 cm in diameter usually present with a thin central scar. All FNH lesions usually have a smooth though ill-defined margin and are typically subcapsular.

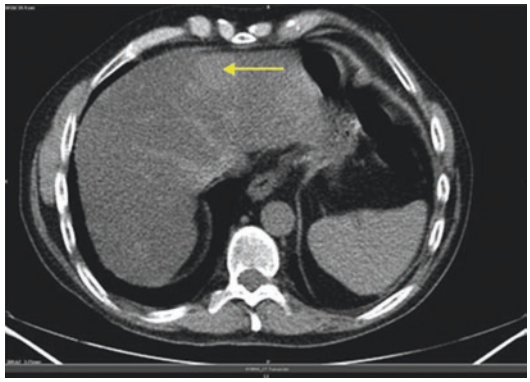

Fig. 4.21 Nodular area in the fourth segment of the liver showing density similar to that of intrahepatic vessels (arrow)

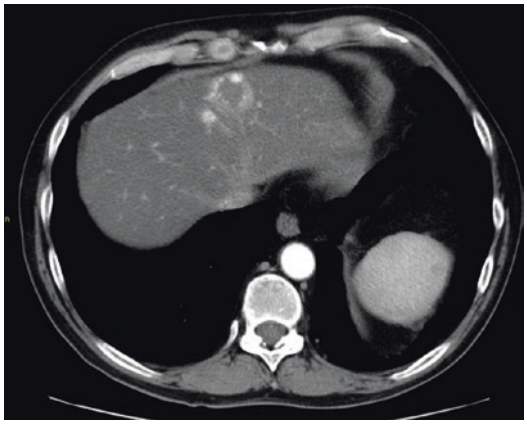

Fig. 4.22 Axial CT image nodular area in the fourth segment of the liver showing hypo-attenuation similar to that of vessels

Hepatic Hemangioma

Hemangioma is the most common benign tumor of the liver. The classic diagnostic findings for hemangioma on unenhanced CT are hypo-attenuation similar to that of vessels. In three-phase ceCT, a typical peripheral fill-in is usually observed.

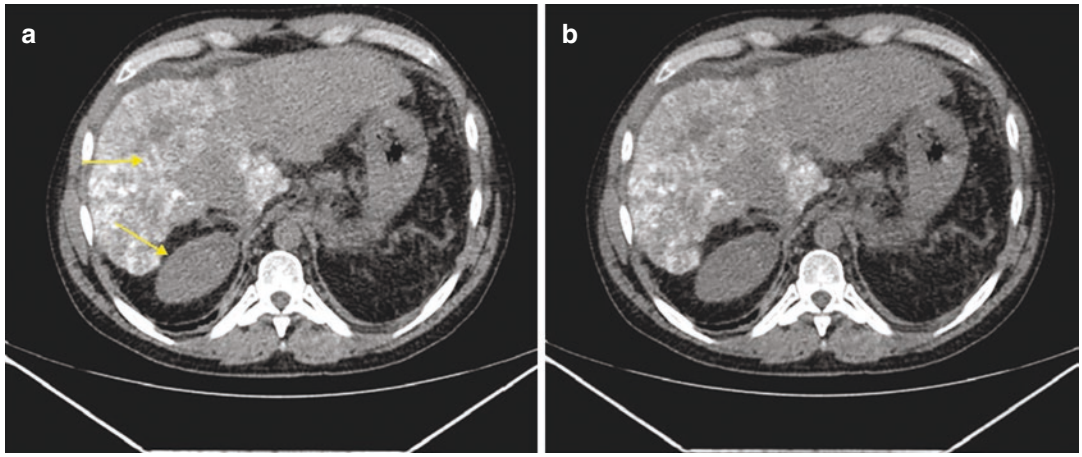

Fig. 4.23 Multiple hyperdense liver nodules (**a**, arrows) more evident after lipiodol administration (**b**)

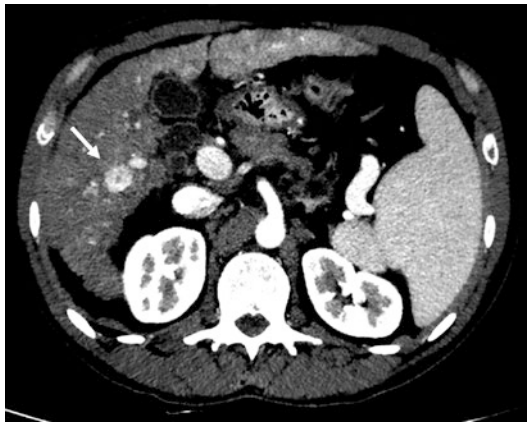

Fig. 4.24 Axial CT image showing a nodular images consistent with HCC, characterized by a wash-in on arterial phase (white arrow)

Metastatic Hepatocarcinoma

Hepatocellular carcinoma (HCC) is the fifth most common tumor in the world. Risk factors for HCC include viral hepatitis, alcoholic liver cirrhosis, and exposure to hepatotoxins. Typical unenhanced CT findings are well-circumscribed hypo-attenuated mass compared to normal liver. On the contrary, HCC tends to appear hyperdense to fatty liver. Clinical complications that need to be excluded are hemorrhage, vascular occlusion (difficult detection with unenhanced CT), and metastatic spread. Two thirds of the metastases are indeed in bones and lungs.

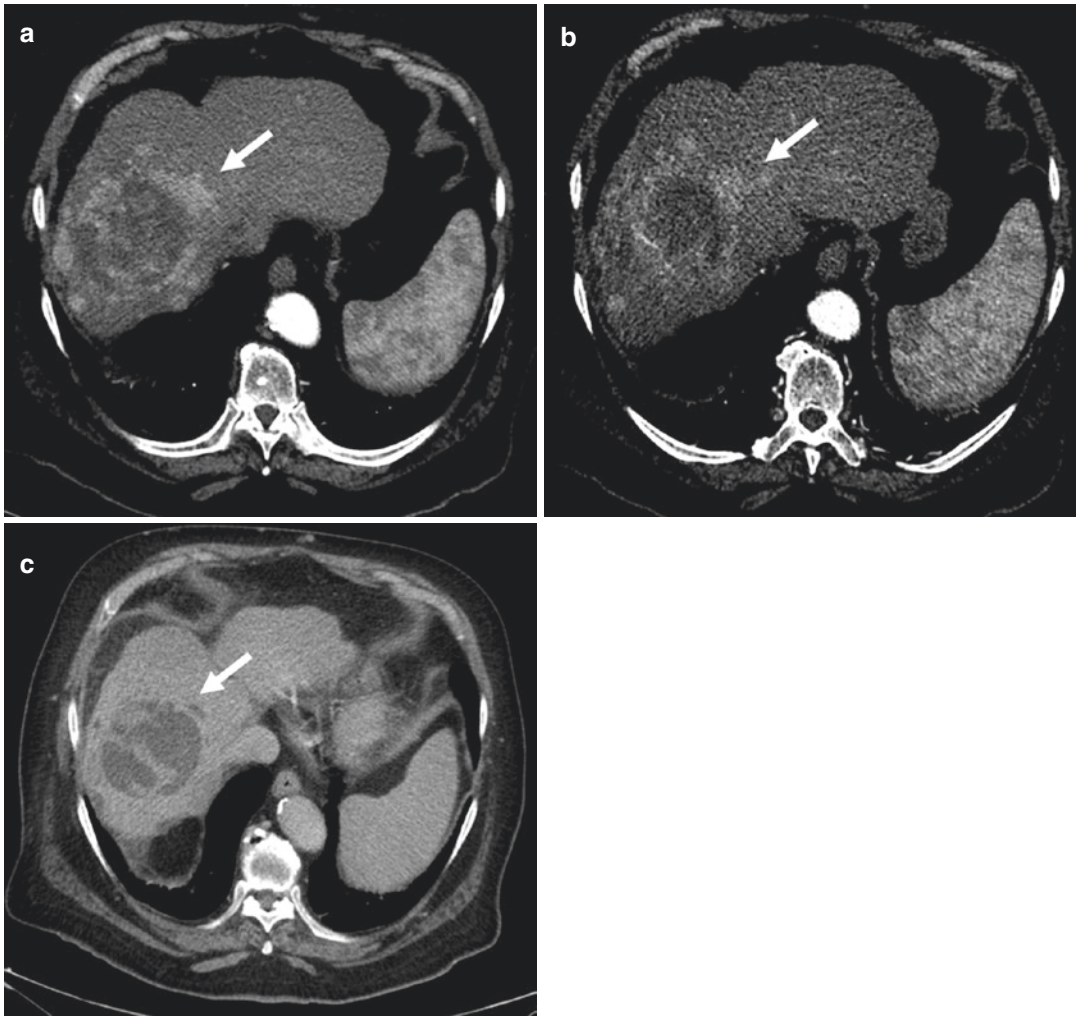

Fig. 4.25 Axial CT images showing a nodular images compatible with HCC, characterized by a wash-in on arterial phase (**a**) and a progressive wash-out in venous (**b**) and late phase (**c**) (white arrow)

Fig. 4.26 Extensive intrahepatic gas

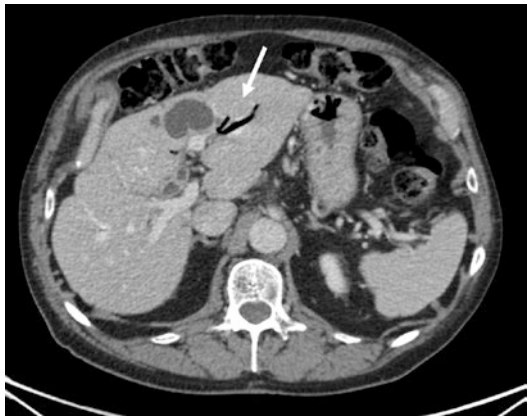

Fig. 4.27 Axial CT image showing an extensive intrahepatic gas (white arrow)

Aerobilia

Accumulation of air in the biliary tree. Noncontrast CT through the upper abdomen demonstrates extensive intrahepatic gas which can be traced down to a dilated common bile duct. Possible causes are recent biliary instrumentation, incompetent sphincter of Oddi, biliary-enteric surgical anastomosis, spontaneous biliary-enteric fistula (cholecystoduodenal accounts for ~70%), infection (rare), and bronchopleural biliary fistula (rare). It is important to distinguish pneumobilia from portal venous gas. Gas within the biliary tree tends to be more central, whereas gas within the portal venous system tends to be peripheral (pushed along by the blood). Also, biliary gas is anti-dependent and typically fills the left lobe of the liver.

Fig. 4.28 Presence of perihepatic and perisplenic fluid in a patient affected by cirrhosis

Fig. 4.29 Axial CT image presence of peri hepatic and peri splenic fluid (white arrow)

Ascites

The development of ascites, an accumulation of fluid in the peritoneal cavity, is an important landmark in the natural history of cirrhosis. The majority of patients who present with ascites have underlying cirrhosis, with the remainder being due to malignancy (10%), heart failure (3%), tuberculosis (2%), pancreatitis (1%), and other rare causes. There are two key factors involved in the pathogenesis of ascites formation—namely, sodium and water retention and portal (sinusoidal) hypertension. CT scan can assess ascites volume and relative distribution between the greater peritoneal cavity and the omental bursa, density of the ascites, thickness of the gallbladder wall, thickness of the parietal peritoneum, and tethered-bowel sign (loops are matted into the mesenterium and do not float freely in the ascites).

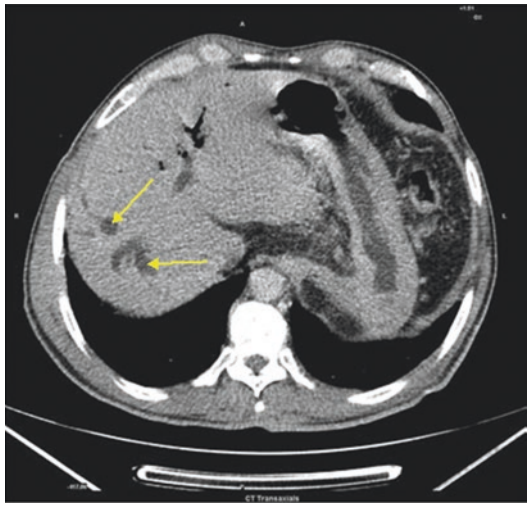

Fig. 4.30 Multiple low-density linear regions in the liver in keeping with intrahepatic biliary dilatation (arrows)

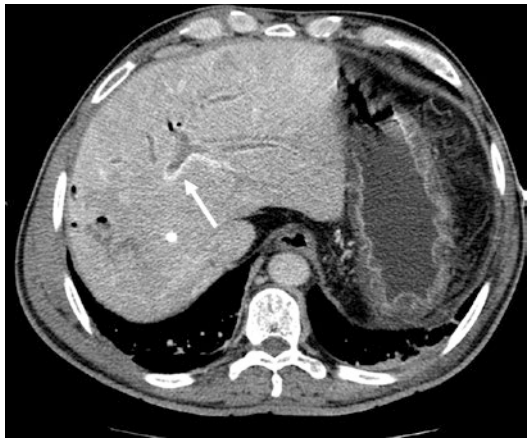

Fig. 4.31 Multiple low-density linear regions in the liver in keeping with intrahepatic biliary dilatation and contrast enhancement of the biliary duct walls (white arrow)

Sclerosing Cholangitis

It is an uncommon idiopathic inflammatory condition which affects the biliary tree resulting in multiple strictures and eventual cirrhosis. The finding of focal, discontinuous areas of minimal intrahepatic biliary dilatation (resulting as multiple linear discontinuous low-density regions on CT) without associated mass lesion appears highly suggestive of sclerosing cholangitis. Moreover the atrophied liver has a lower density than the hypertrophied caudate lobe.

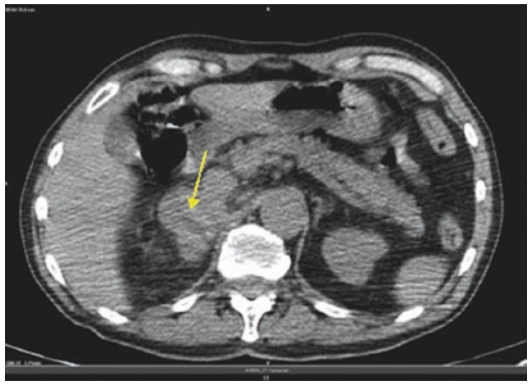

Fig. 4.32 Inhomogeneous and necrotic adrenal lesion (arrow)

Fig. 4.33 Axial CT image showing adrenal lung metastasis with central necrosis and hemorrhage

Lung Cancer Adrenal Metastasis

It appears as focal mass or distortion of the contour of the adrenal gland. Larger lesions may have central necrosis or hemorrhage. These lesions are heterogeneous and may have thick, hyperdense rims. They may also invade contiguous organs, such as the kidneys. They can be detected on CT only if an alteration occurs in the outline, the size, or the internal characteristics of the adrenal gland. However, a normal-appearing gland does not exclude microscopic involvement. The attenuation values of the adrenal glands are more useful than their size for making the diagnosis. Indeed attenuation values of less than 10 HU on unenhanced CT scans are indicative of lipid-containing benign lesions (adrenal adenomas?); however, lipid-poor adrenal adenomas may have attenuation values of more than 10 HU.

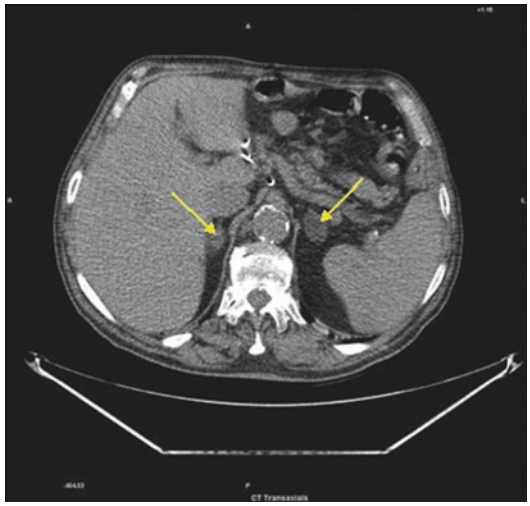

Fig. 4.34 Increased volume of both adrenal glands with nodular appearance (more prominent the left one) and very low HU density (arrows)

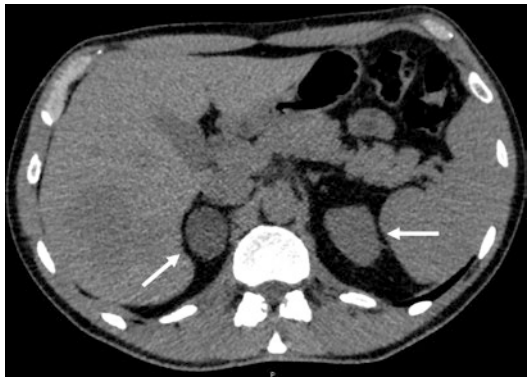

Fig. 4.35 Axial diagnostic CT images increased volume of both adrenal glands with nodular appearance (more prominent the right one) and very low HU density (arrows)

Adrenal Adenoma in Lung Cancer Patient

CT finds a safe threshold value of 10 HU on a native CT scan resulting in a sensitivity of 70% and a high specificity of 98% for the diagnosis of an adenoma. A density equal to or below 10 HU is considered diagnostic of adenoma. Thirty percent of adrenal adenomas do not contain enough intracellular lipid to have a density of less than 10 HU and cannot be differentiated from malignant masses on an unenhanced CT. These adenomas are called lipid poor.

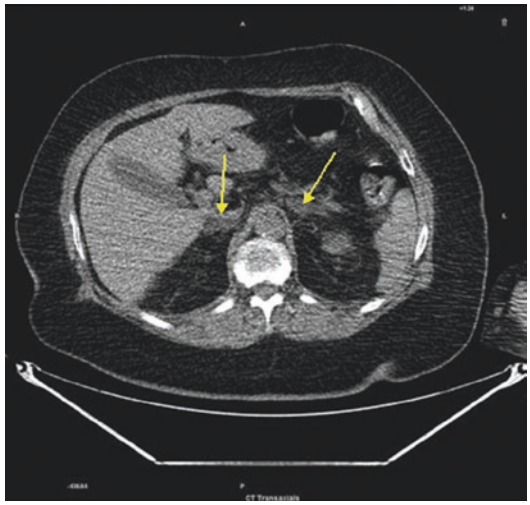

Bilateral Adrenal Hyperplasia

Enlarged limbs of one or both adrenal glands over 10 mm are consistent with hyperplasia. Adrenal shape is maintained. No discrete mass or nodule seen except in cases of Cushings due to macronodular hyperplasia.

Fig. 4.36 Bilateral enlargement of both adrenal glands (arrows)

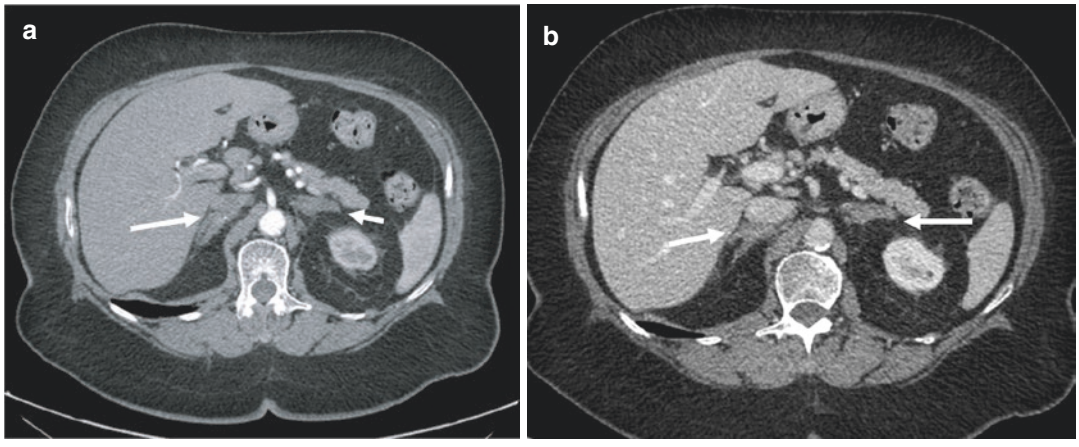

Fig. 4.37 Axial CT images (**a**, **b**) showing bilateral enlargement of both adrenal glands (white arrows)

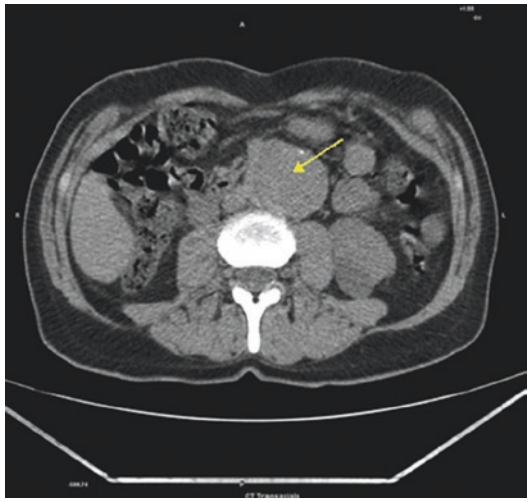

Fig. 4.38 Significant dilatation of the abdominal aorta (arrow)

Abdominal Aortic Aneurysm (AAA)

It refers to a focal dilatation of the abdominal aorta that is 50% greater than the proximal normal segment or that is greater than 3 cm in maximum diameter. CT can assess vertebral erosion or aneurysm rupture. Possible signs are sign of contained rupture (draped aorta sign), high-attenuation (crescent sign), sign of impending rupture, and retro-peritoneal hematoma.

Most abdominal aortic aneurysms are diagnosed during an abdominal imaging test performed for another pathology. When the aneurysm reaches 5 cm in larger diameter or more, or when growing fast, or when symptomatic, the risk of rupture becomes important. In this case an emergent surgical repair is necessary. Endovascular stent graft repair is a minimally invasive procedure to exclude the aneurismal sac, introducing an aortic stent graft inside the diseased aorta. Thus a new circuit for blood flow is created.

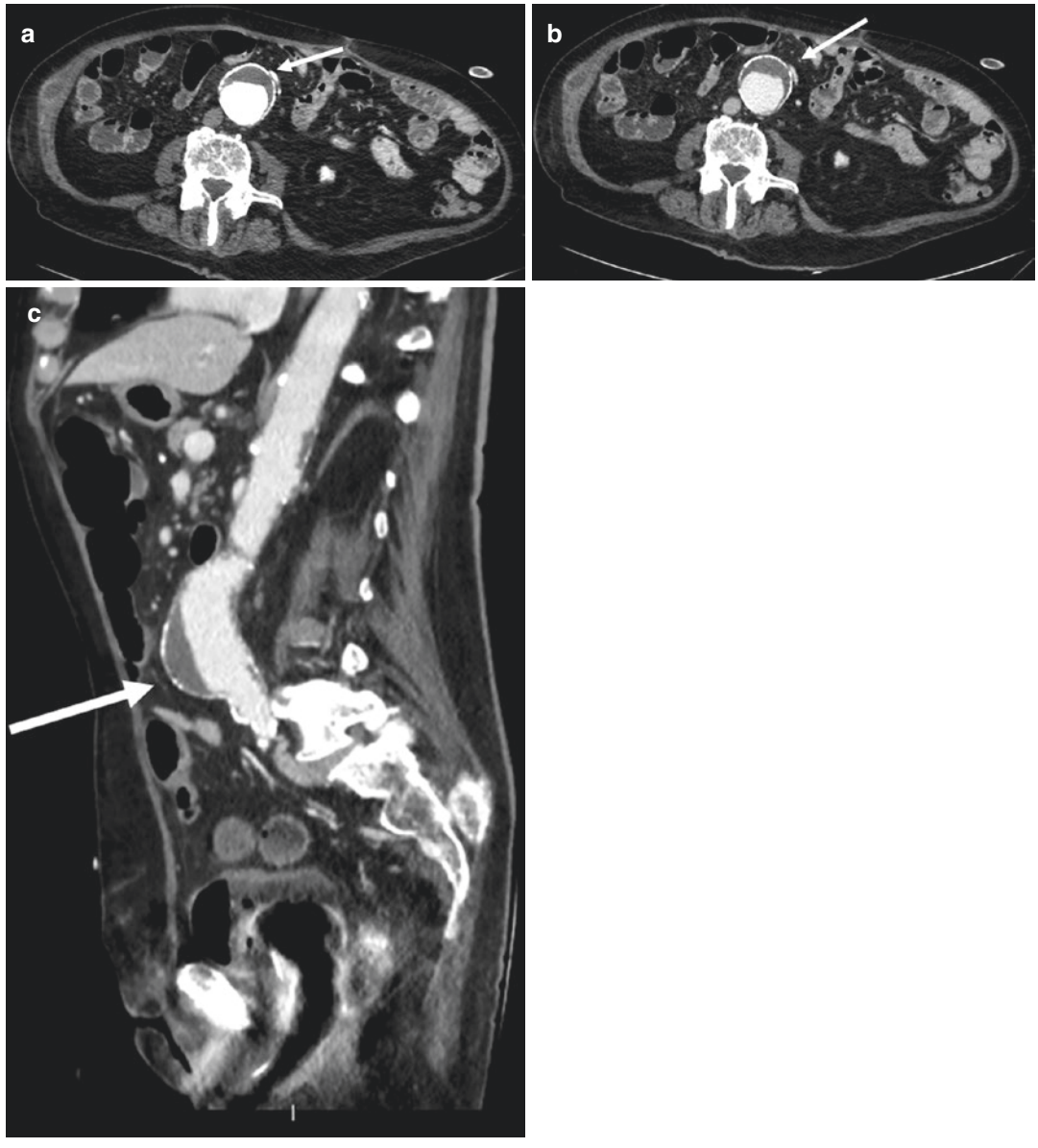

Fig. 4.39 Axial (**a**, **b**) and sagittal (**c**) ceCT images showing a significant dilatation of the abdominal aorta (white arrow)

Fig. 4.40 A cross-section view with the two iliac branches of the graft permeable in the excluded aneurysm

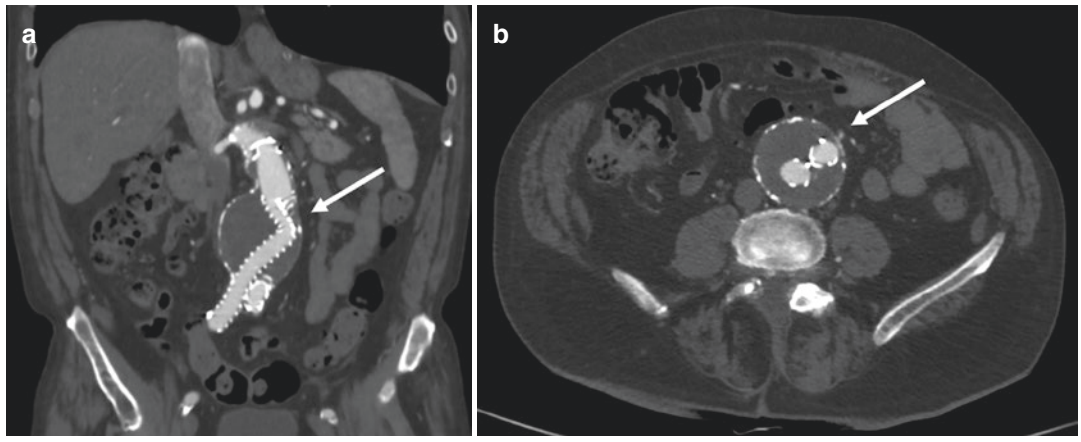

Fig. 4.41 Coronal (**a**) and axial (**b**) CT images showing a cross-section view with the two iliac branches of the graft permeable in the excluded aneurysm (white arrow)

Vascular Calcifications

The left and right common iliac veins come together in the abdomen at the level of the fifth lumbar vertebra, forming the inferior vena cava. They drain blood from the pelvis and lower limbs. The calcium deposit may occur in a thrombus or, more rarely, in the wall of the veins.

Fig. 4.42 Calcified walls of common iliac veins

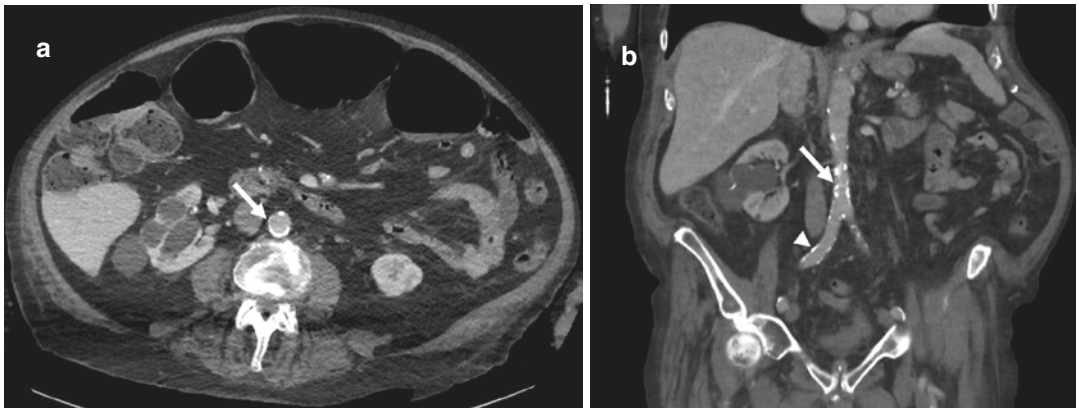

Fig. 4.43 Axial (**a**) and coronal (**b**) CT images showing calcified walls of aorta (white arrows) and common iliac arteries (arrow head)

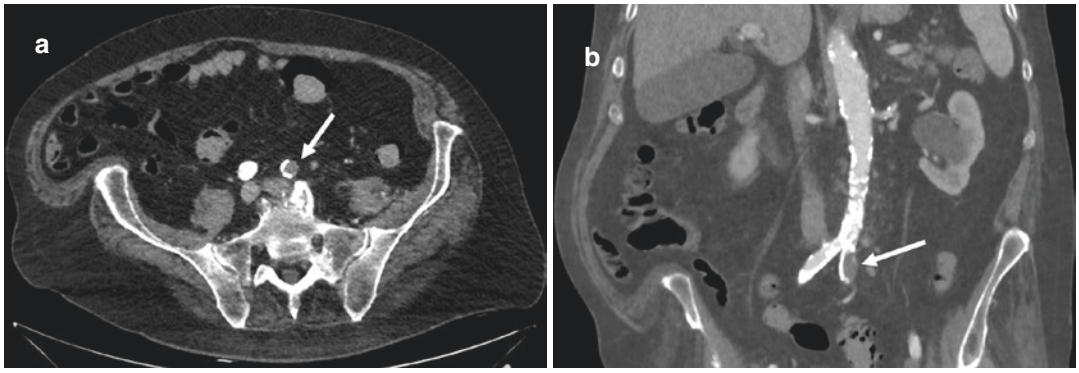

Fig. 4.44 Axial (**a**) and Coronal (**b**) CT post contrast (arterial phase) images of the abdomen showing the complete occlusion of the left iliac artery as a complete endoluminal defect right after the carrefour bifurcation. The vessel is diffusely calcified

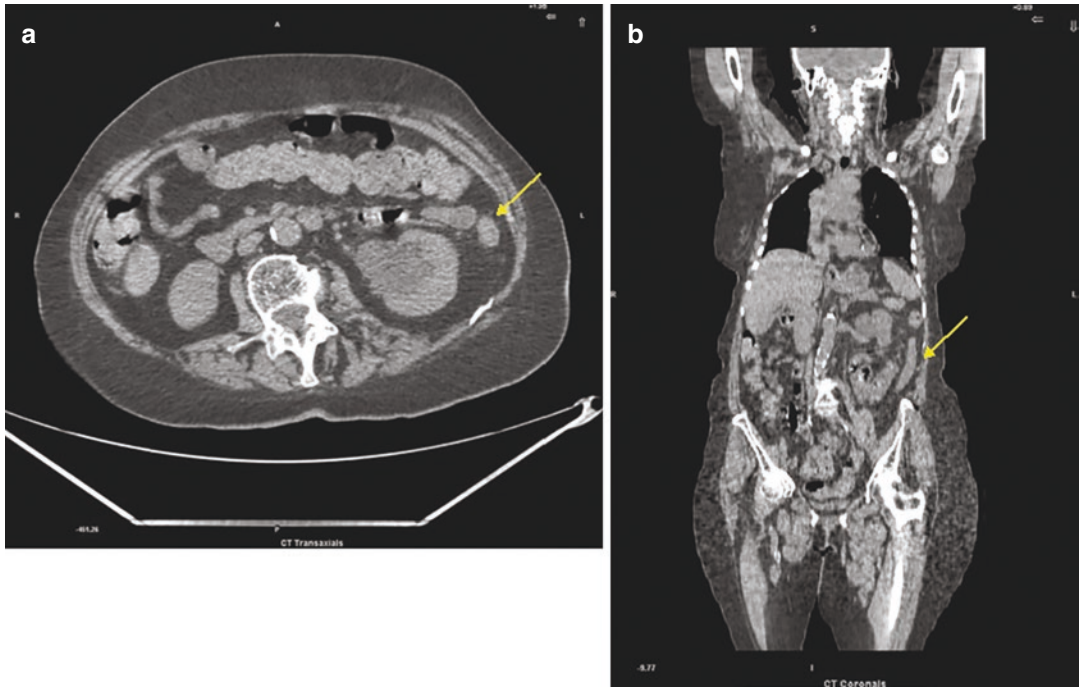

Fig. 4.45 (**a**, **b**) Reduction in the dimension of the trans-axial axes of the colon (arrows)

Corda Coli

Thickening of the walls of the descending colon. Reduction in the dimension of the trans-axial axes compared to the transverse colon. Generally associated with bowel inflammation.

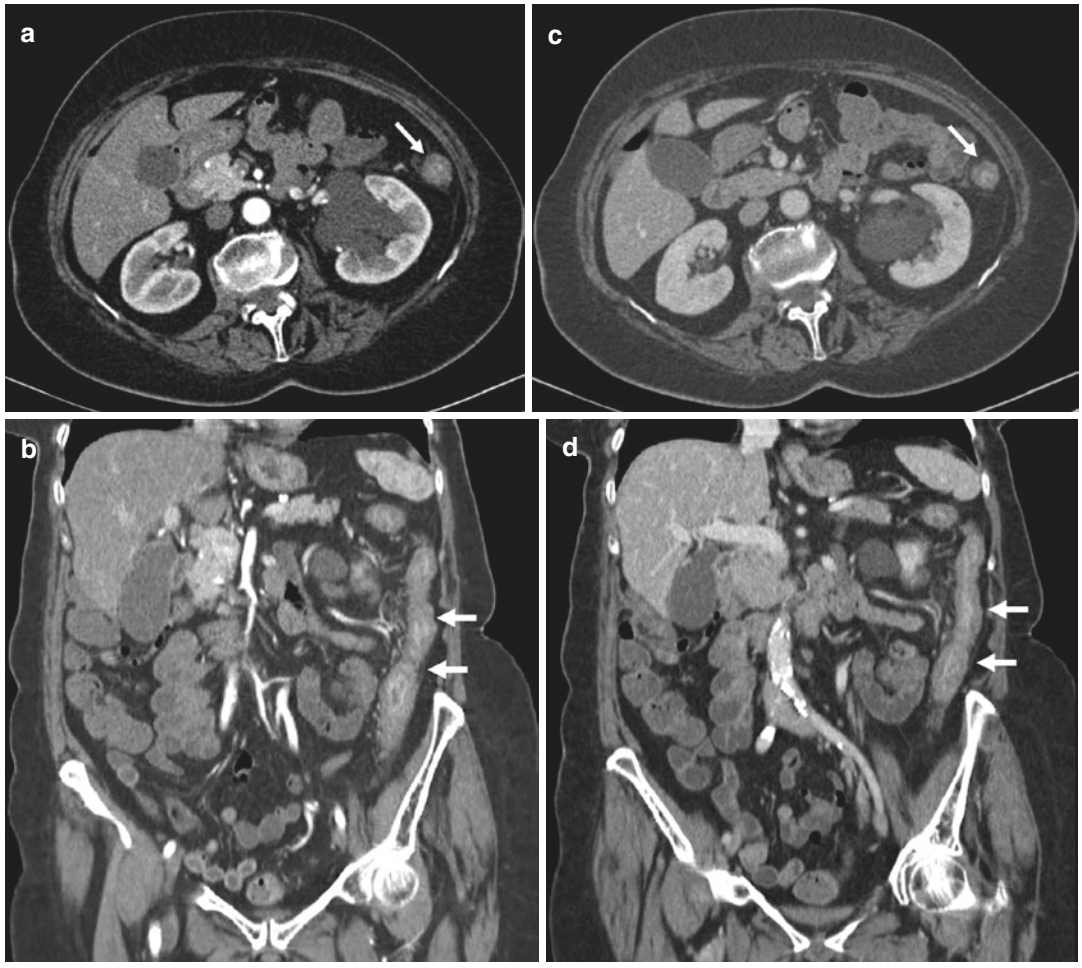

Fig. 4.46 Axial and coronal CT scan images, acquired in arterial phase (**a**, **b**) and venous phase (**c**, **d**), showing reduction in the dimension of the transaxial axes and thickening of the walls of the descending colon (white arrows)

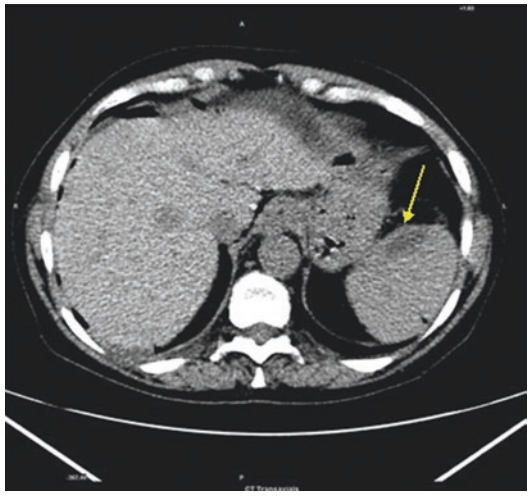

Fig. 4.47 A splenic subcapsular hematoma with low density and closed to the splenic margin (arrow)

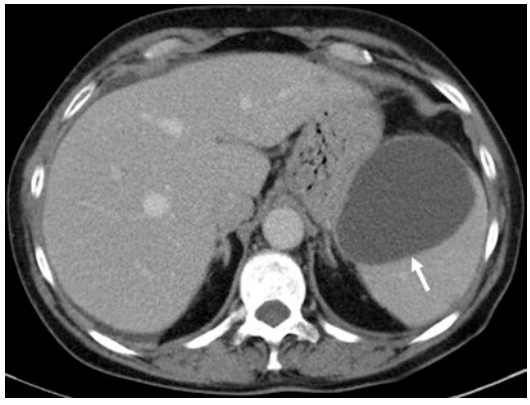

Fig. 4.48 Axial CT scan image acquired in venous phase showing a splenic subcapsular haematoma with low density and closed to the splenic margin (white arrow)

Splenic Hematoma

Subcapsular hematomas are regularly shaped, crescentic, low-density collections closed to the splenic margin. The margins are usually sharp in distinction to a perisplenic clot.

Intrasplenic hematomas are more irregular low-density areas within the spleen. Mass effect and enlargement of the spleen can be detected as well. On non-enhanced images, the hematoma can appear hypo-, iso-, or hyper-attenuating compared with the parenchyma.

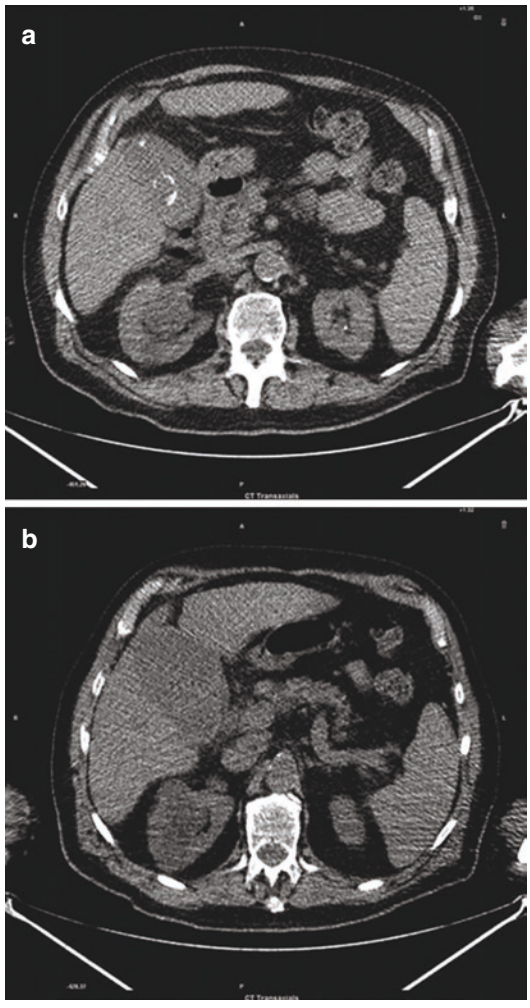

Fig. 4.49 Irregular gallstones within the gallbladder (**a**). Enlargement of the gallbladder without any evident sign of gallstones (**b**)

Cholecystitis

CT scanning may be useful in the diagnosis of cholecystitis by showing various signs: gallstones within the gallbladder (GB), the cystic duct, or both indistinct liver-GB interface; fluid in the GB fossa in the absence of ascites; enlargement of the GB (transverse diameter measuring more than 5 cm); increased bile attenuation by biliary sludge; GB mucosal sloughing; and a halo surrounding the GB, resulting from edema. Features that may be confused with a carcinoma include diffuse or focal thickening of the GB wall (more than 3 mm) in a non-contracted GB and inflammatory infiltrate of the surrounding fat.

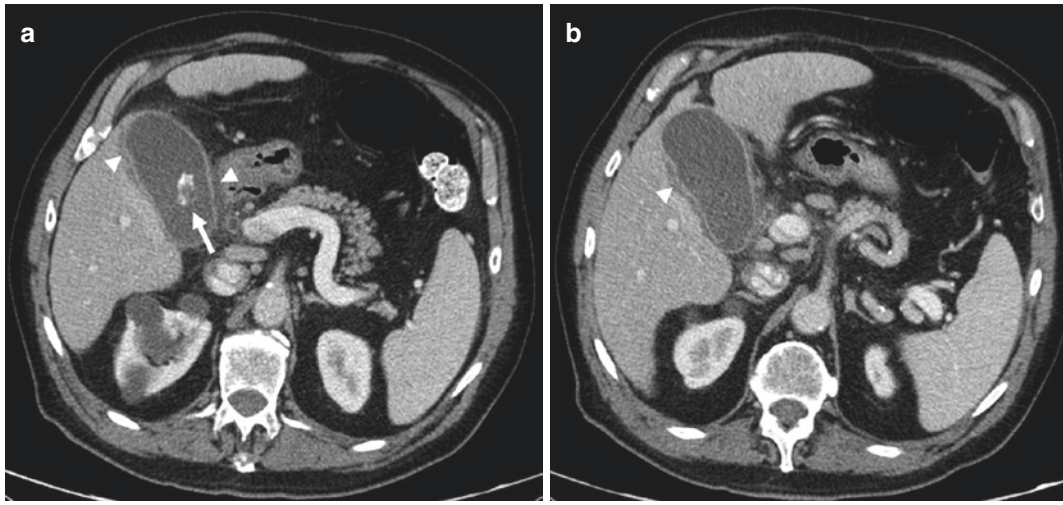

Fig. 4.50 Axial CT scan image acquired in venous phase showing an irregularly-shaped gallstone (white arrow) within the gallbladder (**a**) and an enlargement of the gallbladder without any evident sign of gallstones (**b**). Additional findings are gallbladder wall thickening and a thin layer of pericholecystic fluid (arrow head)

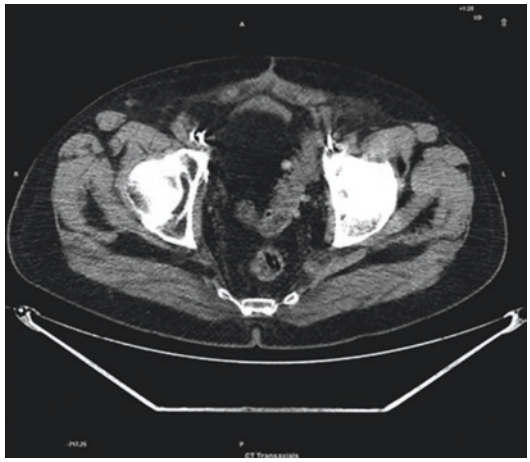

Fig. 4.51 Diverticular disease of the sigmoid

Diverticular Disease

Diverticular disease of the colon begins as diverticulosis with colonic outpouchings, which may develop into diverticulitis in case of diverticular inflammation and perforation. Differentiating one from the other is extremely important since uncomplicated diverticulosis is largely asymptomatic and acute diverticulitis is a potentially life-threatening illness. CT scan shows colic wall protrusions, and it can include pericolic stranding, often disproportionately prominent compared to the amount of bowel wall thickening, segmental thickening of the bowel wall, and enhancement of the colonic wall.

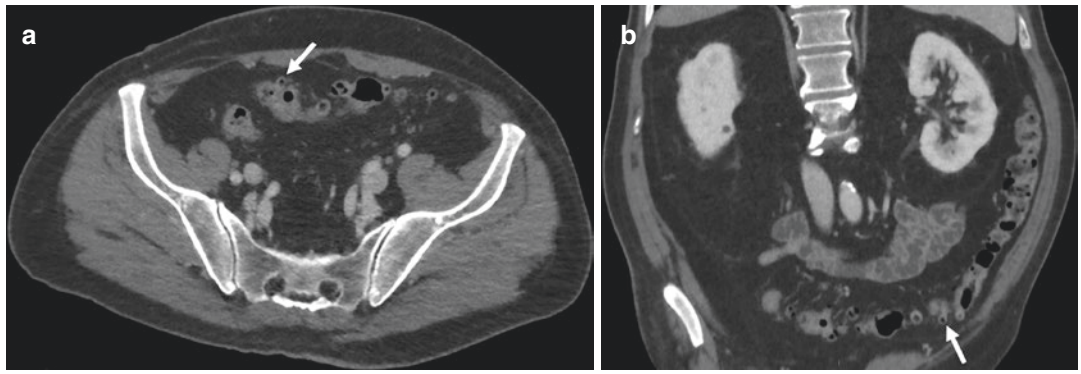

Fig. 4.52 Axial (**a**) and Coronal (**b**) CT scan images acquired in venous phase showing diverticulosis of the sigmoid (**a**) and descending (**b**) colon. Diverticula are usually outlined by gas (white arrow). The colon may be thickened and shortened

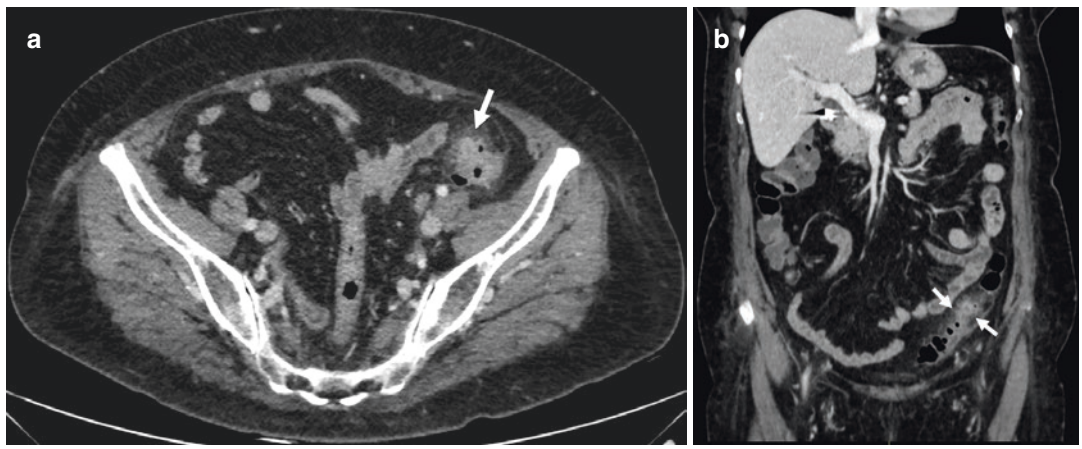

Fig. 4.53 Axial (**a**) and Coronal (**b**) CT scan images acquired in venous phase showing diverticulitis of the sigmoid (**a**) and descending (**b**) colon. The most common findings are pericolic stranding, segmental thickening of bowel wall and enhancement of colonic wall (white arrow)

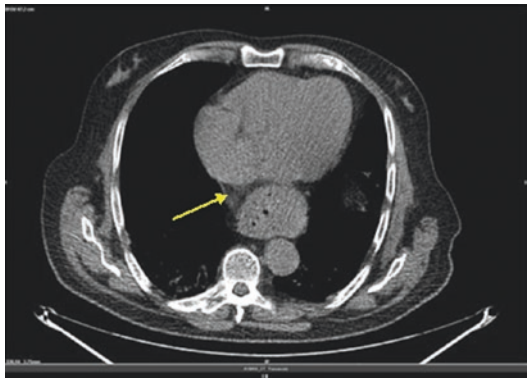

Fig. 4.54 Retrocardiac fat surrounding the lower esophagus with small air areas, compatible with hiatal hernia (arrow)

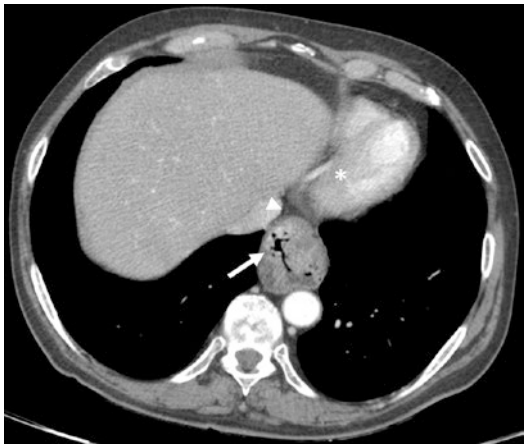

Fig. 4.55 CT scan image acquired in venous phase showing a thin layer of retro-cardiac (* = the left ventricle) fat surrounding the lower esophagus (arrow head) with small air areas, compatible with hiatal hernia (white arrow)

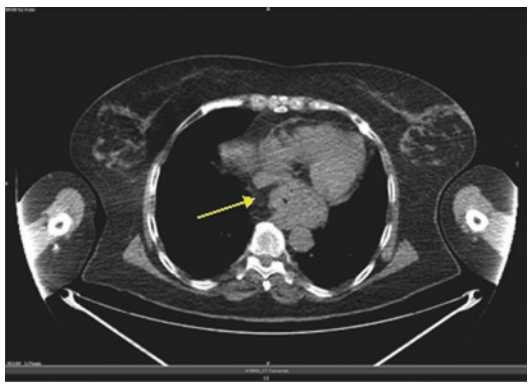

Fig. 4.56 Retrocardiac fat surrounding the lower esophagus with small air areas, compatible with hiatal hernia (arrow)

Hiatal Hernia

Hiatal hernia occurs when part of the stomach protrudes into the thoracic cavity through the esophageal hiatus of the diaphragm. In a sliding hernia (99%), the gastroesophageal junction is above the esophageal hiatus of the diaphragm. On the contrary in a paraesophageal hernia (1%), all or portions of the stomach herniate into the chest, but the gastroesophageal junction is below the diaphragm. However, they are both caused by a weakened or torn phrenoesophageal membrane. CT findings can be used to diagnose unsuspected hernias and to distinguish hernias from masses of the abdominal wall, such as tumors, hematomas, abscesses, undescended testes, and aneurysms. A hiatal hernia appears as a retrocardiac mass with or without an air-fluid level. The mass can usually be traced into the esophageal hiatus on sequential cuts. Herniation of omentum through the esophageal hiatus may result in an increase in fat surrounding the lower esophagus.

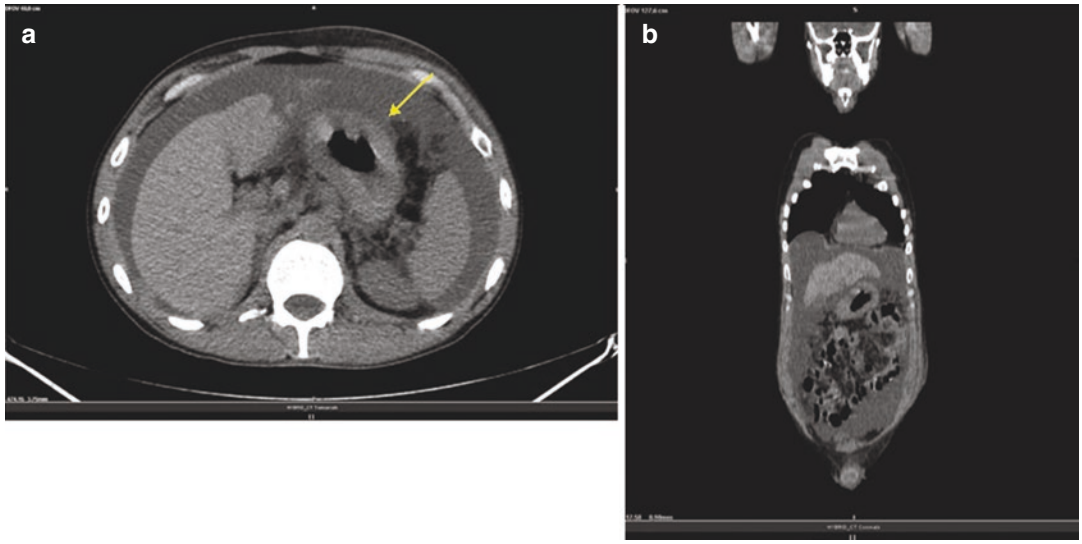

Fig. 4.57 (**a**, **b**) Diffuse thickening of gastric wall associated with accumulation of fluid in the abdominopelvic cavity (arrow)

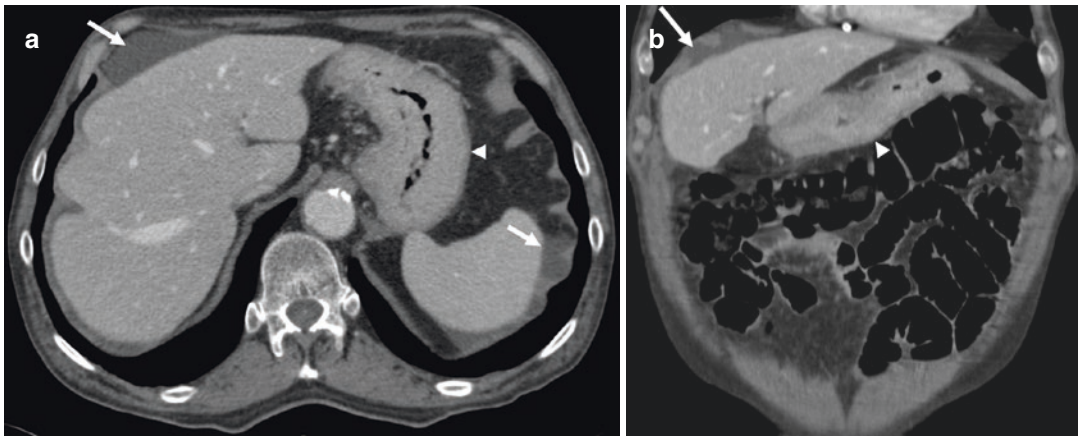

Fig. 4.58 Axial (**a**) and Coronal (**b**) CT scan images acquired in venous phase showing a diffuse thickening of the gastric wall (arrow heads) associated with accumulation of peri-splenic and peri-hepatic fluid (white arrows); the appearance of the stomach is like a "leather bottle"

Linitis Plastica

The stomach is diffusely thickened with a small lumen due to a diffuse proliferation of the connective tissue. The appearance of the stomach is like a "leather bottle." Underlying cause is usually a scirrhous adenocarcinoma with diffuse submucosal infiltration (biopsy often negative), leading to thickening and rigidity to the stomach wall. Differential diagnoses are neoplastic, lymphoma (less rigid), diffuse gastric diverticula, inflammatory (radiotherapy, eosinophilic enteritis, granulomatous disease, Crohn's disease, tuberculosis), scarring, and gastric amyloidosis.

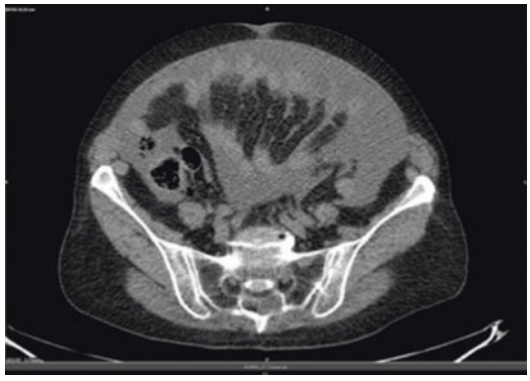

Fig. 4.59 Abnormal thickening of the omental fat associated with omental and peritoneal nodularity

Omental Cake

It is a sign indicative of an abnormally thickened greater omentum. Material of soft-tissue density infiltrates the omental fat. It is typically caused by infiltration of metastatic tumors arising from the stomach, ovary, or colon. Peritoneal tumor seeding may be a result of hematogenous, lymphatic, or direct local spread. More rarely it is a result of tuberculous peritonitis. It presents with massive ascites, thickening, and increased attenuation with nodularity along the greater omentum and peritoneum. CT might be useful even in the detection of other signs of peritoneal carcinomatosis, such as adherence of the intestine to the peritoneum and mural thickening of the intestine and in image-guided needle biopsy.

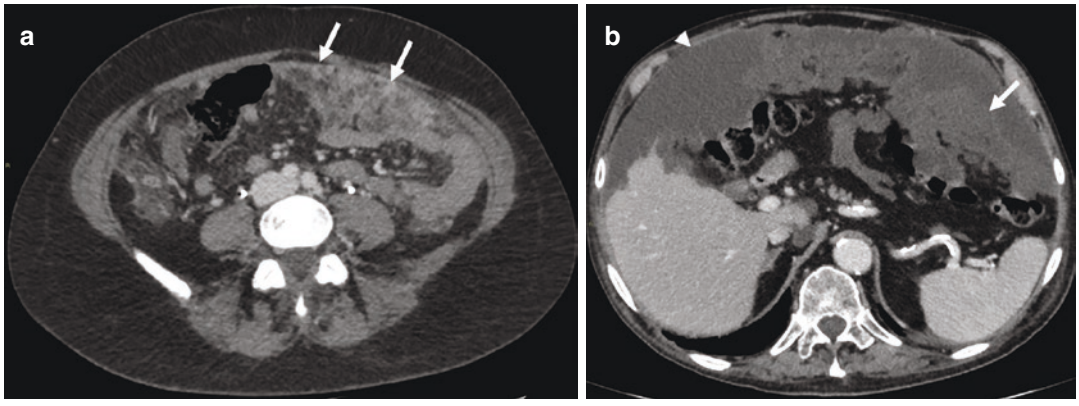

Fig. 4.60 Axial CT scan images (**a**, **b**) acquired in venous phase showing an abnormal thickening of the omental fat associated with omental and peritoneal nodularities (white arrows). Commonly it is associated with abdominal effusion (arrow head)

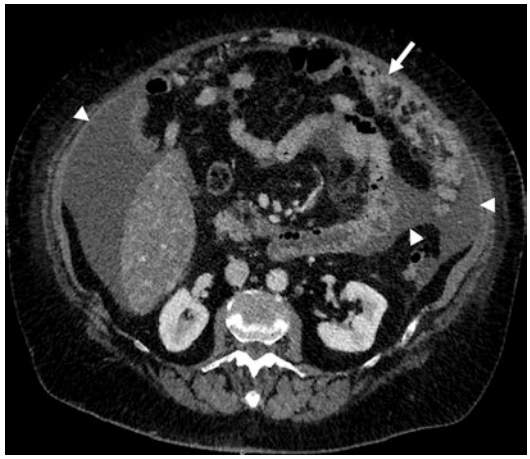

Fig. 4.61 Axial CT scan images acquired in venous phase showing an abnormal thickening of the omental fat associated with omental and peritoneal nodularities (white arrow). Commonly it is associated with abdominal effusion (arrow head)

Pelvis

5

Cristina Nanni, Stefano Fanti, Lucia Zanoni, Rita Golfieri, Alberta Cappelli, and Arrigo Cattabriga

C. Nanni (✉) · S. Fanti · L. Zanoni
Department of Nuclear Medicine, IRCCS Azienda Ospedaliera-Universitaria di Bologna, Bologna, Italy
e-mail: cristina.nanni@aosp.bo.it; stefano.fanti@aosp.bo.it; lucia.zanoni@aosp.bo.it

R. Golfieri · A. Cappelli
Department of Radiology, IRCCS Azienda Ospedaliera-Universitaria di Bologna, Bologna, Italy
e-mail: rita.golfieri@unibo.it; alberta.cappelli@aosp.bo.it

A. Cattabriga
IRCCS Azienda Ospedaliero-Universitaria di Bologna, Bologna, Italy

C. Nanni et al. (eds.), *Radiology for PET/CT Reporting*,
https://doi.org/10.1007/978-3-030-87641-8_5

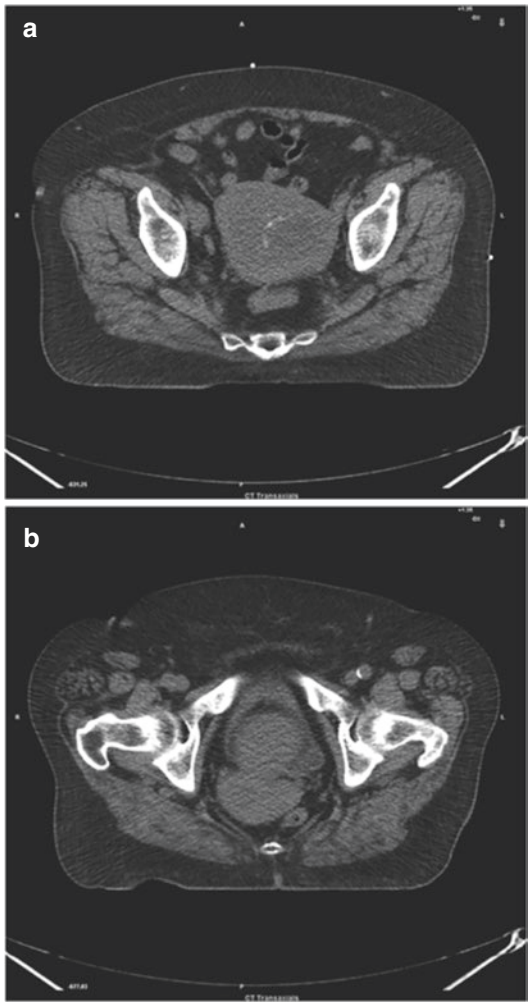

Fig. 5.1 (**a**, **b**) Huge mass in the endometrium involving the uterine body

Fig. 5.2 Axial CT scan image acquired in venous phase showing an hyper attenuating diffuse thickening of the uterine wall, suggestive of endometrial carcinoma. The same lesion can also have an appearance of a hypo-enhancing and hypo-attenuating mass within endometrial cavity

Fig. 5.3 Endometrial and ovary cancer in a breast cancer patient

Endometrial Carcinoma

CT findings in endometrial cancer include:

- Relatively hypo-attenuated mass in the region of the endometrial cavity which may show uniform attenuation or may be heterogeneous, with or without a contrast-enhanced component.
- Polypoid mass surrounded by endometrial fluid.
- Heterogeneous soft-tissue mass/masses and fluid expanding the endometrial cavity.
- Tumor involving multiple regions of the endometrium or the entire endometrial surface.
- Fluid-filled uterine cavity marginated by mural tumor implants.
- Fluid-filled uterine cavity secondary to obstruction of the endocervical canal by tumor that is not depicted or delineated clearly.

Fig. 5.4 Left groin mass suggestive for lymphoma

Fig. 5.5 Axial CT scan image acquired in venous phase showing a left groin mass suggestive for lymphoma. Enlarged nodes are the most common manifestation of lymphoma

Groin Lymphadenopathy

Enlarged nodes are the most common manifestation of lymphoma. Regardless of the area of involvement, nodal disease typically has attenuation similar to the muscle. In most cases, they are homogeneous but occasionally necrotic in case of a more aggressive tumor.

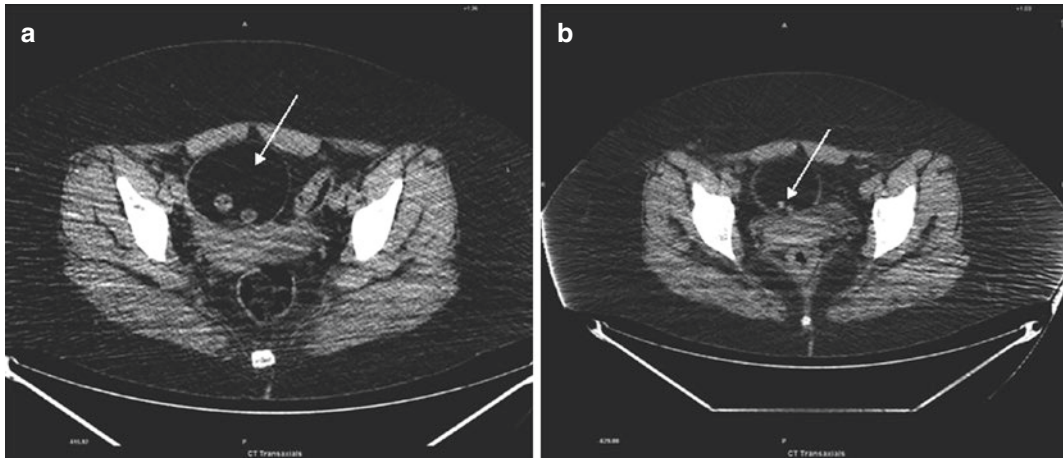

Fig. 5.6 Ovarian mass containing fat fluid level (**a**, arrow) and small calcification (**b**, arrow)

Cystic Teratoma of the Ovary

Dermoids are composed only of dermal and epidermal elements, whereas teratomas have mesodermal and endodermal elements. They interchangeably refer to the most common ovarian neoplasm. Typically CT images show ovarian mass containing fat, fat fluid level, calcification (sometimes tooth), Rokitansky protuberance, or tufts of hair. Malignant transformation should be suspected whenever the size exceeds 10 cm or soft-tissue plugs and cauliflower appearance with irregular borders are detected.

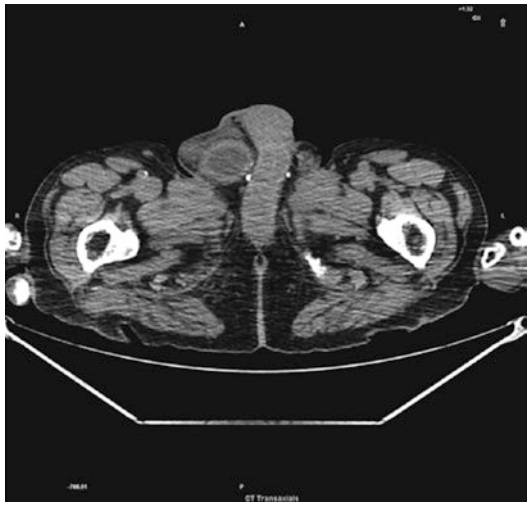

Fig. 5.7 Right scrotal effusion

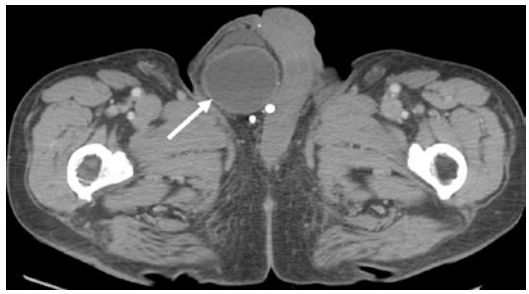

Fig. 5.8 Axial CT scan images acquired in venous phase showing a right scrotal herniation with a moderate amount of liquid (hydrocele)

Fig. 5.9 Left scrotal herniation

Fig. 5.10 Axial CT scan images acquired in venous phase showing a right scrotal herniation with an intestinal loop entering the scrotum

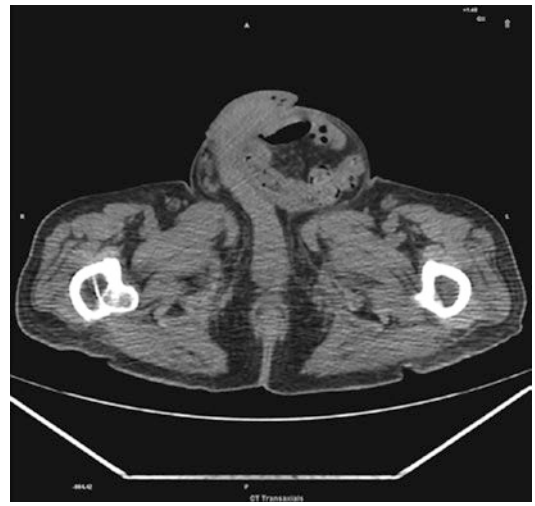

Fig. 5.11 Left scrotal herniation

Scrotal Herniation

Indirect inguinal herniations are caused by the protrusion of peritoneal content through a patent internal inguinal ring, lateral to the inferior epigastric vessels extending along the spermatic cord into the scrotum in men. Advantages of CT include more accurate identification of hernias and their contents and differentiation of hernias from other abdominal masses (tumors, hematomas, abscesses, undescended testes, and aneurysms). Signs of complication within the hernia sac, including bowel obstruction, incarceration, strangulation, and traumatic wall hernia, can be hardly detected.

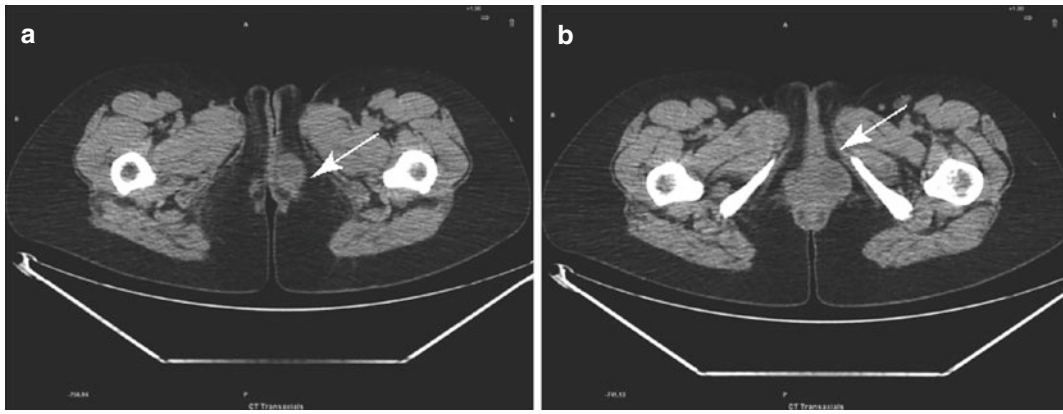

Fig. 5.12 (**a**, **b**) Fluid-density nodule in the left posterior wall of the vagina (arrows)

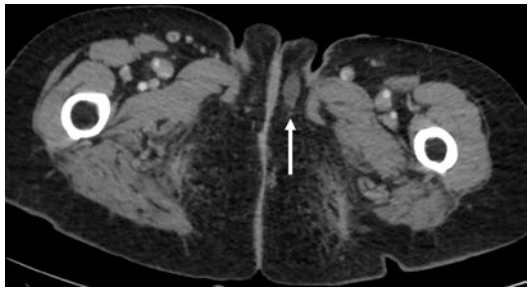

Fig. 5.13 Axial CT image showing typical features of Bartolini gland cyst such as fluid-density nodule in the left posterior wall of vagina (white arrow)

Bartholin Gland Cyst

It is a rounded unilocular cysts lying at the posterior aspect of the vagina. It is located below the level of the pubic symphysis in the posterolateral inferior third of the vagina and is associated with the labia majora. It is usually asymptomatic, but a common complication is infection, turning into *Bartholin gland abscesses* which shows inflammatory features and may require marsupialization. *Neisseria gonorrhoeae* and *Chlamydia trachomatis* are common pathogens. More recent studies report the predominance of opportunistic bacteria such as *Staphylococcus*, *Streptococcus*, and, most commonly, *Escherichia coli*.

Fig. 5.14 Left external iliac mass showing fluid/soft-tissue density

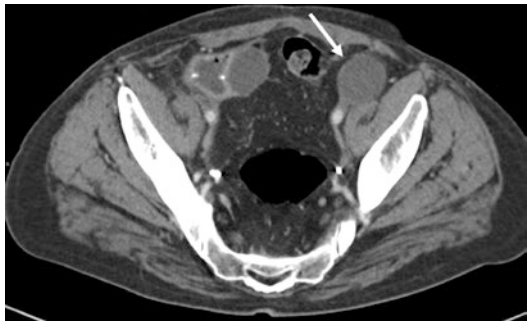

Fig. 5.15 Axial venous phase CT image of the pelvis showing a lymphocele: an ovalar image with fluid/soft tissue density localized in close proximity of the left external iliac vein (white arrow)

Lymphocele

It is a collection of lymphatic fluid within the body not bordered by epithelial lining. It is commonly seen following surgical procedures, after pelvic or retroperitoneal lymphadenectomy or renal transplant surgery. It is important to differentiate from congenital, infectious, and malignant cystic masses. A CT scan will confirm the presence and location of fluid collection, generally represented by a low-attenuation mass with rare but highly suggestive negative attenuation values due to fat within the fluid. Calcification of the lymphocele wall may be also seen.

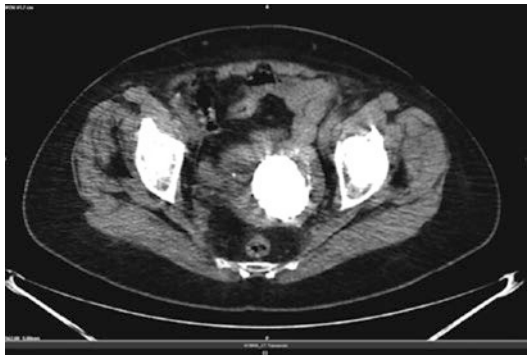

Fig. 5.16 Voluminous rounded calcification within the uterus

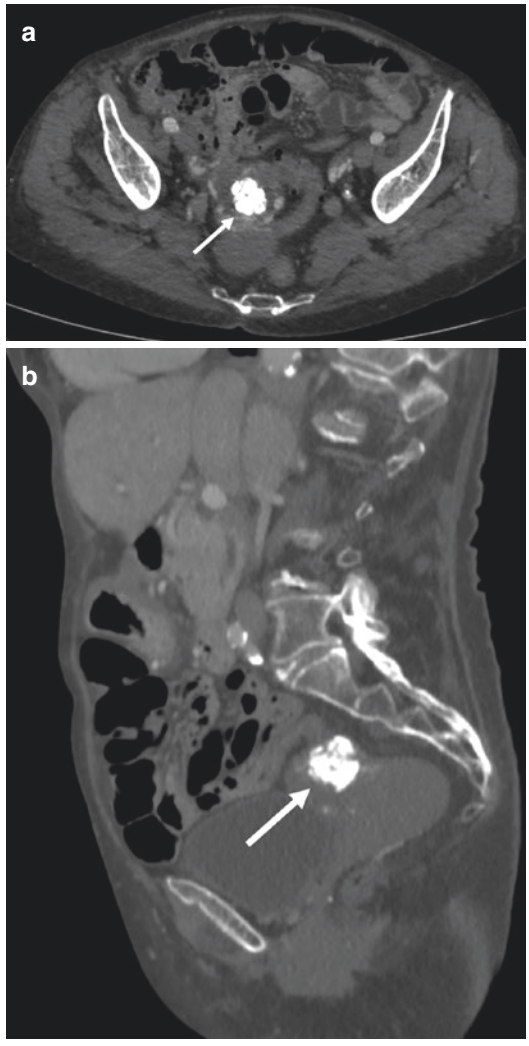

Fig. 5.17 Axial (**a**) and Sagittal (**b**) CT scan images acquired in venous phase showing a voluminous rounded calcification (white arrows), with irregular outlines, within the uterus

Calcifying Fibroma

A tumor composed mainly of fibrous or fully developed connective tissue. The typical finding is a bulky, irregular uterus or a mass in continuity with the uterus. Degenerate fibroids may contain areas of fluid attenuation. Calcification is seen in approximately 4% of fibroids and is typically dense and amorphous. However, when it is thought to be secondary to thrombosed veins from previous red degeneration, calcification can also be confined to the periphery of the fibroid.

Musculoskeletal

6

Cristina Nanni, Stefano Fanti, Lucia Zanoni, Rita Golfieri, Cristina Mosconi, and Arrigo Cattabriga

C. Nanni (✉) · S. Fanti · L. Zanoni
Department of Nuclear Medicine, IRCCS Azienda Ospedaliera-Universitaria di Bologna, Bologna, Italy
e-mail: cristina.nanni@aosp.bo.it; stefano.fanti@aosp.bo.it; lucia.zanoni@aosp.bo.it

R. Golfieri · C. Mosconi
Department of Radiology, IRCCS Azienda Ospedaliera-Universitaria di Bologna, Bologna, Italy
e-mail: rita.golfieri@unibo.it; cristina.mosconi@aosp.bo.it

A. Cattabriga
University of Bologna, Bologna, Italy

C. Nanni et al. (eds.), *Radiology for PET/CT Reporting*,
https://doi.org/10.1007/978-3-030-87641-8_6

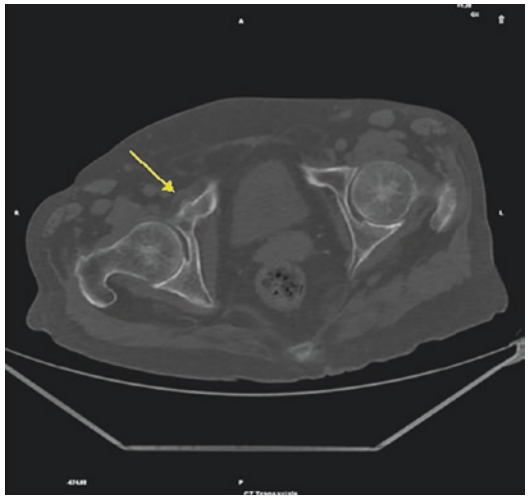

Fig. 6.1 Fracture of the right iliac-pubic ramus

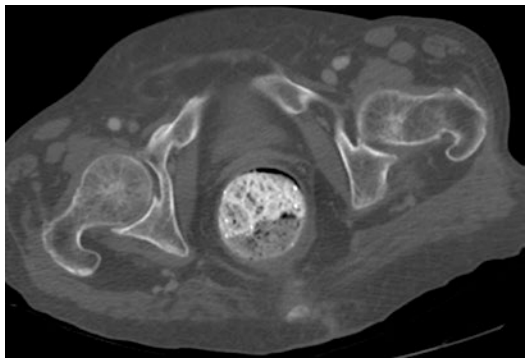

Fig. 6.2 Axial venous phase CT imaging of the pelvis showing an osteoporotic fracture of the right ileopubic ramus (white arrow)

Osteoporotic Fractures of the Pelvis

Pelvic fractures encompass a broad spectrum of injuries, from low-energy osteoporotic fractures to high-energy disruptions of the pelvic ring. Following low-energy trauma fractures are frequently classified as pelvic girdle fractures. CT is both sensitive and specific, and it is a valid alternative to MRI in localizing the fracture line. The CT scan aspect varies depending on the degree of fracture healing; indeed it can high-light sclerotic healing or fresh fracture lines. Important issue is to rule out malignancy and osteomyelitis.

Osteoid Osteoma

Osteoid osteoma is a small benign tumor of bone that is usually present at a young age and causes moderate-to-severe bouts of intermittent pain, often worse at night but partially relieved by non-steroidal anti-inflammatory drugs. It appears as a circumscribed subcortical annular lesion with a double-attenuating sign with thin curvilinear or serpiginous low-density grooves related with enlarged feeding arterioles ("the vascular groove sign"). It is easy to visualize a central nidus among the surrounding dense bone sclerosis (periosteal reaction). CT scan is particularly helpful to define the precise localization of the nidus in the hip or spine.

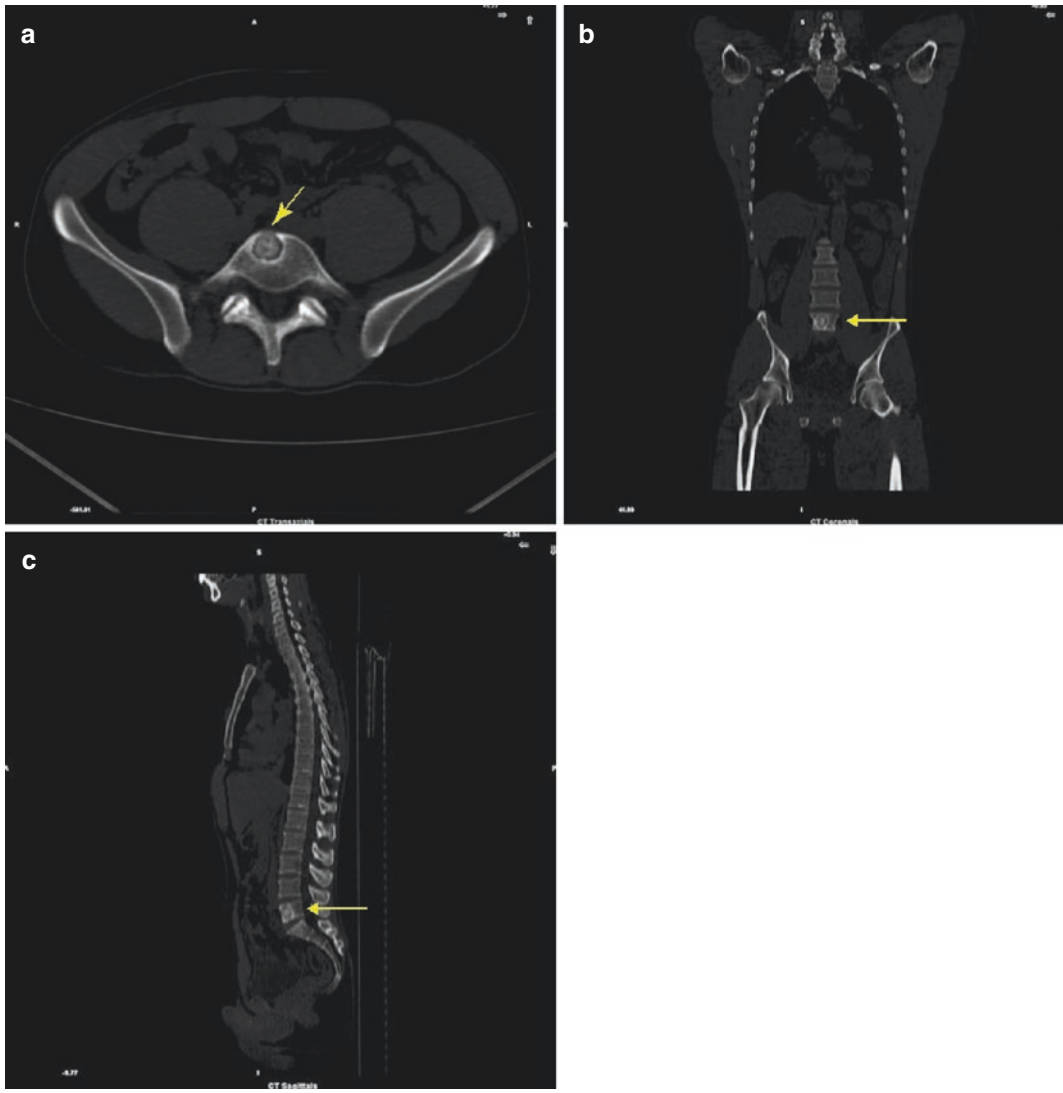

Fig. 6.3 Non-avid round lesion in L5 vertebral body: (**a**) axial, (**b**) coronal, and (**c**) sagittal views (arrows)

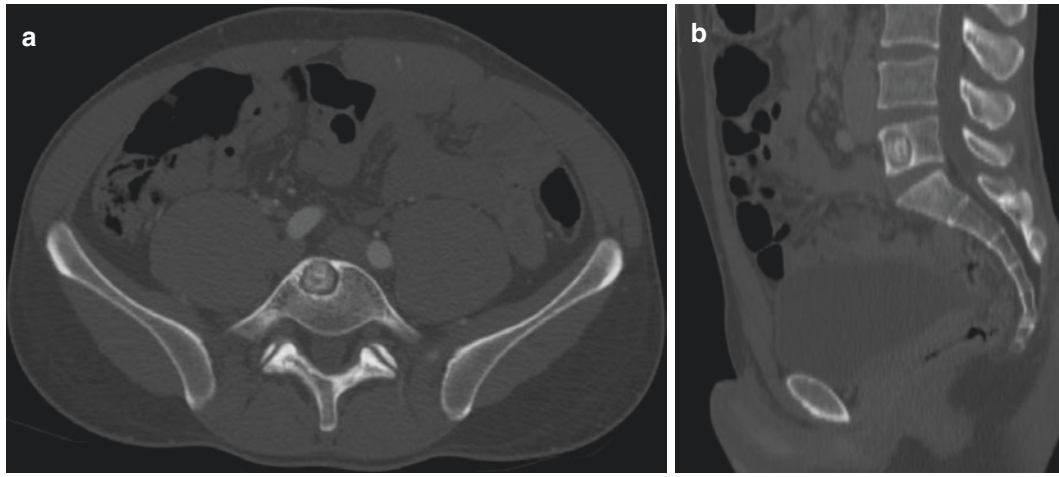

Fig. 6.4 (**a**, **b**) Axial (**a**) and Sagittal (**b**) CT images on bone window settings of an non-avid round lesion in L5 vertebral body

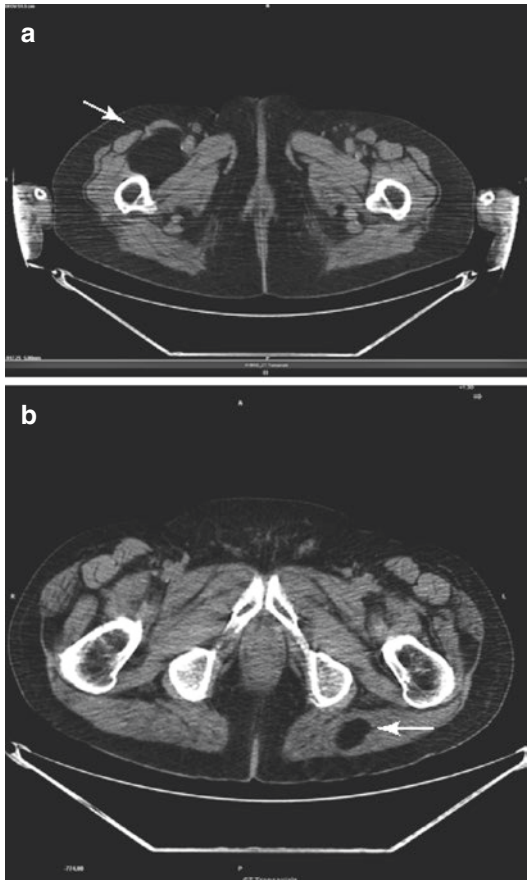

Fig. 6.5 Low-density mass in the right thigh (**a**) or in the left gluteus (**b**)

Lipoma

Lipomas arising from fat in the intramuscular septa cause a diffuse, palpable swelling, which is more prominent when the related muscle is contracted. Lipoma is a slow-growing, benign fatty tumor form characterized by soft, lobulated mass enclosed by a thin, fibrous capsule. There is low-density tissue (typically approximately −65 to −120 HU), identical to subcutaneous adipose tissue. Thin septa can be found.

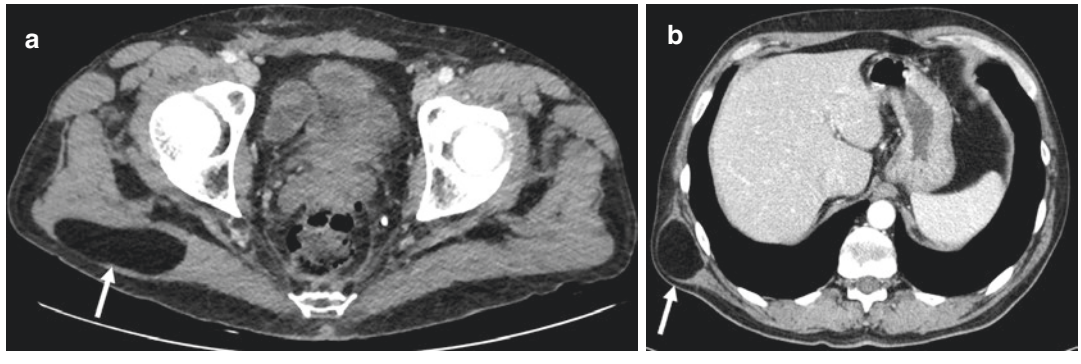

Fig. 6.6 Axial post contrast imaging CT images showing a low-density mass in the right gluteus (**a**) or in the right flank (**b**)

Extramedullary Hematopoiesis (EMH)

EMH is a response to erythropoiesis failure in bone marrow. It is one of the common features of chronic myeloproliferative disorders. The neoplastic stem cells have the capacity to circulate and migrate to secondary hematopoietic organs (mainly spleen and liver and occasionally lymph nodes or other organs) causing macroscopically visible tumor-like masses. The lesions are usually round masses with lobulated margins, they do not calcify and do not usually cause bone erosion, and they appear of low attenuation on non-contrast CT. In the thorax they can be visible with widening of the ribs or around the expanded posterior or anterior part of the ribs: the marrow overflows from the bone, destroys the cortex (however, the cortex can be found intact), and spreads around it. A similar process may start form a vertebral body.

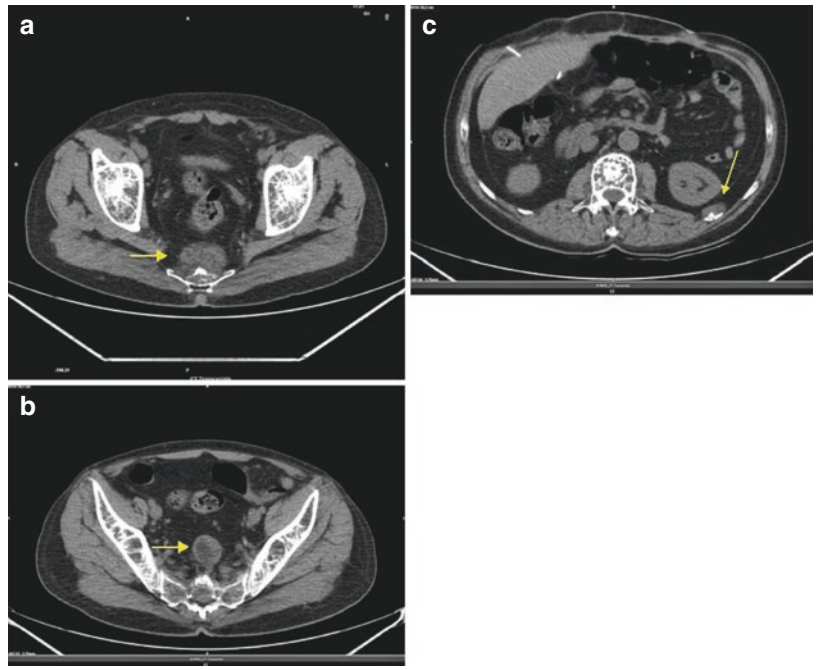

Fig. 6.7 (**a**) Pre-coccyx (arrow), (**b**) presacral (arrow), and (**c**) thoracic tumorlike mass adjacent to a left rib (arrow)

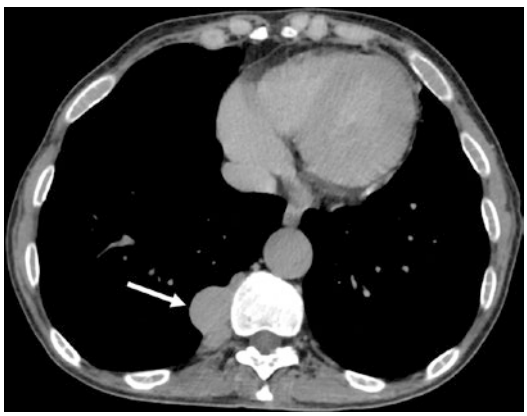

Fig. 6.8 Axial CT image showing a well-defined mass located on the right side of a thoracic vertebra (white arrow)

Vertebral Collapse

The following CT findings are significantly more frequent in benign (osteoporotic) vertebral collapse: cortical fractures of the vertebral body without cortical bone destruction, retropulsion of a bone fragment of the posterior cortex of the vertebral body into the spinal canal, fracture lines within the cancellous bone of the vertebral body, an intravertebral vacuum phenomenon, and a thin diffuse paraspinal soft-tissue mass.

Fig. 6.9 (**a**–**d**) Initial non-traumatic vertebral collapse sagittal (**a**, **b**) and axial (**c**, **d**) views

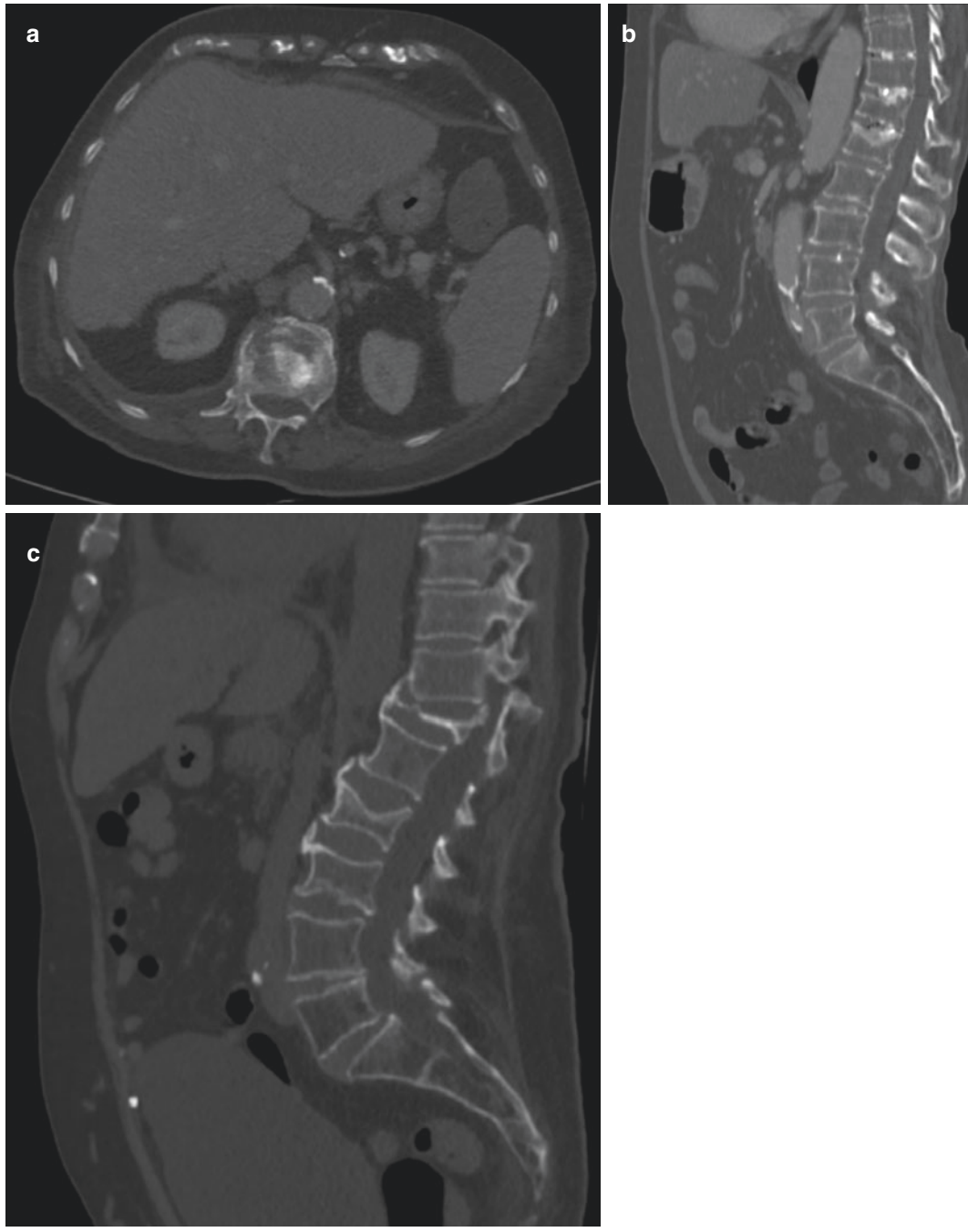

Fig. 6.10 (**a**–**c**) Axial (**a**) and sagittal (**b**, **c**) CT images on bone window settings showing initial non-traumatic vertebral collapse (**a**, **b**), in particular the reduction in height of the anterior wall of vertebral body of D12 and L1. The progression of disease consist in a complete collapse of the vertebral body as seen in **c**, in particular the complete collapse of D12 vertebral body and a significant reduction in height both of L2 and L3

On the contrary, the following CT findings are significantly more frequent in malignant collapse (metastatic or myelomatous): destruction of the anterolateral or posterior cortical bone of the vertebral body, destruction of the cancellous bone of the vertebral body, destruction of a vertebral pedicle, a focal paraspinal soft-tissue mass, and an epidural mass.

Spina Bifida

The main defect of spina bifida is an abnormal opening in the spinal column through which the spinal cord passes. This leaves the spinal cord unprotected and vulnerable to either injury or infection. The outer part of some of the vertebrae is not completely closed. Multiple segmentation anomalies can be found in the spine: partial sagittal partition, butterfly vertebra, hemivertebra, tripedicular vertebra, and widely separated butterfly vertebra.

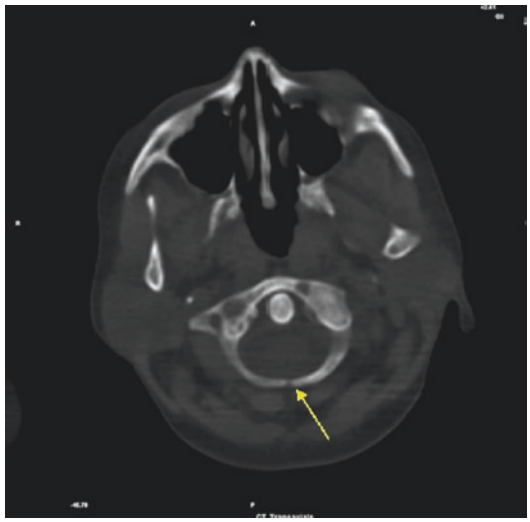

Fig. 6.11 Non-fused posterior arch of C1 (arrow)

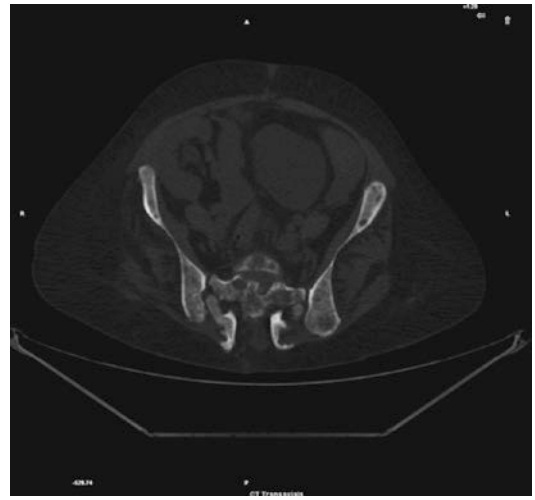

Fig. 6.12 Double spinal cord

Fig. 6.13 Axial CT image of the hip on bone window showing non-fused posterior arch of the sacrum

Vacuum Sign

The vacuum phenomenon appears as an air-density area visible in synovial joints, intervertebral disks, and vertebrae. This phenomenon is explained by gas accumulation, mostly nitrogen, produced by the surrounding soft tissues. In vertebrae, the phenomenon has been described in cases of collapse, usually resulting from osteonecrosis. On CT scans, the sign may appear more heterogeneous and irregular than it does on radiographs. It indicates local bone ischemia associated with a nonhealing vertebral collapse and pseudarthrosis.

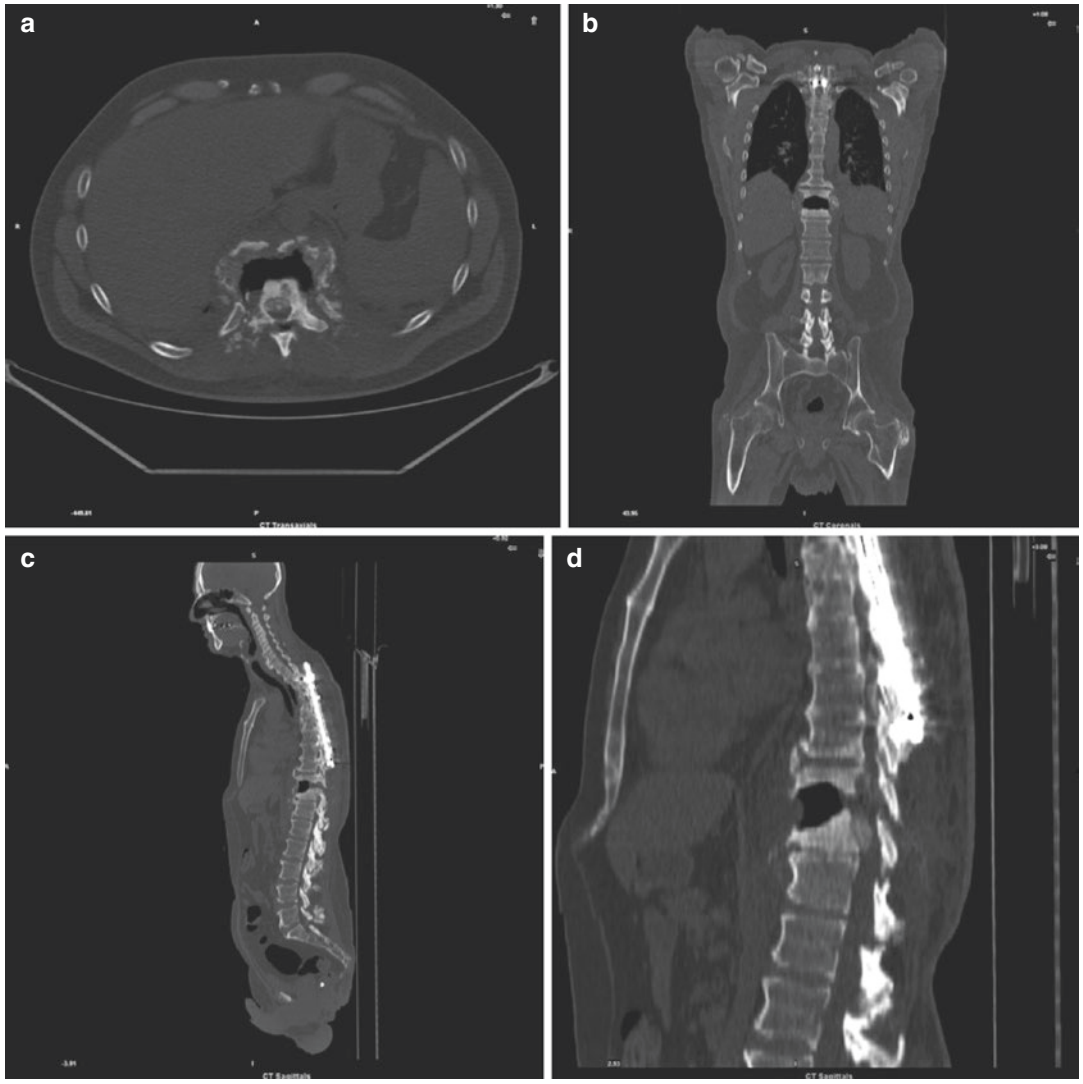

Fig. 6.14 Vertebral collapse with huge gas bubble: (**a**) axial, (**b**) coronal, (**c**) sagittal, and (**d**) sagittal zoom views

Fig. 6.15 (**a**–**d**) Axial (**a**), Coronal (**b**) and Sagittal (**c**, **d**) CT images of the spine on bone window settings showing gas bubble localized in the intervertebral spaces (arrows)

Spondylodiscitis

It is characterized by infection involving the intervertebral disc and adjacent vertebrae. Most common pathogen is Staphylococcus or Streptococcus. Gram-negative rods are typical in IV drug abusers or immunocompromised patients such as *E. coli*, proteus, non-pyogenic, tuberculosis, coccidioidomycosis. Disc space narrowing and irregularity/ill definition/destruction of the endplates can be seen. In untreated cases, bony sclerosis of the two contiguous vertebral bodies may begin during healing phase anywhere from 8 weeks to 8 months after onset. Surrounding paravertebral soft-tissue swelling, collection, and even epidural abscesses may be evident.

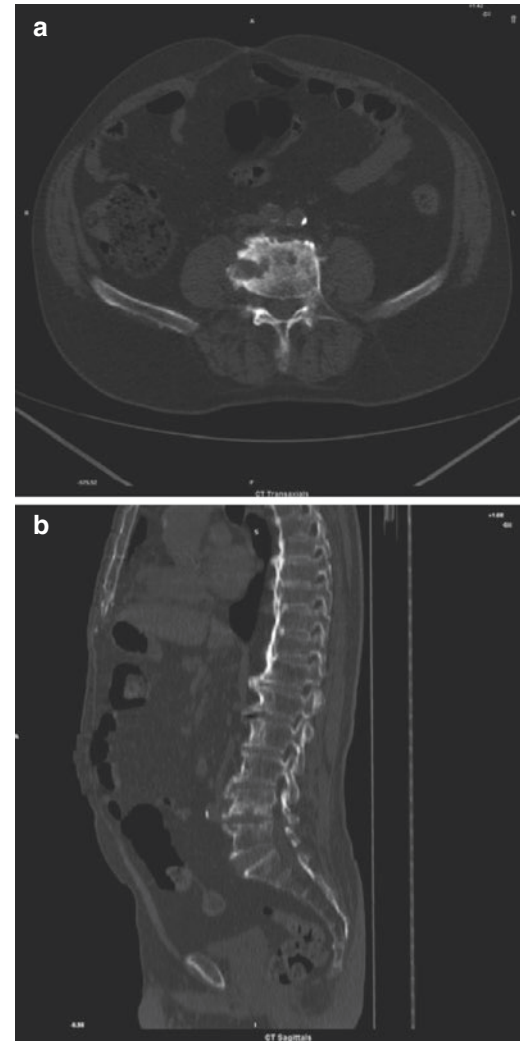

Fig. 6.16 (**a**, **b**) L4/L5 discitis

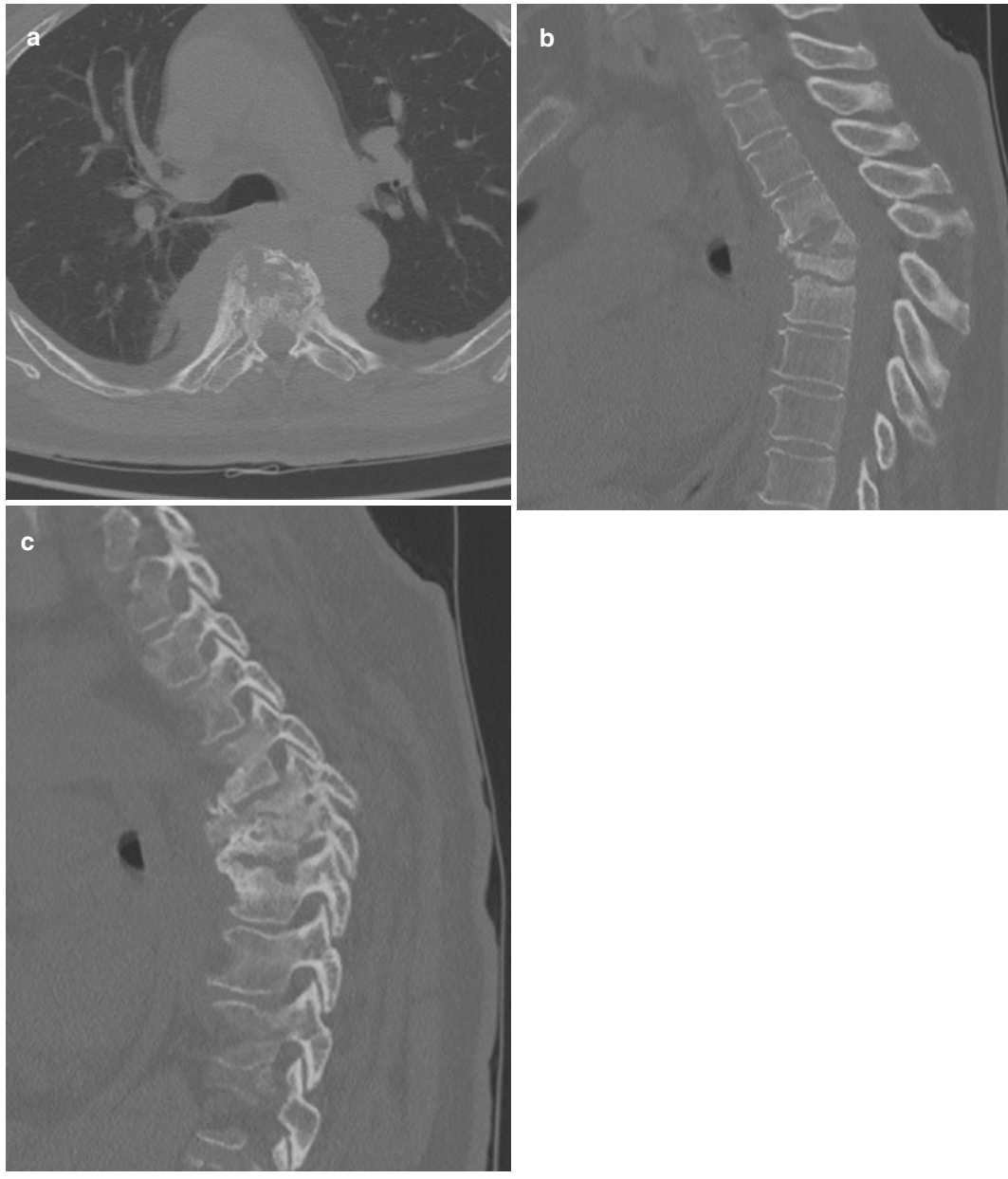

Fig. 6.17 (**a**–**c**) Axial (**a**) and Sagittal (**b**, **c**) CT images of the spine on lung window settings showing vertebral collapse associated with disomogeneous and irregular vertebral endplates

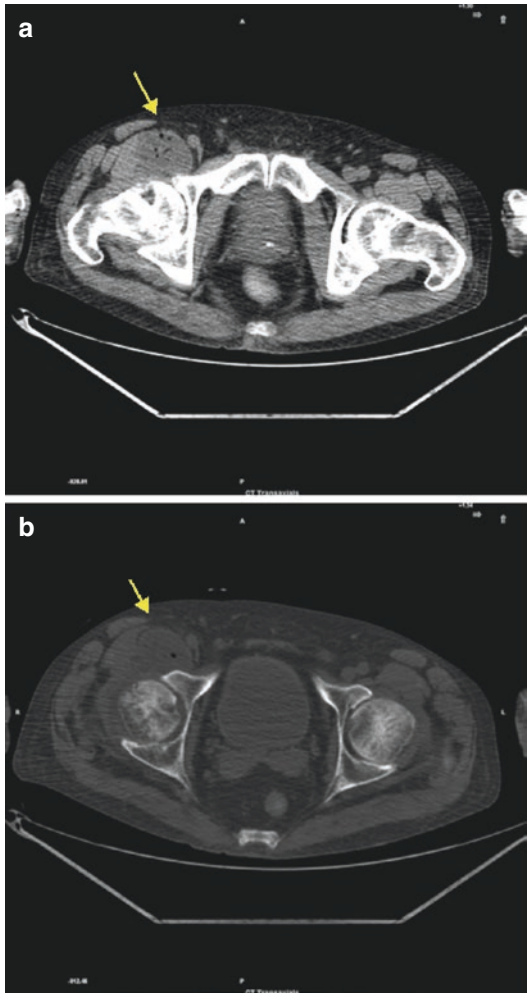

Fig. 6.18 (**a**, **b**) Collection of fluid and air within the soft tissue adjacent to the right hip joint (arrows)

Hip Infection

Visualization of intra-articular effusion with extra-articular extension. Soft-tissue abnormalities can be joint distension, fluid-filled bursa and fluid collection in muscles and peri-muscular fat. Focal areas of low attenuation and gas bulla can be assessed in the muscle. CT is accurate in the detection of painful infection at the site of hip on the basis of soft-tissue findings rather than bone peri-prosthetic abnormalities.

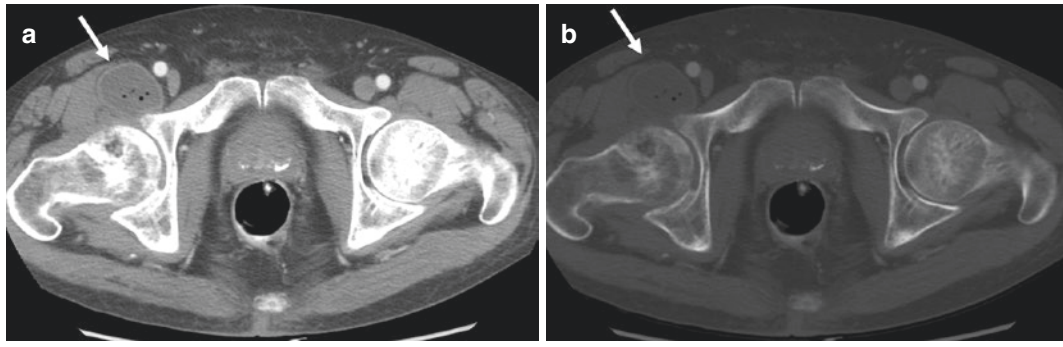

Fig. 6.19 (**a**, **b**) Axial CT venous post contrast image, respectively on soft tissue (**a**) and bone (**b**) window settings, showing fluid collection with contestual air bubbles within the soft tissue adjacent to the right hip joint (arrows)

Intraspongy Hernia

Protrusions of disc material into the surface of the vertebral body. Also called as *Schmorl's nodes*, areas of "vertical disc herniation" through areas of weakness in the endplate. They represent the end result of ischemic necrosis beneath the cartilaginous endplate. The appearances are similar to the typical CT changes of subchondral osteonecrosis. They are typical round, often multiple cystic lesions with indistinct sclerotic margins beneath the cartilaginous endplate. The fibrocartilage lying beneath the endplate appears as a lobulated area. The sclerotic margin represents the interface between the osteonecrotic and normal bone.

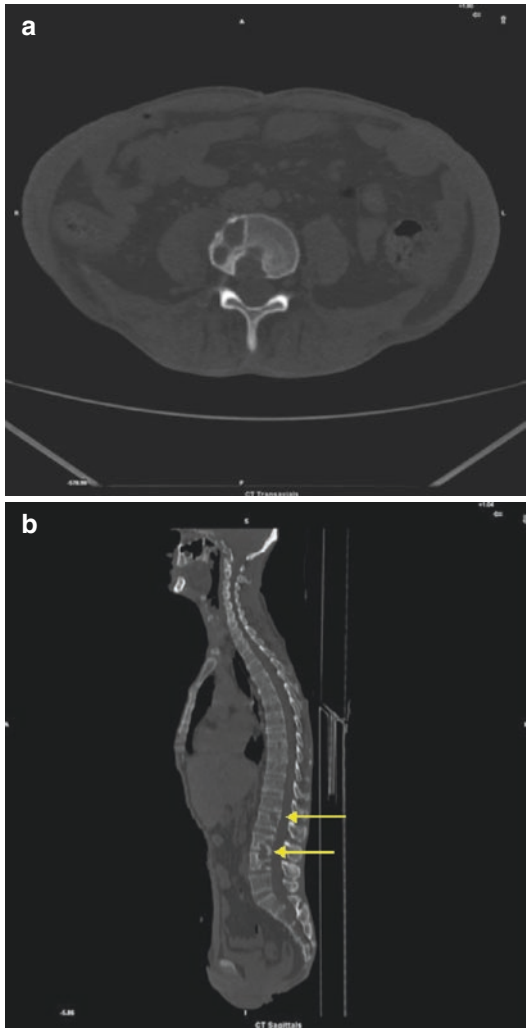

Fig. 6.20 (**a**, **b**) Multiple lesions beneath the cartilaginous endplate of L1–L2 and L3–L4 (arrows) in axial (**a**) and sagittal (**b**) views

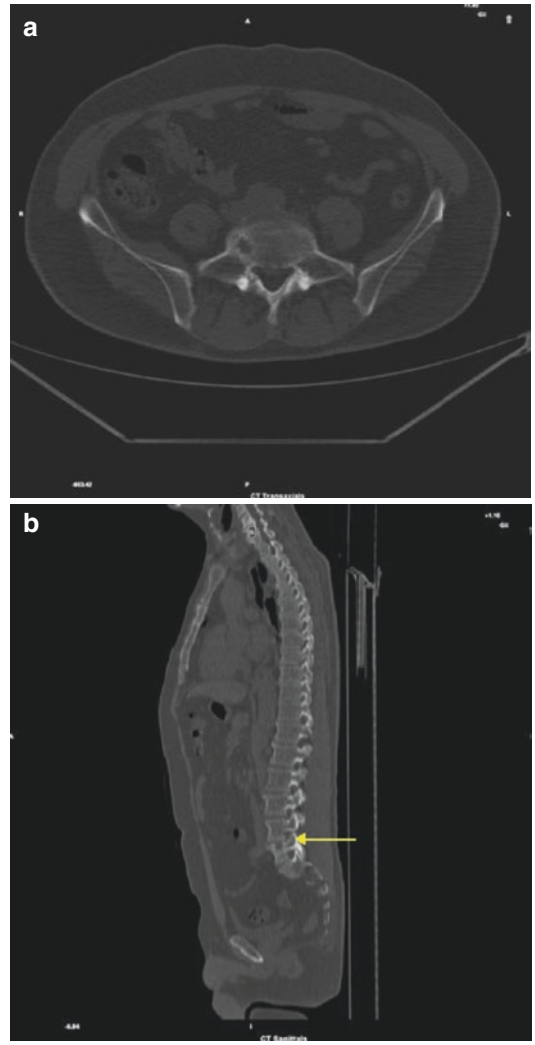

Fig. 6.21 (**a**, **b**) Single lesion beneath the superior cartilaginous endplate of L5 (arrow) in axial (**a**) and sagittal (**b**) views

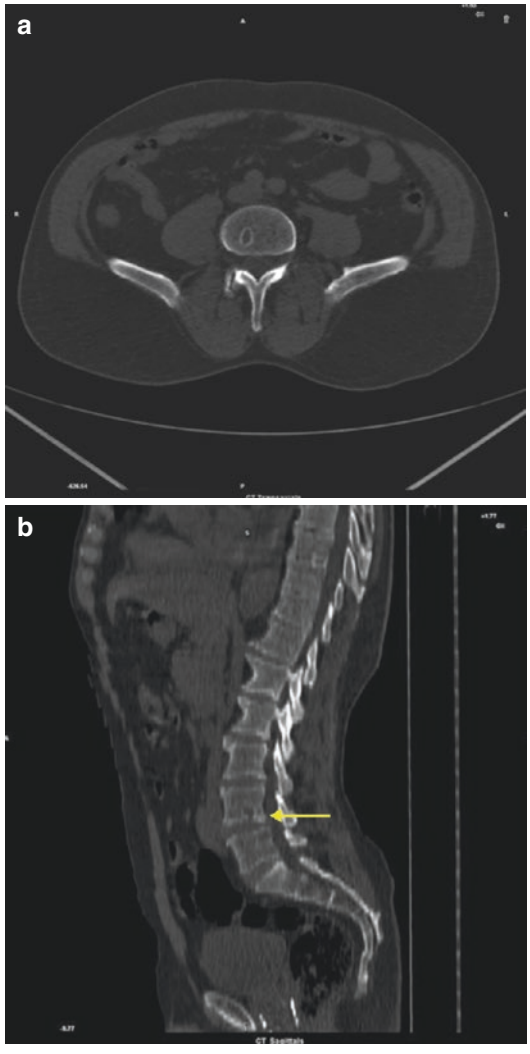

Fig. 6.22 (**a**, **b**) Single lesion beneath the inferior cartilaginous endplate of L4 (arrow) in axial (**a**) and sagittal (**b**) views

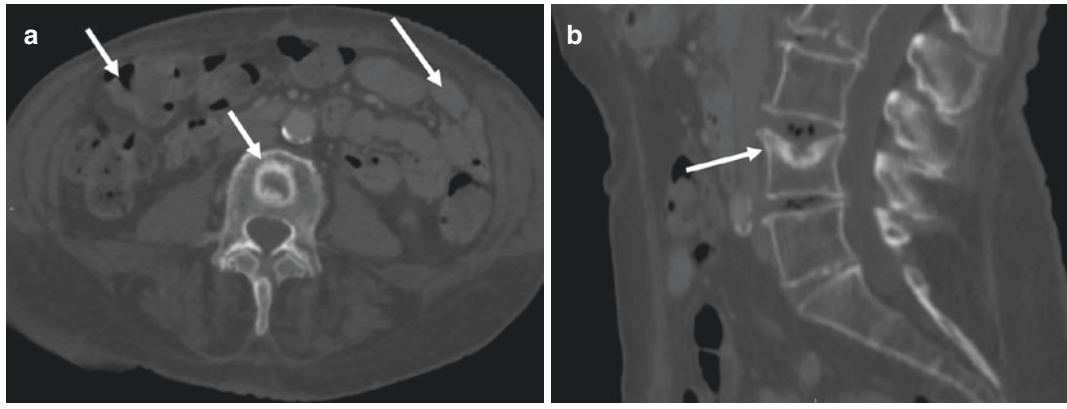

Fig. 6.23 (**a**, **b**) Axial and sagittal CT images on bone window setting of L4 intraspongy hernia characterized by a single lesion beneath the superior cartilaginous endplate (arrow)

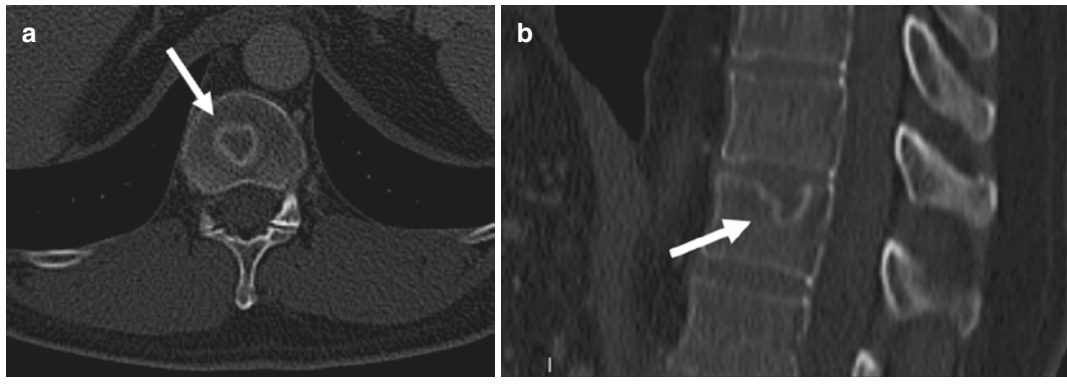

Fig. 6.24 (**a**, **b**) Axial (**a**) and sagittal (**b**) CT images (bone window) of an intraspongy hernia, also called "Schmorl's hernia" characterized by a single lesion beneath the superior cartilaginous endplate (arrow)

Spine Hemangioma

It is a benign, mostly symptomatic lesion, most often located in lower thoracic and upper lumbar spine, in particular in the medullary cavity of bone. Punctuate sclerotic foci representing thickened vertical trabeculae are seen in cross-section imaging giving a "polka-dot" sign.

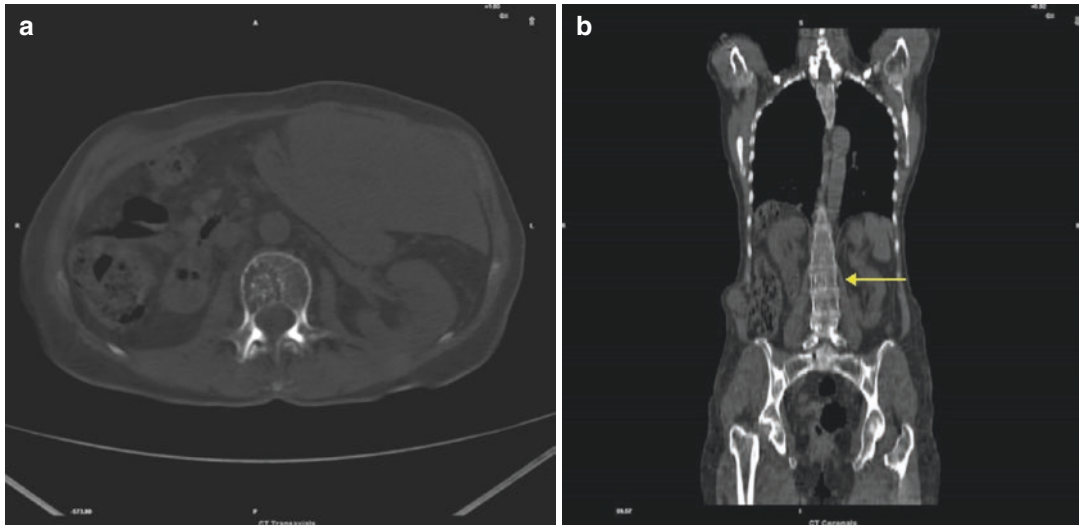

Fig. 6.25 (**a**, **b**) A lumbar vertebral body with punctuate sclerotic foci in axial view (**a**) and corresponding vertical trabecula in coronal view (**b**), typical for spine hemangioma

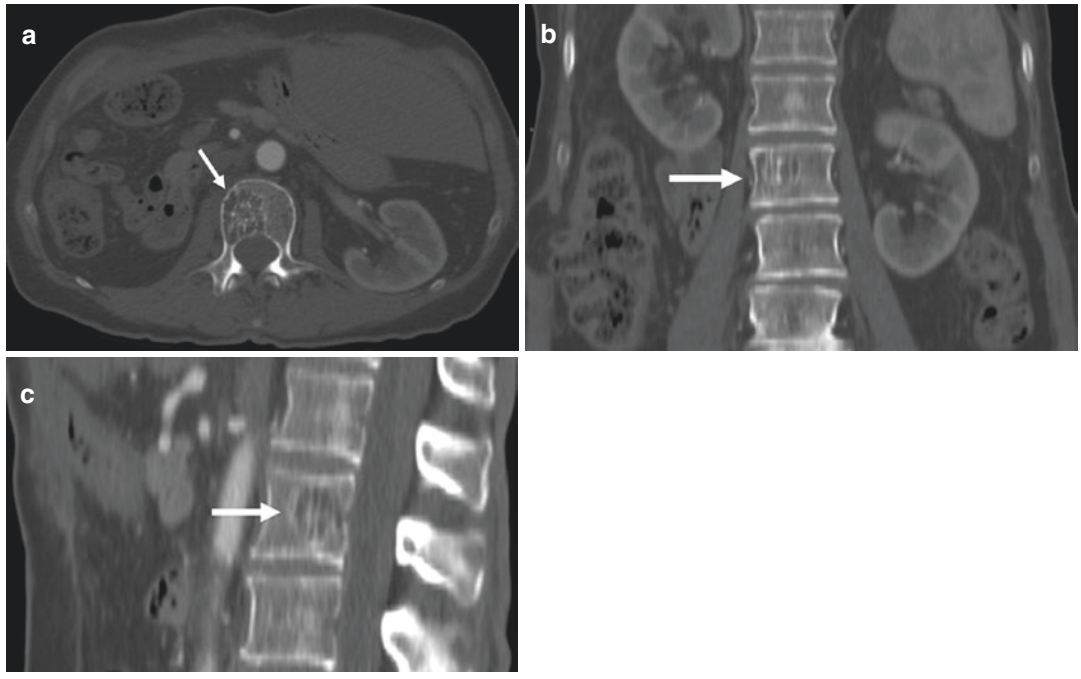

Fig. 6.26 (**a**–**c**) Axial (**a**), coronal (**b**) and sagittal (**c**) CT images of a lumbar vertebral body with punctuate sclerotic foci in axial view (white arrow—**a**) and corresponding vertical trabecula both in coronal view (white arrow—**b**) and sagittal views (white arrow—**c**), typical features of a spine hemangioma

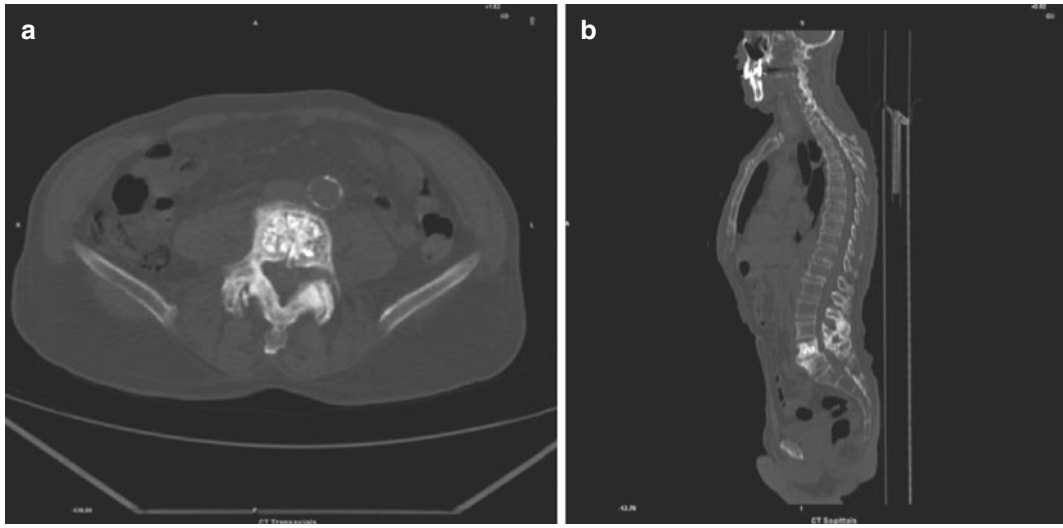

Fig. 6.27 (**a**, **b**) Example of severe sclerotic trabecula in a hemangioma of a lumbar vertebral body

Hip Joint Osteoarthritis

CT scan image obtained through the superior aspect of the hip reveals joint narrowing, osteophyte formation and subchondral cysts typical of osteoarthritis.

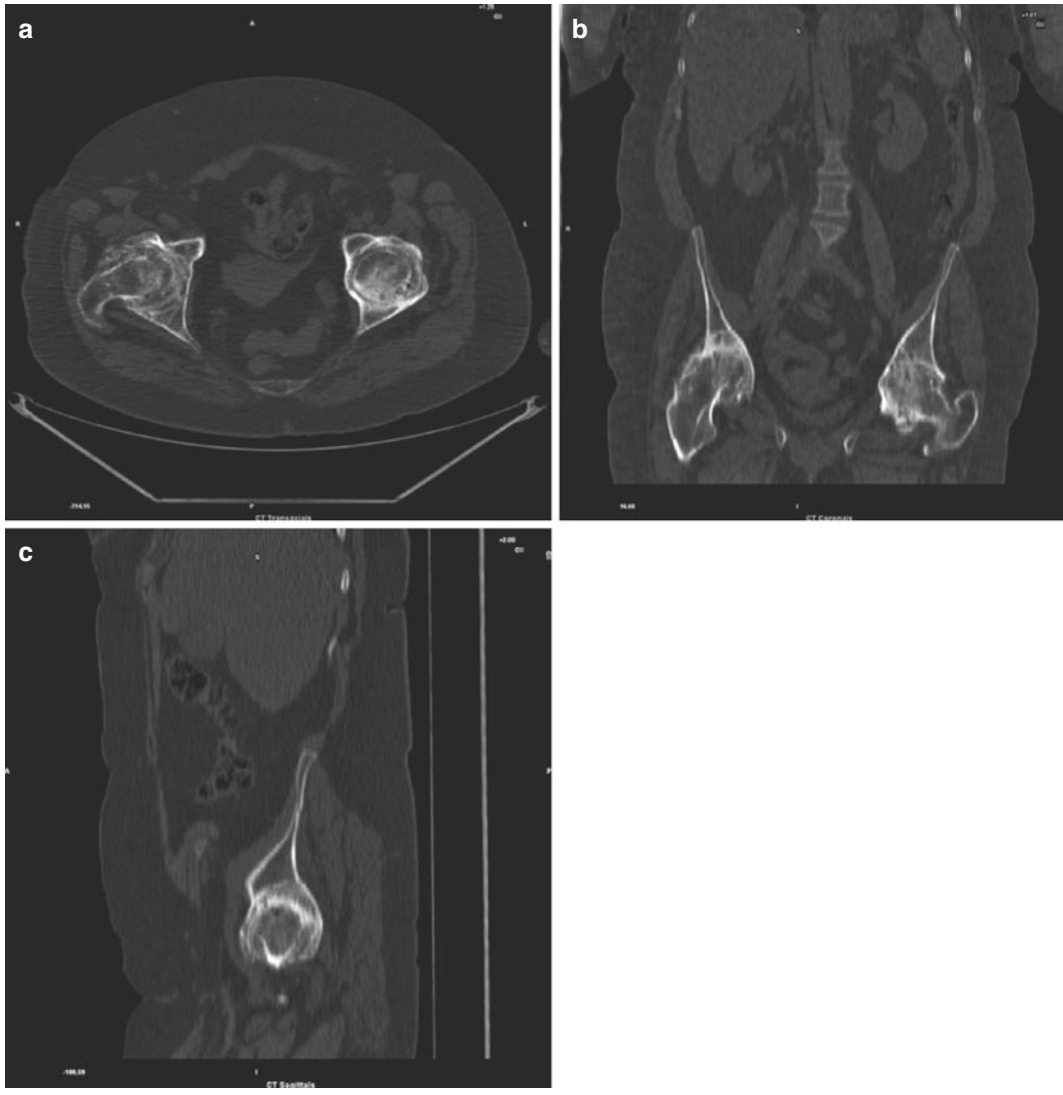

Fig. 6.28 (**a**) Axial, (**b**) coronal, and (**c**) sagittal views

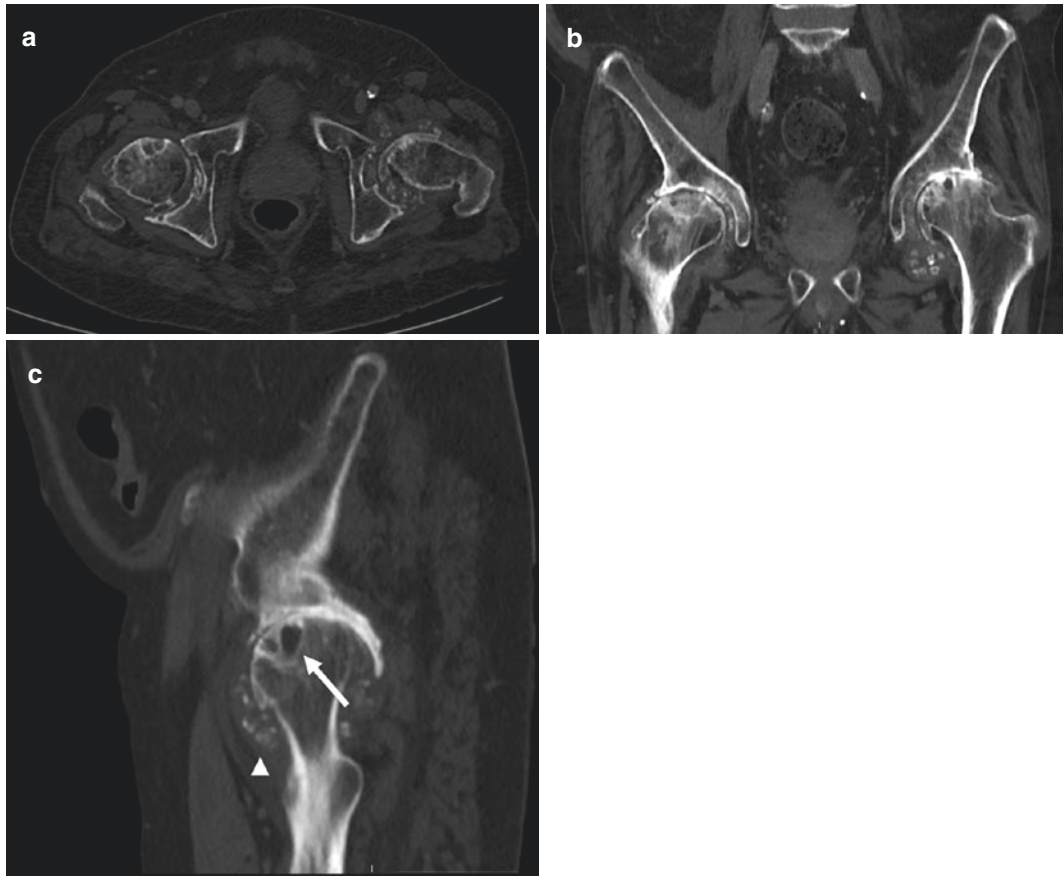

Fig. 6.29 (**a**–**c**) Axial (**a**), coronal (**b**) and sagittal (**c**) CT images on bone window settings of bilateral hip joint osteoartrhitis, especially on the left side. In particular, joint space narrowing, subchondral sclerosis of the femoral head associated with geodic areas (white arrow—**c**) and peri-articular calcifications

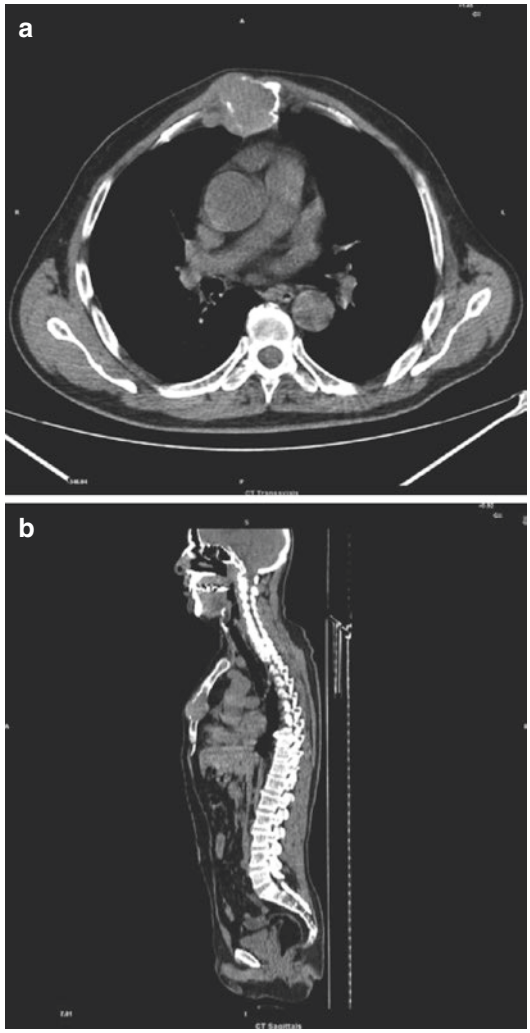

Fig. 6.30 (**a**, **b**) Mass in the sternum showing mainly soft-tissue density but marked erosion of the bone (axial-**a**; sagittal-**b** views)

Sternal Plasmacytoma

A solitary bone plasmacytoma (SBP) arises from the plasma cells located in the bone marrow. CT may demonstrate subtle lytic lesions or small soft-tissue masses, in particular of the sternum, that are not usually visible at radiography. It is typically a well-defined, "punched-out" lytic lesion with associated soft-tissue masses. In advanced plasmacytoma, marked erosion, expansion, and destruction of bone cortex can be assessed.

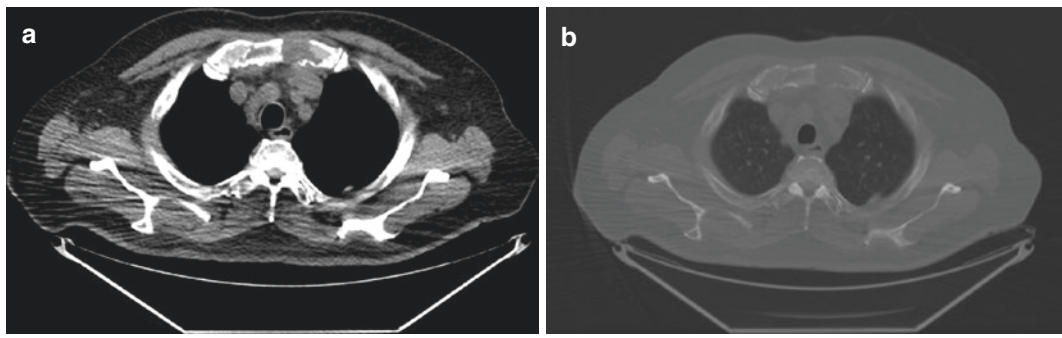

Fig. 6.31 (**a**, **b**) Axial CT images showing a sternal plasmacytoma with soft tissues window (**a**) and bone window (**b**). There is a hyperdense tissue in the left side of the lytic lesion consistent with plasmacytoma

Multiple Myeloma

Multiple myeloma is a neoplastic disorder of plasma B cells characterized by bone marrow infiltration and overproduction of monoclonal immunoglobulins. The two main diffuse patterns are numerous, well-circumscribed punched-out lytic bone lesions and generalized osteopenia (less common and often associated with vertebral compression fractures/vertebra plana). CT findings in multiple myeloma consist of punched-out lytic lesions, expansile lesions with soft-tissue masses, diffuse osteopenia, fractures, and, rarely, osteosclerosis. CT may be useful to determine the extent of extraosseous soft-tissue component in patients with a large disease burden and to assess the risk of fracture in severely affected bones. The follow-up of treated disease may demonstrate the resolution of extramedullary disease and the reappearance of a continuous cortical outline. Fatty marrow content can be seen in these treated cases. A possible advantage of PET over CT is that it can assess continued activity of myeloma in areas of prior bone destruction.

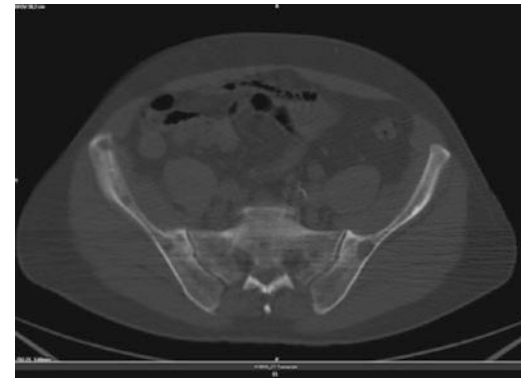

Fig. 6.32 Lytic bone lesions in the pelvis

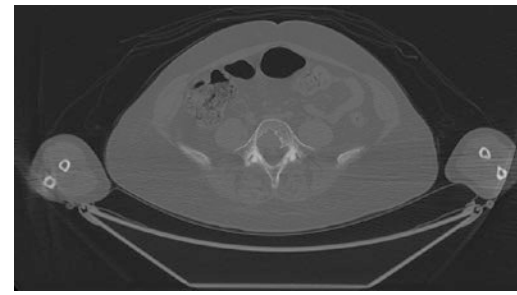

Fig. 6.33 Axial CT images (bone window) showing a large lytic lesion with no osteoblastic reaction in L5 and posterior cortical damage, consistent with multiple myeloma localization

Fig. 6.34 Patient affected by Ewing's sarcoma of the sacrum

Lytic Lesion of the Sacrum

CT scan shows a lytic lesion with minimally sclerotic periosteal reaction. In the staging CT imaging is needed for the evaluation of both the intraosseous extent of the tumor and soft-tissue involvement.

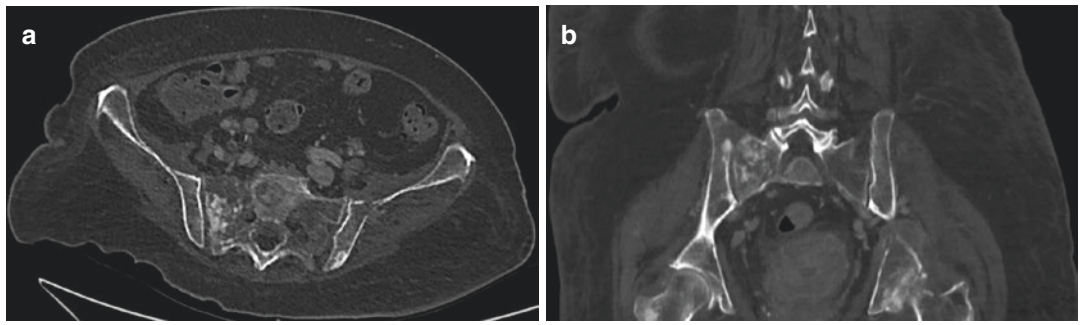

Fig. 6.35 (**a**, **b**) Axial (**a**) and Coronal (**b**) CT images on bone window settings of a lytic lesion of right sacrum

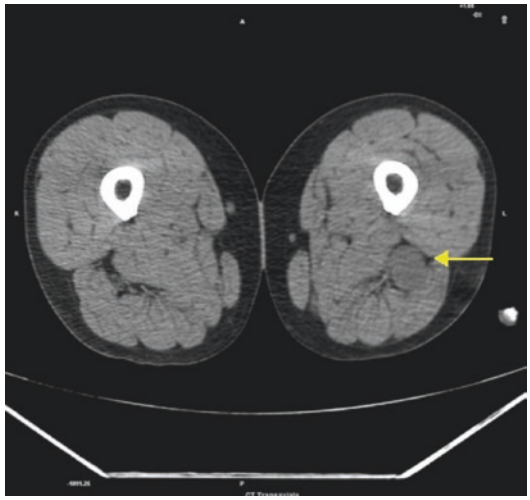

Fig. 6.36 Rounded hypo-dense nodule in the left tight (arrow)

Fig. 6.37 Axial post contrast CT image of a Schwannoma appearing as a rounded hypodense nodule in the context of the left ileo-psoas muscle (white arrow)

Schwannoma

CT scan evidences the presence of a large, sharply delineated, homogeneous, and hypodense (30–40 HU) mass. A schwannoma, also called *neurilemmoma*, is a benign, slow-growing mass or tumor arising from the Schwann cells. Schwann cells are components of myelin sheaths, which cover the axons or branches of nerve cells. They are involved in the proper functioning of nerve cells, in their development and regeneration, and in the conduction of nerve impulses throughout the body. The cause of schwannoma is still unknown. However, individuals who have a family history of neurofibromatosis or von Recklinghausen disease have a higher risk for developing this condition.

Neoplastic Skin Necrosis

Skin necrosis is a condition that usually results in the death of the skin tissue. It occurs typically when insufficient blood and oxygen are supplied to a given skin area. Main causes are wide hematomas and seromas which are unnoticed and untreated for a long period of time, cigarette smoking, and infections.

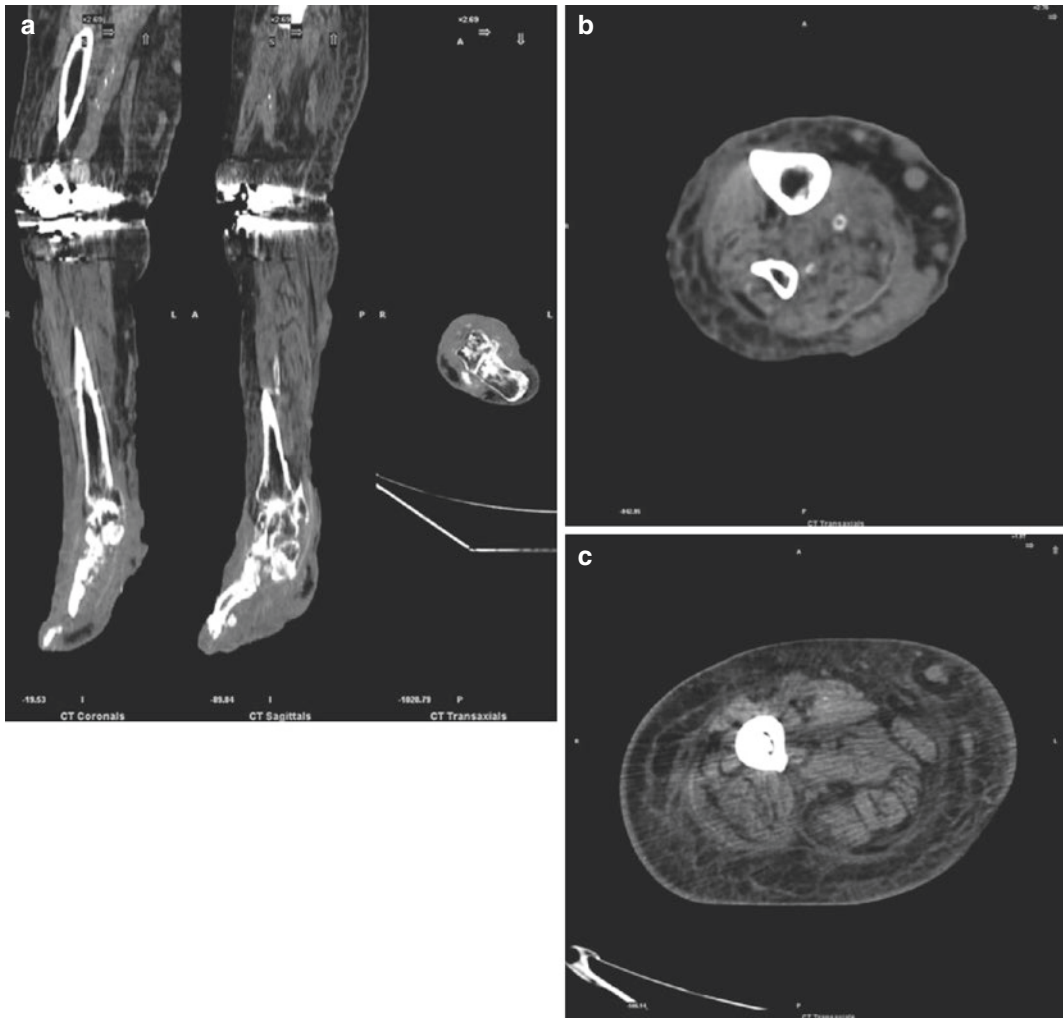

Fig. 6.38 (**a**–**c**) Multiple skin lesions and subcutaneous nodes in the right leg, involving in particular the right foot. History of colon cancer

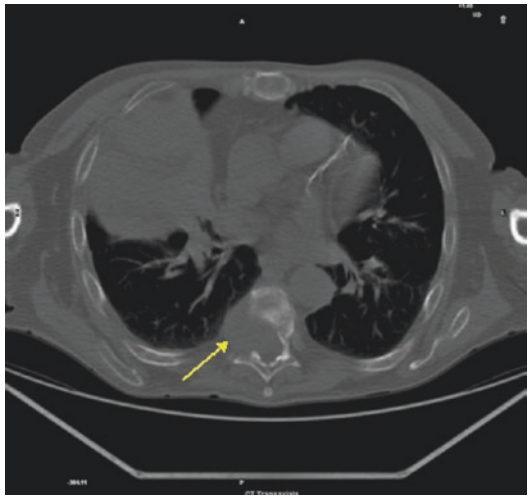

Fig. 6.39 New soft-tissue formation causing bone destruction of the right part of a thoracic vertebral body (arrow) in a patient affected by hepatocarcinoma

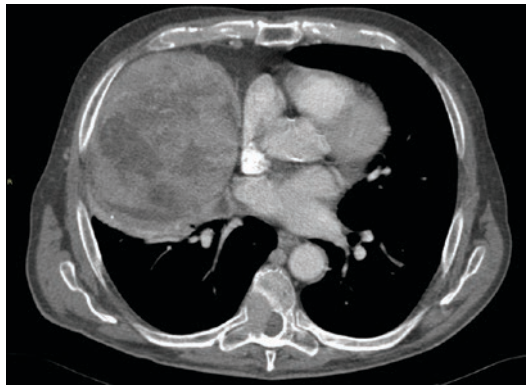

Fig. 6.40 Axial CT post contrast image (venous phase) showing a lytic lesion of the right section of a thoracic vertebral body (arrow) in a patient affected by hepatocarcinoma

Metastatic Hepatocarcinoma

Metastatic lesions at the vertebrae are the most frequent ones with both bone destruction (osteolytic lesions) and soft-tissue formation.

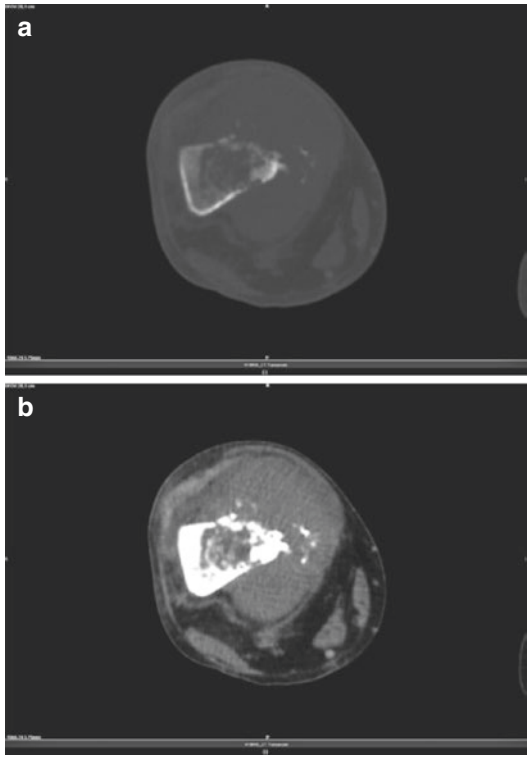

Fig. 6.41 (**a**, **b**) Bony destruction associated with an apparent large effusion

Lymphoma of the Knee

Joint is uncommonly involved by non-Hodgkin's lymphoma (NHL). Musculoskeletal involvement of lymphoma occurs in 25% of patients, typically as metastasis, rarely, as primary lymphoma of bone or soft tissue. Synovial involvement is characterized by nodular deposits of lymphoid infiltrate. A spectrum of morphological changes can be observed: subchondral sclerosis, regional osteopenia, effusion, and bone lytic lesions. Minimal cortical bone abnormality despite an accompanying soft-tisue mass is a characteristic of lymphoma of bone.

Fig. 6.42 Axial (**a**), Sagittal (**b**) and coronal (**c**) images of the right knee on bone window setting showing a lytic lesion of the tibial ephyfisis (white arrow): this is one presentation of skeletal lymphoma

Septic Arthritis of the Knee

It is a destructive arthropathy caused by intra-articular infection. It is usually secondary to hematogenous seeding, whenever trauma or recent instrumentation of the joint can be excluded. Large joints with abundant blood supply to the metaphyses are most affected by bacterial infection. Indeed most commonly involved joints are shoulder, hip, and knee.

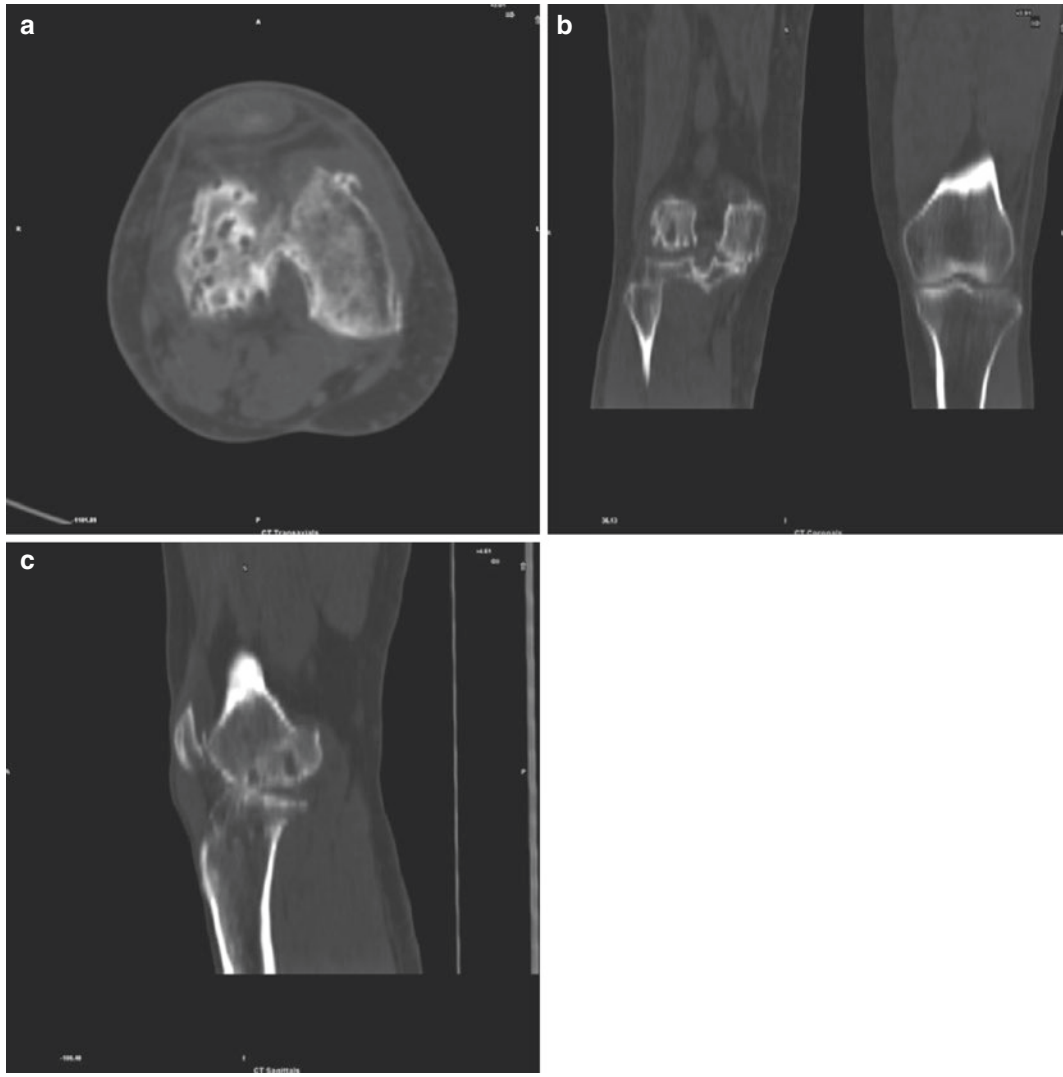

Fig. 6.43 (**a**–**c**) Post-surgical changes and signs of bone remodelling and erosion of the knee. Severe arthritic-degenerative process with joint narrowing. Evidence of multiple diffuse lytic lesions. Moderate joint effusion with synovial and soft-tissue thickening and hyperaemia

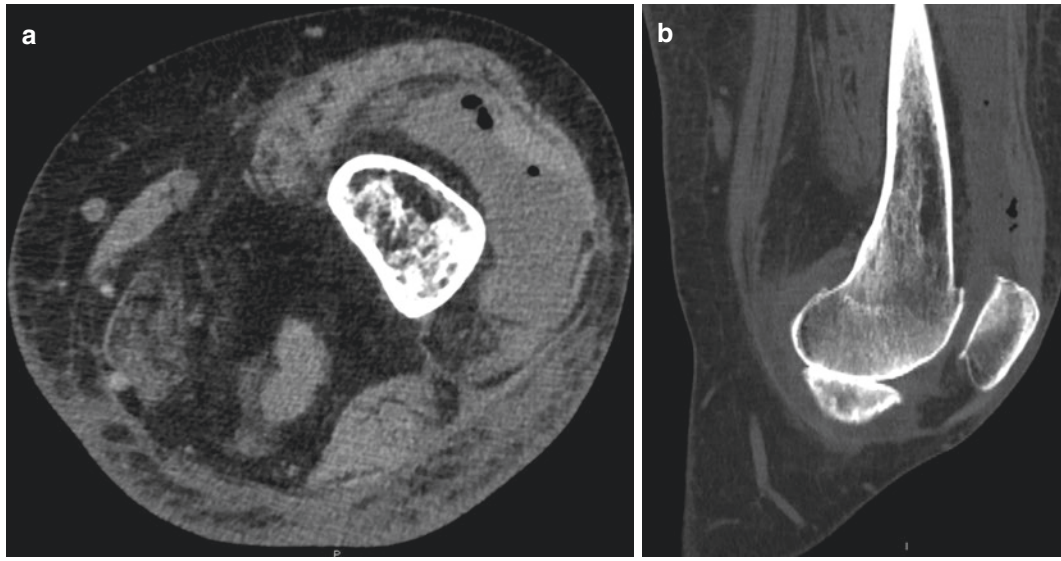

Fig. 6.44 (**a**, **b**) Axial (**a**) and Sagittal (**b**) images of the knee showing periarticular fluid with contestual air bubbles typical for sepctic arthritis